UNIVERSITY OF CAPE TOWN

Non-Holonomic Constraints and Jet Quenching in QCD

Ben Bert

Supervisor:

Assoc. Prof. W. A. Horowitz

August 2026

Thesis presented for the degree of Master of Science in the Department of Physics, University of Cape Town

DEPARTMENT OF
PHYSICS
UNIVERSITY OF CAPE TOWN

Abstract

This thesis presents two complementary investigations into gauge theory, ranging from mathematical foundations of classical field theory to a phenomenological application of quantum chromodynamics (QCD).

In the first part, we re-examine the derivation of the equations of motion from an action principle for classical field theories with non-holonomic constraints, *i.e.*, constraints involving derivatives of the fields. We find that the usual method for gauge fixing in classical and quantum field theories is highly non-trivial for non-holonomic gauge constraints, such as the Coulomb and Lorenz gauges. The subtlety appears at the use of the so-called transposition rule, $\delta(\partial_\nu A^\mu) = \partial_\nu(\delta A^\mu)$, which has been shown not to hold for general non-holonomic constraints in the point-particle context. We provide a sufficient definition of integrable non-holonomic constraints in classical field theory that allows us to prove that the transposition rule holds for all theories with these constraints; we are then able to recover the usual treatment of gauge fixing for gauges of this type.

In the second part, we compute high-p_T R_{AB}, v_2, and v_3 using a perturbative quantum chromodynamics-based energy loss framework that dynamically samples event-by-event hydrodynamic evolution of the medium and incorporates finite path-length corrections appropriate for small collision systems. Our predictions for $\mathrm{Ne} + \mathrm{Ne}$ and $\mathrm{O} + \mathrm{O}$ are in quantitative agreement with recently published R_{AA} data. Strikingly, despite the non-trivial suppression of the charged-particle spectra, we find $v_2 \approx 0$ across all centralities for both symmetric and asymmetric small systems. We argue that any final-state energy loss model will generically predict $v_2 \approx 0$ when v_2 is calculated through hard-soft correlations owing to a fundamental geometric decorrelation between the participant planes of the hard and soft sectors in small systems.

Contents

List of Figures

Acknowledgments

My deepest gratitude goes to my supervisor, A/Prof. Will Horowitz, whose guidance has shaped not just this work but my entire understanding of what it means to do research in physics. What I appreciate most is the degree to which A/Prof. Will Horowitz goes beyond what is expected of a supervisor, his commitment to his students and the standards he holds himself to are commendable.

I would also like to thank Coleridge Faraday for his help with the countless technical challenges that arose throughout this work—from getting the HPC up and running, to the many hours spent at the whiteboard, to even debating the finer points of plotting aesthetics. This work simply would not have been possible without him.

Further, I would like to thank the South African National Research Foundation (NRF), the National Institute for Theoretical and Computational Sciences (NITheCS), and the SA-CERN collaboration for their generous financial support during this work.

Conversations with Wenbin Zhao, Isobel Kolbé, Alexander Rothkopf, and Eder Kikianty were particularly insightful. Computations were performed using facilities provided by the University of Cape Town's ICTS High Performance Computing team: hpc.uct.ac.za – https://doi.org/10.5281/zenodo.10021612

The cohort of graduates at UCT made my MSc experience an enjoyable experience, I will treasure the many breakfast and lunch breaks spent with them.

I would also like to thank my grandparents, Gramps and Gran, for the obvious financial support they provided me with; but beyond that I would like to thank them for giving me the confidence to actually pack up my bags and come down to Cape Town all on my own and complete an MSc!

Lastly, I would like to thank my mother Gaëlle and sibling Jo for all the emotional support they provided. This year was stressful and filled with much self-doubt, but Gaëlle and Jo provided me with a calming escape from it all.

For Dad

Chapter 1

Introduction

1.1 Motivation

1.1.1 From the Greeks to the Quarks

What is matter made of and how does it behave? Few questions have played a more prominent role in the development of human intellect. This thesis is oriented toward the most fundamental level at which these questions can presently be posed.

The earliest attempts to understand the structure and dynamics of matter came from Greek abstractions. Empedocles [1] proposed that all matter is composed of four fundamental elements: earth, water, air, and fire. In contrast, Leucippus and Democritus [2] argued that matter must ultimately consist of indivisible and indestructible particles moving through empty space, which they termed *atomos*. Aristotle [3] rejected this atomistic view in favour of a continuous theory of matter built from the four classical elements of Empedocles, and his framework dominated Western thought for nearly two millennia.

The structure and dynamics of matter remained a subject of philosophical enquiry until the Scientific Revolution shifted the study of Nature toward an epistemology

grounded in systematic observation and experimentation. Lavoisier's [4] work on the conservation of mass and the classification of chemical elements laid the foundations for Dalton's revival of atomic theory. Dalton [5] proposed that each chemical element corresponds to a distinct and indivisible atom, with compounds formed through atoms combining in fixed ratios. Later, Mendeleev's [6] construction of the periodic table in 1869 organized the known elements into a coherent pattern, hinting at a deeper underlying structure that remained to be discovered.

That deeper structure began to emerge at the turn of the twentieth century. Thomson's discovery of the electron in 1897 [7] demonstrated for the first time that atoms are not indivisible. Shortly thereafter, Einstein's theoretical explanation of Brownian motion [8] placed the physical existence of atoms beyond reasonable doubt.

Rutherford's scattering experiments in 1911 revealed that an atom's mass and positive charge are concentrated in a small, dense nucleus [9]. Bohr's subsequent quantized model of the atom [10] provided an important, but *ad hoc*, step towards understanding atomic structure from a theoretical perspective. Bohr's model was later placed on a firmer theoretical foundation by the development of quantum mechanics through the work of Heisenberg, Dirac, Pauli, and Schrödinger [11–14]. The modern picture of atomic structure was not completed until Chadwick's discovery of the neutron in 1932 [15], which established that the atom's nucleus is composed of both protons and neutrons.

Over the following decades, the description of the internal structure of matter became considerably more complicated. Cosmic ray studies [16] and early accelerator experiments [17] uncovered a rapidly growing "zoo" of seemingly elementary particles, presenting a level of complexity that the early Greeks would likely have found deeply unsatisfying. Seeking a more elegant description, Gell-Mann [18] and Zweig [19] independently proposed in 1964 that the zoo of particles could be understood as bound states of a more fundamental and smaller set of degrees of freedom. Gell-Mann [20] named these degrees of freedom "quarks", after Joyce's line in *Finnegans Wake*, "Three quarks for Muster Mark!" [21]—a nod both playful and apt, since the earliest quark models required precisely three quarks to build a baryon. A few years later, deep inelastic scattering experiments at SLAC [22, 23] revealed that protons contain point-

like constituents, providing compelling evidence that quarks correspond to physical objects rather than purely mathematical figments of the theorist's mind. This picture was placed on firm theoretical footing by Bjorken [24], who predicted that the structure functions measured in deep inelastic experiments should exhibit *scaling*, and by Feynman [25], who introduced the parton model to explain this behavior in terms of point-like, quasi-free constituents inside the proton.

The theoretical framework describing the dynamics of quarks, known as the *strong force*, soon followed with the formulation of Quantum Chromodynamics (QCD) whose key property of asymptotic freedom was established by Gross, Wilczek, and by Politzer [26, 27]. The strong force together with the electroweak theory—developed by Glashow, Weinberg, and Salam [28–30]—completed the Standard Model of particle physics, leaving quarks confined within hadrons as the deepest layer of matter's structure confirmed to date.

QCD is on par with humanities most fundamental experimentally verified description of matter and forms the theoretical foundation for the work presented in this thesis.

1.1.2 QCD: The theory of the strong force

Quantum Chromodynamics is a non-Abelian gauge theory, built on an $SU(3)$ colour symmetry, that describes the interactions of quarks *via* the exchange of gluons. Two of QCD's most striking properties—*asymptotic freedom* and *confinement*—together explain why quarks behave as nearly free particles at short distances while never being observed in isolation at long distances [31, 32].

Asymptotic freedom, discovered by Gross, Wilczek, and Politzer [26, 27], states that the strong coupling, α_s, decreases with increasing momentum transfer. In Fig. 1.1, experimental measurements of the running of the coupling are shown in comparison to theoretical computations performed at five loops. The quantitative agreement between high-precision QCD predictions and experimental extractions of α_s, performed using

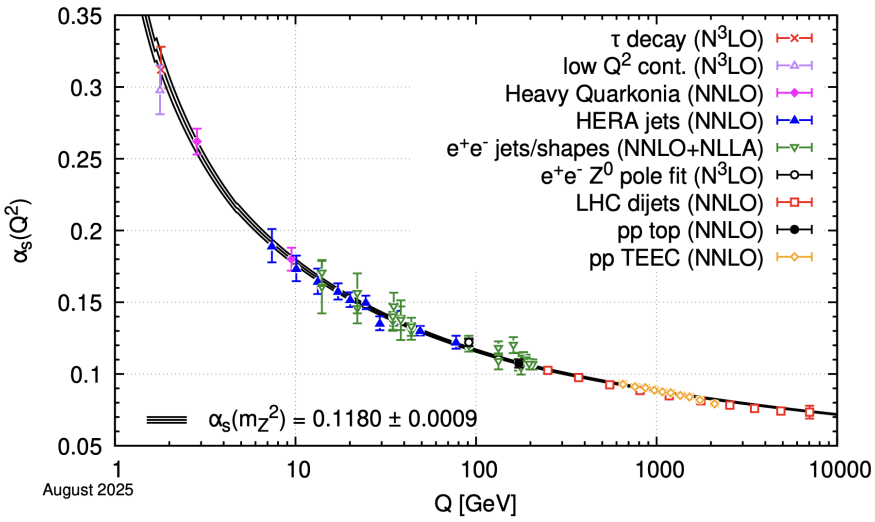

Figure 1.1: Summary of determinations of α_s as a function of the energy scale Q compared to the running of the coupling computed at five loops. Figure taken from [33].

vastly different experimental techniques, constitutes powerful evidence for the validity of QCD as the correct theory of the strong interaction.

Lattice QCD simulations show that coloured states cannot exist as isolated particles, but must rather combine to form colour-neutral bound states, a phenomenon known as confinement. Confinement manifests through hadronization: a quark or gluon produced in a collision does not appear in a detector as a free colour charged particle, but rather fragments into a collimated spray of colour-neutral hadrons, observed as a jet [34, 35].

The mathematical framework describing QCD is known as a gauge theory. Like all gauge theories, QCD possesses a mathematical redundancy in its description of Nature: distinct mathematical configurations can correspond to the same physical state, and this redundancy must be removed through a choice of gauge constraint [36–38]. The typical choices of gauge constraints in QCD involve space-time derivatives of the gauge fields, and are thus the field-theoretic analog of *non-holonomic* constraints in classical point-particle mechanics. The subtleties involved in fixing such a gauge are the subject of the first half of this thesis.

Despite QCD's success as a fundamental theory of quarks and gluons, many questions concerning the emergent behaviour of strongly interacting matter remain elusive. In particular, how QCD matter behaves under the extreme temperatures and densities

realized in heavy-ion collisions remains an active area of both theoretical and experimental investigation, and it is to this subject that the second half of this thesis is devoted.

1.2 Relevant Concepts and Current Problems

1.2.1 Constrained classical mechanics

Here, we discuss some important concepts in constrained classical mechanics and discuss how they relate to the work presented in this thesis: we define what is meant by a holonomic and non-holonomic constraint in classical point-particle mechanics, present the physical equations for a classical point-particle system constrained by non-holonomic constraints and discuss why these equations of motion cannot be derived from Hamilton's variational principle, and finally discuss how non-holonomic constraints arise in gauge theories like QCD.

1.2.1.1 Holonomic and non-holonomic constraints in classical point-particle mechanics

Suppose we have d dimensions of space and a system of N particles; let q_j with $j = 1, \ldots, n = d \times N$ denote the j^{th} generalized coordinate of the system. A *constraint*

$$g_k(q_1, \ldots, q_n, \dot{q}_1, \ldots, \dot{q}_n) = 0, \quad k = 1, \ldots, M < n, \tag{1.1}$$

is a restriction on the motion of the system, which reduces the number of independent degrees of freedom by imposing a relationship between the coordinates and/or velocities of the particles. A *holonomic* constraint is a constraint that can be expressed as a function of the coordinates alone, while a *non-holonomic* constraint is a constraint that is expressed as a function of the velocities and potentially the coordinates. For example,

a pendulum of length L is a holonomic constraint defined by

$$g_{\text{pendulum}}(x, y) \equiv L^2 - x^2 - y^2 = 0. \tag{1.2}$$

The following constraint

$$g_{\text{nh}}(x, y, \dot{x}, \dot{y}) \equiv x\dot{x} + y\dot{y} = 0, \tag{1.3}$$

is an example of a non-holonomic constraint, as it involves the velocities of the particles. A non-holonomic constraint is said to be *integrable* if it can be expressed as a total time derivative of a holonomic constraint. Note that $g_{\text{nh}}(x, y, \dot{x}, \dot{y})$ is integrable, as it can be expressed as

$$g_{\text{nh}}(x, y, \dot{x}, \dot{y}) = \frac{d}{dt}\left(-\frac{1}{2} g_{\text{pendulum}}(x, y)\right), \tag{1.4}$$

since $-(1/2)g_{\text{pendulum}}$ is clearly a holonomic constraint. A non-holonomic non-integrable constraint is one that cannot be expressed as a total time derivative of a holonomic constraint. For example, the constraint

$$g_{\text{nh,non-int}}(x, \dot{y}) = x + \dot{y} = 0, \tag{1.5}$$

is non-holonomic non-integrable.

1.2.1.2 Equations of motion for point particle systems under non-holonomic constraints

Given that a system is constrained by M non-holonomic constraints of the form eq. 1.1, the physical trajectories of the particles in the system are determined by the following equations of motion [39]

$$\frac{d}{dt}\left(\frac{\partial L}{\partial \dot{q}_j}\right) - \frac{\partial L}{\partial q_j} = \lambda_k \frac{\partial g_k}{\partial \dot{q}_j}, \tag{1.6}$$

supplemented with n initial conditions for the generalized coordinates and the M constraints from eq. 1.1. In eq. 1.6, L is the Lagrangian of the system, and the λ_k are M Lagrange multipliers. We present a derivation of eq. 1.6 in appendix A.

Now, as pointed out by Flannery [39], the equations of motion in eq. 1.6 cannot be derived from Hamilton's variational principle [40], which states that the physical trajectories of a system are those which extremize the action. Traditional variational treatments of Hamilton's principle with non-holonomic constraints lead to the so-called *vakonomic* equations of motion; these equations are not equivalent to the physical equations of motion in eq. 1.6, and thus do not reproduce what is observed in Nature [41].

The failure of Hamilton's variational principle to reproduce the physical equations of motion for systems under non-holonomic constraints arises as the transposition rule

$$\delta(\dot{q}_j) = \frac{d}{dt}(\delta q_j), \tag{1.7}$$

does not hold for general non-holonomic constraints. Flannery [39] showed that the transposition rule in eq. 1.7 should be modified so that $\delta(\dot{q}_j)$ and δq_j must satisfy the following

$$\delta g_k - \frac{d}{dt}\left[\left(\frac{\partial g_k}{\partial \dot{q}_j}\right)\delta q_j\right] = \left(\frac{\partial g_k}{\partial \dot{q}_j}\right)\left[\delta\dot{q}_j - \frac{d}{dt}\left(\delta q_j\right)\right] - g_{kj}\delta q_j, \tag{1.8}$$

where

$$g_{kj} = \frac{d}{dt}\left(\frac{\partial g_k}{\partial \dot{q}_j}\right) - \frac{\partial g_k}{\partial q_j}. \tag{1.9}$$

Equation 1.8 can be shown to reduce to eq. 1.7 when the constraints are holonomic or integrable non-holonomic.

1.2.1.3 Gauge fixing in classical field theory

A gauge theory is a theory that possesses a mathematical redundancy in its description of Nature. Distinct mathematical configurations correspond to the same physical state [36–38]. QCD is an example of a gauge theory [31]. The process of removing the mathematical redundancy from a gauge theory is known as gauge fixing.

As an example of a simple gauge theory, we consider the Abelian theory of classical electromagnetism; the theory of electromagnetism is described by the Lagrangian

$$\mathscr{L}_{U(1)} \equiv -\frac{1}{4}F^{\mu\nu}F_{\mu\nu}. \tag{1.10}$$

In eq. 1.10, $F^{\mu\nu} \equiv \partial^\mu A^\nu - \partial^\nu A^\mu$ is the field strength tensor, with the metric given by $\eta_{\mu\nu} = \text{diag}(+ - - -)_{\mu\nu}$.

The Lagrangian in eq. 1.10 is invariant under the gauge transformation [36–38]

$$A^\mu \to A^\mu + \partial^\mu \Lambda, \tag{1.11}$$

where Λ is an arbitrary scalar field. By transforming the A^μ fields through eq. 1.11, the physical quantities of the theory—*i.e.* the electric, $\vec{E}$, and magnetic, $\vec{B}$, fields—are invariant. The invariance of the electric and magnetic fields, despite the transformation of the A^μ fields through eq. 1.11, is precisely the mathematical redundancy we previously alluded to.

Without gauge fixing, path integrals over the Lagrangian in eq. 1.10 would be ill-defined, as functional integration over the physically equivalent gauge fields leads to divergences [42]. Furthermore, the classical equations of motion derived from eq. 1.10 cannot be inverted, and thus no well-defined propagator exists to describe the evolution of the gauge field [42]. Analogous conclusions can be drawn for non-Abelian gauge theories, such as QCD.

In order to remove the redundancy in a general gauge theory, one may gauge fix the theory by imposing a constraint on the gauge field. Common gauge constraints for the electromagnetic field are

$$\partial_\mu A^\mu = 0 \quad \text{Lorenz gauge}, \tag{1.12a}$$

$$\nabla \cdot \mathbf{A} = 0 \quad \text{Coulomb gauge}, \tag{1.12b}$$

$$A^0 = 0 \quad \text{Temporal gauge}, \tag{1.12c}$$

and are defined analogously for QCD. Notice that the Lorenz and Coulomb gauges involve space-time derivatives of the gauge field. Constraints that involve space-time derivatives of the fields are the field theoretic analog of non-holonomic constraints in classical point-particle mechanics.

As was pointed out in Sec. 1.2.1.2, non-holonomic constraints in classical point-particle mechanics cannot be treated using Hamilton's variational principle, and one

would expect the same subtlety to arise—if not, become more pronounced—in classical field theory. In particular, applying Hamilton's principle to gauge theories with non-holonomic gauge constraints might be expected to produce field-theoretic analogs of the vakonomic equations of motion, which would fail to produce the physical equations of motion realized by nature. This potential failure might then be attributed to a breakdown of the field-theoretic analogue of the transposition rule, *i.e.* just as the point-particle relation

$$\delta(\dot{q}_j) = \frac{d}{dt}(\delta q_j), \tag{1.13}$$

fails to hold for general non-holonomic constraints, one would conjecture that

$$\delta(\partial_\nu A^\mu) = \partial_\nu(\delta A^\mu), \tag{1.14}$$

fails to hold for general non-holonomic gauge constraints in field theory. In particular, one would expect that the field-theoretic analogue of Flannery's modified transposition rule in eq. 1.8 would be required for general non-holonomic gauge constraints, and that this modified transposition rule, in the case of integrable non-holonomic constraints (should such a concept exist), would reduce to the standard transposition rule.

These questions have not (as of yet) been identified nor addressed in the literature, and are the subject of the first half of this thesis (see Chapter 2).

1.2.2 High energy phenomenology and the quark-gluon plasma

In this section, we review some important concepts in high energy phenomenology and discuss how they relate to the work presented in this thesis. We discuss the state of matter known as the quark-gluon plasma (QGP), and how high energy partons can be used as probes of the QGP, and finally, we discuss the current open questions in the field of QGP physics that motivate the work presented in this thesis.

1.2.2.1 *What is the QGP?*

In the moments immediately following the Big Bang, the early universe is believed to have existed as a hot, dense soup of deconfined quarks and gluons—a state of matter known as the QGP—rather than as the confined hadrons observed in the universe today [43, 44]. Heavy-ion collision experiments at facilities such as the Relativistic Heavy Ion Collider (RHIC) and the Large Hadron Collider (LHC) recreate the extreme temperatures and energy densities of the early universe by colliding heavy nuclei, such as gold or lead, at ultra-relativistic speeds [45–49].

The study of QGP physics is not primarily concerned with testing the fundamentals of QCD itself, but rather with understanding how collective, many-body phenomena emerge from the underlying microscopic theory. In this sense, the QCD Lagrangian is to QGP physics like the Schrödinger equation is to condensed matter physics. That is: the fundamental equations are taken as given, it is the emergent macroscopic behaviour of the many-body system described by the fundamental equations that is of interest in this field.

A natural question that follows from this emergent perspective is: how many constituent particles are required before such collective behaviour is realized? This question is not unique to heavy-ion physics. Recent ultracold atom experiments have demonstrated that signatures of collective behaviour can emerge in systems of as few as $\mathcal{O}(10)$ interacting particles, despite the apparent inapplicability of a hydrodynamic description on such scales [50]. The analogous question of how few particles are required to generate QGP-like collective behaviour in heavy-ion collisions remains an open and active area of research [51–55], and is one of the central motivations for the study of small collision systems undertaken in the second half of this thesis.

1.2.2.2 *Hard probes: QCD Microscopes*

While the bulk, soft constituents of the QGP are well described by relativistic hydrodynamics [56–61], additional insight into the medium's microscopic properties can be obtained through so-called *hard probes*. Hard probes are high-momentum-transfer par-

tons produced through perturbative QCD processes at the very earliest moments of the collision, prior to the formation of the thermalized medium [62–64]. Because these partons originate from a large momentum transfer, their production cross-sections can be reliably calculated using perturbative QCD, rendering them as well-controlled baselines [65, 66].

Once produced, these hard partons then traverse the surrounding QGP medium before escaping the collision region. During the traversal of the medium, the hard parton interacts with the medium's constituents, and the parton's properties are thereby modified. It is precisely this interaction that is of primary interest, since the details of the parton's modification encode information about the density, temperature, and opacity of the medium through which they traverse [62, 64, 67].

A complication inherent to this approach of studying the QGP is that, due to colour confinement, a hard parton can never be observed directly [31]. After interacting with the medium, the parton hadronizes into a collimated spray of colour-neutral hadrons, observed in a detector as a jet [34, 35]. Consequently, the effects of the QGP on a hard parton are never measured directly; rather, they are inferred indirectly from final-state hadron spectra.

1.2.2.3 Jet quenching observables

One of the interactions that occur between hard partons and the QGP is that of energy loss. As a hard parton traverses the medium, it loses energy through both elastic and inelastic processes, resulting in a modification of the parton's momentum distribution relative to the initial production spectrum [68–72]. The notion that energy loss of energetic partons traversing a QCD medium could lead to an observable suppression of high-momentum hadrons was first proposed by Bjorken [73], and this phenomenon—now commonly referred to as *jet quenching*—is the theoretical framework of the second half of this thesis.

Jet quenching is observed experimentally by comparing the yield of high transverse-momentum (p_T) hadrons produced in heavy-ion (A+B) collisions to the yield produced

in proton-proton (pp) collisions, scaled by the number of binary nucleon-nucleon collisions $\langle N_{\text{coll}} \rangle$. This ratio defines the nuclear modification factor,

$$R_{AB} \equiv \frac{dN^{AB}/dp_T}{\langle N_{\text{coll}} \rangle \, dN^{pp}/dp_T}, \tag{1.15}$$

which, in principle, equals unity in the absence of any medium effects. Experimentally, R_{AB} is observed to be significantly suppressed below unity for high-p_T hadrons produced in heavy-ion collisions [74–77], providing direct evidence for medium-induced parton energy loss.

In Fig. 1.2, we show PHENIX's measured R_{AA} for π^0, η, and direct photons in central $\text{Au} + \text{Au}$ collisions at $\sqrt{s_{NN}} = 200$ GeV [78]. Within experimental uncertainties and for large p_T, the π^0 and η hadrons have an $R_{AA} < 1$ while the photons have an $R_{AA} = 1$. The π^0 and η hadrons are produced from the fragmentation of high energy partons, which lose energy as they traverse the QGP, while the direct photons do not interact with the QGP and thus do not lose energy. The suppression of π^0 and η hadrons, and the lack of suppression of direct photons is thus consistent with the interpretation of partonic energy loss in the QGP.

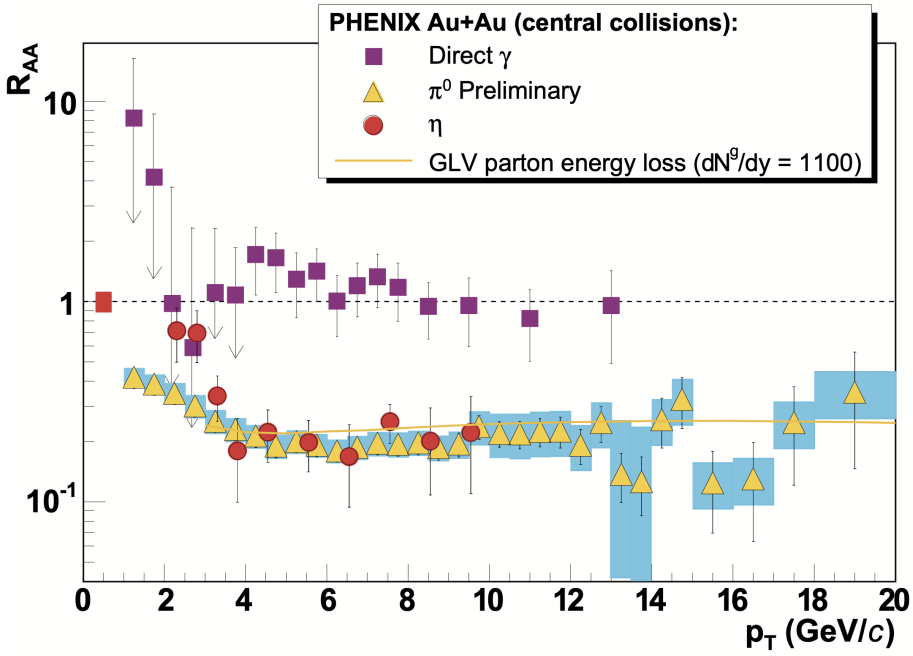

Figure 1.2: Nuclear modification factor, R_{AA} of π^0 (triangles), η (circles), and direct photon (squares). Figure taken from [78].

The magnitude of a parton's energy loss is expected to depend on the path length it traverses through the medium [70, 71, 79–81]: partons traversing a longer path through the QGP are expected to lose more energy than those traversing a shorter path. Since the transverse overlap region of two colliding nuclei is not azimuthally symmetric, partons produced at different azimuthal angles relative to the collision's reaction plane will, on average, traverse different path lengths through the medium. This path-length dependence of the energy loss manifests itself as an azimuthal anisotropy in the yield of final-state high-p_T hadrons; the anisotropy can be characterized through a Fourier decomposition of the form

$$\frac{dN}{d\phi} \propto 1 + 2\sum_{n=1}^{\infty} v_n \cos\left(n\left[\phi - \Psi_n\right]\right), \tag{1.16}$$

where ϕ is the azimuthal angle (relative to the beam pipe) of the observed hadron, Ψ_n is the corresponding reference angle, and the Fourier coefficients v_n quantify the magnitude of the n^{th}-order anisotropy. The second-order coefficient, v_2, encodes the ellipticity of the collision geometry, while the third-order coefficient, v_3, encodes the triangularity of the collision geometry, *etc*.

In Fig. 1.3, we show the measured v_2 of $\pi^{\pm}$, $\mathrm{K}^{\pm}$, $\mathrm{p}+\overline{\mathrm{p}}$, $\Lambda+\bar{\Lambda}$, $\mathrm{K}^0_{\mathrm{S}}$, and the ϕ-meson at 40-50% centrality as a function of p_T [82]. The observed splitting between baryons (made of three quarks) and mesons (made of two quarks) indicates that the energy loss of partons in the QGP is sensitive to the partonic degrees of freedom and not the hadronic degrees of freedom. This is consistent with the expectation that the energy loss occurs at the partonic level, prior to hadronization, and provides further evidence for the existence of a deconfined QGP phase in heavy-ion collisions.

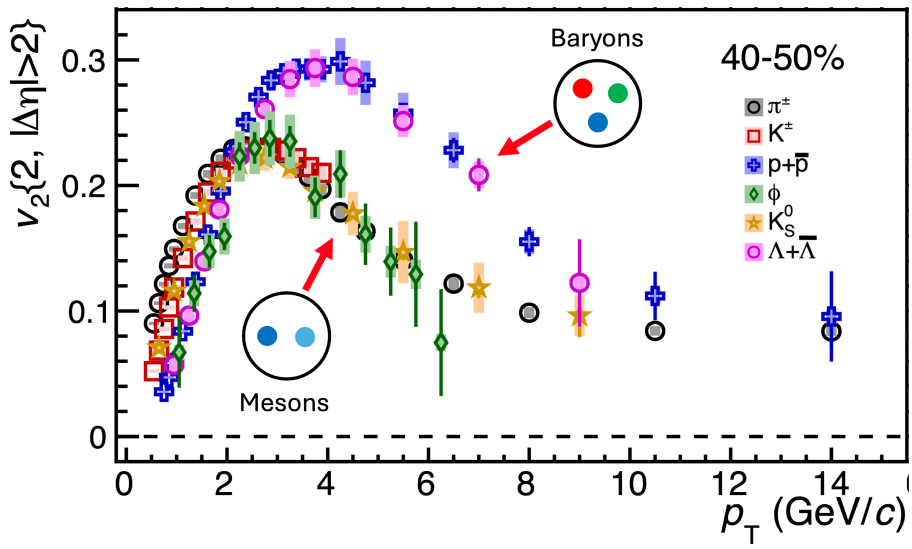

Figure 1.3: The v_2 of $\pi^{\pm}$, $\mathrm{K}^{\pm}$, $\mathrm{p}+\overline{\mathrm{p}}$, $\Lambda+\bar{\Lambda}$, $\mathrm{K}^0_{\mathrm{S}}$, and the ϕ-meson at 40-50% centrality as a function of p_T. Statistical and systematic uncertainties are shown as bars and boxes, respectively. Figure adapted from [82].

1.2.2.4 The $R_{AA} \otimes v_2$ puzzle

A broad class of theoretical models can reproduce the experimentally measured R_{AA} [62, 64, 66]. However, simultaneously describing the azimuthal dependence encoded in the high-p_T v_2 coefficient in conjunction with the R_{AA} has proved to be a considerably more demanding task. Typically, as one tunes a model to reproduce the observed suppression in R_{AA}, the predicted v_2 is systematically under-predicted relative to experimental measurements [83, 84], a tension that has been termed the $R_{AA} \otimes v_2$ *puzzle*.

This puzzle has since been addressed in large collision systems through sufficiently sophisticated energy loss calculations [85–88]. Whether this resolution carries over to small collision systems remains an open question.

The $R_{AA} \otimes v_2$ puzzle in small systems forms the basis for the second half of this thesis, where we endeavour to simultaneously describe R_{AB} and v_n in both large and small collision systems using a pQCD-based energy loss framework (see Chapter 3).

Comment

Chapters 2 and 3 are based on the preprints [89] and [90], respectively. Chapter 2 is an almost verbatim copy of [89], while Chapter 3 presents an expanded version of [90] with additional figures and discussion. The preprint [89] was written with W.A. Horowitz, and the preprint [90] was written with W.A. Horowitz and C. Faraday.

Chapter 2

Integrable Non-Holonomic Constraints and Gauge Fixing in Classical Field Theory

2.1 Introduction

The dynamics of classical field theories are often determined by the Euler-Lagrange equations of motion, derived from Hamilton's principle [40, 91, 92]. Crucial to the derivation of the Euler-Lagrange equations from Hamilton's principle is the *transposition rule*, which in point particle mechanics takes the form

$$\delta\left(\frac{dq^i}{dt}\right) = \frac{d}{dt}\left(\delta q^i\right), \tag{2.1}$$

where q^i is the i^{th} generalized coordinate of the particle. Flannery [39] showed, in the context of point particle mechanics, that the transposition rule does not hold when general non-holonomic constraints $g_j(q^i, \dot{q}^i, t) = 0$ are present, but that the transposition rule does hold when the non-holonomic constraints are integrable, *i.e.*, when the non-holonomic constraints can be expressed as the total time derivative of some func-

tion $f_j(q^i, t)$ that is only dependent on the generalized coordinates q^i and time t

$$g_j(q^i, \dot{q}^i, t) = \frac{df_j(q^i, t)}{dt} = 0. \tag{2.2}$$

Many classical and quantum field theories exhibit gauge symmetry, a reflection of a redundancy in the fundamental degrees of freedom of the theory. For example, the Standard Model of particle physics is constructed using classical gauge-invariant field theories [18, 26–30, 93–95]. Many commonly used gauges, such as the Coulomb and Lorenz gauges, are specified by gauge conditions involving derivatives of the field components. These gauge conditions—which are ubiquitous in the literature [31, 42, 96–104]—therefore impose non-holonomic constraints on the fields.

Traditional treatments of Hamilton's principle for classical field theories under non-holonomic constraints gloss over the subtleties of the functional analysis techniques being utilized; as such, the validity of the transposition rule in the presence of these non-holonomic constraints is often overlooked and simply assumed without justification [31, 42, 96–104]. In this chapter, we present a detailed study of functionals and functional derivatives allowing us to develop the necessary tools to carefully examine the validity of the transposition rule in classical field theories with non-holonomic constraints. We then apply these tools to carefully re-examine the derivation of the equations of motion from Hamilton's principle in the presence of non-holonomic constraints. The results of our careful analysis lead us to conclude that the assumption of the transposition rule is far from trivial in the context of classical field theory. Similar to point particle mechanics, the transposition rule

$$\delta(\partial_\nu A^\mu) = \partial_\nu(\delta A^\mu) \tag{2.3}$$

is expected to not hold for field theories with general non-holonomic constraints.

One is then naturally led to ask: is there a concept of integrability for non-holonomic constraints in field theories, and does the transposition rule hold for field theories with these types of constraints? In this work, we provide a definition of integrable non-holonomic constraints in the context of field theory and show that this defini-

tion is sufficient for the transposition rule to hold under these types of constraints. We show that the Coulomb and Lorenz gauges are particular examples of our definition of integrable, non-holonomic constraints, and thus one can justify the usual gauge fixing treatment of these gauges in classical field theory. In contrast to the Coulomb and Lorenz gauges, there exist gauges used in the literature that are non-holonomic and non-integrable, *e.g.* the 't Hooft-Veltman gauge [105–113]. The 't Hooft-Veltman gauge—as per our definition—constitutes a non-integrable, non-holonomic constraint, and we therefore expect the standard application of Hamilton's principle to fail when fixing to this gauge.

2.2 Proof of the Transposition Rule for Integrable Non-Holonomic Constraints

Suppose we are to impose a constraint g on the spacetime derivatives of the field components $\partial_\nu A^\mu$ of a classical field theory in d dimensions. Here and in what follows, we shall assume that all field components A^μ and their spacetime derivatives $\partial_\nu A^\mu$ belong to the function space of all infinitely differentiable functions on Minkowski spacetime, denoted here as $C^\infty(\mathbb{M})$. The spacetime manifold is taken to be $\mathbb{M} = [t_i, t_f] \times \mathbb{R}^{d-1}$, where $t_i < t_f$ are real numbers and the manifold $\mathbb{M}$ is over a flat metric $\eta^{\mu\nu} = \text{diag}(1, -1, \ldots, -1)$. As is common in the physics literature, we will further require that the A^μ fields vanish at the spatial boundaries of $\mathbb{M}$, *i.e.* $A^\mu(x) = 0$ as $x^i \to \pm\infty \; \forall \; i \in \{1, \ldots, d-1\}$; by imposing such a condition, we are excluding the possibility of plane wave solutions.

We shall further require that the constraint g is satisfied for all spacetime points $x \in \mathbb{M}$, so that we may write

$$g[\partial_\nu A^\mu](x) = 0, \quad \forall x \in \mathbb{M}, \tag{2.4}$$

where the square brackets indicate that g depends functionally on derivatives of the

field components $\partial_\nu A^\mu$, and the parentheses indicate dependence on the spacetime point x. The derivatives of the field components $\partial_\nu A^\mu$ are to be considered as independent from the field components A^μ as is usually done in the literature [31, 42, 96–104].

Now consider the following vector functional $f^\nu = f^\nu[A^\mu](x)$, which is dependent on the field components A^μ but independent of the spacetime derivatives of the field components $\partial_\nu A^\mu$. Suppose that one of the field components, which we will denote as A^{μ_D}, is specially singled out by f^ν in the sense that one of the spatial components of the vector functional f^ν can be written as[1]

$$f^{\mu_D} = A^{\mu_D} \text{ for some } \mu_D \in \{1, \ldots, d-1\}, \tag{2.5}$$

and that the remaining components of f^ν are independent of A^{μ_D}, *i.e.*

$$f^\nu = f^\nu[A^\mu : \mu \neq \mu_D](x) \text{ for all } \nu \neq \mu_D. \tag{2.6}$$

The field component A^{μ_D} will be referred to as the *dependent* field component, and we will refer to the remaining field components A^μ with $\mu \neq \mu_D$ as the *independent* field components. Lastly, we will require that f^ν with $\nu \neq \mu_D$ can be written as functional power-series of the independent field components A^μ with $\mu \neq \mu_D$; *i.e.*

$$f^\nu(x) = \sum_{I=0}^{\infty} c^\nu_{i_0,\ldots,i_{d-1}} (A^0(x))^{i_0} \ldots (A^{\mu_D-1}(x))^{i_{\mu_D-1}} (A^{\mu_D+1}(x))^{i_{\mu_D+1}} \ldots (A^{d-1}(x))^{i_{d-1}}, \tag{2.7}$$

where the coefficients $c^\nu_{i_0,\ldots,i_{d-1}}$ are real numbers, and the index set I runs over all $d-1$ tuples of non-negative integers $\{i_0, \ldots, i_{\mu_D-1}, i_{\mu_D+1} \ldots, i_{d-1}\}$.

Our proof of the transposition rule shall be presented for *integrable non-holonomic* constraints, which we define to mean that the non-holonomic constraint g can be expressed as the covariant divergence of a vector functional f^ν which satisfies the conditions mentioned above; *i.e.*

$$0 = g[\partial_\nu A^\mu](x) \equiv \sum_{\nu=0}^{d-1} \partial_\nu f^\nu[A^\mu](x), \quad \forall x \in \mathbb{M}, \tag{2.8}$$

[1] One could take $f^{\mu_D} = r A^{\mu_D}$ for some $r > 0$; in such a case, one could just rescale all field components by $1/r$ to recover eq. 2.5.

For the sake of simplicity, we shall restrict ourselves to the case where g and f^ν are only implicitly dependent on the spacetime coordinates x through their dependence on the derivatives of the field components $\partial_\nu A^\mu$ and the field components A^μ, respectively. In this chapter, we make use of explicit summation—rather than the Einstein summation convention—to prevent possible confusion later, as the summation will often be limited to run over a subset of the field components. We would like to further point out that the definition of integrability we have given in eq. 2.8 includes the restrictions we have imposed on the vector functional f^ν; thus, the integrability condition in eq. 2.8 is a *sufficient* condition for the transposition rule to hold, but it is not—as far as the authors can tell—a *necessary* condition. Our definition of integrability will, however, be general enough to include the Coulomb and Lorenz gauges as particular examples (see Sec. 2.3.2 for further details).

With these conventions in place, we have the following:

$$\partial_{\mu_D} f^{\mu_D}[A^{\mu_D}](x) = -\sum_{\nu\neq\mu_D} \partial_\nu f^\nu[A^\mu : \mu \neq \mu_D](x) \tag{2.9a}$$

$$\implies A^{\mu_D}[A^\mu : \mu \neq \mu_D](x) = -\int_{-\infty}^{x^{\mu_D}} d\tilde{x}^{\mu_D} \sum_{\nu\neq\mu_D} \partial_\nu f^\nu[A^\mu : \mu \neq \mu_D](x^0, \ldots, \tilde{x}^{\mu_D}, \ldots, x^{d-1}), \tag{2.9b}$$

where we have used the assumption that the field component A^{μ_D} vanishes as $x^{\mu_D} \to -\infty$. If we had allowed $\mu_D = 0$ in eq. 2.5 then we would have required A^0 vanishes as $x^0 \to -\infty$, which is generally an undesirable condition. In what follows, it will be useful to define the following functional

$$B = B[\partial_\nu A^\mu : \nu, \mu \neq \mu_D](x) \equiv -\sum_{\nu\neq\mu_D} \partial_\nu f^\nu[A^\mu : \mu \neq \mu_D](x). \tag{2.10}$$

Equation 2.10 will then allow us to rewrite eq. 2.9b as

$$A^{\mu_D}[\partial_\nu A^\mu : \nu, \mu \neq \mu_D](x) = \int_{-\infty}^{x^{\mu_D}} d\tilde{x}^{\mu_D}\, B[\partial_\nu A^\mu : \nu, \mu \neq \mu_D](x^0, \ldots, \tilde{x}^{\mu_D}, \ldots, x^{d-1}). \tag{2.11}$$

2.2.1 Functional Calculus with Dependent Field Components

As is evident from eq. 2.11, the non-holonomic constraint g resulted in the A^{μ_D} field component being functionally dependent on the derivatives of the independent field components $\partial_\nu A^\mu$ with $\nu, \mu \neq \mu_D$. We are ultimately interested in computing all the variations $\delta(\partial_\nu A^\mu)$ of the derivatives of the field components A^μ; thus, we are tasked with defining the variation of the independent field components $A^\mu \in C^\infty(\mathbb{M})$ with $\mu \neq \mu_D$. Due to the functional dependence of A^{μ_D}, we should expect that the variations δA^{μ_D} of the dependent field component will induce variations in the independent field components; likewise, we should expect the derivatives of the dependent field component $\partial_\nu A^{\mu_D}$ to induce derivatives in the independent field components $\partial_\nu A^\mu$. The purpose of this section is to make these expectations precise. In this section we will adapt the approaches taken in [114–117] to develop the functional framework necessary to prove the transposition rule.

We begin by defining a *functional* F as a map from the space of n-tuples of infinitely differentiable functions on $\mathbb{M}$, denoted as $(C^\infty(\mathbb{M}))^n$, to the real numbers $\mathbb{R}$, where $n \in \mathbb{N}$. We denote the space of all such functionals by $\mathscr{F}$; *i.e.*

$$F \in \mathscr{F} \implies F[h_1(\cdot), \ldots, h_n(\cdot)] \in \mathbb{R} \quad \forall\, (h_1, \ldots, h_n) \in (C^\infty(\mathbb{M}))^n. \tag{2.12}$$

In eq. 2.12, we use the notation $(\cdot)$ to indicate that each function h_i requires an argument from $\mathbb{M}$; we will use the notation (x) to indicate that we are evaluating the argument $(\cdot)$ at the specific point $x \in \mathbb{M}$. Now, to define a *functional derivative*, we consider the following object

$$F(\alpha|\gamma_i) \equiv F[h_1(\cdot), \ldots, h_i(\cdot) + \alpha\gamma_i(\cdot), \ldots, h_n(\cdot)], \tag{2.13}$$

where $F(\alpha|\gamma_i)$ is to be understood as a function of the real, spacetime independent parameter α; furthermore, the $\gamma_i \in C_c^\infty(\mathbb{M})$ in eq. 2.13 is a test function from the space of all infinitely differentiable functions with compact support that vanish at the temporal boundaries—*i.e.* $\gamma_i(x) = 0 \;\forall\; x \in \{t_i, t_f\}$. By ensuring that the test functions vanish

at the temporal boundaries, we will be able to make use of integration by parts when applying our formalism to Hamilton's principle in Sec. 2.3.1. In what follows, we will assume that $F(\alpha|\gamma_i)$ is differentiable with respect to α around $\alpha = 0$.

Next, we follow [115] and define a *distribution* as a linear functional D which maps from the space of test functions $C_c^\infty(\mathbb{M})$ to the real numbers $\mathbb{R}$ such that for every compact set $\mathbb{K} \subset \mathbb{M}$, there is a real number $\tau \geq 0$ and an integer $N \geq 0$ such that

$$|D[\gamma(\cdot)]| \leq \tau \sum_{|\kappa| \leq N} \sup_{\mathbb{K}} \left| \frac{\partial^{|\kappa|}\gamma(\cdot)}{\partial x_0^{\kappa_0} \cdots \partial x_{d-1}^{\kappa_{d-1}}} \right|, \quad \forall\, \gamma \in C_c^\infty(\mathbb{K}), \tag{2.14}$$

where $|\kappa| = \kappa_0 + \ldots + \kappa_{d-1}$ is the magnitude of a multi-index of non-negative integers $\kappa = (\kappa_0, \ldots, \kappa_{d-1})$ and d is the dimension of the manifold $\mathbb{M}$. We shall denote the space of all distributions on $\mathbb{M}$ as $\mathscr{D}'(\mathbb{M})$. The prime on $\mathscr{D}'(\mathbb{M})$ is standard notation used to indicate that the space of distributions is dual to the space of test functions. Note that the inequalities in eq. 2.14 are called semi-norm estimates, and their structure is motivated through topological considerations of the space of test functions $C_c^\infty(\mathbb{M})$; see [115] for further details.

Now, suppose $F : (C^\infty(\mathbb{M}))^n \to \mathbb{R}$ is a functional and define $D_G F_i : C_c^\infty(\mathbb{M}) \to \mathbb{R}$ as

$$D_G F_i[\gamma_i(\cdot)] \equiv \int d^d x \frac{\partial F}{\partial h_i(x)} \gamma_i(x), \tag{2.15}$$

where $\partial F / \partial h_i(x)$ is a function in $C^\infty(\mathbb{M})$. $D_G F_i$ in eq. 2.15 satisfies the conditions in eq. 2.14 [115] and thus $D_G F_i$ is a distribution; furthermore, $D_G F_i$ is uniquely defined by the function $\partial F / \partial h_i(x) \in C^\infty(\mathbb{M})$ up to a set of measure zero [115]. Note that the function $\partial F / \partial h_i(x)$ has no dependence on the test function $\gamma_i(x)$. Now, if the following limit holds for all $\gamma_i \in C_c^\infty(\mathbb{M})$

$$\lim_{\alpha \to 0} \frac{(F(\alpha|\gamma_i) - F(0|\gamma_i)) - \alpha D_G F_i[\gamma_i(\cdot)]}{\alpha} = 0, \tag{2.16}$$

then we call $D_G F_i$ the *Gâteaux derivative* [117–119] of the functional F with respect to the function h_i in the direction of γ_i and $\partial F / \partial h_i(x)$ is the *functional derivative* of F with respect to h_i at the point $x \in \mathbb{M}$. In eq. 2.15, we have left the bounds of integration implicit, but it is to be understood that the integration is over the entire manifold $\mathbb{M}$.

By making use of eq. 2.15 and 2.16, we shall often write the following

$$\int d^d x \frac{\partial F}{\partial h_i(x)} \gamma_i(x) = \left. \frac{\partial F[h_1(\cdot), \ldots, h_i(\cdot) + \alpha\gamma_i(\cdot), \ldots, h_n(\cdot)]}{\partial \alpha} \right|_{\alpha=0} \equiv \lim_{\alpha \to 0} \frac{F(\alpha|\gamma_i) - F(0|\gamma_i)}{\alpha}. \tag{2.17}$$

Taking the Dirac delta distribution $\delta^d(x) = \lim_{\beta \to 0} \delta^d_\beta(x)$ as the limit of a sequence of functions in $C^\infty_c(\mathbb{M})$, one may choose the arbitrary test function as $\gamma_i(x) = \delta^d_\beta(x - y)$ for some fixed but arbitrary $y \in \mathbb{M}$. Equation 2.17 then yields

$$\frac{\partial F}{\partial h_i(y)} = \left. \frac{\partial F[h_1(\cdot), \ldots, h_i(\cdot) + \alpha\delta^d(\cdot - y), \ldots, h_n(\cdot)]}{\partial \alpha} \right|_{\alpha=0}, \tag{2.18}$$

where the limits involved in defining the delta distribution are implied but suppressed for notational simplicity. Notice the use of the notation "$(\cdot - y)$" which indicates that the argument of the function in question (in this case the delta function) is to be shifted by y. In what follows, we shall assume that for all functionals that we consider the limit in eq. 2.16 exists for all test functions in $C^\infty_c(\mathbb{M})$.

Now, we define the variation δF of the functional F as:

$$\delta F \equiv \sum_{i=1}^n \Big(F(\alpha|\gamma_i) - F(0|\gamma_i) \Big) \tag{2.19a}$$

$$= \sum_{i=1}^n \left(\left. \frac{\partial F[h_1(\cdot), \ldots, h_i(\cdot) + \alpha\gamma_i(\cdot), \ldots, h_n(\cdot)]}{\partial \alpha} \right|_{\alpha=0} \right) \alpha + \mathcal{O}(\alpha^2) \tag{2.19b}$$

$$= \sum_{i=1}^n \int d^d x \frac{\partial F}{\partial h_i(x)} \gamma_i(x) \alpha + \mathcal{O}(\alpha^2). \tag{2.19c}$$

In this work, we shall concern ourselves with infinitesimal variations, and thus we shall drop all terms of order $\mathcal{O}(\alpha^2)$ and higher. Note that the variation δF defined in eq. 2.19 is dependent on the choice of $\{\gamma_i : i = 1, \ldots, n\}$, and thus the variation δF is to be thought of as a variation in the directions determined by $\{\gamma_i : i = 1, \ldots, n\}$. To be more precise, one should write δF as $\delta_\gamma F$ to indicate the dependence on the choice of $\{\gamma_i : i = 1, \ldots, n\}$, but this notation will prove to be cumbersome.

Notice that eq. 2.11 implies that the dependent field component A^{μ_D} is functionally dependent on the derivatives of the independent field components $\partial_\nu A^\mu$, with $\nu, \mu \neq \mu_D$; however, A^{μ_D} is also a function of the spacetime coordinates $x \in \mathbb{M}$. Therefore,

A^{μ_D} is a mapping from $(C^\infty(\mathbb{M}))^{d-1}$ to $C^\infty(\mathbb{M})$, rather than a functional as defined in eq. 2.12. We are thus required to consider more general mappings than functionals; we shall refer to these more general mappings as *function-valued functionals*. A function-valued functional G is a map from $(C^\infty(\mathbb{M}))^m$ to $C^\infty(\mathbb{M})$ where $m \in \mathbb{N}$, and we shall denote the space of all such function-valued functionals as $\mathscr{G}$; *i.e.*

$$G \in \mathscr{G} \implies G[h_1(\cdot), \ldots, h_m(\cdot)] \in C^\infty(\mathbb{M}) \quad \forall\, (h_1, \ldots, h_m) \in (C^\infty(\mathbb{M}))^m. \tag{2.20}$$

Note that the variations of function-valued functionals are precisely the variations used in Hamilton's principle in classical field theory; see Sec. 2.3.1 for further details.

Functional derivatives and variations of function-valued functionals may be defined in a manner similar to that of functionals. This becomes clear if one considers the *function-valued functional* $G[\ldots](\circ) \in \mathscr{G}$ as a different *functional* $G[\ldots](x) \in \mathscr{F}$ for each fixed $x \in \mathbb{M}$. Note the use of the $(\circ)$ notation to indicate that the function-valued functional G takes arguments from $\mathbb{M}$, and these arguments are to be distinguished from the arguments of the h_i functions. We refer the reader to appendix B.3 for examples of how the function-valued functional notation is applied.

In what follows, we will need to consider the variations and derivatives of the constraints g and f^ν as well as the variations and derivatives of the dependent field component A^{μ_D}. Since g, f^ν and A^{μ_D} are dependent on the independent field components A^μ and their derivatives $\partial_\nu A^\mu$, with $\nu, \mu \neq \mu_D$, the variations and derivatives of g, f^ν and A^{μ_D} will induce variations on the independent field components and their derivatives. The precise form of these induced variations and derivatives will arise through chain rule type relations for function-valued functionals. The chain rule relations can be proven as a direct consequence of the definitions provided in eq. 2.17 and 2.19, the proofs of which are presented in appendix B.1.

Here, we shall state the relevant chain rule relations required for our proof of the transposition rule: Consider the function-valued functional $G \in \mathscr{G}$, and suppose we compose G with a set of function-valued functionals $\{G^j \in \mathscr{G} : j = 1, \ldots, m\}$; the

following chain rule relations then hold:

$$\frac{\partial G(x)}{\partial h_i(y)} = \sum_{j=1}^{m} \int d^d z \, \frac{\partial G(x)}{\partial G^j(z)} \frac{\partial G^j(z)}{\partial h_i(y)} \tag{2.21a}$$

$$\delta G(x) = \sum_{j=1}^{m} \int d^d z \, \frac{\partial G(x)}{\partial G^j(z)} \delta G^j(z) \tag{2.21b}$$

$$\partial^x_\nu G(x) = \sum_{j=1}^{m} \int d^d z \, \frac{\partial G(x)}{\partial G^j(z)} \partial^z_\nu G^j(z), \tag{2.21c}$$

where we have used the following shorthand notation:

$$G(x) \equiv G[\{G^j[h_1(\cdot), \ldots, h_n(\cdot)](\circ) : j = 1, \ldots, m\}](x) \tag{2.22a}$$

$$\frac{\partial G(x)}{\partial h_i(y)} \equiv \left. \frac{\partial G[\{G^j[h_1(\cdot), \ldots, h_i(\cdot) + \alpha \delta^d(\cdot - y), \ldots, h_n(\cdot)](\circ) : j = 1, \ldots, m\}](x)}{\partial \alpha} \right|_{\alpha=0} \tag{2.22b}$$

$$\frac{\partial G(x)}{\partial G^j(z)} \equiv \left. \frac{\partial G[\ldots, G^j[h_1(\cdot), \ldots, h_n(\cdot)](\circ) + \alpha \delta^d(\circ - z), \ldots](x)}{\partial \alpha} \right|_{\alpha=0} \tag{2.22c}$$

$$\begin{aligned} \delta G(x) \equiv \sum_{i=1}^{n} \Big\{ & G[\{G^j[h_1(\cdot), \ldots, h_i(\cdot) + \alpha \gamma_i(\cdot), \ldots, h_n(\cdot)](\circ) : j = 1, \ldots, m\}](x) \\ & - G[\{G^j[h_1(\cdot), \ldots, h_i(\cdot), \ldots, h_n(\cdot)](\circ) : j = 1, \ldots, m\}](x) \Big\} \end{aligned} \tag{2.22d}$$

$$\partial^x_\nu \equiv \frac{\partial}{\partial x^\nu}. \tag{2.22e}$$

In eq. 2.22, we use the following notation

$$\begin{aligned} G[\{G^j[h_1(\cdot), \ldots, h_n(\cdot)](\circ) : j = 1, \ldots, m\}](x) = G[G^1[h_1(\cdot), \ldots, h_n(\cdot)](\circ), \ldots, \\ G^m[h_1(\cdot), \ldots, h_n(\cdot)](\circ)](x), \end{aligned} \tag{2.23}$$

while in eq. 2.22e, we use ∂^x_ν to denote differentiation with respect to the spacetime coordinates x^ν which is to be distinguished from ∂^z_ν which denotes differentiation with respect to the coordinates z^ν. One should note that the chain rule for the spacetime derivative in eq. 2.21c is only valid when G has the following translational property

$$G[h_1(\cdot + y), \ldots, h_n(\cdot + y)](x) = G[h_1(\cdot), \ldots, h_n(\cdot)](x + y), \tag{2.24a}$$

the restriction of which is not a problem for our purposes as all the function-valued functionals which we will take spacetime derivatives of in our proof of the transposition rule satisfy eq. 2.24. We would like to point out that the function-valued functional G is dependent on the $m \in \mathbb{N}$ function-valued functionals G^j, while we have allowed each of the G^j function-valued functionals to depend on $n \in \mathbb{N}$ functions h_i, where m and n need not be equal. In principle, each of the G^j function-valued functionals may depend on a different number of functions n_j; we take n to be the maximum of all n_j for notational simplicity.

2.2.2 Proof of the Transposition Rule for Independent Components

To prove the transposition rule for the independent field components A^μ, with $\mu \neq \mu_D$, we consider the variation of the identity map $\mathbb{1} \in \mathscr{G}$ acting on the independent field components A^μ:

$$\begin{aligned}
\delta A^\mu(x) &= \delta(\mathbb{1}[A^\mu(\cdot)](x)) && \text{2.25a}\\
&= \mathbb{1}[A^\mu(\cdot) + \alpha\gamma^\mu(\cdot)](x) - \mathbb{1}[A^\mu(\cdot)](x) && \text{2.25b}\\
&= (A^\mu(x) + \alpha\gamma^\mu(x)) - A^\mu(x) && \text{2.25c}\\
&= \alpha\gamma^\mu(x), && \text{2.25d}
\end{aligned}$$

where we have made use of eq. 2.19 in eq. 2.25b. Now, if one considers the derivative of the independent component A^μ, as a function in $C^\infty(\mathbb{M})$, then similarly to eq. 2.25, one can compute the variation of the derivative $\partial_\nu A^\mu$:

$$\begin{aligned}
\delta(\partial^x_\nu A^\mu(x)) &= \delta(\partial^x_\nu \mathbb{1}[A^\mu(\cdot)](x)) && \text{2.26a}\\
&= \partial^x_\nu \mathbb{1}[A^\mu(\cdot) + \alpha\gamma^\mu(\cdot)](x) - \partial^x_\nu \mathbb{1}[A^\mu(\cdot)](x) && \text{2.26b}\\
&= \partial^x_\nu (A^\mu(x) + \alpha\gamma^\mu(x)) - \partial^x_\nu A^\mu(x) && \text{2.26c}\\
&= \alpha\partial^x_\nu \left(\gamma^\mu(x)\right) && \text{2.26d}\\
&= \partial^x_\nu(\delta A^\mu(x)), && \text{2.26e}
\end{aligned}$$

where we have again made use of eq. 2.19 in eq. 2.26b. Note that in both eq. 2.25 and eq. 2.26a we have made use of the definition of the variation in eq. 2.19, and have not made use of the chain rule relation in eq. 2.21b; we make this choice because the identity map $\mathbb{1}$ is trivial enough that the definition of the variation in eq. 2.19 may be applied directly.

The results of eq. 2.26a show that the transposition rule holds for the $d-1$ independent field components A^{μ}, with $\mu \neq \mu_D$, and thus we may write

$$\delta(\partial_\nu A^\mu) = \partial_\nu(\delta A^\mu), \quad \forall \mu \neq \mu_D. \tag{2.27}$$

2.2.3 Proof of the Transposition Rule for the Dependent Component

The proof of the transposition rule for the dependent field component A^{μ_D} is more intricate than the independent case due to the functional dependence that A^{μ_D} has on the derivatives of the independent field components $\partial_\nu A^\mu$ with $\nu, \mu \neq \mu_D$; we will thus have to pay close attention to the chain rule relations derived in appendix B.1.

We will prove the transposition rule, $\delta(\partial_\nu A^{\mu_D}) = \partial_\nu(\delta A^{\mu_D})$, for the dependent field component in two separate cases: first for $\nu = \mu_D$ and second for $\nu \neq \mu_D$. In both cases we will need the variation δA^{μ_D}, which can be calculated using the definition of the variation from eq. 2.19 as follows:

$$\delta A^{\mu_D}(x) = \sum_{(\rho,\sigma)\neq\mu_D} \left(\frac{\partial A^{\mu_D}[\ldots, \partial_\rho A^\sigma(\cdot) + \alpha\gamma^\sigma_\rho(\cdot), \ldots](x)}{\partial\alpha} \right) \Bigg|_{\alpha=0} \tag{2.28a}$$

$$= \sum_{(\rho,\sigma)\neq\mu_D} \frac{\partial}{\partial\alpha} \left(\int_{-\infty}^{x^{\mu_D}} d\tilde{x}^{\mu_D}\, B[\ldots, \partial_\rho A^\sigma(\cdot) + \alpha\gamma^\sigma_\rho(\cdot), \ldots](x^0, \ldots, \tilde{x}^{\mu_D}, \ldots, x^{d-1}) \right) \Bigg|_{\alpha=0} \tag{2.28b}$$

$$= \int_{-\infty}^{x^{\mu_D}} d\tilde{x}^{\mu_D}\, \delta B(x^0, \ldots, \tilde{x}^{\mu_D}, \ldots, x^{d-1}), \tag{2.28c}$$

where in eq. 2.28b, we have used the expression of A^{μ_D} from eq. 2.11.

Case 1: $\nu = \mu_D$

If we act ∂_{μ_D} on our expression for δA^{μ_D} derived in eq. 2.28c, we find—by a simple application of the fundamental theorem of calculus—the following

$$\partial^x_{\mu_D}(\delta A^{\mu_D}(x)) = \partial^x_{\mu_D}\left(\int_{-\infty}^{x^{\mu_D}} d\tilde{x}^{\mu_D}\ \delta B(x^0,\ldots,\tilde{x}^{\mu_D},\ldots,x^{d-1})\right) = \delta B(x). \tag{2.29}$$

Now, acting ∂_{μ_D} and then δ on A^{μ_D}, we can again make use of the fundamental theorem of calculus to find

$$\delta(\partial^x_{\mu_D} A^{\mu_D}(x)) = \delta\left(\partial^x_{\mu_D}\left(\int_{-\infty}^{x^{\mu_D}} d\tilde{x}^{\mu_D}\ B(x^0,\ldots,\tilde{x}^{\mu_D},\ldots,x^{d-1})\right)\right) \tag{2.30a}$$

$$= \delta B(x). \tag{2.30b}$$

Therefore, we have shown that $\delta(\partial_{\mu_D} A^{\mu_D}) = \partial_{\mu_D}(\delta A^{\mu_D})$.

Case 2: $\nu \neq \mu_D$

In this case, we will start by acting ∂_ν on the dependent field component A^{μ_D}, in doing so we find:

$$\partial^x_\nu A^{\mu_D}(x) = \partial^x_\nu\left(\int_{-\infty}^{x^{\mu_D}} d\tilde{x}^{\mu_D}\ B(x^0,\ldots,\tilde{x}^{\mu_D},\ldots,x^{d-1})\right) \tag{2.31a}$$

$$= \int_{-\infty}^{x^{\mu_D}} d\tilde{x}^{\mu_D}\ \partial^x_\nu B(x^0,\ldots,\tilde{x}^{\mu_D},\ldots,x^{d-1}), \tag{2.31b}$$

where in eq. 2.31b, the integral is over the x^{μ_D} component, so we could bring the ∂_ν derivative through the integral as $\nu \neq \mu_D$. We may now make use of the expression derived in eq. B.26 to write

$$\partial^x_\nu A^{\mu_D}(x) = \int_{-\infty}^{x^{\mu_D}} d\tilde{x}^{\mu_D} \sum_{(\rho,\sigma)\neq(\mu_D)} \int d^d y\ \frac{\partial B(x^0,\ldots,\tilde{x}^{\mu_D},\ldots,x^{d-1})}{\partial(\partial^y_\rho A^\sigma(y))}\partial^y_\nu(\partial^y_\rho A^\sigma(y)). \tag{2.32}$$

Next, we act δ on $\partial_\nu A^{\mu_D}$, and make use of the product rule for variations from appendix B.1.4 to find:

$$\delta(\partial^x_\nu A^{\mu_D}(x)) = \delta\left(\sum_{(\rho,\sigma)\neq(\mu_D)}\int_{-\infty}^{x^{\mu_D}} d\tilde{x}^{\mu_D}\int d^d y\,\frac{\partial B(x^0,\ldots,\tilde{x}^{\mu_D},\ldots,x^{d-1})}{\partial(\partial^y_\rho A^\sigma(y))}\partial^y_\nu(\partial^y_\rho A^\sigma(y))\right) \tag{2.33a}$$

$$= \sum_{(\rho,\sigma)\neq(\mu_D)}\int_{-\infty}^{x^{\mu_D}} d\tilde{x}^{\mu_D}\int d^d y\,\delta\left(\frac{\partial B(x^0,\ldots,\tilde{x}^{\mu_D},\ldots,x^{d-1})}{\partial(\partial^y_\rho A^\sigma(y))}\right)\partial^y_\nu(\partial^y_\rho A^\sigma(y)) \tag{2.33b}$$

$$+ \sum_{(\rho,\sigma)\neq(\mu_D)}\int_{-\infty}^{x^{\mu_D}} d\tilde{x}^{\mu_D}\int d^d y\,\frac{\partial B(x^0,\ldots,\tilde{x}^{\mu_D},\ldots,x^{d-1})}{\partial(\partial^y_\rho A^\sigma(y))}\delta\Big(\partial^y_\nu(\partial^y_\rho A^\sigma(y))\Big)$$

$$= \sum_{(\rho,\sigma)\neq(\mu_D)}\int_{-\infty}^{x^{\mu_D}} d\tilde{x}^{\mu_D}\int d^d y \tag{2.33c}$$

$$\Bigg(\overbrace{\sum_{(\rho',\sigma')\neq(\mu_D)}\int d^d z\,\frac{\partial^2 B(x^0,\ldots,\tilde{x}^{\mu_D},\ldots,x^{d-1})}{\partial(\partial^z_{\rho'}A^{\sigma'}(z))\partial(\partial^y_\rho A^\sigma(y))}\delta(\partial^z_{\rho'}A^{\sigma'}(z))}^{eq.\ \text{B.34b}}\Bigg)\partial^y_\nu(\partial^y_\rho A^\sigma(y))$$

$$+ \sum_{(\rho,\sigma)\neq(\mu_D)}\int_{-\infty}^{x^{\mu_D}} d\tilde{x}^{\mu_D}\int d^d y\,\frac{\partial B(x^0,\ldots,\tilde{x}^{\mu_D},\ldots,x^{d-1})}{\partial(\partial^y_\rho A^\sigma(y))}\delta\Big(\partial^y_\nu(\partial^y_\rho A^\sigma(y))\Big),$$

where in eq. 2.33c, we have used the expression derived in eq. B.34b. Next, we will rearrange the first expression in eq. 2.33c, to make use of the expression derived in

eq. B.39.

$$\delta(\partial^x_\nu A^{\mu_D}(x)) = \int_{-\infty}^{x^{\mu_D}} d\tilde{x}^{\mu_D} \sum_{(\rho',\sigma')\neq(\mu_D)} \int d^d z \tag{2.34a}$$

$$\left[\left(\sum_{(\rho,\sigma)\neq(\mu_D)} \int d^d y \, \frac{\partial^2 B(x^0,\ldots,\tilde{x}^{\mu_D},\ldots,x^{d-1})}{\partial(\partial^z_{\rho'} A^{\sigma'}(z))\partial(\partial^y_\rho A^\sigma(y))} \partial^y_\nu(\partial^y_\rho A^\sigma(y))\right) \delta\Big(\partial^z_{\rho'} A^{\sigma'}(z)\Big)\right]$$

$$+ \sum_{(\rho,\sigma)\neq(\mu_D)} \int_{-\infty}^{x^{\mu_D}} d\tilde{x}^{\mu_D} \int d^d y \, \frac{\partial B(x^0,\ldots,\tilde{x}^{\mu_D},\ldots,x^{d-1})}{\partial(\partial^y_\rho A^\sigma(y))} \delta\Big(\partial^y_\nu(\partial^y_\rho A^\sigma(y))\Big)$$

$$\overset{eq.\ \text{B.39}}{=} \sum_{(\rho',\sigma')\neq(\mu_D)} \int_{-\infty}^{x^{\mu_D}} d\tilde{x}^{\mu_D} \int d^d z \, \partial^x_\nu \left(\frac{\partial B(x^0,\ldots,\tilde{x}^{\mu_D},\ldots,x^{d-1})}{\partial(\partial^z_{\rho'} A^{\sigma'}(z))}\right) \delta\Big(\partial^z_{\rho'} A^{\sigma'}(z)\Big) \tag{2.34b}$$

$$+ \sum_{(\rho',\sigma')\neq(\mu_D)} \int_{-\infty}^{x^{\mu_D}} d\tilde{x}^{\mu_D} \int d^d z \, \partial^z_\nu \left(\frac{\partial B(x^0,\ldots,\tilde{x}^{\mu_D},\ldots,x^{d-1})}{\partial(\partial^z_{\rho'} A^{\sigma'}(z))}\right) \delta\Big(\partial^z_{\rho'} A^{\sigma'}(z)\Big)$$

$$+ \sum_{(\rho,\sigma)\neq(\mu_D)} \int_{-\infty}^{x^{\mu_D}} d\tilde{x}^{\mu_D} \int d^d y \, \frac{\partial B(x^0,\ldots,\tilde{x}^{\mu_D},\ldots,x^{d-1})}{\partial(\partial^y_\rho A^\sigma(y))} \delta\Big(\partial^y_\nu(\partial^y_\rho A^\sigma(y))\Big)$$

$$\overset{\text{IBP}}{=} \sum_{(\rho',\sigma')\neq(\mu_D)} \int_{-\infty}^{x^{\mu_D}} d\tilde{x}^{\mu_D} \int d^d z \, \partial^x_\nu \left(\frac{\partial B(x^0,\ldots,\tilde{x}^{\mu_D},\ldots,x^{d-1})}{\partial(\partial^z_{\rho'} A^{\sigma'}(z))}\right) \delta\Big(\partial^z_{\rho'} A^{\sigma'}(z)\Big) \tag{2.34c}$$

$$- \sum_{(\rho',\sigma')\neq(\mu_D)} \int_{-\infty}^{x^{\mu_D}} d\tilde{x}^{\mu_D} \int d^d z \, \frac{\partial B(x^0,\ldots,\tilde{x}^{\mu_D},\ldots,x^{d-1})}{\partial(\partial^z_{\rho'} A^{\sigma'}(z))} \partial^z_\nu \left(\delta\Big(\partial^z_{\rho'} A^{\sigma'}(z)\Big)\right)$$

$$+ \sum_{(\rho,\sigma)\neq(\mu_D)} \int_{-\infty}^{x^{\mu_D}} d\tilde{x}^{\mu_D} \int d^d y \, \frac{\partial B(x^0,\ldots,\tilde{x}^{\mu_D},\ldots,x^{d-1})}{\partial(\partial^y_\rho A^\sigma(y))} \delta\Big(\partial^y_\nu(\partial^y_\rho A^\sigma(y))\Big),$$

where in eq. 2.34c, we have used integration by parts to move the ∂^z_ν derivative off of the functional derivative of B. In eq. 2.27, we showed that the transposition rule for the independent components, $\delta(\partial_\nu A^\mu) = \partial_\nu(\delta A^\mu)\ \forall \mu \neq \mu_D$, holds. This proof followed trivially since the field components $A^\mu\ \forall \mu \neq \mu_D$ were allowed to vary independently. Recall, that we have the expression, $\partial_{\mu_D} A^{\mu_D} = -\sum_{\nu\neq\mu_D} \partial_\nu f^\nu[A^\mu : \mu \neq \mu_D](x)$. Hence, we see that the only dependent derivative is $\partial_{\mu_D} A^{\mu_D}$, and all the other derivatives $\partial_\nu A^\mu\ \forall \nu, \mu \neq \mu_D$ are independent. Thus, we may conclude that the derivatives $\partial_\nu A^\mu\ \forall \nu, \mu \neq \mu_D$ will vary independently, and therefore the variation δ will commute with the derivatives of the derivatives of the independent field components, *i.e.* $\delta(\partial_\nu(\partial_\rho A^\mu)) = \partial_\nu(\delta(\partial_\rho A^\mu))$ for all $\mu \neq \mu_D$. Returning to our calculation, one will

notice—after commuting the variation δ past the ∂_ν spacetime-derivative in the second term of eq. 2.34c—that the second and third terms cancel in eq. 2.34c. Thus, we have

$$\delta(\partial^x_\nu A^{\mu_D}(x)) = \partial^x_\nu \left(\int_{-\infty}^{x^{\mu_D}} d\tilde{x}^{\mu_D} \sum_{(\rho',\sigma')\neq(\mu_D)} \int d^d z \, \frac{\partial B(x^0,\ldots,\tilde{x}^{\mu_D},\ldots,x^{d-1})}{\partial(\partial^z_{\rho'} A^{\sigma'}(z))} \delta(\partial^z_{\rho'} A^{\sigma'}(z)) \right) \tag{2.35a}$$

$$= \partial^x_\nu \left(\int_{-\infty}^{x^{\mu_D}} d\tilde{x}^{\mu_D} \, \delta B(x^0,\ldots,\tilde{x}^{\mu_D},\ldots,x^{d-1}) \right) \tag{2.35b}$$

where in eq. 2.35a, we pulled out the ∂_ν spacetime derivative from the first term in eq. 2.34c. In eq. 2.35b, we used the chain rule for variations from eq. 2.21b. Our final movement in the proof of the transposition rule, will be to recognize the term in the parenthesis of eq. 2.35b as the variation of the dependent field component, which was derived in eq. 2.28c. We may thus write

$$\delta(\partial^x_\nu A^{\mu_D}(x)) = \partial^x_\nu(\delta A^{\mu_D}). \tag{2.36}$$

Hence, we may finally conclude our proof of the transposition rule for all field components A^μ and therefore write:

$$\boxed{\delta(\partial_\nu A^\mu) = \partial_\nu(\delta A^\mu) \quad \forall\nu \;\&\; \forall\mu} \tag{2.37}$$

2.3 Classical Field Theory with Constraints

In this section we shall apply the formalism developed in Sec. 2.2 along with the transposition rule derived therein to classical field theories with integrable non-holonomic constraints. We shall first derive the Euler-Lagrange equations for classical field theories with integrable non-holonomic constraints in Sec. 2.3.1, before then applying the formalism to the specific example of classical electrodynamics in Sec. 2.3.2.

2.3.1 Hamilton's Principle and the Euler-Lagrange Equations

Consider a classical field theory in d spacetime dimensions described by the Lagrangian density $\mathscr{L}$ with d field components A^μ, and suppose that the theory is placed under an integrable non-holonomic constraint

$$g[\partial_\nu A^\mu](x) = 0. \tag{2.38}$$

We will require the variations to respect the constraint in eq. 2.38, *i.e.*

$$g[\partial_\nu A^\mu + \delta(\partial_\nu A^\mu)](x) = 0. \tag{2.39}$$

Equation 2.39 then implies the following

$$0 = g[\partial_\nu A^\mu + \delta(\partial_\nu A^\mu)](x) \tag{2.40a}$$

$$= \overbrace{g[\partial_\nu A^\mu](x)}^{0} + \sum_{\mu,\nu=0}^{d-1} \int d^d y \, \frac{\partial g(x)}{\partial(\partial^y_\nu A^\mu(y))} \, \delta(\partial^y_\nu A^\mu(y)) \tag{2.40b}$$

$$\implies 0 = \sum_{\mu,\nu=0}^{d-1} \int d^d y \, \frac{\partial g(x)}{\partial(\partial^y_\nu A^\mu(y))} \, \delta(\partial^y_\nu A^\mu(y)) \tag{2.40c}$$

where we have expanded to first order in the variation δ. Multiplying both sides of eq. 2.40c by an arbitrary function $\Lambda(x)$—that is independent of the A^μ field components and their derivatives—yields

$$0 = \sum_{\mu,\nu=0}^{d-1} \int d^d y \, \frac{\partial}{\partial(\partial^y_\nu A^\mu(y))} [\Lambda(x) g(x)] \, \delta(\partial^y_\nu A^\mu(y)). \tag{2.41}$$

The Λ function will perform the role of a Lagrange multiplier [98, 120–122]. We may now vary the action S—which is dependent on the field components A^μ and their derivatives $\partial_\nu A^\mu$ which are varied independently from each other—and through Hamil-

ton's principle [40], set the variation to zero:

$$0 = \delta S[A^\mu, \partial_\nu A^\mu] \tag{2.42a}$$

$$= \int d^d x \; \delta \mathscr{L}[A^\mu, \partial_\nu A^\mu](x) \tag{2.42b}$$

$$= \int d^d x \; d^d y \left(\sum_{\mu=0}^{d-1} \frac{\partial \mathscr{L}(x)}{\partial A^\mu(y)} \; \delta A^\mu(y) + \sum_{\mu,\nu=0}^{d-1} \frac{\partial \mathscr{L}(x)}{\partial(\partial^y_\nu A^\mu(y))} \; \delta(\partial^y_\nu A^\mu(y)) \right) \tag{2.42c}$$

$$= \int d^d x \; d^d y \Bigg(\sum_{\mu=0}^{d-1} \frac{\partial}{\partial A^\mu(y)} [\mathscr{L}(x) + \Lambda(x) g(x)] \; \delta A^\mu(y) \tag{2.42d}$$

$$+ \sum_{\mu,\nu=0}^{d-1} \frac{\partial}{\partial(\partial^y_\nu A^\mu(y))} [\mathscr{L}(x) + \Lambda(x) g(x)] \; \delta(\partial^y_\nu A^\mu(y)), \Bigg)$$

in eq. 2.42c we have applied the chain rule for variations in eq. 2.21b to the Lagrangian density $\mathscr{L}$. In eq. 2.42d, we have added two zeros in the form of the variation of the constraint multiplied by the Lagrange multiplier $\Lambda(x)$ to the variation of the action: The first zero arises as both g and Λ are independent of the A^μ field components; thus, $\partial(\Lambda g)/\partial A^\mu = 0$. The second zero comes from eq. 2.40c.

Next we shall make use of the transposition rule in eq. 2.37 and perform an integration by parts on the second term in eq. 2.42d:

$$\delta S = \int d^d x \; d^d y \Bigg(\sum_{\mu=0}^{d-1} \frac{\partial}{\partial A^\mu(y)} [\mathscr{L}(x) + \Lambda(x) g(x)] \; \delta A^\mu(y) \tag{2.43a}$$

$$+ \sum_{\mu,\nu=0}^{d-1} \frac{\partial}{\partial(\partial^y_\nu A^\mu(y))} [\mathscr{L}(x) + \Lambda(x) g(x)] \; \partial^y_\nu(\delta A^\mu(y)) \Bigg)$$

$$= \int d^d x \; d^d y \Bigg(\sum_{\mu=0}^{d-1} \frac{\partial}{\partial A^\mu(y)} [\mathscr{L}(x) + \Lambda(x) g(x)] \tag{2.43b}$$

$$- \sum_{\mu,\nu=0}^{d-1} \partial^y_\nu \left(\frac{\partial}{\partial(\partial^y_\nu A^\mu(y))} [\mathscr{L}(x) + \Lambda(x) g(x)] \right) \Bigg) \; \delta A^\mu(y)$$

Now, the integrable non-holonomic constraint g induces a functional dependence between the field components and their variations, as discussed in Sec. 2.2. Thus, the variations δA^μ are not all independent; rather the δA^{μ_D} variation will depend functionally on the independent variations δA^μ, with $\mu \neq \mu_D$. Therefore, we may not set the integrand of the variation of the action to zero for each field component independently—

as is ordinarily done when deriving the Euler-Lagrange equations for unconstrained dynamical systems. Instead, the argument goes as follows: Choose Λ, the Lagrange multiplier, such that

$$\int d^d x \left(\frac{\partial}{\partial A^{\mu_D}(y)} [\mathscr{L}(x) + \Lambda(x) g(x)] - \sum_{\nu=0}^{d-1} \partial_\nu^y \left(\frac{\partial}{\partial(\partial_\nu^y A^{\mu_D}(y))} [\mathscr{L}(x) + \Lambda(x) g(x)] \right) \right) = 0. \tag{2.44}$$

The remaining $d-1$ field variations δA^μ, with $\mu \neq \mu_D$, are all independent; thus, by the fundamental theorem of the calculus of variations [123], Hamilton's principle (*i.e.* $\delta S = 0$) implies that $\forall \mu \neq \mu_D$

$$\int d^d x \left(\frac{\partial}{\partial A^{\mu}(y)} [\mathscr{L}(x) + \Lambda(x) g(x)] - \sum_{\nu=0}^{d-1} \partial_\nu^y \left(\frac{\partial}{\partial(\partial_\nu^y A^{\mu}(y))} [\mathscr{L}(x) + \Lambda(x) g(x)] \right) \right) = 0. \tag{2.45}$$

Supplemented with initial conditions, eq. 2.44 yields one equation to solve for Λ, while eq. 2.45 provides an additional $d-1$ equations to determine the independent A^μ components. Once these independent components have been determined, the dependent component A^{μ_D} can be obtained through its functional dependence on the independent components, thereby solving the dynamical system.

Upon closer inspection, one may notice that this procedure of including constraints into the classical field theory is mathematically equivalent to adjoining the constraints weighted by the Lagrange multipliers to the original Lagrangian; *i.e.*

$$\mathscr{L} \mapsto \mathscr{L}_{\text{adjoined}} \equiv \mathscr{L} + \overbrace{\mathscr{L}_{\text{constraint}}}^{\Lambda g}, \tag{2.46}$$

and then solving the usual Euler-Lagrange equations supplemented with the constraint equation in eq. 2.38. The result in eq. 2.46, derived in the context of classical field theory, is directly analogous to the standard result obtained when applying the method of Lagrange multipliers in the mechanics of point particles, where one similarly adjoins the Lagrangian by constraint terms weighted by multipliers [120, 121].

The authors would like to emphasize that the result in point particle mechanics analogous to eq. 2.46 is only valid for integrable non-holonomic constraints; if the constraint were non-integrable in point particle mechanics, then the resulting equations

of motion which arise from the adjoined Lagrangian would lead to the incorrect (*i.e.* in disagreement with experiment) vakonomic equations [122, 124–126]. We conjecture that the same is true in the context of classical field theory, and that the adjoined Lagrangian in eq. 2.46 will only yield the correct equations of motion for integrable non-holonomic constraints.

2.3.2 Classical Electrodynamics with Integrable Non-Holonomic Constraints

In this section, we demonstrate the applicability of our results to classical electrodynamics by gauge fixing the electromagnetic field using the Coulomb and Lorenz gauges. We show that both gauges are integrable non-holonomic constraints as defined in eq. 2.8, and therefore the transposition rule in eq. 2.37 holds. We shall also provide an example of a non-integrable non-holonomic gauge known as the 't Hooft-Veltman (tHV) gauge.

Classical electrodynamics may be formulated in terms of $U(1)$ gauge fields and the following Lagrangian density [36, 38]

$$\mathscr{L}_{U(1)} \equiv -\frac{1}{4}\sum_{\mu,\nu=0}^{3} F^{\mu\nu}F_{\mu\nu}, \tag{2.47}$$

where $F^{\mu\nu} \equiv \partial^\mu A^\nu - \partial^\nu A^\mu$ is the field strength tensor, with the metric given by $\eta_{\mu\nu} = \text{diag}(+\,-\,-\,-)_{\mu\nu}$. The $\mathscr{L}_{U(1)}$ Lagrangian density is gauge invariant and can be subjected to gauge fixing [36–38]. The Coulomb and Lorenz gauges impose the following constraints on the A^μ gauge field:

$$g_{Lorenz}[\partial_\nu A^\mu(\cdot)](x) \equiv \sum_{\mu=0}^{3} \partial_\mu A^\mu(x) = 0 \tag{2.48a}$$

$$g_{Coulomb}[\partial_\nu A^\mu(\cdot)](x) \equiv \sum_{i=1}^{3} \partial_i A^i(x) = 0. \tag{2.48b}$$

While the tHV gauge condition is given by

$$g_{tHV}[A^\mu(\cdot), \partial_\nu A^\mu(\cdot)](x) \equiv \sum_{\mu=0}^{3} \left(\partial_\mu A^\mu(x) + \omega A^\mu(x) A_\mu(x) \right) = 0, \tag{2.49}$$

where $\omega \neq 0$ is a real parameter [105–113].

To match the notation used in eq. 2.8, one may express the Lorenz gauge choice as

$$g_{Lorenz}[A^\mu(\cdot), \partial_\nu A^\mu(\cdot)](x) = \sum_{\nu=0}^{3} \partial_\nu f^\nu_{Lorenz}[A^\mu(\cdot)](x) = 0, \tag{2.50}$$

where the function $f^\nu_{Lorenz}[A^\mu(\cdot)](x)$ is

$$f^\nu_{Lorenz}[A^\mu(\cdot)](x) \equiv A^\nu(x). \tag{2.51}$$

In the Lorenz gauge, any of the spatial components of the gauge field A^i with $i = 1, 2, 3$ may be chosen as the dependent field component A^{μ_D}, with the remaining components being independent. Thus, the Lorenz gauge is an integrable, non-holonomic constraint as defined in eq. 2.8. The Coulomb gauge works similarly, except now the function defining the integrability condition takes the form,

$$f^\nu_{Coulomb}[A^\mu(\cdot)](x) \equiv \begin{cases} 0 & \text{if } \nu = 0, \\ A^\nu(x) & \text{if } \nu = 1, 2, 3. \end{cases} \tag{2.52}$$

Notice that there is no way to express the tHV gauge in the form given in eq. 2.8. Therefore, the tHV gauge is a non-integrable, non-holonomic constraint.

Since the Coulomb and Lorenz gauges are non-holonomic constraints that satisfy the condition of integrability, one may freely adjoin the constraints in eq. 2.48 to eq. 2.47 as is commonly done in the literature [42, 96–104]. Flannery [39] showed that in the context of point particle mechanics, non-integrable non-holonomic constraints lead to a modification of the transposition rule. We expect to find an analogous result in field theory, which would have implications for gauges such as the tHV gauge. We leave this analysis for future work.

2.4 Conclusions

In this chapter, we identified a subtlety previously unrecognized in the derivation of the equations of motion for a classical field subject to general non-holonomic constraints: the transposition rule, $\delta(\partial_\nu A^\mu) = \partial_\nu(\delta A^\mu)$, for such systems is expected to no longer hold in general. Gauge fixing in field theory imposes constraints on the field; therefore, this expected failure of the transposition rule calls into question classical field theory results that use a gauge that depends on the derivatives of the field.

We defined integrability in the context of non-holonomic constraints in field theory and proved that the transposition rule holds for both holonomic and integrable, non-holonomic constraints. As a result, we have shown that the equations of motion for field theories with such constraints can be derived by varying the action in the usual way. We applied our formalism to the $U(1)$ gauge field in the Coulomb and Lorenz gauges, which are non-holonomic yet integrable as defined here.

Our results place the gauge fixing of gauge theories with non-holonomic but integrable gauges—such as the Coulomb or Lorenz gauges—on a more rigorous footing, avoiding *ad hoc* methodologies, and further provide insight into the subtleties involved in gauge fixing classical and quantum gauge theories. The formalism developed in this chapter was presented in the context of gauge fixing a classical field theory composed of a vector field A^μ; however, the formalism is general and may be applied to more general classical field theories (for instance, Yang-Mills theory) with integrable non-holonomic constraints.

The future work we envisage includes performing an analysis on non-integrable, non-holonomic constraints in field theory, and exploring how/if the transposition rule must be modified in such scenarios. Often one fixes a gauge classically by adjoining the original Lagrangian with the gauge constraint multiplied by a Lagrange multiplier. In point particle mechanics, such a procedure leads to the so-called vakonomic equations of motion; experiment has shown decisively that, when the results of vakonomic mechanics and the Lagrange-d'Alembert equations of motion differ, the Lagrange-

d'Alembert equations give the correct classical path [41]. Initial investigations of the classical A^μ solution in the 't Hooft-Veltman gauge have shown that the physical $\vec{E}$ and $\vec{B}$ fields are nevertheless reproduced by a vakonomic treatment of the gauge constraint [127]. It would be very interesting to understand why it appears that following a seemingly incorrect procedure for fixing the gauge nevertheless yields the correct physical $\vec{E}$ and $\vec{B}$ fields. Similarly, in point particle mechanics, one must include the additional terms from the modified transposition rule for non-integrable, non-holonomic constraints [39] in order to derive the correct equations of motion from the Dirac-Bergmann algorithm [128]; thus one would expect that there are terms missing in a BRST-type gauge fixing treatment of non-integrable, non-holonomic gauges, such as the 't Hooft-Veltman gauge, which may or may not have physical consequences.

"And now for something completely different" — *Monty Python*

Chapter 3

Energy loss predicts no v_2 in small systems

3.1 Introduction

The existence of the quark-gluon plasma (QGP) in central heavy-ion collisions at RHIC and the LHC is by now well established, with $\mathrm{Au} + \mathrm{Au}$ and $\mathrm{Pb} + \mathrm{Pb}$ collisions providing a rich body of supporting evidence [45, 47–49]. Among the most compelling signatures are the large azimuthal anisotropies at low transverse momentum [129–131], the enhanced production of strange hadrons [132–134], and the suppression of quarkonia [135–137]. In the hard sector, the suppression of hadrons in high-energy collisions of $\mathrm{A} + \mathrm{A}$ nuclei relative to scaled proton-proton collisions, quantified by the nuclear modification factor

$$R_{AA} \equiv \frac{dN^{AA}/dp_T}{\langle N_{\mathrm{coll}} \rangle \, dN^{pp}/dp_T} \ll 1, \tag{3.1}$$

provides direct evidence for medium-induced partonic energy loss [74–77], as was originally proposed by Bjorken [73].

A broad class of theoretical models can reproduce the experimentally measured R_{AA} [62, 64, 66]. However, simultaneously describing the azimuthal dependence encoded in second Fourier coefficient v_2 alongside R_{AA} has proved to be a considerably

more demanding task, with early energy loss calculations systematically under predicting v_2 [83, 84]. This $R_{AA} \otimes v_2$ *puzzle* has since been addressed in large collision systems by incorporating realistic hydrodynamic medium evolution and event-by-event geometric fluctuations into the energy loss calculation [85–88], lending strong support to the picture of path-length dependent partonic energy loss in the QGP. Whether this picture carries over to small collision systems remains an open and pressing question.

In the asymmetric small systems of $p/d/^3\mathrm{He} + \mathrm{Pb/Au}$, qualitative signatures reminiscent of QGP formation have also been reported, for example, non-zero low-p_T v_2 [51–54], strangeness enhancement [138, 139], and quarkonium suppression [140]. The interpretation in the hard sector is, however, considerably less clear. Measurements of $R_{p\mathrm{Pb}}$ by ATLAS [141] and ALICE [142] yield values at or above unity, in tension with the suppression expected from final-state energy loss [143–146]. By contrast, the PHENIX collaboration [147] reports a photon-normalized $R_{d\mathrm{Au}} \sim 0.75$, in qualitative agreement with the energy loss expectation [143–146]. The picture is further complicated by measurements of non-zero positive high-p_T v_2 in $p + \mathrm{Pb}$ by ATLAS [148], ALICE [149], and CMS [150], which are suggestive of path-length dependent energy loss, yet arise in a system showing no clear suppression.

Proposals by [151, 152] suggested that $\mathrm{O} + \mathrm{O}$ collision systems could provide an alternative small-system environment to $p + \mathrm{Pb}$ in which path-length dependent energy loss may occur and be experimentally observable. In response to these proposals, the LHC collided $\mathrm{O} + \mathrm{O}$ in 2025 and measured a clear suppression of charged-particle yields [153, 154]. This suppression was found to be consistent with expectations from path-length dependent energy loss models [155–159]. With the observation of suppression in $\mathrm{O} + \mathrm{O}$ collisions now strongly supporting a path-length dependent energy loss interpretation, a natural next step is to perform a full experimental analysis on the high-p_T azimuthal v_2—where there are already hints of large anisotropy [160–162]—and compare it with theoretical predictions.

As pointed out in [163], applying existing path-length dependent energy loss models to small collision systems often requires extrapolating the models beyond their intended domain of validity. For instance, radiative energy loss formalisms based on the opacity expansion assume a sufficiently large medium, allowing terms that are

exponentially suppressed with system size to be neglected [70, 71, 79, 80]. Similarly, BDMPS-Z based approaches rely on the assumption that the hard parton undergoes many scatterings while traversing the medium [79, 80, 164–167], an assumption that is not justifiable in small systems. A similar assumption of a large number of collisions is used in models of collisional energy loss, where the elastic energy loss probability distribution is commonly approximated as Gaussian by invoking the central limit theorem [168–171].

More recently, corrections to opacity-expansion-based radiative energy loss formalisms have been derived that include terms previously neglected due to their exponential suppression with system size [172, 173]. The phenomenological implications of these corrections for both small and large collision systems were explored in [171]. Subsequently, [163] employed an elastic energy loss kernel derived within the hard thermal loop (HTL) formalism [174–179], enabling a consistent treatment of elastic energy loss in small collision systems. These radiative and elastic small-system corrections were then incorporated into a unified phenomenological framework in [155]; this framework, representing the culmination of these small-system improvements, will be referred to as the "Cape Town version 1.0" (CTv1.0) energy loss model [146, 155, 159, 163, 171] throughout this chapter.

In this work, we present a model which builds on the CTv1.0 energy loss model, and we describe in considerable detail the improvements that constitute the new Cape Town version 2.0 (CTv2.0) implementation. A central aim of the present work is to quantify the effects of this improvement on the calculation and the resulting jet quenching observables, which were first presented in a short Letter format in [90]. In [172], it was shown that the choice of a dynamic medium evolution has non-trivial effects on the energy loss; those conclusions guided our primary advancement of CTv2.0 over CTv1.0, which is to replace the static effective medium approximation with a full dynamic sampling of the hydrodynamic temperature profile on an event-by-event basis. We include the dynamic evolution of the medium as the azimuthal anisotropy of high-p_T particles is expected to be sensitive to this evolution [180–182].

In order to calculate observables like R_{AB} and v_n from an energy loss model in a phenomenological analysis, the energy loss must be calculated for a large number

of trajectories through the medium, which is computationally expensive. To address this computational challenge, one can compute and tabulate the energy loss for a defined set of parameters, and then establish a mapping from each trajectory through the medium to a subset of these parameters. In the CTv1.0 model, trajectories were mapped onto parameters that allowed for a calculation of energy loss with a static medium [146, 155, 159, 163, 171]. In CTv2.0, we use an alternative set of parameters that allows for an accurate and tractable calculation of the energy loss with a dynamic medium.

This chapter is organized as follows: Sec. 3.2 presents the CTv2.0 energy-loss formalism. Sec. 3.3 explains how we compute hadronic $R_{AB}(p_T)$ and the high-p_T azimuthal harmonics $v_n(p_T)$. Sec. 3.4 describes the χ^2 calibration procedure used to extract the effective coupling α_s^{eff}, the treatment of theoretical and experimental uncertainties, and the datasets employed in the extraction procedure. Sec. 3.5 presents the calibrated large-system comparisons and the model predictions for small systems ($\mathrm{Ne}+\mathrm{Ne}$, $\mathrm{O}+\mathrm{O}$, and $p+\mathrm{Pb}$). In Sec. 3.6, we summarize the main conclusions. In appendix C.1, we compare our implementation of the DGLV radiative energy loss to the CUJET2.0 formalism [183]. In appendix C.2, we discuss the uncertainty of the extraction of the angle of the hard sector participant plane. In appendix C.3, we compare our energy loss model to all available experimental data for R_{AB} and v_n in large and small systems from RHIC and the LHC.

3.2 Energy loss model

In the following section we describe the energy loss model used in this work. Our model includes both radiative and elastic energy loss mechanisms, which are described in Sec. 3.2.1 and Sec. 3.2.2, respectively. The model we present calculates the energy loss dynamically along a parton's trajectory through the medium on an event-by-event basis; we describe the parametrization of the parton trajectory in Sec. 3.2.4. Finally, we compare the results of our energy loss model to that of CTv1.0 [146, 155, 159, 163, 171] in Sec. 3.2.5.

3.2.1 Radiative energy loss

The radiative energy loss formulation presented in this work is based on the DGLV [70, 71, 184] energy loss framework along with its short path length correction (SPLC) developed in [172, 173].

The radiative energy loss kernel of a single gluon emission can be expressed in terms of the medium density ρ *via*:

$$\frac{dE_{rad}^{DGLV}}{dx} = \frac{9C_R\alpha_s^3 E}{2\pi^2}\int dz d^2\mathbf{q} d^2\mathbf{k}\,\frac{\rho(z)}{\left(\mathbf{q}^2+\mu^2\right)^2} \tag{3.2a}$$
$$\times\left\{\frac{-2\left(1-\cos\left\{\left(\omega_1+\tilde{\omega}_m\right)z\right\}\right)}{\left((\mathbf{k}-\mathbf{q})^2+m_g^2+M^2x^2\right)}\left[\frac{(\mathbf{k}-\mathbf{q})\cdot\mathbf{k}}{\mathbf{k}^2+m_g^2+M^2x^2}-\frac{(\mathbf{k}-\mathbf{q})^2}{(\mathbf{k}-\mathbf{q})^2+m_g^2+M^2x^2}\right]\right\},$$

$$\frac{dE_{rad}^{SPLC}}{dx} = \frac{9C_R\alpha_s^3 E}{2\pi^2}\int dz d^2\mathbf{q} d^2\mathbf{k}\,\frac{\rho(z)}{\left(\mathbf{q}^2+\mu^2\right)^2}\frac{e^{-\sqrt{\mu^2+q^2}z}}{2} \tag{3.2b}$$
$$\times\left\{\frac{\mathbf{k}^2\left(1-\frac{2C_R}{C_A}\right)\left(1-\cos\left\{\left(\omega_0+\tilde{\omega}_m\right)z\right\}\right)}{(\mathbf{k}^2+m_g^2+M^2x^2)^2}\right.$$
$$\left.+\frac{\mathbf{k}\cdot(\mathbf{k}-\mathbf{q})\left(\cos\left\{\left(\omega_0+\tilde{\omega}_m\right)z\right\}-\cos\left\{\left(\omega_0+\tilde{\omega}_1\right)z\right\}\right)}{(\mathbf{k}^2+m_g^2+M^2x^2)((\mathbf{k}-\mathbf{q})^2+m_g^2+M^2x^2)}\right\},$$

$$\frac{dE_{rad}}{dx} = \frac{dE_{rad}^{DGLV}}{dx}+\frac{dE_{rad}^{SPLC}}{dx}. \tag{3.2c}$$

To match the notation used in [71, 172, 173], we have made use of the following:

$$\omega \equiv xE, \tag{3.3a}$$
$$\omega_0 \equiv \mathbf{k}^2/2\omega, \tag{3.3b}$$
$$\omega_1 \equiv (\mathbf{k}-\mathbf{q})^2/2\omega, \tag{3.3c}$$
$$\tilde{\omega}_m \equiv (m_g^2+M^2x^2)/2\omega. \tag{3.3d}$$

Eq. 3.2a is the DGLV contribution to the radiative energy loss while eq. 3.2b is the SPLC term. In appendix C.1, we compare our form of the DGLV radiative energy loss formalism to that of [183]. To match our notation of the SPLC term in eq. 3.2b to the original form presented in [172, 173], one should substitute the medium density ρ for

the scattering center density $\bar{\rho}$ through the relation in eq. 3.9. In eq. 3.2 and throughout the remainder of this chapter, we use $C_A = 3$ and $C_F = 4/3$ [71]. The two momenta $\mathbf{k}$ and $\mathbf{q}$ are the transverse momentum of the radiated gluon and the transverse momentum exchanged between the radiated gluon and the medium, respectively. Further, x in eq. 3.2 is the fractional momentum carried away by the hard parton, M is the mass of the incident parton, and α_s is the strong coupling. In eq. 3.2, we allow the Debye and gluon masses—which were assumed constant along a given path in the CTv1.0 model [146, 155, 159, 163, 171]—to explicitly depend on the position in the path *via* the following relations:

$$\mu = \mu(z) = T(z)\sqrt{4\pi\alpha_s\left(1 + \frac{n_f}{6}\right)}, \tag{3.4a}$$

$$m_g = m_g(z) = \mu(z)/\sqrt{2}, \tag{3.4b}$$

where $T(z)$ is the temperature of the medium at position z along the parton's trajectory, and $n_f = 2$ is the number of active quark flavours in the plasma. In this work, the temperature profiles are obtained from a hydrodynamic simulation [185] performed with initial conditions obtained from the IP-Glasma model [186–188]; the initial conditions are then evolved with the MUSIC viscous relativistic $(2+1)$D hydrodynamics code [189–191], followed by UrQMD microscopic hadronic-transport [192, 193]. It should be noted that the energy loss of all hard partons in our model occurs before the hadronic phase of the parton's evolution.

The z integral in eq. 3.2 runs from 0 to infinity, but the integral has effective lower and upper bounds that are determined by cutoffs on the medium density (discussed further in Sec. 3.2.4). The upper bound for the transverse radiated gluon momentum $|\mathbf{k}|$ is

$$k_{max} = \mathrm{Min}\left(\sqrt{2xE\sqrt{\mu^2 + \mathbf{q}^2}}, 2x(1-x)E\right), \tag{3.5}$$

which ensures that the energy loss receives no contributions from regions of phase space where either the large formation time assumption or the collinear assumption are no longer valid [163, 171, 194]. The integrals over $|\mathbf{q}|$ are bounded from above by

$$q_{max} = \sqrt{3\mu E}, \tag{3.6}$$

consistent with [71, 195]. The integrated radiative energy loss is then obtained by

$$\Delta E_{rad} = \int dx \frac{dE_{rad}}{dx}. \tag{3.7}$$

In fig. 3.1, we show the numerical results for the integrated radiative energy loss. The energy loss is calculated using a *static brick* scattering center density that takes the form

$$\bar{\rho}(z) = \frac{1}{L}\theta(L-z). \tag{3.8}$$

To convert the scattering center density $\bar{\rho}(z)$ in eq. 3.8 to the medium density $\rho(z)$ needed in eq. 3.2, we use the relation [173]

$$\rho = \frac{2\mu^2 L}{C_A^2 \pi \alpha_s^2 \lambda}\bar{\rho}, \tag{3.9}$$

where

$$\lambda = \frac{2\mu^2}{C_A^2 \pi \alpha_s^2} \frac{\pi^2}{4\zeta(3)(4+n_f)T^3}, \tag{3.10}$$

is the mean free path of the parton in the medium [163, 196]. In the top (bottom) panel of fig. 3.1, the energy loss is shown for $E = 10$ GeV ($E = 100$ GeV), at a constant temperature of $T = 0.25$ GeV, strong coupling of $\alpha_s = 0.3$, for gluons and charm quarks. The $|\mathbf{k}|$ integral in eq. 3.2 is cut off at k_{max} defined in eq. 3.5; it was shown in [155, 171, 197] that this cutoff choice reduces the SPLC contribution significantly. From the top and bottom panels of fig. 3.1, we see that for small lengths, L, the radiative energy loss grows quadratically with L, while for large lengths the radiative energy loss shows linear growth in L, consistent with [171, 172].

Eq. 3.2 provides access to the single gluon radiation spectrum. We account for multiple gluon emissions as follows. The single emission kernel is obtained by noting that the total energy lost during radiation is equal to the number of radiated gluons (N^g) multiplied by the fractional energy carried away (xE) by each radiated gluon; *i.e.*

$$\frac{dN^g}{dx} = \frac{1}{xE}\frac{dE_{rad}}{dx}. \tag{3.11}$$

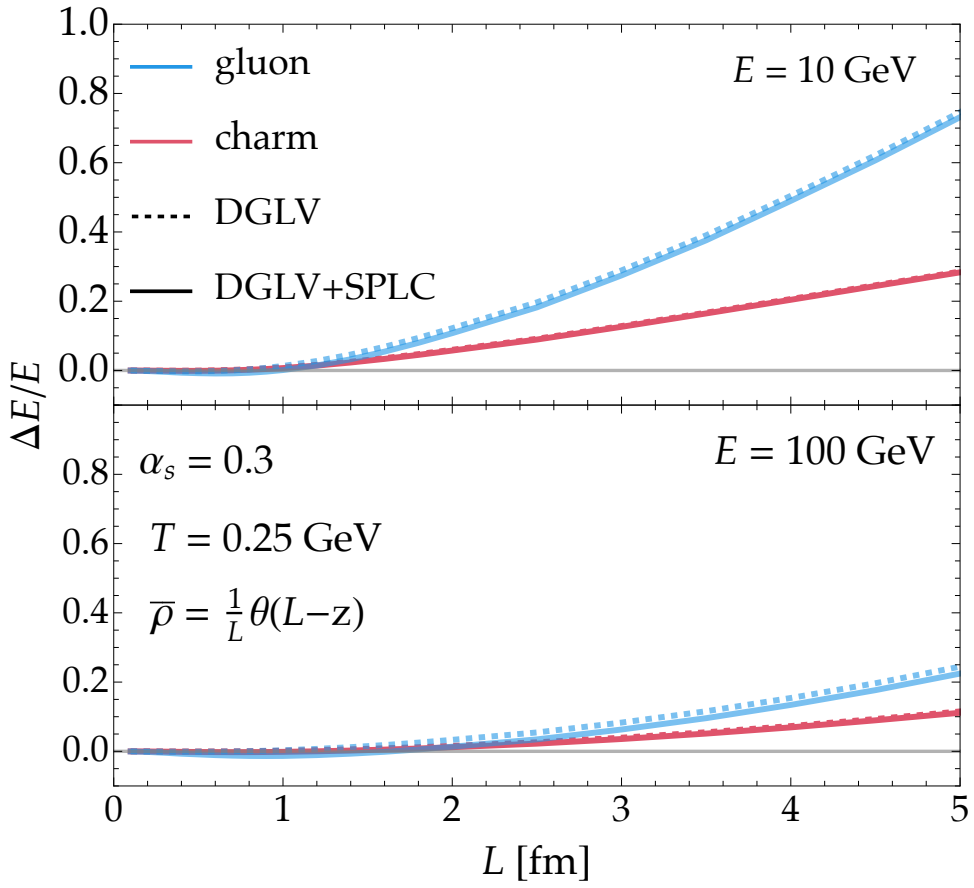

Figure 3.1: Integrated radiative energy loss from eq. 3.2 for DGLV and DGLV+SPLC. All curves are plotted as a function of the length L of the static brick scattering center density eq. 3.8, and are evaluated at a constant temperature $T = 0.25$ GeV and constant strong coupling $\alpha_s = 0.3$. Gluons are shown in blue and charm quarks are shown in red. The top (bottom) panel shows results of eq. 3.2 for 10 GeV (100 GeV).

The number of radiated gluons is then

$$N^g = \int_0^1 dx \frac{dN^g}{dx}. \tag{3.12}$$

We define the probability distribution $p^1_{rad}(x)$ associated with the emission of a single gluon with fractional momentum x as

$$p^1_{rad}(x) \equiv \frac{1}{N^g}\frac{dN^g}{dx}. \tag{3.13}$$

We define the probability associated with no energy loss as

$$p^0_{rad}(x) \equiv \delta(x). \tag{3.14}$$

Now, we define $p^2_{rad}(x)$ as the probability distribution for emitting two gluons with a total fraction x of the initial parton energy E; $p^2_{rad}(x)$ can be obtained through the sum of the two random variables associated with two single emission distributions. We follow [198] and assume that the two single emissions are independent of each other, which allows us to write $p^2_{rad}(x)$ as the convolution of two single emissions,

$$p^2_{rad}(x) = \int dx_1 p^1_{rad}(x_1) p^1_{rad}(x - x_1). \tag{3.15}$$

Similarly, $p^{rad}_3(x)$ is the convolution of the $p^1_{rad}(x)$ and the $p^2_{rad}(x)$ distributions. Continuing this procedure, we arrive at an expression for the fractional energy loss distribution for an arbitrary number n of gluon emissions,

$$p^n_{rad}(x) = \int dx_{n-1} p^{n-1}_{rad}(x_{n-1}) p^1_{rad}(x - x_{n-1}). \tag{3.16}$$

As done in [198], we assume that the number of gluon emissions follows a Poisson distribution so that the probability of radiative fractional energy loss is then

$$\tilde{P}_{rad}(x) = \sum_{n=0}^{\infty} \frac{(N^g)^n}{n!} e^{-N^g} p^n_{rad}(x). \tag{3.17}$$

The use of the tilde in eq. 3.17 will become clear shortly. In general, $p^n_{rad}(x)$ has support for $x \in [0, n]$. However, physical constraints imply that x cannot be greater than 1. We address this *probability leakage* by integrating $\tilde{P}_{rad}(x)$ from 0 to 1, and then place the rest of the weight of the distribution into a delta function centered at $x = 1$ [163]. We define P_{rad} as

$$P_{rad}(x) \equiv \tilde{P}_{rad}(x) + w_{rad}\delta(x - 1) \tag{3.18a}$$

$$= \sum_{n=0}^{\infty} \frac{(N^g)^n}{n!} e^{-N^g} p^n_{rad}(x) + w_{rad}\delta(x - 1). \tag{3.18b}$$

In eq. 3.18, we use the weight

$$w_{rad} \equiv \int_1^{\infty} dx \tilde{P}_{rad}(x), \tag{3.19}$$

which is interpreted as the probability of a parton entering the medium and then losing

all of its energy due to radiation.

3.2.2 Elastic energy loss

In this section we describe two different approaches to calculating the elastic energy loss of a hard parton moving through a QGP medium. Both approaches are based on HTL effective field theory [174–179]. The first approach is based on the work of Braaten and Thoma (BT) [68, 69] and makes use of HTL propagators at small momentum transfers and vacuum propagators at large momentum transfers. The second approach we present is based on the work of [179] and is calculated with HTL propagators for all momentum transfers; in what follows we will refer to this method of calculating the energy loss as the *HTL-only* approach. As was done in [146, 155, 163], we have included both the BT and HTL-only approaches in order to provide an estimate of the theoretical uncertainty associated with the transition from the HTL propagators to vacuum propagators in the elastic energy loss sector of our model.

3.2.2.1 Braaten and Thoma elastic energy loss

The BT approach makes use of two asymptotic energy regimes to find expressions for the form of the elastic energy loss: $E \ll M^2/T$ and $E \gg M^2/T$, where M is the mass of the incident parton and T is the temperature of the medium. In the first regime, the elastic energy loss is given by

$$\frac{dE_{el}^{BT}}{dz} = 2C_R\pi\alpha_s^2T^2\left[\frac{1}{v} - \frac{1-v^2}{2v^2}\log\frac{1+v}{1-v}\right] \times \log\left(2^{\frac{n_f}{6+n_f}}B(v)\frac{ET}{m_gM}\right)\left(1+\frac{n_f}{6}\right). \tag{3.20}$$

In eq. 3.20, v is the velocity of the hard parton. In the second regime, the elastic energy loss is given by

$$\frac{dE_{el}^{BT}}{dz} = 2C_R\pi\alpha_s^2T^2\left(1+\frac{n_f}{6}\right) \times \log\left(2^{\frac{n_f}{2\left(6+n_f\right)}}0.92\frac{\sqrt{ET}}{m_g}\right). \tag{3.21}$$

The two results in eq. 3.20 and eq. 3.21 are then stitched together using the smooth function $B(v)$, which satisfies the constraints outlined in [69]. The integrated BT elastic energy loss ΔE_{el}^{BT} can then be calculated from Eq. 3.20 and Eq. 3.21

$$\Delta E_{el}^{BT} = \int dz\ \frac{dE_{el}^{BT}}{dz}. \tag{3.22}$$

For the BT elastic energy loss, we follow [163] and assume that the elastic energy loss follows a Gaussian distribution according to the central limit theorem. Thus, the distribution of elastic energy loss is Gaussian with the mean provided by average elastic energy loss ΔE_{el}^{BT}, and width by the fluctuation dissipation theorem [169, 183]

$$\sigma = \frac{2}{E}\int dz\frac{dE_{el}^{BT}}{dz}T(z), \tag{3.23}$$

where z integrates along the path of the parton, and $T(z)$ is the temperature along the path. We therefore obtain the following probability distribution for losing a fraction ϵ of the incoming parton energy E due to elastic energy loss

$$P_{el}^{BT}(\epsilon) \equiv \frac{E}{\sqrt{2\pi}\sigma}\exp\left[-\left(\frac{\epsilon E+\Delta E_{el}^{BT}}{\sqrt{2}\sigma}\right)^2\right]. \tag{3.24}$$

3.2.2.2 HTL-only elastic energy loss

Here, we will quote some of the key results needed to perform the HTL-only elastic energy loss calculation. The interaction rate dN_{el}/dz, where N_{el} is the number of elastic scatters and z is the distance that the parton has traveled through the medium, can be

written in terms of the incoming (outgoing) parton energy E (E') as [163, 179]

$$\begin{aligned}\frac{dN_{el}}{dz} =& \frac{4C_R\alpha_s^2}{\pi}\int\frac{d^3qd\omega}{2\pi}\frac{E}{E'}\delta\left(\omega+E-E'\right)\\ &\times\frac{n_B(\omega)}{q}\left(1-\frac{\omega^2}{q^2}\right)^2\left\{\sum_m\left[C_{LL}^m\left|\Delta_L\right|^2\right.\right.\\ &\left.\left.+2C_{LT}^m\,\mathrm{Re}\left(\Delta_L\Delta_T\right)+C_{TT}^m\left|\Delta_T\right|^2\right]\right\}.\end{aligned} \tag{3.25}$$

In eq. 3.25, we use the notation of [155] to write $|\vec{q}|\equiv q$; additionally, $n_B(\omega)$ is the Bose distribution, while Δ_L and Δ_T are the longitudinal and transverse propagators and are defined as

$$\Delta_{L,T}(q)\equiv\frac{1}{q^2-\Pi_{L,T}(q)}, \tag{3.26}$$

where $\Pi_{L,T}$ is the longitudinal and transverse self-energy, respectively, and are defined as:

$$\Pi_L\equiv\mu^2\left(1-x^2\right)\left(1-\frac{x}{2}\ln\frac{x+1}{x-1}\right), \tag{3.27a}$$

$$\Pi_T\equiv\frac{\mu^2}{2}\left(2+x^2-\frac{x\left(1-x^2\right)}{2}\ln\frac{x+1}{x-1}\right). \tag{3.27b}$$

In eq. 3.27, we have further defined $x\equiv\omega/q$. The C_{IJ}^m coefficients are defined as

$$C_{IJ}^m\equiv\int_{\frac{1}{2}(\omega+q)}^{\infty}k^0kdk\left(n_m\left(k^0-\omega\right)-n_m\left(k^0\right)\right)c'_{IJ}. \tag{3.28}$$

In eq. 3.28, n_m are statistical distributions (Bose and Fermi distributions for gluons and quarks, respectively); the c'_{IJ} coefficients are defined to be:

$$\begin{aligned}c'_{LL}\equiv&\left(\left(1+\frac{\omega}{2E}\right)^2-\frac{q^2}{4E^2}\right)\\ &\times\left(\left(1-\frac{\omega}{2k^0}\right)^2-\frac{q^2}{4\left(k^0\right)^2}\right),\end{aligned} \tag{3.29a}$$

$$c'_{LT}\equiv 0, \tag{3.29b}$$

$$\begin{aligned}c'_{TT}\equiv&\frac{1}{2}\left(\left(1+\frac{\omega}{2E}\right)^2+\frac{q^2}{4E^2}-\frac{1-v^2}{1-\frac{\omega^2}{q^2}}\right)\\ &\times\left(\left(1+\frac{\omega}{2k^0}\right)^2+\frac{q^2}{4\left(k^0\right)^2}-\frac{1-v_k^2}{1-\frac{\omega^2}{q^2}}\right),\end{aligned} \tag{3.29c}$$

where v_k and v are the velocities of the medium parton and the incident parton, respectively. The C_{IJ}^m coefficients can be calculated analytically using the following thermal integral

$$I_n^m \equiv \int_{\frac{1}{2}(\omega+q)}^{\infty} dk \left(n_m(k-\omega) - n_m(k)\right) k^n. \tag{3.30}$$

For bosons $(+)$ and fermions $(-)$, respectively, these integrals evaluate to:

$$I_0^{\pm} = \pm T \log\left(\frac{1 \mp e^{-\kappa_+}}{1 \mp e^{-\kappa_-}}\right), \tag{3.31a}$$

$$I_1^{\pm} = \pm T^2 \left[\mathrm{Li}_2\left(\pm e^{-\kappa_-}\right) - \mathrm{Li}_2\left(\pm e^{-\kappa_+}\right)\right] + \kappa_+ T I_0^{\pm}, \tag{3.31b}$$

$$I_2^{\pm} = \pm 2T^3 \left[\mathrm{Li}_3\left(\pm e^{-\kappa_-}\right) - \mathrm{Li}_3\left(\pm e^{-\kappa_+}\right)\right] + 2\kappa_+ T I_1^{\pm} - \kappa_+^2 T^2 I_0^{\pm}, \tag{3.31c}$$

where Li_n is the polylogarithm function, and we have defined $\kappa_\pm \equiv (\omega \pm q)/2T$.

Lastly, we perform a change of variables by using $\omega = \epsilon E$ to convert the scattering rate in eq. 3.25 to a single elastic scattering kernel:

$$\frac{dN_{el}}{d\epsilon} = \frac{d\omega}{d\epsilon}\frac{d}{d\omega}\int dz \frac{dN_{el}}{dz} \tag{3.32a}$$

$$= E\frac{d}{d\omega}\int dz \frac{dN_{el}}{dz}. \tag{3.32b}$$

Previous applications of the HTL elastic energy loss [146, 155, 163] assumed that the scattering rate was independent of z, allowing one to approximate the elastic scattering kernel as

$$\frac{dN_{el}}{d\epsilon} \simeq LE\frac{dN_{el}}{dzd\omega}. \tag{3.33}$$

The approximation in eq. 3.33 was made to simplify the non-trivial z-dependence introduced by the temperature's path dependence. In this work we relax the assumption of z-independence and use the more general form of the elastic scattering kernel given in eq. 3.32.

Similarly to the radiative energy loss, we can define the integrated HTL-only elastic

energy loss through the number of scatters *via*

$$\Delta E_{el}^{HTL} = \int_{-\infty}^{1} d\epsilon \, \frac{dE_{el}^{HTL}}{d\epsilon}, \tag{3.34}$$

with the corresponding expression for $dE_{el}^{HTL}/d\epsilon$

$$\frac{dE_{el}^{HTL}}{d\epsilon} = \epsilon E \frac{dN_{el}}{d\epsilon}. \tag{3.35}$$

Note that the energy loss in eq. 3.34 is dependent on the parton mass *via* $E = \sqrt{M^2 + p^2} \approx \sqrt{M^2 + p_T^2}$.

In close analogy with eq. 3.18, one can assume that the elastic collisions are independent of one another and that the distributions associated with each collision follow a Poisson distribution. Under these assumptions—and after accounting for the probability leakage that occurs due to the physical constraints on the domains of integration—we obtain the following distribution for multiple elastic collisions

$$P_{el}^{HTL}(\epsilon) = \sum_{n=0}^{\infty} \frac{(N_{el})^n}{n!} e^{-N_{el}} p_n^{el}(\epsilon) + w_{el}\delta(\epsilon - 1). \tag{3.36}$$

In eq. 3.36, N_{el} is the average number of collisions in an event and is calculated as

$$N_{el} \equiv \int_{-\infty}^{1} d\epsilon \frac{dN_{el}}{d\epsilon}. \tag{3.37}$$

The $p_n^{el}(\epsilon)$ terms in eq. 3.36 are the probability distributions associated with n elastic collisions occurring given that the collisions carry fractional momentum ϵ and take the form

$$p_n^{el}(\epsilon) = \int d\epsilon_{n-1} p_{n-1}^{el}(\epsilon_{n-1}) p_1^{el}(\epsilon - \epsilon_{n-1}), \tag{3.38}$$

with

$$p_0^{el}(\epsilon) \equiv \delta(\epsilon) \tag{3.39a}$$

$$p_1^{el}(\epsilon) \equiv \frac{1}{N_{el}} \frac{dN_{el}}{d\epsilon}. \tag{3.39b}$$

The weight w_{el} is interpreted as the probability of the parton losing all of its energy through elastic collisions; w_{el} arises due to the same probability leakage that occurred in the radiative energy loss sector, and is calculated *via*

$$w_{el} \equiv \int_1^\infty d\epsilon \sum_{n=0}^{\infty} \frac{(N_{el})^n}{n!} e^{-N_{el}} p_n^{el}(\epsilon). \tag{3.40}$$

3.2.3 Total energy loss

The total energy loss of the hard parton moving through the medium is

$$P_{tot}(\epsilon) = \int dx\ P_{el}(x) P_{rad}(\epsilon - x), \tag{3.41}$$

where P_{el} is the elastic energy loss distribution for either the BT (eq. 3.24) or HTL-only (eq. 3.36) approaches, and P_{rad} is the radiative energy loss distribution (eq. 3.18).

3.2.4 Parametrization of trajectories

In this section, we describe our method of parametrizing trajectories of hard partons through the medium, and how we use this parametrization to compute the energy loss of an arbitrary trajectory through the medium.

3.2.4.1 Computational challenges of energy loss calculations in phenomenology

In order to perform our phenomenological analysis, the energy loss needs to be calculated on an event-by-event basis using a hydrodynamic medium. The most straight forward approach would have been to directly use the hydrodynamic medium as our background in our energy loss calculation, but this approach is computationally expensive. To get a sense of the relative computational cost of this direct approach, consider

the typical resolution needed to accurately sample the QGP in our model: typically ~ 20 angles and a grid of size $\sim 15 \times 15$ fm^2 with intervals of ~ 0.05 fm are needed to resolve the geometry of each event; to then capture the event-by-event fluctuations, the energy loss would need to be calculated another $\sim 10^3$ times, one for each event. Thus, this direct approach requires $\sim 10^9$ evaluations of the energy loss per collision type. Instead of the direct approach, we will introduce two parameters, ρ_0 and t_c, to model the effects of the medium density and the path length of a given trajectory (to be discussed in the following section). Using the fitted parameter method, we find that the entire phase space of possible paths requires a grid of ρ_0 and t_c parameters such that $\rho_0 \in [1, 100]$ fm^{-3} and $t_c \in [0.4, 11]$ fm with intervals of 10 fm^{-3} and 1 fm, respectively; this results in a total of $\sim 10^2$ evaluations of the energy loss per collision type. Thus, calculating the energy loss by using the fitted parameter method proves to be seven orders of magnitude faster than the more direct method. We will demonstrate in Sec. 3.2.4 that evaluating the energy loss in terms of the fitted parameters closely resembles the energy loss calculation done if we were to use the true hydrodynamic temperature profile.

3.2.4.2 *Parametrization of trajectories on a path-by-path basis*

In this work we follow [196], and treat the QGP as a mixture of Bose and Fermi gases, which allows us to relate the medium density $\rho(z)$ to the temperature $T(z)$ of the medium *via*

$$\rho(z) = \left(2(N_c^2 - 1) + \frac{3N_c n_f C_F}{C_A}\right) \frac{\zeta(3)}{\pi^2} T^3(z) \tag{3.42a}$$

$$= \frac{24\zeta(3)}{\pi^2} T^3(z), \tag{3.42b}$$

where $T(z)$ is a temperature profile obtained from a realistic hydrodynamic simulation of the QGP medium. By choosing the medium density in this manner, we are able to capture the detailed dynamics of the medium along the parton's trajectory on a path-by-path and event-by-event basis. To obtain the relation in eq. 3.42, we have used the

following standard thermodynamic results [163, 196]:

$$\sigma_{gg} = \frac{C_A^2 \pi \alpha_s^2}{2\mu^2}, \tag{3.43a}$$

$$\sigma_{qg} = \frac{C_F}{C_A}\sigma_{gg}, \tag{3.43b}$$

$$\rho_g = 2\left(N_c^2 - 1\right)\frac{\zeta(3)}{\pi^2}T^3, \tag{3.43c}$$

$$\rho_q = 3N_c n_f \frac{\zeta(3)}{\pi^2}T^3, \tag{3.43d}$$

$$\rho = \rho_g + \frac{\sigma_{qg}}{\sigma_{gg}}\rho_q. \tag{3.43e}$$

In eq. 3.43 ζ is the Riemann zeta function, ρ_q and ρ_g are the density of quarks and gluons, respectively, σ_{gg} and σ_{qg} are the gluon-gluon and quark-gluon cross sections, respectively, and $N_c = 3$ is the number of colours.

In this work the trajectories taken by the hard partons are parametrized by modelling the medium density through a power law of the form

$$\rho_{fit}\left(z, \tau_0, \rho_0, t_c\right) = \rho_0 \left(\frac{\tau_0}{z}\right)^{\beta} \theta\left(t_c - z\right)\theta\left(z - \tau_0\right). \tag{3.44}$$

Our prescription of the parametrization of the medium density in eq. 3.44 is motivated by the work done in [199], where it was shown that a power-law medium density of the form of eq. 3.44 accurately approximates medium-induced energy loss; we confirm this result numerically in fig. 3.4. Note that by including $\theta\left(z - \tau_0\right)$ in the parametrization of the medium density in eq. 3.44, we are effectively excluding energy loss that occurs before the formation time of the medium. In eq. 3.44 we fix the formation time as $\tau_0 = 0.4$ fm/c to be consistent with the hydrodynamic model. We then fix the β parameter by using the Levenberg-Marquardt method [200] to fit a power-law of the form $1/z^{\beta}$ to a set of paths through central $\mathrm{Pb} + \mathrm{Pb}$ collisions; we find a fitted value of $\beta = 1.2$. Note that in [199], they model $n(z)$, a *linear* medium density, as a power law of the form $n(z) \sim 1/z^{\alpha} \sim (\rho_{fit})^{1/3}$, and find a scaling parameter of $\alpha = 0.5$. Additionally, in [199], the formation time of the medium is $\tau_0 = 0.1$ fm/c, and thus they include regions of the medium's evolution where the medium's temperature cools more steeply. Thus, our findings of $\beta/3 = 0.4 < \alpha = 0.5$ is consistent with [199].

The procedure for choosing the ρ_0 and t_c parameters is determined on a path-by-path basis and will be described in the following paragraph. Eq. 3.42 along with eq. 3.44 allows us to write the temperature distribution for each path in a parametric form

$$T_{fit}\left(z, \tau_0, \rho_0, t_c\right) = \left(\frac{\pi^2 \rho_{fit}\left(z, \tau_0, \rho_0, t_c\right)}{24\zeta(3)}\right)^{1/3} \tag{3.45}$$

In the following discussion, we will find it useful to use a parameter, denoted here as T_0, which will represent the temperature at the start of a trajectory, rather than the parameter ρ_0, which represents the density at the start of a trajectory. The T_0 parameter can be related to the ρ_0 parameter through eq. 3.44 and eq. 3.45 *via*

$$T_0 \equiv \left(\frac{\pi^2 \rho_0}{24\zeta(3)}\right)^{1/3}. \tag{3.46}$$

It should be noted that the parametrization of the medium density is only reliant on two independent parameters, ρ_0 and t_c, or equivalently T_0 and t_c.

The temperature distributions obtained from the hydrodynamic models are taken to be zero after a critical temperature of $T \simeq 150$ MeV is reached [188]; the t_c parameter is chosen to be the time at which the critical temperature occurs for the particular path. Once t_c has been determined, we choose the ρ_0 parameter by imposing the following condition

$$\int dz T(\mathbf{x}_0 + z\hat{\phi}, \tau_0) = \int dz T_{fit}\left(z, \tau_0, \rho_0, t_c\right), \tag{3.47}$$

where T is the temperature distribution obtained from the hydrodynamic model sampled along the trajectory defined by the initial position $\mathbf{x}_0$ and the azimuthal angle $\hat{\phi}$, and T_{fit} is defined in eq. 3.45. The condition in eq. 3.47 ensures that the integrated energy loss of the parametric temperature distribution closely approximates the integrated energy loss of the hydrodynamic temperature distribution.

In fig. 3.2, a comparison is made for a variety of collision systems between the temperature profiles obtained from the hydrodynamic simulations and the corresponding fitted temperature of eq. 3.45. The comparison is made for two characteristic paths: 1— a *central* path starting near the center of the collision region and 2— a *peripheral* path starting near the edge of the collision region. All central paths are defined by $\mathbf{x}_0 = (0, 0)$

fm and $\hat{\phi} = 0$. Peripheral paths for $p + \mathrm{Pb}$ and $\mathrm{O} + \mathrm{O}$ are defined by $\mathbf{x}_0 = (0, 1.)$ fm and $\hat{\phi} = 0$, while the peripheral path for $\mathrm{Pb} + \mathrm{Pb}$ is defined by $\mathbf{x}_0 = (1.5, 4.5)$ fm and $\hat{\phi} = 1$. The paths we consider in fig. 3.2 are representative of the range of trajectories that may be taken by hard partons moving through the medium. The fitted parameters for $p + \mathrm{Pb}$ central and peripheral are $\rho_0 = 16.4$ fm^{-3} (T_0 = 0.4 GeV) and $t_c = 3.5$ fm, and $\rho_0 = 9.9$ fm^{-3} (T_0 = 0.3 GeV) and $t_c = 3.6$ fm, respectively. The fitted parameters for $\mathrm{O} + \mathrm{O}$ central and peripheral are $\rho_0 = 10.6$ fm^{-3} (T_0 = 0.3 GeV) and $t_c = 3.3$ fm, and $\rho_0 = 6.1$ fm^{-3} (T_0 = 0.3 GeV) and $t_c = 2.2$ fm, respectively. The fitted parameters for $\mathrm{Pb} + \mathrm{Pb}$ central and peripheral are $\rho_0 = 73.3$ fm^{-3} (T_0 = 0.6 GeV) and $t_c = 9.2$ fm, and $\rho_0 = 29.9$ fm^{-3}, T_0 = 0.4 GeV and $t_c = 5.8$ fm, respectively.

In general we find that the fitted temperature profiles closely resemble the hydrodynamic temperature profiles in central $\mathrm{Pb} + \mathrm{Pb}$ collisions from $t = \tau_0$ to $t = t_c$. For smaller collision systems such as p+Pb, the fitted temperature profiles tend to be cooler (hotter) than the hydrodynamic temperature profiles at earlier (later) times.

In fig. 3.3, we show the DGLV differential energy loss dE/dz from eq. 3.2a for p+Pb (top), O+O (middle), and Pb+Pb (bottom) at 0-5% centrality with $\alpha_s = 0.3$ and $p_T = 10$ GeV for charm quarks. Note that the conclusions that follow from this section will extend to gluons and other quark flavours. The dE/dz is calculated using the hydrodynamic temperature profile (dashed) and the fitted temperature profile (solid) for the same two characteristic paths described in fig. 3.2. For $\mathrm{Pb} + \mathrm{Pb}$, we see that the dE/dz calculated using the fitted temperature profile closely resembles the dE/dz calculated using the hydrodynamic temperature profile for both the central and peripheral paths. For p+Pb and O+O, we see that the dE/dz calculated using the fitted temperature profile deviates from the dE/dz calculated using the hydrodynamic temperature profile at early times, which is consistent with the deviation of the fitted temperature profile from the hydrodynamic temperature profile at early times as shown in fig. 3.2.

In fig. 3.4, we show the DGLV contribution to the integrated energy loss $\Delta E/E$ from eq. 3.7 as a function of p_T for $p + \mathrm{Pb}$ (top), $\mathrm{O} + \mathrm{O}$ (middle), and $\mathrm{Pb} + \mathrm{Pb}$ (bottom) at 0-5% centrality with $\alpha_s = 0.3$ for charm quarks. The $\Delta E/E$ is calculated using the hydrodynamic temperature profile (dashed) and the fitted temperature profile (solid) for the same two characteristic paths described in fig. 3.2. For all three collision systems,

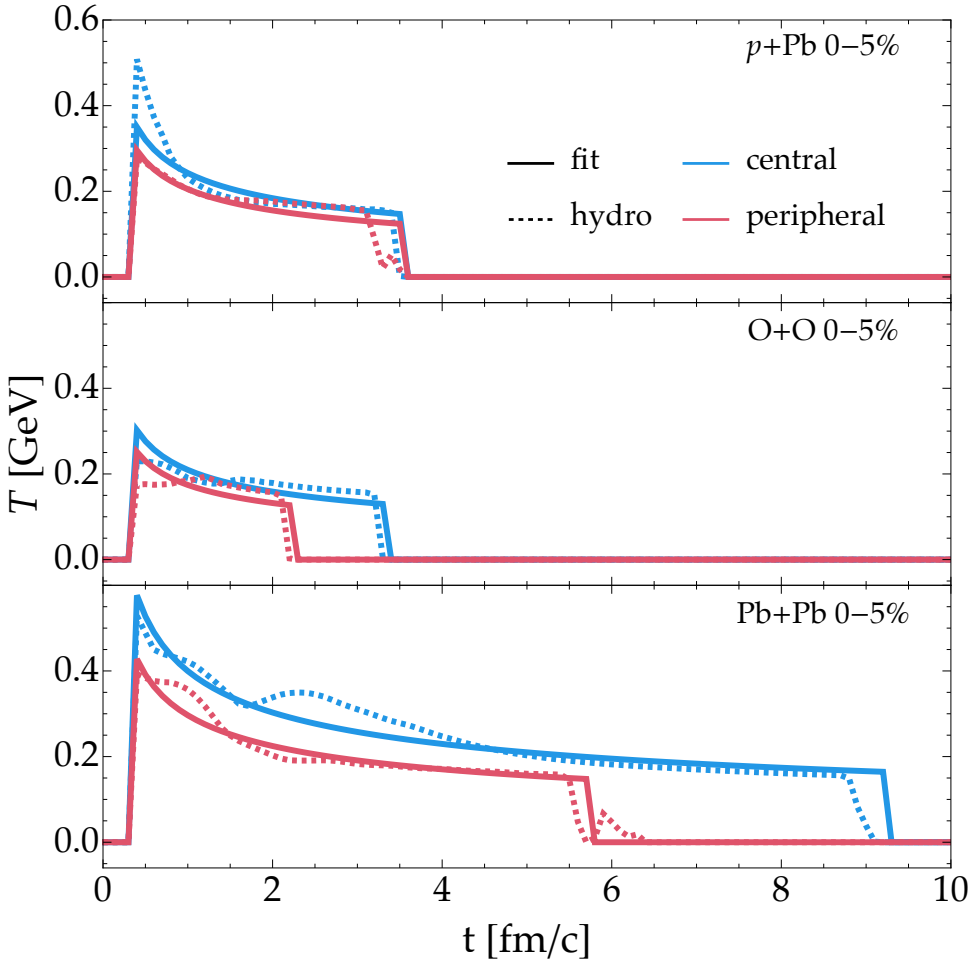

Figure 3.2: Temperature profile from the hydrodynamic model (dashed) and from the fit of temperature profile (solid) from eq. 3.45 for $p + \mathrm{Pb}$ (top), $\mathrm{O} + \mathrm{O}$ (middle) and $\mathrm{Pb} + \mathrm{Pb}$ (bottom) collision systems at 0-5% centrality for two different characteristic trajectories.

the differences between the integrated energy loss $\Delta E/E$ calculated using the fitted temperature profile and the integrated energy loss calculated using the hydrodynamic temperature profile are negligible for all relevant p_T due to the fitting procedure in eq. 3.47.

While β from eq. 3.44 is fitted to central $\mathrm{Pb} + \mathrm{Pb}$ temperature profiles, it is not necessarily optimal for smaller collision systems; this is evident in fig. 3.2, where the fitted temperature profiles for $p + \mathrm{Pb}$ and $\mathrm{O} + \mathrm{O}$ collisions deviate from the hydrodynamic temperature profiles at early times. However, we find that using a single value of β across all collision systems still allows us to accurately capture the energy loss of trajectories through the medium as shown in fig. 3.4. We thus conclude that the energy loss produced in our model is not particularly sensitive to the value of β.

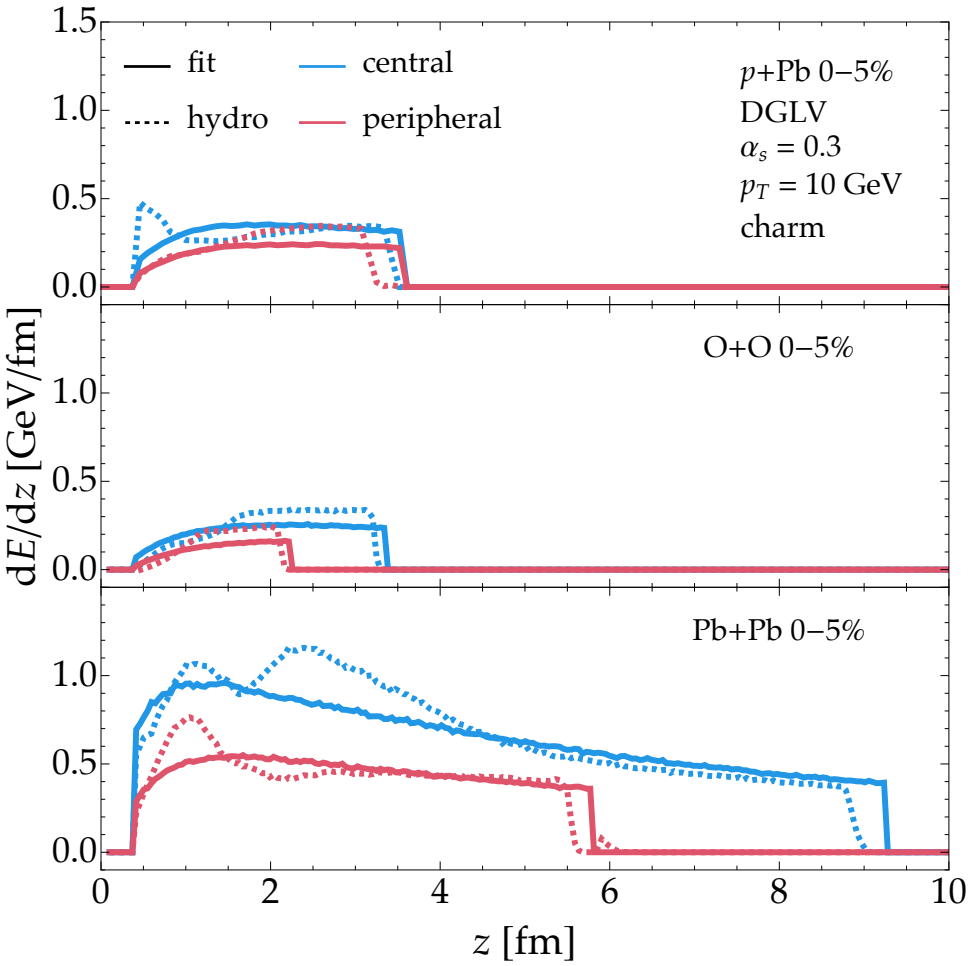

Figure 3.3: Differential DGLV energy loss dE/dz for charm quarks calculated at 10 GeV and $\alpha_s = 0.3$ using hydrodynamic temperature profile (dashed) and fitted temperature profile (solid) for $p + \mathrm{Pb}$ (top), $\mathrm{O} + \mathrm{O}$ (middle) and $\mathrm{Pb} + \mathrm{Pb}$ (bottom) collision systems at 0-5% centrality. Paths are the same as in fig. 3.2.

In fig. 3.5, fig. 3.6 and fig. 3.7 we show $\Delta E/E$ at fixed p_T for charm quarks as a function of the $T_0,\ \rho_0$ and t_c parameters, respectively. The plots in fig. 3.5, fig. 3.6 and fig. 3.7 show that the energy loss grows monotonically in the $T_0,\ \rho_0$ (which is related to T_0 through eq. 3.46), and t_c parameters. We thus conclude that the energy loss of a parton with a trajectory through a hotter and longer lived medium will be larger than the energy loss of a parton with a trajectory through a cooler and shorter lived medium. In fig. 3.7, we see that as t_c approaches 0.4 fm (the formation time of the medium), the energy loss approaches zero, which is consistent with the t_c parameter serving as an effective cut off on the z integral of eq. 3.2.

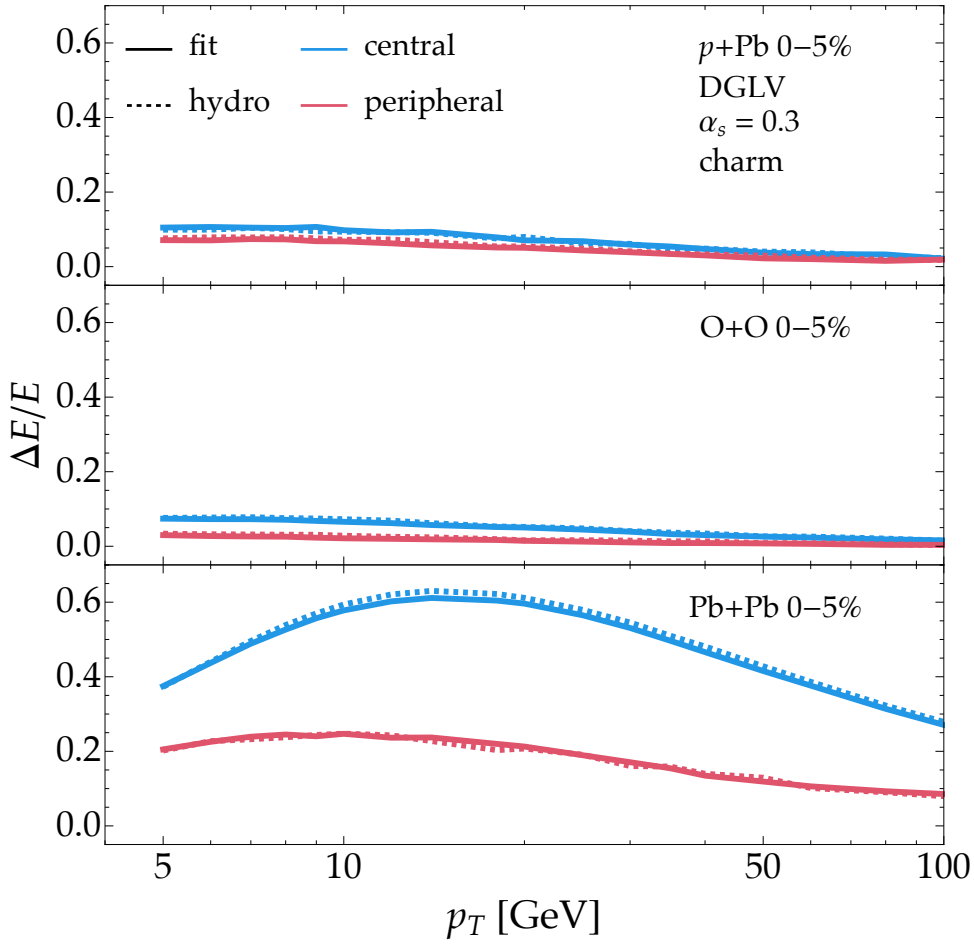

Figure 3.4: DGLV $\Delta E/E$ as a function of p_T for charm quarks calculated using hydrodynamic temperature profile (dashed) and fitted temperature profile (solid) for $p + \mathrm{Pb}$ (top), $\mathrm{O} + \mathrm{O}$ (middle) and $\mathrm{Pb} + \mathrm{Pb}$ (bottom) collision systems at 0-5% centrality. Paths are the same as in fig. 3.2.

3.2.4.3 *Parametrization of global geometry of the collision system*

In what follows we shall describe how we assign to each collision system a probability distribution, $P_{geo}(T_0, t_c|\phi)$, for the T_0 and t_c parameters (or ρ_0 and t_c *via* eq. 3.46). We classify these probability distributions by the angle of the parton's trajectory through the medium, which will allow us to consider the spatial azimuthal anisotropies of the medium. The prescription we propose for $P_{geo}(T_0, t_c|\phi)$ is

$$P_{geo}(T_0, t_c|\phi) \propto \int d^2\mathbf{x}_0 \, \rho_{\text{coll}}(\mathbf{x}_0) \delta\left(T_0(\mathbf{x}_0, \phi) - T_0\right) \delta\left(t_c(\mathbf{x}_0, \phi) - t_c\right). \tag{3.48}$$

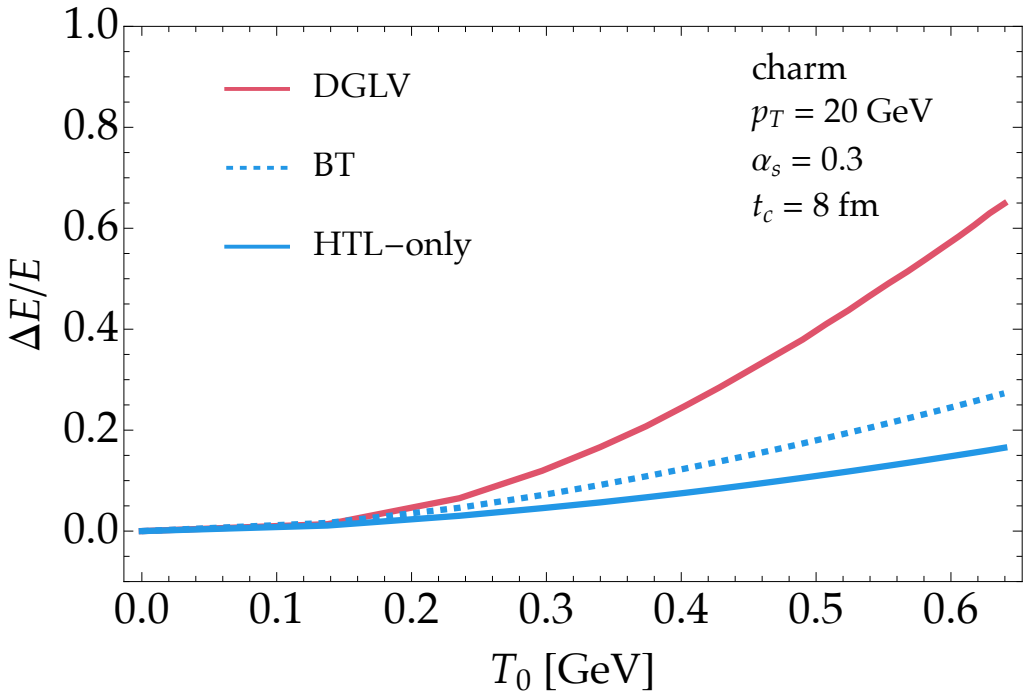

Figure 3.5: $\Delta E/E$ for DGLV (red), BT (blue-dashed), and HTL-Only (blue) as a function of initial temperature T_0 with $t_c = 8$ fm held constant.

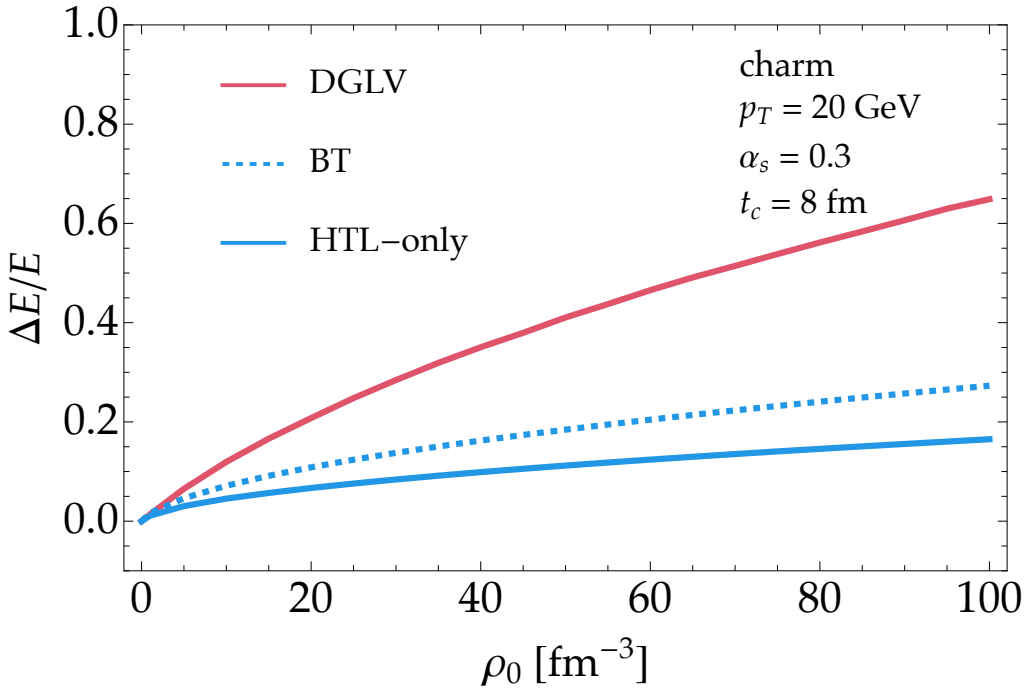

Figure 3.6: $\Delta E/E$ for DGLV (red), BT (blue-dashed), and HTL-Only (blue) as a function of ρ_0 fitted parameter with $t_c = 8$ fm held constant.

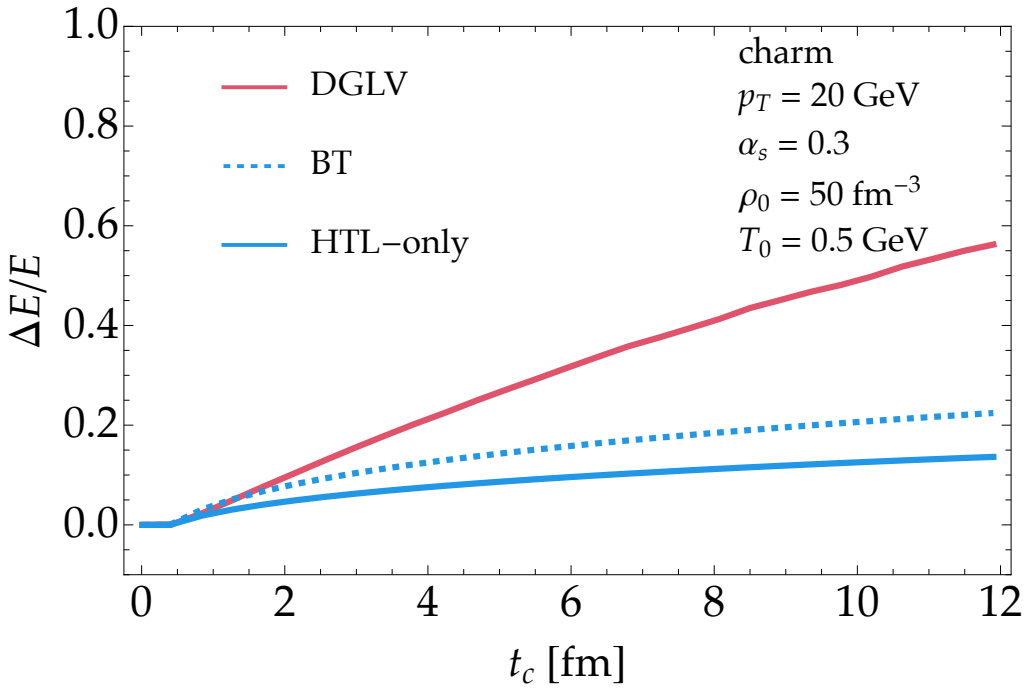

Figure 3.7: $\Delta E/E$ for DGLV (red), BT (blue-dashed), and HTL-Only (blue) as a function of t_c fitted parameter with $\rho_0 = 50$ fm^{-3} and $T_0 = 0.5$ GeV held constant.

In eq. 3.48, $\rho_{\text{coll}}(\mathbf{x}_0)$ is the density of binary nucleon-nucleon collisions at the initial position $\mathbf{x}_0$ of the hard parton. $T_0(\mathbf{x}_0, \phi)$ and $t_c(\mathbf{x}_0, \phi)$ are the fitted parameters obtained from paths through the medium with initial position $\mathbf{x}_0$ and azimuthal angle ϕ using the procedure described in the previous section. Eq. 3.48 follows after assuming that the initial parton spectrum scales like the density of binary nucleon-nucleon collisions $\rho_{\text{coll}}(\mathbf{x}_0)$. The energy loss, through eq. 3.44 and eq. 3.45, can be calculated as a function of the (T_0, t_c) parameters; one may then average the energy loss over the $P_{geo}(T_0, t_c|\phi)$ distributions to obtain results that account for the global geometry of the collision.

In Fig. 3.8, the 2D distribution of the T_0 and t_c parameters are shown for Pb + Pb 0-5% collision system at $\sqrt{s_{NN}} = 5.02$ TeV. We see there is a strong correlation between the T_0 and t_c parameters; this correlation arises as paths with a hotter initial temperature T_0 will generally start near the center of the collision overlap region and thus will have to traverse a larger region of the medium before reaching the critical temperature.

In fig. 3.9, fig. 3.10 and fig. 3.11 we show the numerical results for the $P_{geo}(\rho_0, t_c)$

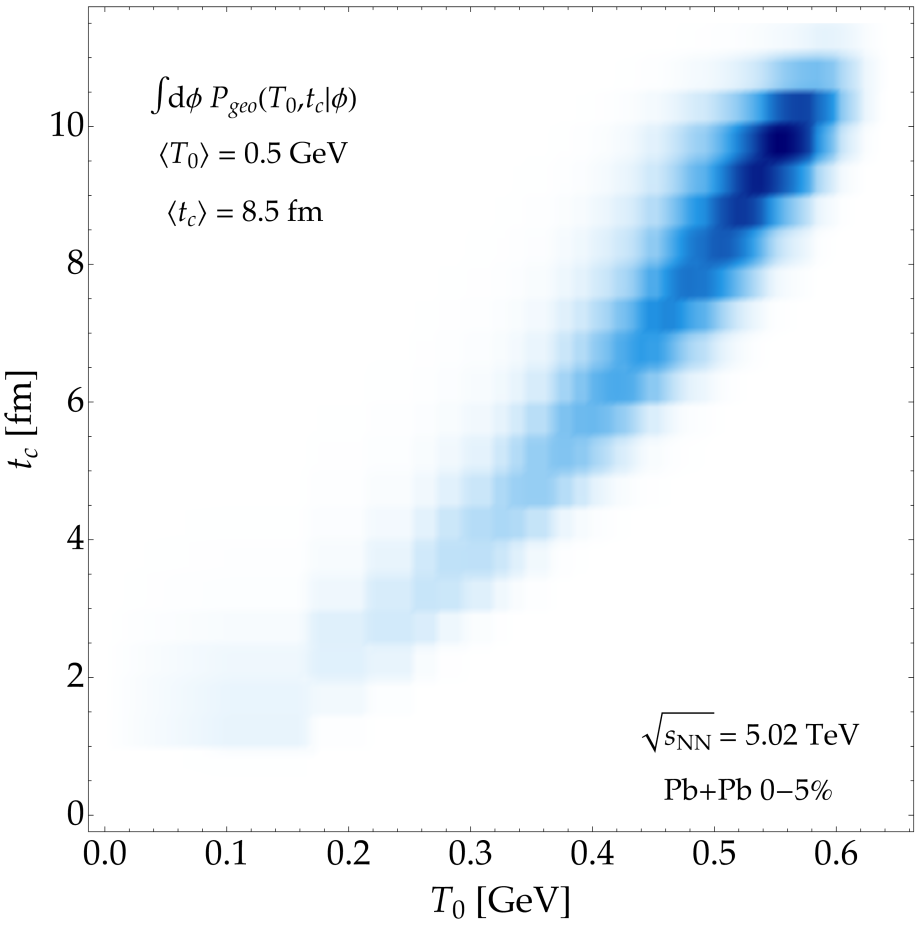

Figure 3.8: Eq. 3.48 as a function of the fitted parameter t_c and initial temperature T_0 with ϕ integrated out for $\mathrm{Pb}+\mathrm{Pb}$ 0-5% collision system. The colour gradient in the plot represents the probability density. The mean temperature T_0 and mean t_c of the distribution are $\langle T_0 \rangle = 0.5$ GeV and $\langle t_c \rangle = 8.5$ fm, respectively.

distribution in eq. 3.48 for $\mathrm{Pb}+\mathrm{Pb}$ at $0-5\%$ centrality, $\mathrm{Pb}+\mathrm{Pb}$ at $70-80\%$ centrality, $p+\mathrm{Pb}$ at $0-5\%$ centrality, and $\mathrm{Au}+\mathrm{Au}$ at $0-5\%$ centrality. Note that in fig. 3.9, fig. 3.10 and fig. 3.11 the angular components of the P_{geo} distributions have been integrated out; furthermore, we show the expectation values obtained from the P_{geo} distributions for the T_0, ρ_0, and t_c parameters for the respective collision systems. The T_0, ρ_0 and t_c parameters are all positively correlated with the system size and centrality of the collision system. The ordering of the average T_0 and ρ_0 values indicates that central $\mathrm{Pb}+\mathrm{Pb}$ collisions are hotter than central $\mathrm{Au}+\mathrm{Au}$ collisions, which are in turn hotter than central $p+\mathrm{Pb}$ collisions. Similarly, the ordering of the average t_c values indicates that central $\mathrm{Pb}+\mathrm{Pb}$ collisions have the longest lifetime, followed by central $\mathrm{Au}+\mathrm{Au}$, and then central $p+\mathrm{Pb}$ collisions. In fig. 3.9 (fig. 3.10), there is a spike in the distribution

at $T_0 = 0$ ($\rho_0 = 0$) for $\mathrm{Pb} + \mathrm{Pb}$ collisions at $70 - 80\%$ centrality; this spike arises from the fact that there are many paths in this system that do not traverse any appreciable amount of medium, and thus have $T_0 = 0$ ($\rho_0 = 0$).

It should be noted that the average effective temperatures obtained from the CTv1.0 model for 0-5% $\mathrm{Pb} + \mathrm{Pb}$, $\mathrm{Au} + \mathrm{Au}$, and $p + \mathrm{Pb}$ collisions satisfy the ordering [163]

$$\langle T_{\mathrm{eff}}^{\mathrm{Au+Au}} \rangle < \langle T_{\mathrm{eff}}^{\mathrm{Pb+Pb}} \rangle < \langle T_{\mathrm{eff}}^{p+\mathrm{Pb}} \rangle, \tag{3.49}$$

whereas the average initial temperatures extracted in the CTv2.0 model satisfy

$$\langle T_0^{p+\mathrm{Pb}} \rangle < \langle T_0^{\mathrm{Au+Au}} \rangle < \langle T_0^{\mathrm{Pb+Pb}} \rangle. \tag{3.50}$$

This apparent discrepancy arises because the CTv1.0 model is parameterized in terms of an effective temperature rather than the initial temperature. Within the Bjorken expansion approximation used in the CTv1.0 model, the effective temperature is related to the initial temperature by

$$T_{\mathrm{eff}} \approx \frac{\int \mathrm{d}^2\mathbf{x}\, T^6(\mathbf{x}, \tau_0)}{\int \mathrm{d}^2\mathbf{x}\, T^3(\mathbf{x}, \tau_0)} \left(\frac{2\tau_0}{L_{\mathrm{eff}}}\right)^{1/3} \simeq T_0 \left(\frac{2\tau_0}{L_{\mathrm{eff}}}\right)^{1/3}. \tag{3.51}$$

Consequently,

$$T_0 \sim T_{\mathrm{eff}} L_{\mathrm{eff}}^{1/3},$$

so the system-size dependence encoded in L_{eff} modifies the ordering of the average T_0 compared to the ordering of the average T_{eff}. Indeed, ordering the quantities $T_{\mathrm{eff}} L_{\mathrm{eff}}^{1/3}$ obtained from the CTv1.0 model reproduces the same ordering as the average initial temperatures extracted in the CTv2.0 model.

3.2.5 Comparison of CTv1.0 and CTv2.0 models

In this section, we provide a step by step modification of the CTv1.0 model [146, 155, 159, 163, 171] to a form that is comparable to the CTv2.0 model in order to explore

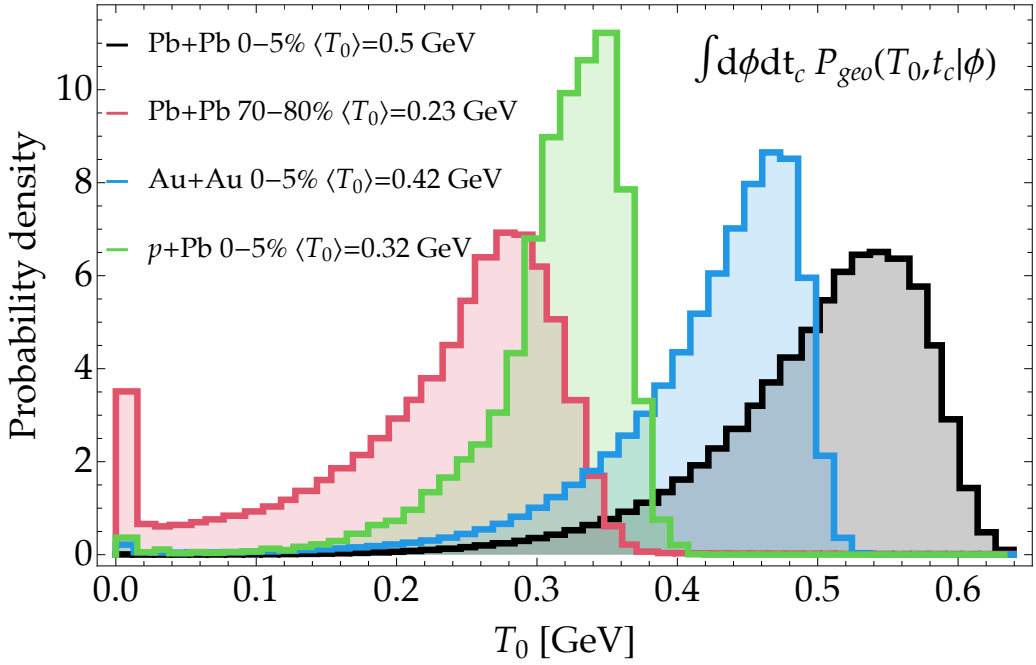

Figure 3.9: Eq. 3.48 as a function of the initial temperature T_0 with ϕ and t_c integrated out for $\mathrm{Pb}+\mathrm{Pb}$ at $0-5\%$ centrality (black), $\mathrm{Pb}+\mathrm{Pb}$ at $70-80\%$ centrality (red), $\mathrm{Au}+\mathrm{Au}$ at $0-5\%$ centrality (blue), and $p+\mathrm{Pb}$ at $0-5\%$ centrality (green).

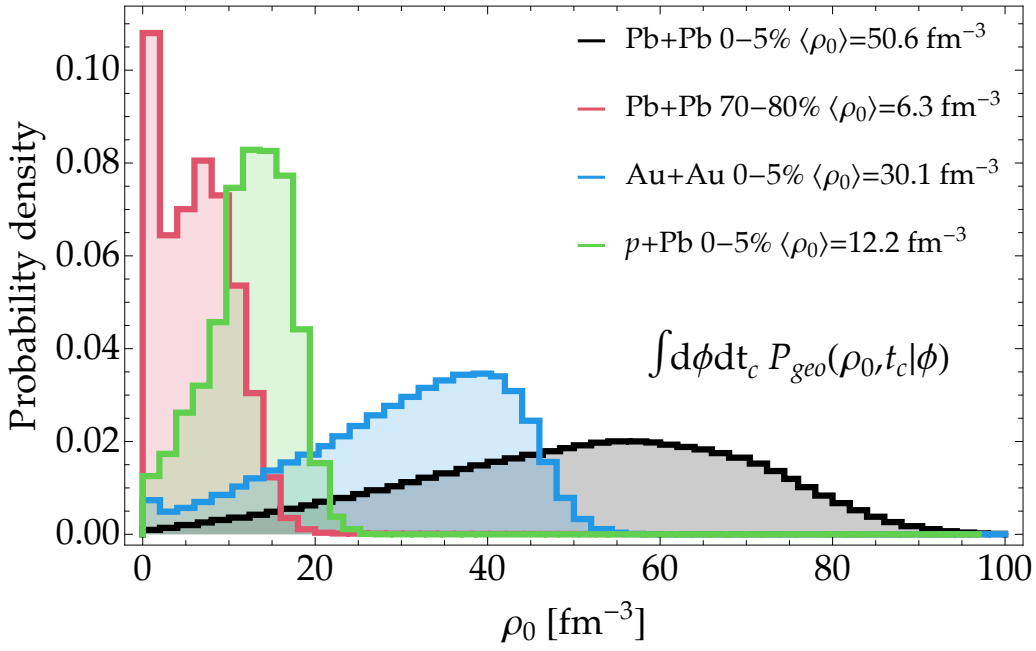

Figure 3.10: Eq. 3.48 as a function of the fitted parameter ρ_0 with ϕ and t_c integrated out for $\mathrm{Pb}+\mathrm{Pb}$ at $0-5\%$ centrality (black), $\mathrm{Pb}+\mathrm{Pb}$ at $70-80\%$ centrality (red), $\mathrm{Au}+\mathrm{Au}$ at $0-5\%$ centrality (blue), and $p+\mathrm{Pb}$ at $0-5\%$ centrality (green).

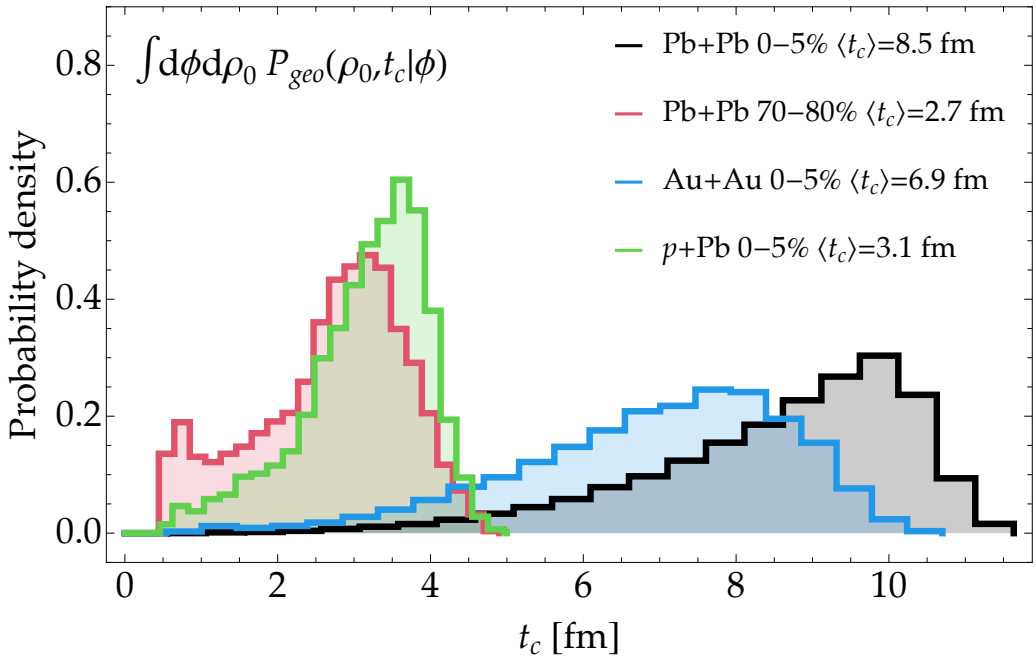

Figure 3.11: Eq. 3.48 as a function of the fitted parameter t_c with ϕ and ρ_0 integrated out for $\mathrm{Pb}+\mathrm{Pb}$ at $0-5\%$ centrality (black), $\mathrm{Pb}+\mathrm{Pb}$ at $70-80\%$ centrality (red), $\mathrm{Au}+\mathrm{Au}$ at $0-5\%$ centrality (blue), and $p+\mathrm{Pb}$ at $0-5\%$ centrality (green).

the physical consequences of the differences between the two models. We will first compare the radiative energy loss obtained using the CTv1.0 model to the radiative energy loss obtained using the CTv2.0 model; then we will compare the elastic energy loss obtained using the CTv1.0 model to the elastic energy loss obtained using the CTv2.0 model. The CTv1.0 and CTv2.0 models differ in three main respects:

- The CTv1.0 model uses a scattering center density that decays exponentially, whereas the CTv2.0 model uses a medium density that decays according to a power law. The medium density and scattering center density are related through eq. 3.9.

- The CTv1.0 model includes energy loss during the pre-thermalization stage (*i.e.* $t < \tau_0$) by employing a smooth extrapolation of the exponential scattering center density. In contrast, the CTv2.0 model excludes any energy loss prior to thermalization, as made explicit by the θ-function in eq. 3.44.

- For any particular path, the CTv1.0 model evaluates the Debye mass and gluon mass at a fixed temperature, whereas the CTv2.0 model incorporates the medium

evolution into the determination of the Debye and gluon masses (see eq. 3.4).

In fig. 3.12, we evaluate the DGLV+SPLC integrated energy loss $\Delta E/E$ for charm quarks as a function of p_T using the CTv1.0 model with the exponential scattering center density and compare it to the integrated energy loss obtained using the CTv2.0 model with the power-law medium density. The parameters used in both implementations are chosen to be the average fitted parameters for $\mathrm{Pb}+\mathrm{Pb}$ 0-5%, $\mathrm{Pb}+\mathrm{Pb}$ 70-80%, and $p+\mathrm{Pb}$ 0-5% collision systems; the average parameters in the CTv2.0 model are determined by the mean of the P_{geo} distributions, while the average parameters in the CTv1.0 model are determined by the mean of the $P_L(L_{\text{eff}})$ distributions and its corresponding mean effective temperature T_{eff} (for details on how $P_L(L_{\text{eff}})$ and T_{eff} are determined, refer to [171]). The average fitted parameters for each collision system are:

- $p+\mathrm{Pb}$ 0-5%: CTv2.0 – $\rho_0 = 12.2$ fm^{-3} ($T_0 = 0.3$ GeV), $t_c = 3.1$ fm; CTv1.0 – $L_{\text{eff}} = 0.9$ fm, $T_{\text{eff}} = 0.4$ GeV [163].
- $\mathrm{Pb}+\mathrm{Pb}$ 0-5%: CTv2.0 – $\rho_0 = 50.6$ fm^{-3} ($T_0 = 0.5$ GeV), $t_c = 8.5$ fm; CTv1.0 – $L_{\text{eff}} = 4.8$ fm, $T_{\text{eff}} = 0.31$ GeV [163].
- $\mathrm{Pb}+\mathrm{Pb}$ 70-80%: CTv2.0 – $\rho_0 = 6.3$ fm^{-3} ($T_0 = 0.23$ GeV), $t_c = 2.7$ fm; CTv1.0 – $L_{\text{eff}} = 1.4$ fm, $T_{\text{eff}} = 0.27$ GeV [163].

For all collision systems and for all p_T considered, a single fixed value of α_s in the CTv2.0 implementation results in more energy loss than the CTv1.0 implementation. Note that we will fix α_s for CTv2.0 by comparing to large system data; in Sec. 3.4 we will find a fixed α_s in the CTv2.0 model that is about 20% smaller than the α_s obtained in the CTv1.0 model [155].

In order to systematically compare the effects that the choice of scattering center densities in the CTv1.0 implementation and the choice of medium densities in the CTv2.0 implementation have on the energy loss, we modify the form of the scatter-

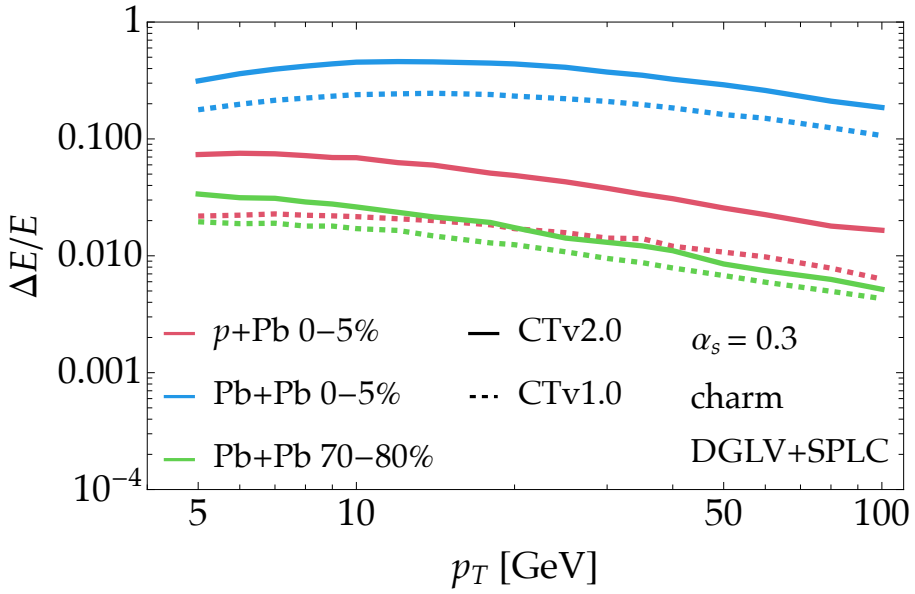

Figure 3.12: Comparison of DGLV+SPLC $\Delta E/E$ as a function of p_T for the CTv1.0 energy loss model (dashed) and the CTv2.0 energy loss model (solid). All curves are evaluated at α_s= 0.3 for charm quarks. The CTv1.0 and CTv2.0 energy loss models are evaluated using their respective average parameters for p + Pb 0-5% (red), Pb + Pb 0-5% (blue), and Pb + Pb 70-80% (green) collision systems.

ing center density in the CTv1.0 implementation as follows:

$$\bar{\rho}_{\text{CTv1.0}}(z) = \begin{cases} \frac{2}{L_{\text{eff}}} \exp\left(-\frac{2z}{L_{\text{eff}}}\right) & \text{exp,} \\ n_e \exp\left(-\frac{z}{a}\right) \theta(z-\tau_0) & \text{exp w/co,} \\ \frac{n_{pl}}{z^{1.2}} \theta(z_{max}-z)\theta(z-\tau_0) & \text{power-law,} \end{cases} \tag{3.52}$$

where the various parameters in the *exponential with cutoff* and *power-law* prescriptions are chosen such that the following conditions are satisfied:

$$1 = \int dz\ \bar{\rho}_{\text{CTv1.0}}(z), \tag{3.53a}$$

$$L_{\text{eff}}/2 = \int dz\ z\bar{\rho}_{\text{CTv1.0}}(z). \tag{3.53b}$$

The *exponential* prescription in eq. 3.52 corresponds to the original CTv1.0 implementation [146, 155, 159, 163, 171] and is commonly used in the literature [71, 168, 183]. The *exponential with cutoff* (exp w/co) prescription is designed to highlight the effects

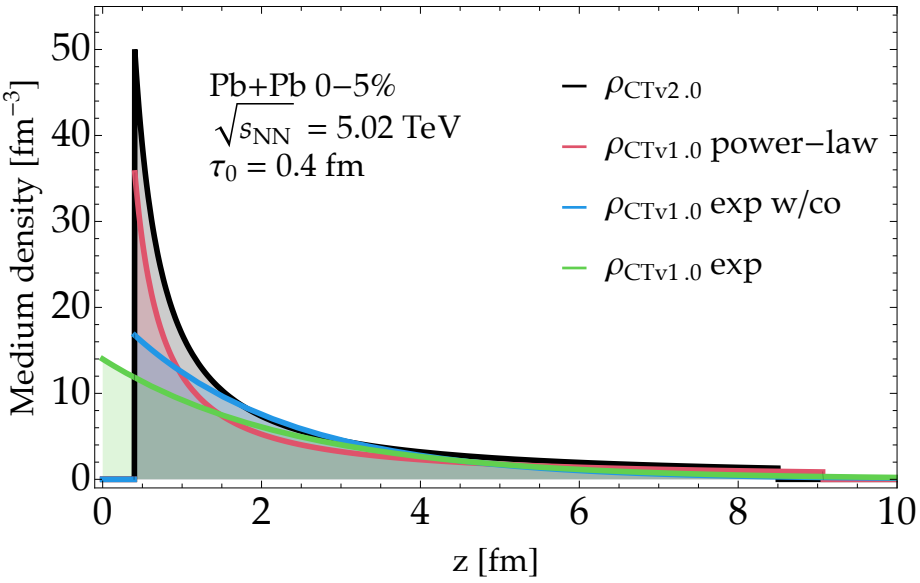

Figure 3.13: Comparison of medium densities in CTv2.0 and CTv1.0 implementations of energy loss model. The CTv1.0 curves come from the scattering center density definitions in eq. 3.52 and are then converted to medium densities through eq. 3.9.

on the energy loss caused by removing contributions from before the formation time of the medium. The *power-law* prescription is proposed to highlight the effects on the energy loss that are caused by the parametric form (*i.e.* power-law versus exponential decay) of the scattering center density. Note that the form of the scattering center density is important, since the LPM effect implies that dE/dz is proportional to the scattering center density [164, 166].

In fig. 3.13, we show the scattering center densities defined in eq. 3.52 converted to medium densities *via* eq. 3.9 alongside the CTv2.0 medium density. We use the same ρ_0, t_c and L_{eff} average parameters as those specified for the $\text{Pb} + \text{Pb}$ 0-5% collision system in fig. 3.12. We choose the parameters in this manner in order to perform a controlled comparison of the two implementations. The $\rho_{\text{CTv1.0}}$ exponential with cutoff medium density has a normalization of $n_e = 0.61$, while the $\rho_{\text{CTv1.0}}$ power-law medium density has a normalization of $n_{pl} = 0.36$ and has a cut off at $z_{max} = 9.07$ fm. The quoted values for n_e, n_{pl} and z_{max} are found by satisfying the conditions in eq. 3.53.

From fig. 3.13, we see that only the $\rho^{\text{exp}}_{\text{CTv1.0}}$ medium density is non-zero at $z = 0$, which is consistent with the definition of the exponential scattering center density in

eq. 3.52. At $z = \tau_0 = 0.4$ fm, one finds the following ordering of the medium densities:

$$\rho_{\text{CTv2.0}} > \rho^{\text{power-law}}_{\text{CTv1.0}} > \rho^{\text{exp w/co}}_{\text{CTv1.0}} > \rho^{\text{exp}}_{\text{CTv1.0}}. \tag{3.54}$$

The ordering in eq. 3.54 is determined by contribution that the parameters ρ_0, n_{pl}, n_e and L_{eff} have on the respective medium densities. For $z > \tau_0$, the medium densities decay exponentially ($\rho^{\text{exp w/co}}_{\text{CTv1.0}}$, $\rho^{\text{exp}}_{\text{CTv1.0}}$) or with a power-law ($\rho^{\text{power-law}}_{\text{CTv1.0}}$, $\rho_{\text{CTv2.0}}$). The $\rho_{\text{CTv2.0}}$ and $\rho^{\text{power-law}}_{\text{CTv1.0}}$ densities are zero for $z > t_c = 8.5$ fm and $z > z_{max} = 9.07$ fm, respectively, while the $\rho^{\text{exp w/co}}_{\text{CTv1.0}}$ and $\rho^{\text{exp}}_{\text{CTv1.0}}$ densities decay to zero as $z \to \infty$.

As an additional intermediate step between the CTv1.0 implementation and the CTv2.0 implementation, we explore the effects of a *static* version of the CTv2.0 implementation. The comparison is done by using the power-law parametric form for the scattering center density, from eq. 3.44, and evaluating the Debye and gluon masses, from eq. 3.4, at a fixed temperature. Note that the static CTv2.0 model and power-law CTv1.0 prescription use the same parametric form for the medium densities, and both models evaluate the Debye and gluon masses at the same fixed average temperature. The only difference between the static CTv2.0 model and the power-law CTv1.0 prescription is that the static CTv2.0 model uses a different parametrization of the trajectories through the medium compared to the power-law CTv1.0 prescription.

In fig. 3.14, we show the energy loss from the SPLC term in eq. 3.2b after performing the x-integration while leaving the z-integration unevaluated. All models except the exponential prescription of the CTv1.0 model have no energy loss for $z < \tau_0$ due to the presence of a cut-off at τ_0 from eq. 3.44 and eq. 3.52. For $z > \tau_0$ the power-law prescription has a larger magnitude of energy loss than the exponential prescription of the CTv1.0 model. The increased magnitude in the energy loss from the power-law prescription is a direct consequence of the power-law scattering center density carrying more of its support at larger times compared to the exponential prescription. The same conclusion can be made when comparing the exponential with cutoff and exponential prescriptions. Comparing the static CTv2.0 model with the power-law CTv1.0 prescription in fig. 3.14, we observe a larger magnitude of energy loss in CTv2.0, indicating that the average parameters used in the CTv2.0 model result in a larger magnitude of energy loss than the average parameters used in the CTv1.0 model. The magnitude

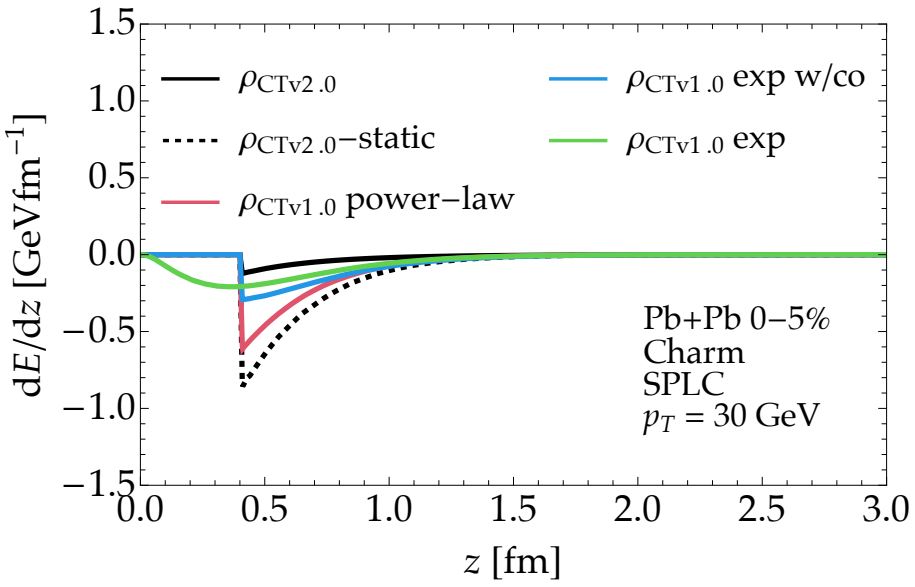

Figure 3.14: SPLC energy loss for charm quarks differential in z calculated using medium densities from fig. 3.13.

of the energy loss in the SPLC is significantly decreased in the CTv2.0 implementation of the energy loss when compared to all the CTv1.0 models and the static CTv2.0 model. The observed decrease in the magnitude of the energy loss is a consequence of the high temperatures at small z when the medium evolution is included in the Debye and gluon masses (see eq. 3.4). These higher temperatures increase both the Debye and gluon masses, as shown in fig. 3.15, thereby reducing the SPLC contribution to the energy loss. Since the SPLC term depends on inverse powers of μ and m_g (with powers ≥ 1), increases in these masses lead directly to a decrease of the corresponding energy loss contribution.

In fig. 3.15, we use the average fitted parameters for a $\mathrm{Pb} + \mathrm{Pb}$ collision system at 0-5% centrality to compare the Debye mass, from eq. 3.4a, as a function of $T(z)$ to the Debye mass evaluated at a fixed temperature of $T = 0.3$ GeV (which is the average temperature of a $\mathrm{Pb} + \mathrm{Pb}$ collision system at 0-5% centrality). We see in fig. 3.15 that the constant Debye mass is larger than the dynamic Debye mass in the regions $z < 0.4$ fm and $z > 2.5$ fm, while the roles are reversed in the region 0.4 fm $\leq z \leq 2.5$ fm. We use fig. 3.15 to highlight the effects of including the evolution of the medium into the Debye and gluon masses on the energy loss; these effects are explored in what follows.

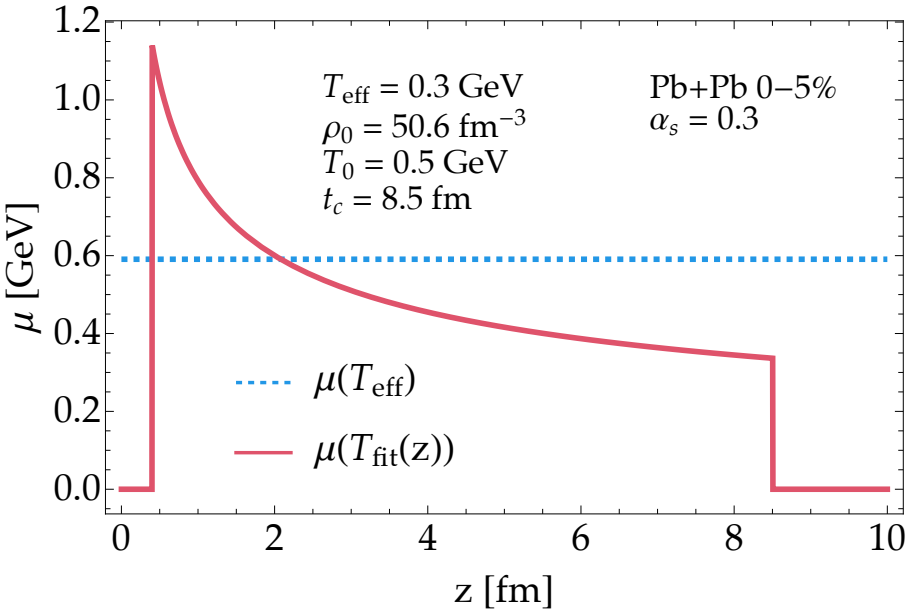

Figure 3.15: Comparison of Debye mass evaluated at fixed effective temperature of $T_{\text{eff}} = 0.3$ GeV and Debye mass evaluated as a function fitted temperature profile (eq. 3.45) for $\rho_0 = 50.6$ fm^{-3}, $T_0 = 0.5$ GeV and $t_c = 8.5$ fm. The values for T_{eff}, ρ_0, T_0 and t_c correspond to the average parameters for a $\text{Pb} + \text{Pb}$ collision system at 0-5% centrality.

In fig. 3.16, we present the same plot as fig. 3.14, but for the DGLV term (eq. 3.2a) instead of the SPLC term (eq. 3.2b). Comparing the exponential and exponential with cutoff curves in the CTv1.0 implementation, one notices an increase in the energy loss of the exponential with cutoff curve for $z \lesssim 5$ fm; the observed increase arises as the exponential with cutoff scattering center density has a smaller region of support ($\tau_0 \leq z < \infty$) compared to the exponential model ($0 \leq z < \infty$); thus the exponential with cutoff has a larger normalization factor (as apparent in fig. 3.13). Comparison of the power-law prescription and exponential with cutoff models of the CTv1.0 implementation shows a decrease in the energy loss of the power-law for 2 fm $\lesssim z \lesssim 5$ fm and an increase for $z \lesssim 2$ fm $\& \; z \gtrsim 5$ fm; these results can be accredited to the size of the scattering center densities in the three different regions (as shown in fig. 3.13). A comparison between the power-law CTv1.0 and static CTv2.0 implementations reveals an increase in the energy loss for the static CTv2.0 case. Consistent with the findings of the SPLC comparison in fig. 3.14, one can conclude that the average parameters used in the CTv2.0 model tend to result in a larger magnitude of energy loss when compared to the average parameters used in the CTv1.0 model. Upon comparing the CTv2.0 model

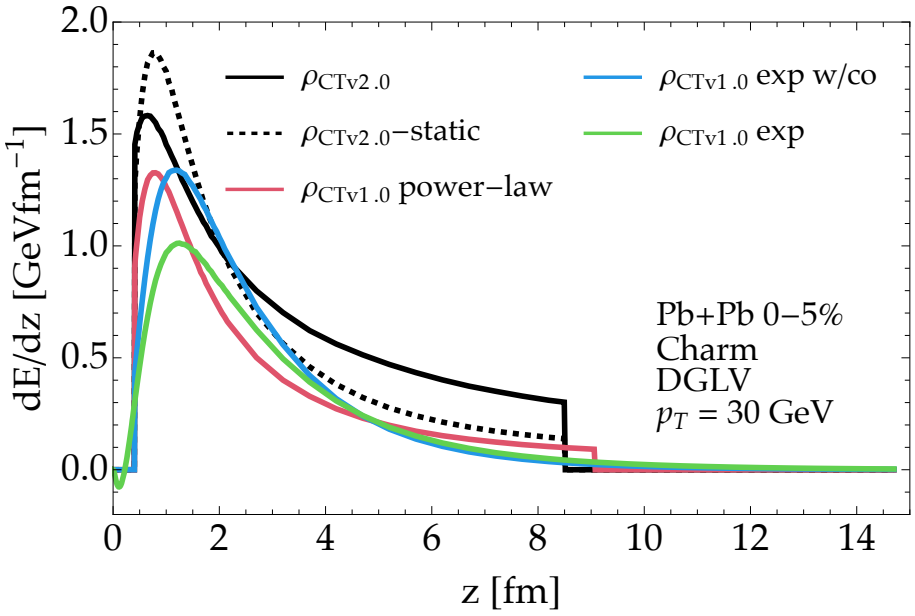

Figure 3.16: DGLV energy loss for charm quarks differential in z calculated using medium densities from fig. 3.13.

with the static implementation of the CTv2.0 model, one will note that there are two regions of interest: $z \lesssim 2.5$ fm and $z \gtrsim 2.5$ fm. The CTv2.0 model exhibits less energy loss than the static CTv2.0 model in the first region; in the second region, the trend is reversed, and the CTv2.0 model shows more energy loss than the static CTv2.0 model.

To understand this behaviour, we consider the effects of the Debye and gluon masses present in the DGLV and SPLC terms from eq. 3.2 (as shown in fig. 3.15). In the region $z \lesssim 2.5$ fm, the μ and m_g terms in the DGLV expression are large, and thus the energy loss is suppressed in the CTv2.0 model when compared to the static CTv2.0 implementation. The large values of the μ and m_g terms arise as the temperature at small z is significantly higher than the average temperature used in the static implementation. In the region $z \gtrsim 2.5$ fm, the temperature drops below the average value, which decreases the μ and m_g terms in the CTv2.0 setting, thereby leading to an increased energy loss relative to the static CTv2.0 implementation.

In fig. 3.17, we plot the results of $\Delta E/E$ for the SPLC contribution. Focusing on the CTv1.0 curves, one observes the following ordering

$$|\Delta E_{\text{exp w/co}}| < |\Delta E_{\text{exp}}| < |\Delta E_{\text{power-law}}|, \tag{3.55}$$

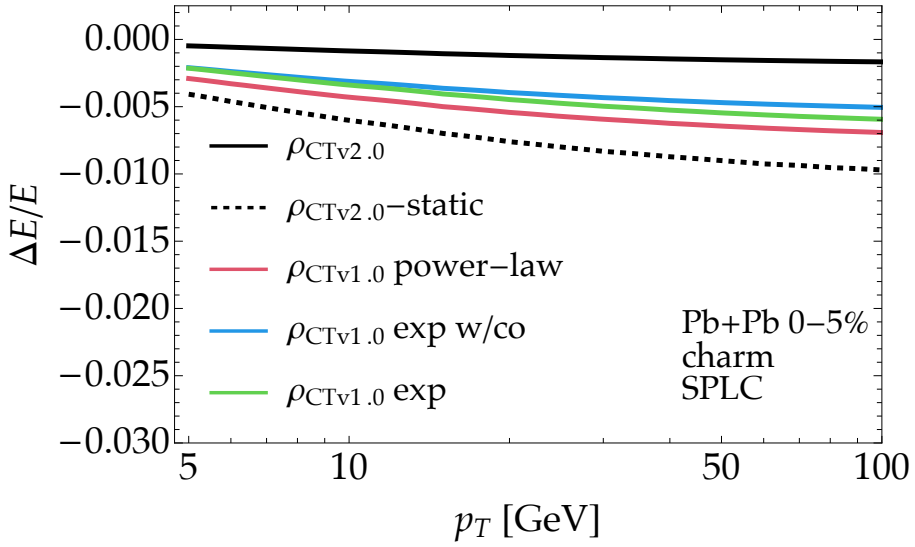

Figure 3.17: SPLC energy loss for charm quarks calculated using medium densities from fig. 3.13.

which is independent of the parton's energy. The inequality on the left, $|\Delta E_{\mathrm{exp\ w/co}}| < |\Delta E_{\mathrm{exp}}|$, is consistent with the findings of [172], where it was shown that the majority of the SPLC contribution comes from small z regions. The $|\Delta E_{\mathrm{exp}}| < |\Delta E_{\mathrm{power\text{-}law}}|$ is observed, even though the power-law prescription lacks a contribution at small z. This ordering can be explained by examining the behaviour of the scattering center densities: the power-law profile decreases more slowly with increasing z compared to the exponential profile (as shown in fig. 3.13 and fig. 3.14). This slower falloff compensates for the absence of a small-z contribution in the power-law case, resulting in a greater overall magnitude of energy loss. Comparing the energy loss between the power-law CTv1.0 and static CTv2.0 implementations, we observe a greater magnitude of energy loss in the static CTv2.0 model, consistent with what was observed in fig. 3.14. The magnitude of energy loss from the SPLC term in the CTv2.0 model is the smallest among all the curves shown. As discussed in the analysis of fig. 3.14, this decrease arises from incorporating medium evolution in the Debye and gluon masses.

Fig. 3.18 shows the $\Delta E/E$ computed from the DGLV term in eq. 3.2a. The exponential and power-law curves for the CTv1.0 model show little discrepancy across all energy scales. This behaviour can be understood by examining fig. 3.16: in the small-z region, the exponential profile yields greater energy loss than the power-law prescrip-

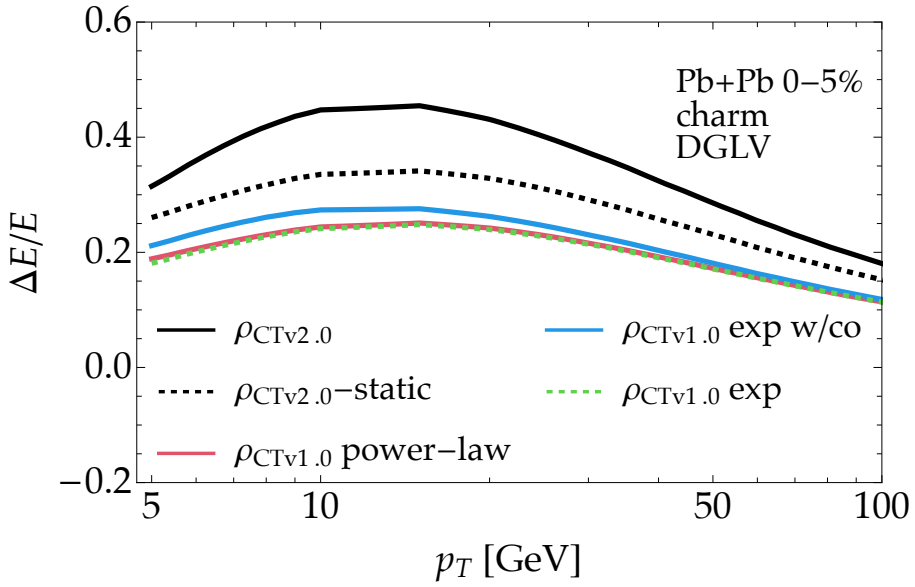

Figure 3.18: DGLV energy loss for charm quarks calculated using medium densities from fig. 3.13.

tion, while in the large-z region, the power-law profile results in greater energy loss than the exponential. These opposing effects balance each other for all p_T, leading to the observed agreement in the integrated energy loss. The exponential with cutoff prescription exhibits an increase of approximately 15% in energy loss over the exponential prescription at low energies, decreasing to less than 10% at higher energies. As seen in fig. 3.16, small-z regions contribute minimally to the overall energy loss contribution from the DGLV term. The exponential with cutoff profile has increased support in the large-z regions compared to the standard exponential case, resulting in a larger total energy loss. Comparing the power-law CTv1.0 and static CTv2.0 curves, we again observe greater energy loss in the latter. As was mentioned in the analysis of fig. 3.16, the CTv2.0 model has average parameters that result in a larger magnitude of energy loss compared to the average parameters used in the CTv1.0 implementation. Furthermore, the CTv2.0 model shows an additional $\sim 30\%$ increase in energy loss over the static CTv2.0 model. This increase arises from the lower temperatures associated with the gluon and Debye masses in the dynamic case at large z (as shown in fig. 3.15 and eq. 3.4).

In fig. 3.19, we show the HTL-only (top) and BT (bottom) elastic energy loss $\Delta E/E$ for charm quarks as a function of p_T calculated using the CTv1.0 model [146, 155, 159,

163, 171] and the CTv2.0 model. The L_{eff} and T_{eff} parameters in the CTv1.0 implementation and the ρ_0 and t_c parameters in the CTv2.0 implementation are chosen to be the average fitted parameters for a $\mathrm{Pb} + \mathrm{Pb}$ collision system at 0-5% centrality. For both HTL-only and BT, the CTv2.0 results in larger elastic energy loss than the CTv1.0 implementation across all p_T values considered. The observed increase in the elastic energy loss from the CTv2.0 model can be attributed to the same factors that were identified in the comparison of the radiative energy loss: the parametrization of trajectories in the CTv2.0 model results in average parameters that lead to a larger magnitude of energy loss compared to the average parameters used in the CTv1.0 implementation, and the inclusion of medium evolution in the Debye and gluon masses results in a increase of the integrated energy loss. Note that our comparison of the elastic energy loss between CTv1.0 and CTv2.0 implementations is not as substantial as the comparison of the radiative energy loss. The comparatively more simple analysis arises because the elastic energy loss in both models does not include the scattering center density as a factor in the integrand. Thus, the differences in the energy loss from the two implementations are driven primarily by the differences in the Debye and gluon masses and the parametrization of trajectories.

In summary of the energy loss analysis, the parametric form of the power-law scattering medium density leads to an increase in the magnitude of the radiative energy loss when compared to the exponential form, which arises due to the late time contributions being more pronounced in the power-law case. Additionally, the inclusion of medium evolution in the Debye and gluon masses results in a decrease of the magnitude of both radiative and elastic energy loss at earlier times (where the temperatures are larger) and an increase at later times (where the temperatures are smaller). Additionally, the parametrization of trajectories in the CTv2.0 model gives average parameters (T_0, t_c) that result in a larger magnitude of both radiative and elastic energy loss compared to the average parameters $(L_{\text{eff}}, T_{\text{eff}})$ used in the CTv1.0 model.

The CTv2.0 model was developed as an improvement over the CTv1.0 model with the goal of providing access to the high-p_T v_n observable; the calculation of the v_n motivated the accurate event-by-event description of the medium evolution used by the CTv2.0 model. While the energy loss from the CTv2.0 model is larger than the

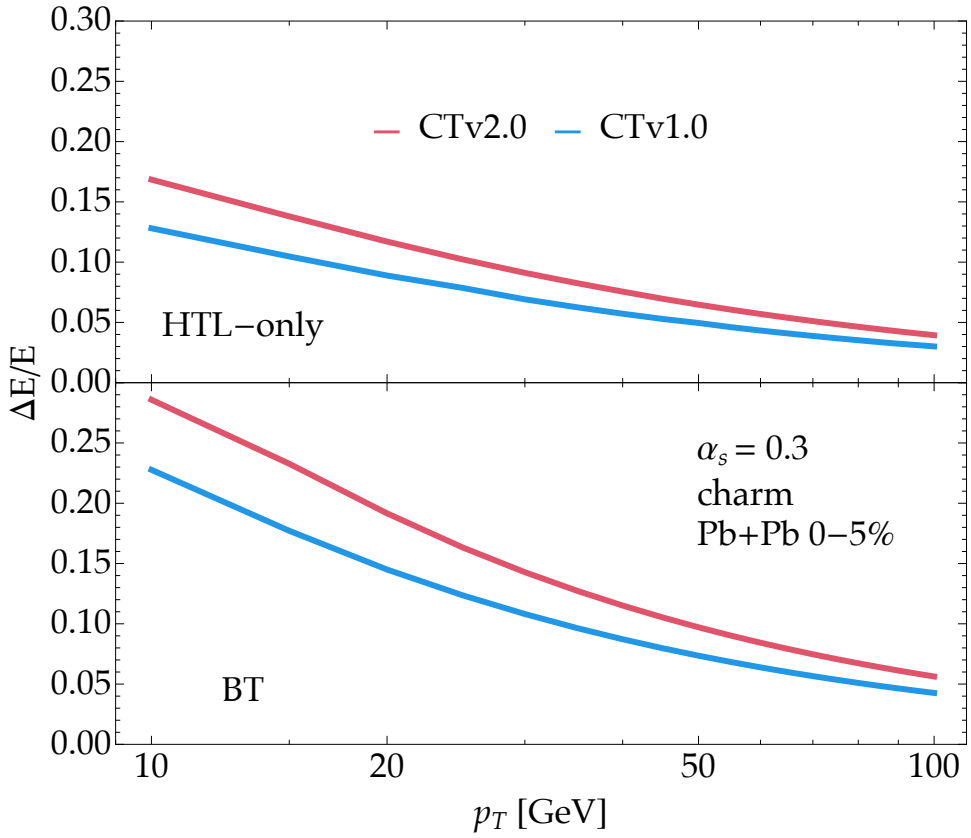

Figure 3.19: Top (Bottom): HTL-only (BT) elastic $\Delta E/E$ as a function of p_T for CTv2.0 (red) and CTv1.0 (blue) implementations of energy loss model. All curves are evaluated at α_s= 0.3 for charm quarks. The curves are evaluated at the average extracted parameters for a $\mathrm{Pb}+\mathrm{Pb}$ 0-5% collision system and take on the values of: $\rho_0 = 50.6$ fm^{-3}, T_0 = 0.5 GeV and $t_c = 8.5$ fm for the CTv2.0 model and $L_{\text{eff}} = 4.8$ fm, $T_{\text{eff}} = 0.3$ GeV for the CTv1.0 model.

energy loss from the CTv1.0 model, the difference in energy loss will not have any phenomenological consequences for the R_{AB} predicted in large systems; both implementations will be tuned to large system data (see Sec. 3.4 for further details), and thus the large system R_{AB} calculated in the two implementations will be in agreement with each other.

3.3 Observables from energy loss formalism

In this section we explain how we calculate $R_{AB}(p_T)$ and the high-p_T $v_n(p_T)$ coefficients from the CTv2.0 energy loss model described in the preceding sections.

3.3.1 Nuclear modification factor

3.3.1.1 Partonic R_{AB}

The nuclear modification factor of the parton q for a collision system of two nuclei A+B is defined as

$$R^q_{AB}(p^f_T) \equiv \frac{dN^q_{AB,f}/dp^f_T}{N_{\text{coll}}\, dN^q_{pp,f}/dp^f_T}, \tag{3.56}$$

where $dN^q_{AB,f}/dp^f_T$ and $dN^q_{pp,f}/dp^f_T$ are the differential spectra of the final state partons in A + B collisions and $p + p$ (proton-proton) collisions, respectively. The factor N_{coll} is the average number of binary collisions for the centrality class under consideration, calculated using the Glauber model [201, 202].

In order to access the partonic R_{AB} on theoretical grounds, we make the following assumptions:

1. We assume, consistent with [168, 196], that the partonic spectrum of the initial state in an A + B collision scales like the partonic spectrum of the initial state in an $p + p$ collision, weighted by N_{coll}; *i.e.*

$$\frac{dN^q_{AB,i}(p^i_T)}{dp^i_T} = N_{\text{coll}} \frac{dN^q_{pp,i}(p^i_T)}{dp^i_T}. \tag{3.57}$$

   The assumption made in eq. 3.57 corresponds to disregarding any nPDF effects on the parent parton's initial state [203, 204].

2. We assume that all modifications to the A + B spectrum arise from the final state energy loss through interactions with the medium, so that we can write

$$\begin{aligned}\frac{dN^q_{AB,f}(p^f_T)}{dp^f_T} = &\int dx dp^i_T\, P(x|p^i_T) \\ &\times \frac{dN^q_{AB,i}(p^i_T)}{dp^i_T} \delta(p^f_T - (1-x)p^i_T).\end{aligned} \tag{3.58}$$

   In eq. 3.58, $P(x|p^i_T)$ is the probability of a parton losing fractional momentum x given that the parton started with initial momentum p^i_T. The Dirac delta in

eq. 3.58 ensures that the condition $p_T^f = (1-x)p_T^i$ is satisfied.

Under the assumptions of eq. 3.57 and eq. 3.58 the partonic R_{AB}^q, from eq. 3.56 becomes

$$R_{AB}^q(p_T^f) = \int \frac{dx}{1-x} P\left(x|p_T^f\right) \frac{f^q\left(\frac{p_T^f}{1-x}\right)}{f^q(p_T^f)}. \tag{3.59}$$

In eq. 3.59 we made the approximation

$$P\left(x|\frac{p_T^f}{1-x}\right) \approx P\left(x|p_T^f\right). \tag{3.60}$$

Note that for the quark production spectra, we have defined the following notational device

$$f^q(p_T^f) \equiv \frac{dN_{pp,i}^q}{dp_T^f}. \tag{3.61}$$

As done in [163], we determine the heavy quark production spectra using FONLL [65] and compute the gluon and light quark production spectra at leading order as done in [66, 205].

For the theoretical results on pion suppression presented here, we used gluon and light quark production spectra $f^q\left(p_T^f\right)$ at $\sqrt{s_{NN}} = 5.5$ TeV instead of $\sqrt{s_{NN}} = 5.02$ TeV, as the former was more readily available. We do not anticipate that this choice will have a significant impact on our conclusions.

3.3.1.2 Hadronic R_{AB}

The hadronic R_{AB}^h is defined analogously to eq. 3.56 as

$$R_{AB}^h(p_T^f) \equiv \frac{dN_{AB,f}^h/dp_T^f}{N_{\text{coll}}\, dN_{pp,f}^h/dp_T^f}. \tag{3.62}$$

In the following we will rewrite eq. 3.62 in terms of the partonic R_{AB}^q and the fragmentation function $D_q^h(z)$. The fragmentation function gives the probability density of producing a hadron h from a parton q as a function of the momentum fraction $z \equiv p_h/p_q$ where p_h and p_q are the momenta of the hadron and parton, respectively [196]. In this

chapter, our D and B meson fragmentation functions are from [206], while our π meson fragmentation functions are from [207].

From the definition of the fragmentation function, the final state spectrum of the hadrons is then

$$\frac{dN^h_{pp/AB,f}(p_h)}{dp_h} = \sum_q \int_0^1 dz\, D^h_q(z) \times \frac{dN^q_{pp/AB,f}}{dp_q}(p_q)\,\delta(p_h - zp_q), \tag{3.63}$$

where the sum $\sum_q$ runs over all the partons producing the specified hadron. Inserting eq. 3.63 in eq. 3.62 allows us to write the hadronic R^h_{AB} in terms of the partonic R^q_{AB} as follows

$$R^h_{AB}(p_T) = \left(\sum_q \int_0^1 \frac{dz}{z} D^h_q(z) f^q\left(\frac{p_T}{z}\right)\right)^{-1} \times \left(\sum_q \int_0^1 \frac{dz}{z} D^h_q(z) f^q\left(\frac{p_T}{z}\right) R^q_{AB}\left(\frac{p_T}{z}\right),\right) \tag{3.64}$$

in eq. 3.64, and in what follows, we have dropped the f superscript so that $p^f_T = p_T$.

3.3.1.3 *Geometry average of the R_{AB}*

In order for our theoretical R^h_{AB} to be comparable to experimental data, we must average the calculated R^h_{AB} over the trajectories that a parton may take through the medium. As discussed in Sec. 3.2.4, each trajectory in our model can be characterized by the set of parameters (ρ_0, t_c), and the geometry of the collision system's ℓ^{th} event in the direction ϕ (azimuhtal to the beam pipe) can be encoded in the distribution $P^\ell_{geo}(\rho_0, t_c|\phi)$ defined in eq. 3.48. Now, eq. 3.64 gives us access to the hadronic R^h_{AB} in terms of $P(x|p_T)$, which is the probability of a parton losing fractional momentum x given that the hadron produced by the parton has momentum p_T; we take P to be the P_{tot} distribution calculated in eq. 3.41. Since P_{tot} is a function of the (ρ_0, t_c) parameters, we have that $R^h_{AB} = R^h_{AB}(\rho_0, t_c)$. We are thus able to obtain the geometry averaged

hadronic $R_{AB}^{h,\ell}$ for a collision system's ℓ^{th} event in the direction ϕ *via*

$$R_{AB}^{h,\ell}(p_T,\phi) = \int d\rho_0 dt_c \; P_{geo}^{\ell}(\rho_0, t_c|\phi) \; R_{AB}^{h}(p_T, \rho_0, t_c) \tag{3.65}$$

where N_e is the number of events. In what follows, we exclusively use the geometry averaged hadronic $R_{AB}^{h,\ell}$; thus, for notational simplicity, we will drop the superscript h and write R_{AB}^{ℓ}.

3.3.2 High-p_T azimuthal anisotropy

3.3.2.1 Fourier expansions of azimuthal anisotropy

Anisotropy in the observed spectra of high-p_T final state hadrons can be characterized on an event-by-event basis by a Fourier expansion of the form [85]

$$\frac{R_{AB}^{\ell}(p_T,\phi)}{R_{AB}^{\ell}(p_T)} = 1 + 2\sum_{n=1}^{\infty} v_n^{\text{hard},\ell} \cos\left(n\left[\phi - \psi_n^{\text{hard},\ell}(p_T)\right]\right), \tag{3.66}$$

where the $v_n^{\text{hard},\ell}$ terms are the unique Fourier coefficients. In our model, the $R_{AB}^{\ell}(p_T,\phi)$ is calculated from eq. 3.65, and $R_{AB}^{\ell}(p_T)$ is the average of $R_{AB}^{\ell}(p_T,\phi)$ over ϕ for a particular event ℓ; *i.e.*

$$R_{AB}^{\ell}(p_T) \equiv \frac{1}{2\pi}\int_0^{2\pi} d\phi R_{AB}^{\ell}(p_T,\phi). \tag{3.67}$$

By making use of orthogonality properties in the Fourier expansion from eq. 3.66, the $v_n^{\text{hard},\ell}$ coefficients can be solved for using the following expression

$$v_n^{\text{hard},\ell} = \int_0^{2\pi} d\phi \; \frac{R_{AB}^{\ell}(\phi)}{2\pi R_{AB}^{\ell}} \cos\left(n\left[\phi - \psi_n^{\text{hard},\ell}\right]\right). \tag{3.68}$$

The $\psi_n^{\text{hard},\ell}$ reference angles from eq. 3.66 can be found through the following expression [85]

$$\psi_n^{\text{hard},\ell}(p_T) = \frac{1}{n}\text{arctan2}\left(\int_0^{2\pi} d\phi\, R_{AB}^{\ell}\,(p_T,\phi)\cos(n\phi),\right. \\ \left.\int_0^{2\pi} d\phi\, R_{AB}^{\ell}\,(p_T,\phi)\sin(n\phi)\right). \tag{3.69}$$

In eq. 3.69, arctan2 is the two-argument arctangent function that keeps track of the signs of the numerator and denominator to determine the correct quadrant of the angle [188]. Note that the $\psi_n^{\text{hard},\ell}$ angles are determined by the orientation of the anisotropy of the R_{AB}^{ℓ} calculated from our energy loss model, and thus the $\psi_n^{\text{hard},\ell}$ angles are aligned with anisotropy coming from the hard sector.

To compare the $v_n^{\text{hard},\ell}$ coefficients from eq. 3.68 to experimental data, one must average over the $v_n^{\text{hard},\ell}$ coefficients determined on an event-by-event basis; *i.e.*

$$v_n^{\text{hard}}(p_T) = \frac{1}{N_e}\sum_{\ell}^{N_e} v_n^{\text{hard},\ell}(p_T). \tag{3.70}$$

To highlight the importance of including the event-by-event fluctuations into the calculation of the azimuthal harmonics, we define the following unphysical quantity

$$v_n^{\text{hard,nf}} \equiv \int_0^{2\pi} d\phi\, \frac{\langle R_{AB}\,(\phi)\rangle}{2\pi\langle R_{AB}\rangle}\cos\left(n\left[\phi - \psi_n^{\text{hard,nf}}\right]\right), \tag{3.71}$$

where the averaging $\langle\ldots\rangle$ in eq. 3.71 is over all events, and the "nf" suffix stands for *no fluctuations*. The $\psi_n^{\text{hard,nf}}$ angles are calculated analogously to eq. 3.69, with R_{AB} instead of $\langle R_{AB}\rangle$. By calculating the $v_n^{\text{hard,nf}}$ coefficients as defined in eq. 3.71, the event-by-event fluctuations present in the initial state are effectively integrated out; this results in a more homogeneous background over which the energy loss occurs, leading to a reduced anisotropy.

3.3.2.2 *Scalar product* v_n

The anisotropy induced by the medium is commonly measured through the scalar-product (SP) method, $v_n\{\text{SP}\}$, or the two-particle cumulant method, $v_n\{2\}$ [208–215].

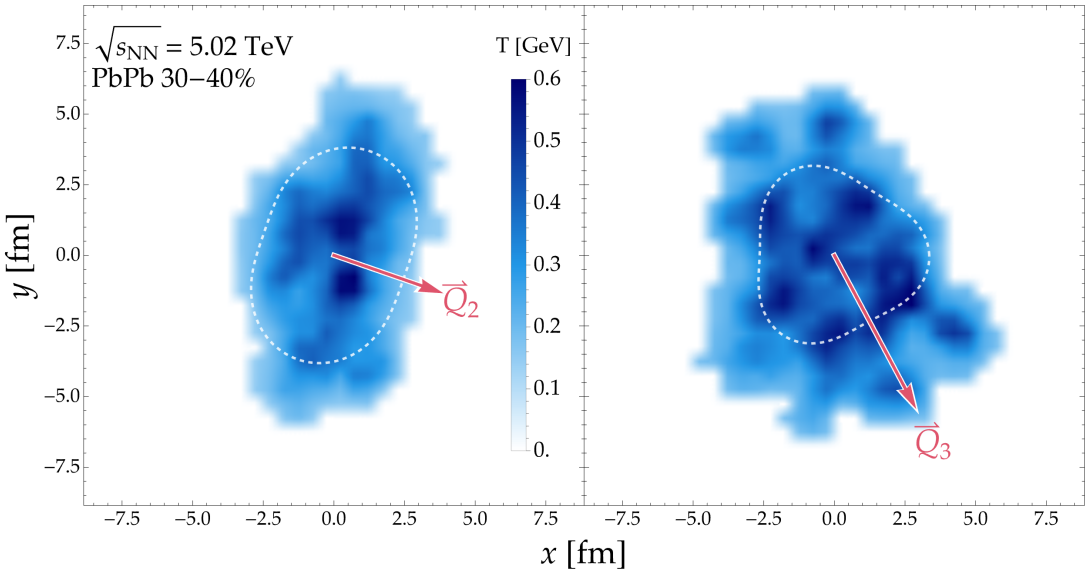

Figure 3.20: Hydrodynamic temperature distributions for representative elliptical (top) and triangular (bottom) events from the hydrodynamic framework for PbPb 30-40% events at proper time $\tau = 0.4$ fm/c. Top (Bottom): $\vec{Q}_2$ ($\vec{Q}_3$) vector defined through eq. 3.73 is plotted over the temperature distribution for a particular event with strong spatial ellipticity (triangularity). The dashed lines are plotted to guide the reader's eye.

The two measurements of anisotropy become identical, in principle, once non-flow contributions are subtracted from the two-particle cumulant [216, 217]. In this work we will report the v_n^{hard} anisotropy from eq. 3.70 and the scalar-product anisotropy $v_n\{\text{SP}\}$, which is defined as [208]

$$v_n\{\text{SP}\}(p_T) \equiv \frac{(N_h N_e)^{-1} \sum_{\ell=1}^{N_e} \sum_{j=1}^{N_h} \vec{Q}_n^{\ell} \cdot \vec{u}_n^{\ell j}(p_T)}{\sqrt{(N_e)^{-1} \sum_{\ell=1}^{N_e} \vec{Q}_n^{\ell} \cdot \vec{Q}_n^{\ell}}}. \tag{3.72}$$

The $\vec{Q}_n^{\ell} = (\vec{Q}_n^{x,\ell}, \vec{Q}_n^{y,\ell})$ flow vectors provide an approximation to the soft participant plane and are defined in terms of the final state particles *via* [218]

$$\mathcal{Q}_n^{\ell} \equiv \sum_k e^{in\phi^{\ell k}}, \tag{3.73}$$

where the real and imaginary parts of $\mathcal{Q}_n^{\ell}$ are the x and y components of the $\vec{Q}_n^{\ell}$ vector, respectively. In fig. 3.20, we show the $\vec{Q}_2^{\ell}$ and $\vec{Q}_3^{\ell}$ vectors obtained from the IP-Glasma+MUSIC+UrQMD framework for highly elliptical and highly triangular events, respectively. As evident from fig. 3.20, the $\vec{Q}_n^{\ell}$ vectors are aligned with the anisotropy of the hydrodynamic background and thus provide a good approximation to the soft

participant plane.

To access the $\vec{Q}_n^{\,\ell}$ vectors in our energy loss model, we make use of IP-Glasma [186–188], which is then evolved with the MUSIC viscous relativistic $(2+1)$ D hydrodynamics code [189–191], followed by UrQMD microscopic hadronic transport [192, 193]. The k index in eq. 3.73 is summed over final state particles and the azimuthal angle is [188]

$$\phi^{\ell k} = \arctan 2\left(p_x^{\ell k}, p_y^{\ell k}\right) \tag{3.74}$$

where $p_x^{\ell k}$ and $p_y^{\ell k}$ are the x and y components of the particle momentum. The vector $\vec{u}_n^{\,\ell j}$ is defined as

$$\vec{u}_n^{\,\ell j} \equiv \left(\cos n\phi^{\ell j}, \sin n\phi^{\ell j}\right), \tag{3.75}$$

where $\phi^{\ell j}$ is the azimuthal direction of the j^{th} hadronic candidate in the ℓ^{th} event.

In order to calculate $v_n\{\mathrm{SP}\}$ from our energy loss model we rewrite the numerator in eq. 3.72 as follows:

$$\left\langle\left\langle \vec{u}_n \cdot \vec{Q}_n \right\rangle\right\rangle = \frac{1}{N_e}\frac{1}{N_h}\sum_{\ell=1}^{N_e}\sum_{j=1}^{N_h} \vec{Q}_n^{\,\ell} \cdot \vec{u}_n^{\,\ell j}(p_T) \tag{3.76a}$$

$$= \frac{1}{N_e}\sum_{\ell=1}^{N_e} \frac{\int d\phi\, \rho^{\ell}(p_T,\phi)\vec{Q}_n^{\,\ell} \cdot \vec{u}_n^{\,\ell}(p_T,\phi)}{\int d\phi\, \rho^{\ell}(p_T,\phi)}. \tag{3.76b}$$

In eq. 3.76b, we use a density of states $\rho^{\ell}(p_T,\phi)$, which allows us to pass from the discrete sum over the observed hadrons to an integral. We choose the density of states to take the form

$$\rho^{\ell}(p_T,\phi) \propto \frac{d^2N_{AB}^{\ell}(p_T,\phi)}{dp_T d\phi}. \tag{3.77}$$

The form of $\rho^{\ell}(p_T,\phi)$ chosen in eq. 3.77 is made as the number of observed hadrons, by definition, will scale like $d^2N_{AB}^{\ell}/dp_T d\phi$. Inserting eq. 3.76 and eq. 3.77 into eq. 3.72, one obtains

$$\begin{aligned} v_n\{\mathrm{SP}\}(p_T) = \frac{1}{N_e}\sum_{\ell=1}^{N_e}\left(\int_0^{2\pi} d\phi\, R_{AB}^{\ell}(p_T,\phi)\vec{Q}_n^{\,\ell} \cdot \vec{u}_n^{\,\ell}(\phi)\right) \\ \times \left(2\pi R_{AB}^{\ell}(p_T)\sqrt{\left\langle \vec{Q}_n \cdot \vec{Q}_n \right\rangle}\right)^{-1}, \end{aligned} \tag{3.78}$$

where $\langle\cdots\rangle$ denotes averaging over events and we have made use of $d^2N^{\ell}_{AB}/dp_Td\phi \propto R^{\ell}_{AB}(p_T,\phi)$. If one then makes use of the orthogonality properties of the Fourier expansion, one can rewrite eq. 3.78 as [217, 219, 220]

$$v_n\{\mathrm{SP}\} = \frac{\left\langle \sqrt{\vec{Q}_n\cdot\vec{Q}_n}\,\cos\left[n\left(\psi_n^{\mathrm{hard}}-\psi_n^{\mathrm{soft}}\right)\right]v_n^{\mathrm{hard}}\right\rangle}{\sqrt{\left\langle\vec{Q}_n\cdot\vec{Q}_n\right\rangle}}, \tag{3.79}$$

where $\langle\cdots\rangle$ again denotes averaging over events. In eq. 3.79, we have defined the soft-sector participant plane angles for the ℓ^{th} event as

$$\psi_n^{\mathrm{soft},\ell} \equiv \frac{1}{n}\mathrm{arctan2}\left(Q_n^{x,\ell},Q_n^{y,\ell}\right). \tag{3.80}$$

Thus, the $\psi_n^{\mathrm{soft},\ell}$ angles align with the soft participant plane, analogously to how the $\psi_n^{\mathrm{hard},\ell}$ angles align with the hard participant plane.

In fig. 3.21 and fig. 3.22, we compare the v_n^{hard} coefficients (eq. 3.70) with the $v_n\{\mathrm{SP}\}$ terms (eq. 3.78) and with the $v_n^{\mathrm{hard,nf}}$ terms (eq. 3.71) for D^0 mesons. Fig. 3.21 (fig. 3.22) compares the predictions made by the different methods of calculating the v_2 (v_3) coefficients; the curves are calculated for $\mathrm{Pb}+\mathrm{Pb}$ 0-5% (top)and $\mathrm{Pb}+\mathrm{Pb}$ 30-40% (bottom) collision systems. We see that the $v_n^{\mathrm{hard,nf}}$ magnitudes are decreased significantly when compared to the v_n^{hard} coefficients, showing event-by-event fluctuations play a crucial role in determining the azimuthal anisotropy, in agreement with the findings of [85]. The importance of this effect is especially pronounced for the v_3 coefficients, which drop effectively zero for all p_T.

3.4 Statistical analysis

In the formulation of the model we have presented here, the strong coupling constant α_s serves as an effective free parameter that requires calibration against experimental data. In this section, we outline the statistical framework employed to constrain α_s using available experimental measurements of high-p_T R_{AA} and v_n. We shall refer to

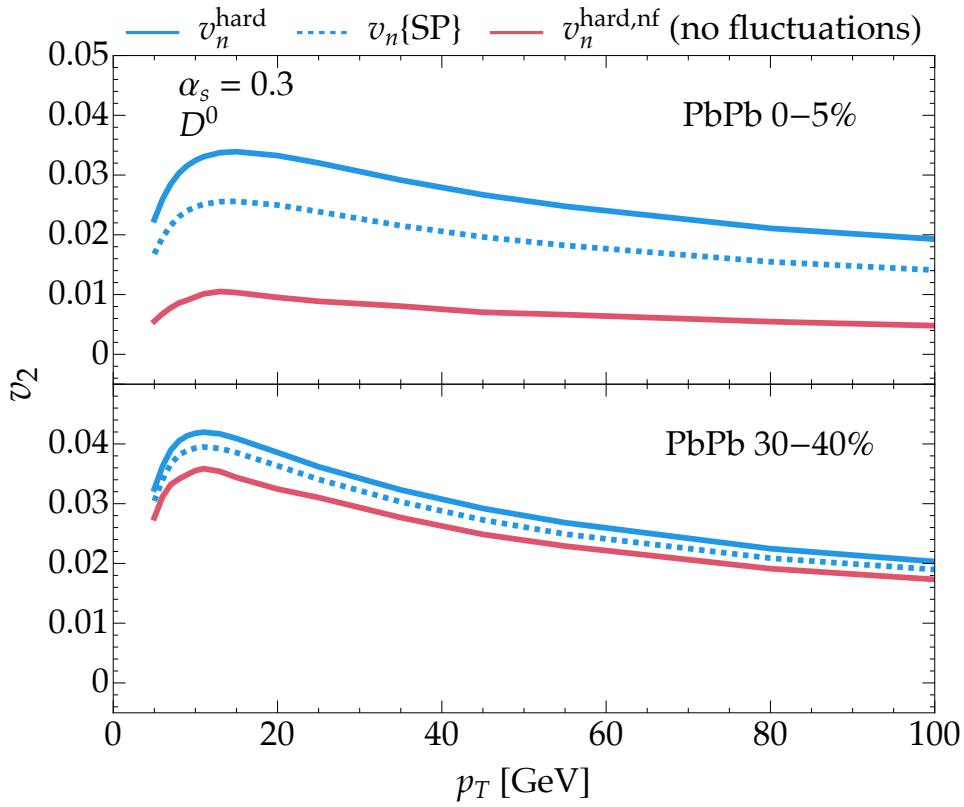

Figure 3.21: Comparison of Fourier v_2 from eq. 3.68, Scalar Product v_2 from eq. 3.78, and the Fourier v_2 without fluctuations from eq. 3.71 as a function of p_T for D^0 mesons. All curves are calculated using the CTv2.0 implementation of the energy loss model with the strong coupling fixed at $\alpha_s = 0.3$. The top (bottom) panel shows the results where the geometric average is calculated over a PbPb 0-5% (30-40%) centrality collision system.

the effective strong coupling constant determined through this calibration process as α_s^{eff}.

In Sec. 3.4.1, we describe the χ^2 minimization procedure used to extract the best-fit value of α_s^{eff}. In Sec. 3.4.2, we discuss the theoretical uncertainties in our predictions that arise from our energy loss model. In Sec. 3.4.3 we discuss which experimental data sets we use to constrain our model. In Sec. 3.4.4, we discuss the range of experimental data that our model is capable of describing. In Sec. 3.4.5, we examine how the extracted value of α_s^{eff} translates into an extracted jet transport coefficient $\hat{q}$.

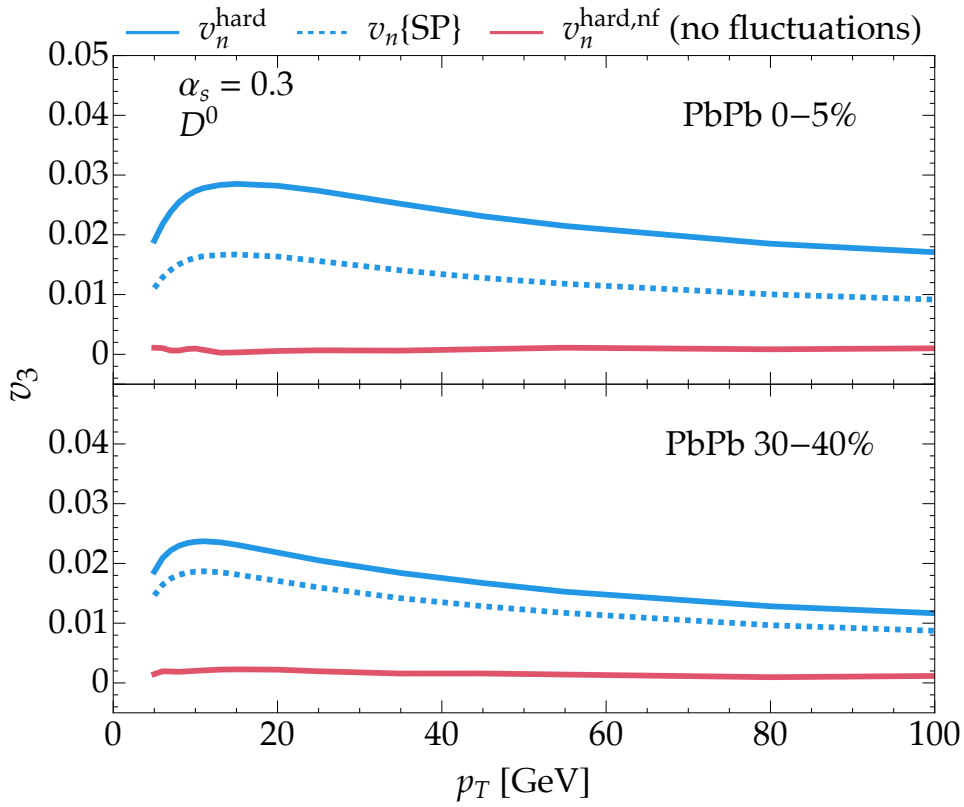

Figure 3.22: Same as fig. 3.21 but for v_3 instead of v_2.

3.4.1 Minimization procedure

The procedure used here closely follows what was done in [155]; as such, we will present an abbreviated version of the details presented therein.

We determine the effective strong coupling α_s^{eff} by minimizing the $\chi^2(\alpha_s^{\text{eff}})$ function, which is defined through [221]

$$\chi^2\left(\alpha_s^{\text{eff.}}\right) \equiv \sum_{i,j}^{N} \left[y_i - \mu_i\left(\alpha_s^{\text{eff.}}\right)\right] \left(C^{-1}\right)_{ij} \left[y_j - \mu_j\left(\alpha_s^{\text{eff.}}\right)\right], \tag{3.81}$$

where $\vec{y} = (y_1, \ldots, y_N)$ is a vector of N experimental data points, $\vec{\mu}(\alpha_s^{\text{eff}})$ is the corresponding vector of theoretical predictions parametrized by α_s^{eff}, and C is the $N \times N$ covariance matrix encoding the experimental uncertainties and their correlations. Minimization of $\chi^2(\alpha_s^{\text{eff}})$ with respect to α_s^{eff} yields the best-fit value of the effective strong coupling.

Contributions to the covariance matrix arise from measurement uncertainties and their correlations. Experimental measurements typically report three classes of uncertainties [141, 222, 223]: *Type A* uncertainties, which include statistical and systematic components that are uncorrelated in p_T; *Type B* uncertainties, which correspond to systematic effects that are correlated in p_T but whose detailed correlation structure is unknown; and *Type C* uncertainties, which are fully correlated in p_T and are dominated by overall normalization effects.

We denote the total standard deviations associated with Type A, Type B, and Type C uncertainties for the data point $y_{k,i}$ by $\sigma^{\mathrm{A}}_{k,i}, \sigma^{\mathrm{B}}_{k,i}$, and $\sigma^{\mathrm{C}}_{k,i}$, respectively. The covariance matrix C_k for a given dataset (k indexes a single centrality class within a single experiment) can be written as the sum of the three contributions,

$$C_{k,ij} = C^{\mathrm{A}}_{k,ij} + C^{\mathrm{B}}_{k,ij} + C^{\mathrm{C}}_{k,ij}. \tag{3.82}$$

The Type A contribution accounts for uncertainties that are uncorrelated and is given by

$$C^{\mathrm{A}}_{k,ij} = \sigma^{\mathrm{A}}_{k,i}\,\sigma^{\mathrm{A}}_{k,j}\,\delta_{ij}, \tag{3.83}$$

with no implicit sum over i and j.

The Type B contribution represents systematic uncertainties that are correlated. In the absence of detailed information on the exact structure of the correlation, we follow JETSCAPE [224, 225], and assume a length-correlated form for the Type B uncertainties, allowing us to write

$$C^{\mathrm{B}}_{k,ij} = \exp\left[-\left|\frac{p_{k,i} - p_{k,j}}{\ell_k\,(p^{\max}_k - p^{\min}_k)}\right|^{\alpha}\right]\,\sigma^{\mathrm{B}}_{k,i}\,\sigma^{\mathrm{B}}_{k,j}, \tag{3.84}$$

where $p_{k,i}$ is the transverse momentum of the i^{th} data point in dataset k, and $p^{\min}_k$ ($p^{\max}_k$) denotes the minimum (maximum) momentum included in the analysis for that dataset. The parameter ℓ_k is the correlation length and the parameter α is the correlation exponent. As done in the JETSCAPE framework [224, 225], we take $\alpha = 1.9$, and we set the correlation length to $\ell_k = 0.2$.

Table 3.1: Experimental datasets used in the global extraction of α_s^{eff} for the large-system-constrained model presented in this chapter.

Experiment	Collision system	Centrality (%)	Hadron species	Observable	p_T range (GeV)
ALICE [226]	PbPb	0-10	D^0	R_{AA}	20-50
ALICE [227]	PbPb	0-50	$h^{\pm}$	R_{AA}	20-50
ATLAS [141]	PbPb	0-50	$h^{\pm}$	R_{AA}	20-50
CMS [77]	PbPb	0-50	$h^{\pm}$	R_{AA}	20-50
CMS [228]	PbPb	0-10	D^0	R_{AA}	20-50
ALICE [229]	PbPb	0-50	$h^{\pm}$	v_2	20-50
ATLAS [211]	PbPb	0-50	$h^{\pm}$	v_2	20-50
CMS [210]	PbPb	0-50	$h^{\pm}$	v_2	20-50
CMS [213]	PbPb	0-50	D^0	v_2	20-50
PHENIX [230]	AuAu	0-50	π^0	R_{AA}	10-50
PHENIX [222]	AuAu	0-50	π^0	R_{AA}	10-50

Finally, the Type C contribution is given by

$$C^{\text{C}}_{k,ij} = \sigma^{\text{C}}_{k,i}\,\sigma^{\text{C}}_{k,j}. \tag{3.85}$$

In this work, we shall make the simplifying assumption that all contributions from different centrality classes and experiments are completely uncorrelated, which leads to the following expression

$$C_{ij} = \sum_{k=1}^{N_{\text{exp}}} C_{k,ij}, \tag{3.86}$$

where N_{exp} is the total number of experimental data sets used in the analysis. See [155] for a detailed discussion of the implications of the covariance modelling choices.

In this chapter, we extract a best-fit value of the effective strong coupling α_s^{eff} along with its associated one-standard-deviation uncertainty. The latter is defined by the values of α_s^{eff} for which the χ^2 function increases by one unit relative to χ^2_{min}, the minimum of the χ^2 function [221].

3.4.2 Theoretical uncertainties

The modelling of energy loss in high-p_T partons *via* pQCD involves numerous simplifying assumptions that each introduce theoretical uncertainty into the predictions of said model. In this work, we will follow [155] and include theoretical uncertainties within our model from two sources:

1. The upper limit on the transverse radiated gluon momentum $|\mathbf{k}|$, chosen to enforce the collinear and large formation time approximations that lead to eq. 3.5. To assess the sensitivity of our model to the upper bound of $|\mathbf{k}|$, we vary $|\mathbf{k}|_{\max}$ by factors of 0.5 and 2 and call this factor the "$\mathbf{k}_{\max}$ multiplier," as discussed in [155, 171].

2. There is uncertainty in the transition between HTL and vacuum propagators for elastic energy loss (as discussed in Sec. 3.2.2). We quantify for this uncertainty by comparing two cases: HTL-only and BT.

While many additional sources of theoretical uncertainty could be considered, we focus on these two because they are straightforward to estimate and permit a quantitative assessment of their impact. Although these two sources of uncertainty do not exhaust the full theoretical uncertainty, they provide a useful measure of the sensitivity of our predictions to modelling assumptions. Furthermore, [155] showed that these uncertainties are substantial, suggesting that they constitute a significant fraction of the total theoretical uncertainty.

We follow [155] and implement the theoretical uncertainty of our model's prediction by treating each choice of the $\mathbf{k}_{\max}$ multiplier and each choice of the elastic energy loss calculation (HTL-only vs BT) as an independent model—which results in six independent models—and apply the statistical analysis described in Sec. 3.4.1 to each of these models.

Table 3.2: Various experimental datasets used in the global extraction of α_s^{eff}.

Experiment	Collision system	Centrality (%)	Hadron species	Observable
ALICE [226]	PbPb	0-10	D^0	R_{AA}
ALICE [227]	PbPb	0-50	$h^{\pm}$	R_{AA}
ALICE [231]	PbPb	0-40	$\pi^{\pm}$	R_{AA}
ATLAS [141]	PbPb	0-50	$h^{\pm}$	R_{AA}
CMS [77]	PbPb	0-50	$h^{\pm}$	R_{AA}
CMS [228]	PbPb	0-10	D^0	R_{AA}
ALICE [232]	PbPb	30-50	D	v_2
ALICE [229]	PbPb	0-50	$h^{\pm}$	v_2
ATLAS [211]	PbPb	0-50	$h^{\pm}$	v_2
CMS [209]	PbPb	0-50	D^0	v_2
CMS [210]	PbPb	0-50	$h^{\pm}$	v_2
CMS [213]	PbPb	0-50	D^0	v_2
CMS [214]	PbPb	0-10	D^0	v_2
ALICE [229]	PbPb	0-50	$h^{\pm}$	v_3
ATLAS [211]	PbPb	0-50	$h^{\pm}$	v_3
CMS [209]	PbPb	0-50	D^0	v_3
CMS [210]	PbPb	0-50	$h^{\pm}$	v_3
CMS [213]	PbPb	0-50	D^0	v_3
PHENIX [230]	AuAu	0-50	π^0	R_{AA}
PHENIX [222]	AuAu	0-50	π^0	R_{AA}

3.4.3 Experimental data

In this work, we explore several datasets for extracting the effective strong coupling α_s^{eff}. Our primary extraction of α_s^{eff} is based on large system measurements of R_{AA} and v_2 for inclusive charged hadrons, $h^{\pm}$, π^0, and D mesons produced in 0-50% centrality $\mathrm{Au}+\mathrm{Au}$ collisions at $\sqrt{s_{NN}} = 0.2$ TeV and 0-50% $\mathrm{Pb}+\mathrm{Pb}$ collisions at $\sqrt{s_{NN}} = 5.02$ TeV. Our model is fit to final-state hadron data with p_T in the range $10 \text{ GeV} \leq p_T \leq 50 \text{ GeV}$ for $\sqrt{s_{NN}} = 0.2$ TeV and $20 \text{ GeV} \leq p_T \leq 50 \text{ GeV}$ for $\sqrt{s_{NN}} = 5.02$ TeV. We use the lower p_T cut of 10 GeV for RHIC data and 20 GeV for LHC data to ensure that we are in the region of phase space where our perturbative energy loss model is expected to be valid; we have further restricted our analysis to include data from 0-50% central heavy-ion collisions, where QGP formation is well established and where the interpretation of suppression is not subject to significant selection biases or additional model dependencies [233–237]. We use a larger p_T cut for the LHC data than for the RHIC data as we will see that the extracted α_s^{eff} values we obtain from the LHC data stabilize

at $p_T \simeq 20$ GeV[1].

All experimental data published prior to January 2026 that satisfy our selection criteria are included in the global fit; a complete list of the datasets is provided in Table 3.1. With this selection, the global analysis incorporates a total of 46 data points from RHIC and 149 data points from the LHC. As done in [155], we will refer to this procedure as the *global extraction* of α_s^{eff}, and to predictions obtained using the extracted α_s^{eff} value as *large-system-constrained model results*. Note that our large-system-constrained model also excludes any v_3 data (discussed further in Sec. 3.4.4 and fig. 3.24 therein). Note that we use $v_n\{\text{SP}\}$ predictions from our model (eq. 3.78), and not v_n^{hard}, to compare to v_2 data.

In addition to the primary global extraction of α_s^{eff} described above, we perform independent extractions of α_s^{eff} using different subsets of observables, including fits based solely on R_{AA} data or solely on v_n coefficients. We also consider combined fits using various combinations of observables, for example $R_{AA}+v_2$, $R_{AA}+v_3$, and v_2+v_3; by comparing the results of these different extraction strategies, we can assess the robustness of our model's predictions and identify potential tensions between different observables. A complete list of all experimental datasets used in these additional extractions is provided in Table 3.2 [2].

3.4.4 Model coverage

In this section we discuss the span of predictions that our theoretical model can produce relative to the experimental data used for the coupling extraction in Table 3.1. We evaluate our model at set values of α_s^{eff} ranging from 0.1 to 0.45 in steps of 0.05; in addition to varying α_s^{eff}, we evaluate our model using HTL-only and BT elastic energy loss and for $\mathbf{k}_{\max}$ multipliers of 0.5, 1, and 2 (as discussed in Sec. 3.4.2).

[1] In [90], we used extractions from $10\text{ GeV} \leq p_T \leq 50$ GeV for LHC data. This results in a negligible change to the predictions of our model. We increased the p_T cut for LHC data to 20 GeV in this chapter as the stabilizing of the extracted α_s^{eff} was unknown to us at the time of the analysis performed in [90].

[2] At the time of writing of this chapter, the authors are not aware of any published experimental datasets that include B meson results that are within the $0-50\%$ centrality cut.

In fig. 3.23 (fig. 3.24), we show model calculations for R_{AA} (v_n) as a function of p_T compared to a representative set of experimental data used in the extraction of α_s^{eff}. All R_{AA} (v_n) theory curves decrease (increase) monotonically as a function of α_s^{eff}. In fig. 3.23 (fig. 3.24), all theory curves are evaluated using the HTL-only and BT elastic energy loss implementations, and all curves are shown for the $\mathbf{k}_{\text{max}}$ multiplier equal to unity for visual purposes. As evident from fig. 3.23, our model is capable of covering all the experimental R_{AA} data in the allowed p_T ranges for extraction (10 GeV $\leq p_T \leq$ 50 GeV for $\sqrt{s_{NN}} = 0.2$ TeV and 20 GeV $\leq p_T \leq$ 50 GeV for $\sqrt{s_{NN}} = 5.02$ TeV). The results of the top and bottom panels of fig. 3.24 show that our model is capable of sufficiently covering all v_2 experimental data in the allowed p_T range used for extraction; however, as is evident in the middle panel of fig. 3.24, the model's predictions are not able to reproduce the negative experimental v_3 data in the allowed p_T range.

3.4.5 Global extraction of α_s and $\hat{q}$

The formulation of the energy loss implemented in our model is most conveniently written in terms of the strong coupling α_s. Much of the literature [63, 224, 238–241] instead frames results in terms of the jet transport coefficient $\hat{q}$, which is defined as the average squared transverse momentum transfer per unit path length [242]. In this section we present a calculation that will express our results in terms of the jet transport coefficient rather than the strong coupling. However, it should be noted that the mapping from α_s to $\hat{q}$ is strongly model dependent [63]. The results that follow should be interpreted with this caveat in mind.

The jet transport coefficient may be written in terms of the elastic scattering rate Γ_{el} as [242]

$$\hat{q} \equiv \int_0^{q_{max}} d^2\mathbf{q} \frac{d\Gamma_{\text{el}}}{d^2\mathbf{q}} \mathbf{q}^2, \tag{3.87}$$

where $\mathbf{q}$ is the transverse momentum exchanged with the medium, and q_{max} is an ultraviolet cutoff on the momentum transfer. In this work, we follow [155] and choose

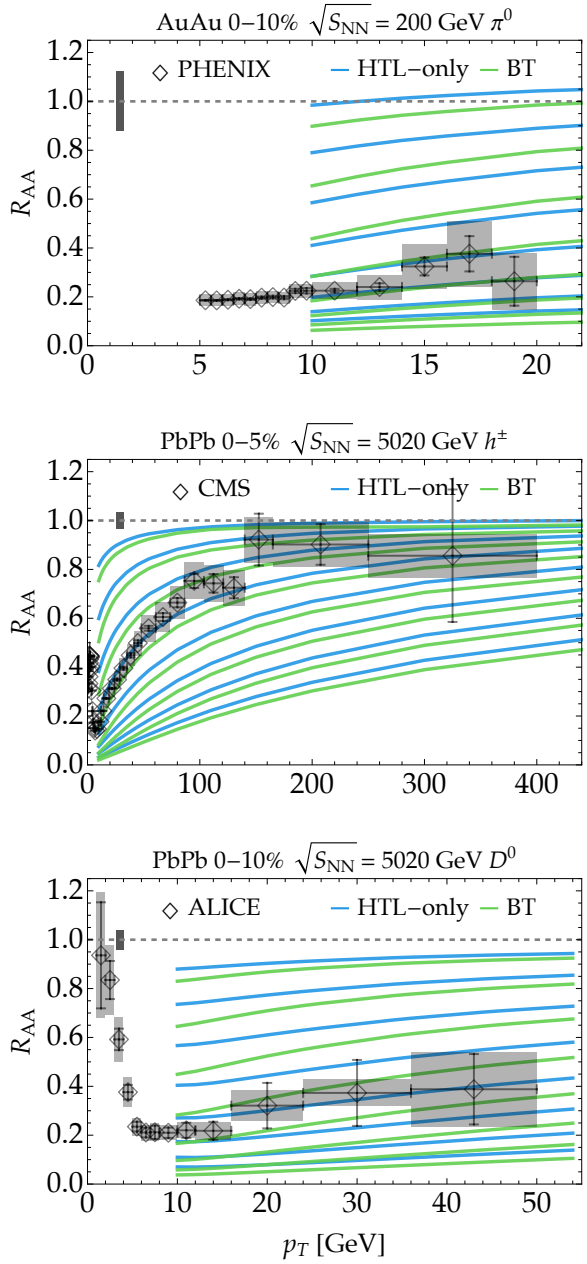

Figure 3.23: Model coverage of representative experimental R_{AA} data. Experimental R_{AA} data from PHENIX [222], CMS [77], and ALICE [226]. Theory curves are evaluated at values of α_s^{eff} ranging from 0.1 to 0.45 in steps of 0.05; all curves are evaluated at $\mathbf{k}_{\max}$ multiplier = 1. Bands around unity are experimental normalization uncertainties

$q_{max} = \sqrt{3\mu E}$, which is consistent with the cutoff chosen in eq. 3.6 and with [71, 195].

The number of scatterings in the BT elastic energy loss is divergent in the infrared and thus the scattering rate cannot be computed [155]. In order to compute $\hat{q}$ in the BT implementation, we follow [242] and use

$$\frac{d\Gamma_{\text{el}}^{BT}}{d^2\mathbf{q}} \simeq 4\alpha_s^2 C_R \frac{1}{\mathbf{q}^2\left(\mathbf{q}^2+\mu^2\right)} \times \frac{\zeta(3)}{\zeta(2)}\left(1+\frac{1}{4}n_f\right)T^3, \tag{3.88}$$

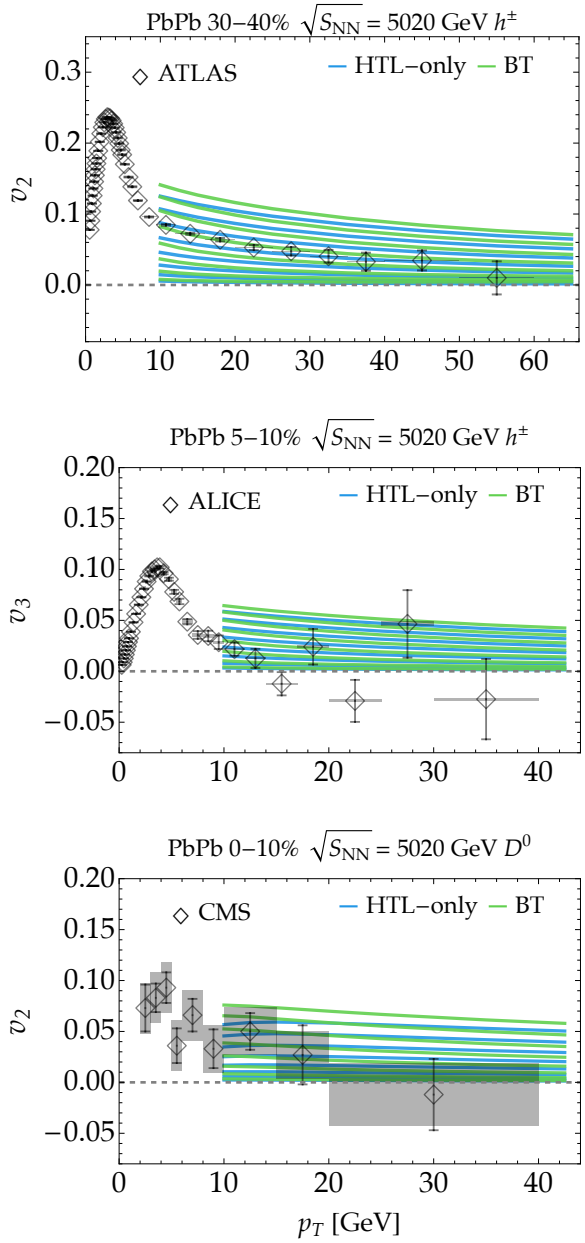

Figure 3.24: Model coverage of representative experimental v_n data. Experimental v_n data from ATLAS [211], ALICE [229], and CMS [209]. Theory curves are evaluated at values of α_s^{eff} ranging from 0.1 to 0.45 in steps of 0.05; all curves are evaluated at $\mathbf{k}_{\max}$ multiplier = 1.

which yields a transport coefficient of

$$\hat{q}^{BT} = 4\pi\alpha_s^2 C_R \ln\left(\frac{q_{max}^2}{\mu^2}+1\right) \times \frac{\zeta(3)}{\zeta(2)}\left(1+\frac{1}{4}n_f\right)T^3. \tag{3.89}$$

To compute the jet transport coefficient in the HTL-only implementation of the elas-

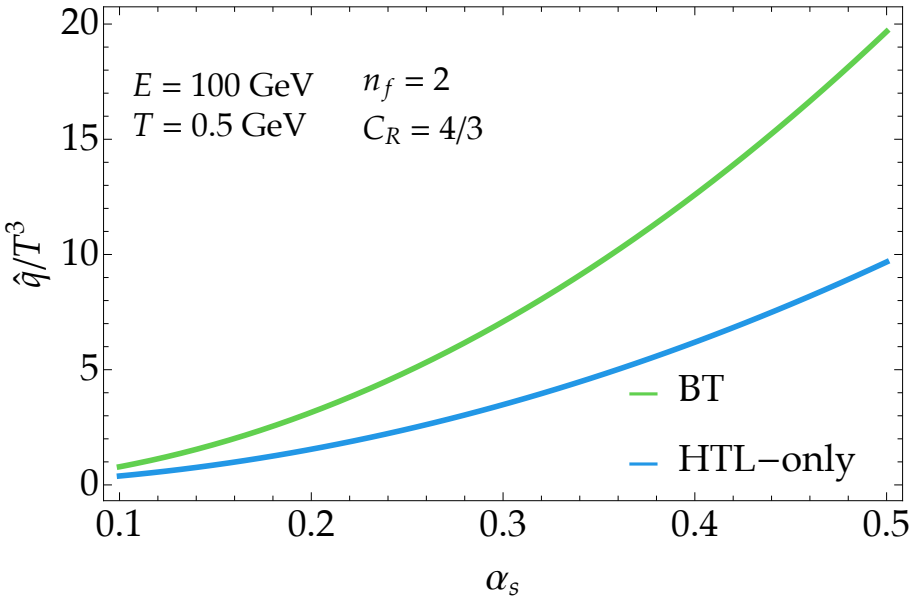

Figure 3.25: Comparison of $\hat{q}/T^3$ as a function α_s for BT and HTL-only collisional energy loss implementations. The BT curve is calculated with eq. 3.89, while the HTL-only curve is calculated by evaluating eq. 3.87 using the elastic scattering rate defined in eq. 3.90.

tic energy loss, we follow [155] and use the following scattering rate

$$\frac{d\Gamma_{\rm el}^{HTL}}{d^2\mathbf{q}} = \frac{dN_{el}}{dzd^2\mathbf{q}} \tag{3.90a}$$

$$= \frac{2C_R\alpha_s^2}{\pi}\int_{-E+\sqrt{M^2+\mathbf{q}^2}}^{\infty} d\omega \frac{n_B(\omega)}{q}\left(1-\frac{\omega^2}{q^2}\right)^2$$

$$\sum_m \left[C_{LL}^m\left|\Delta_L\right|^2 + 2C_{LT}^m \,\mathrm{Re}\left(\Delta_L\Delta_T\right) + C_{TT}^m\left|\Delta_T\right|^2\right], \tag{3.90b}$$

and then evaluate eq. 3.87 numerically to obtain $\hat{q}^{HTL}$.

In fig. 3.25, we evaluate $\hat{q}/T^3$ as a function of the strong coupling α_s for the BT and HTL-only implementations of the elastic energy loss. Consistent with [155, 243], we evaluate both the BT and HTL-only curves at $E = 100$ GeV, $n_f = 2$, and $C_R = 4/3$. We choose to evaluate curves at a temperature of $T = 0.5$ GeV as this is the characteristic temperature of a central $\mathrm{Pb}+\mathrm{Pb}$ collision system in our model (as shown in fig. 3.8 and fig. 3.9). The results of fig. 3.25 reveal that the BT implementation of the jet transport coefficient at $\alpha_s \sim 0.3$ can result in $\hat{q}/T^3$ that are $\sim 100\%$ larger in the BT version of the elastic energy loss compared to the HTL-only elastic energy loss. The sensitivity of the

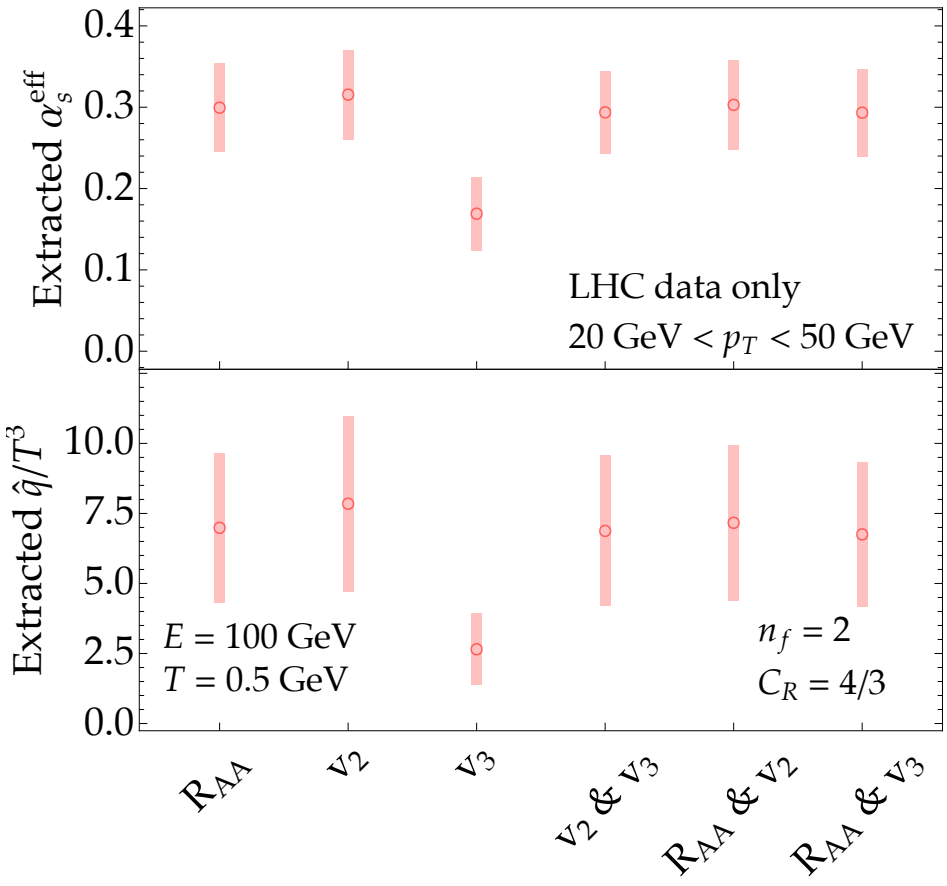

Figure 3.26: Top (Bottom): Extracted α_s^{eff} ($\hat{q}/T^3$) using various subsets of all LHC experimental data from Table 3.2. The horizontal axis shows the subset of observables from which α_s^{eff} ($\hat{q}/T^3$) was extracted. The bands for the extracted α_s^{eff} ($\hat{q}/T^3$) correspond to the largest extracted α_s^{eff} ($\hat{q}/T^3$) value plus its upper one-standard-deviation confidence interval, and the smallest extracted α_s^{eff} ($\hat{q}/T^3$) value minus its lower one-standard-deviation confidence interval, across combinations of the $\mathbf{k}_{\text{max}}$ multiplier and the elastic energy loss implementation.

jet transport coefficient to the choice of model highlights the caution that one should have when interpreting the values of our extracted $\hat{q}$.

In the top (bottom) panel of fig. 3.26, the extracted α_s^{eff} ($\hat{q}/T^3$) is shown where the extraction has been done on a variety of subsets of all the experimental data from Table 3.2. The bands for the extracted α_s^{eff} ($\hat{q}/T^3$) correspond to the largest extracted α_s^{eff} ($\hat{q}/T^3$) value plus its upper one-standard-deviation confidence interval, and the smallest extracted α_s^{eff} ($\hat{q}/T^3$) value minus its lower one-standard-deviation confidence interval, across combinations of the $\mathbf{k}_{\text{max}}$ multiplier and the elastic energy loss implementation.

For the R_{AA} only and v_2 only extractions, the extracted α_s^{eff} values are $0.3^{+0.05}_{-0.05}$ and

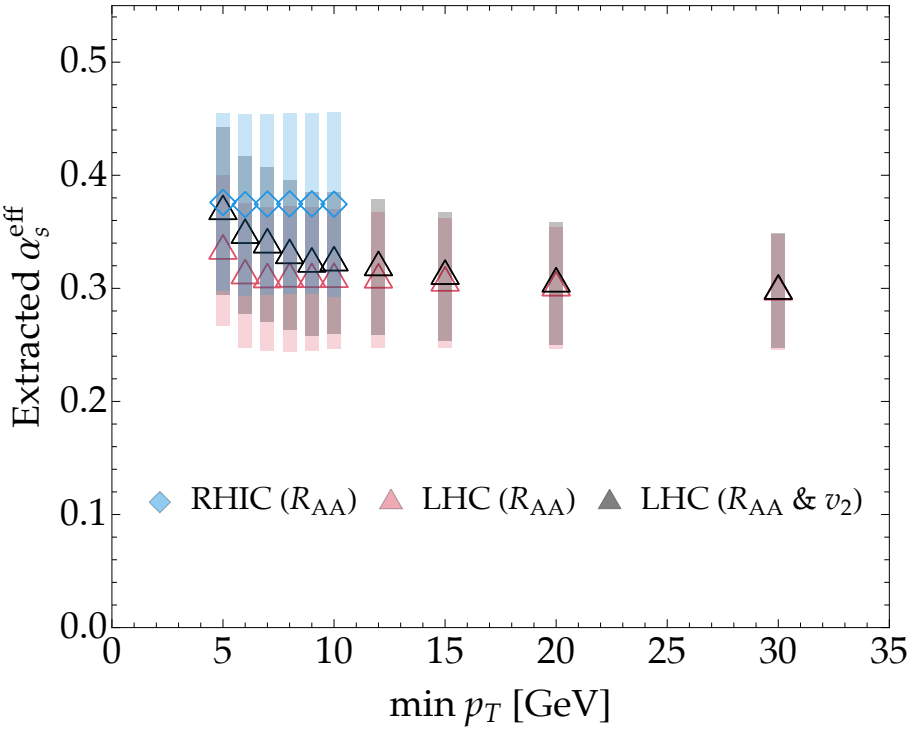

Figure 3.27: Extracted α_s^{eff} as a function of the lower p_T bound of the experimental data included in the extraction. Extractions using large system R_{AA} RHIC data are shown as blue diamonds. Extractions using only large system R_{AA} data from the LHC are shown as red triangles, while extractions using large system R_{AA} and v_2 data from the LHC are shown as gray diamonds.The bands for the extracted α_s^{eff} correspond to the largest extracted α_s^{eff} value plus its upper one-standard-deviation confidence interval, and the smallest extracted α_s^{eff} value minus its lower one-standard-deviation confidence interval, across combinations of the $\mathbf{k}_{\text{max}}$ multiplier and the elastic energy loss implementation.

$0.32^{+0.06}_{-0.06}$, respectively. The extracted α_s^{eff} for the R_{AA} only and v_2 only are quite similar, suggesting that our model is able to consistently describe both the R_{AA} and v_2 data. The R_{AA} & v_2 extraction yields an extracted $\alpha_s^{\text{eff}} = 0.3^{+0.06}_{-0.06}$, which is consistent with the R_{AA} only and v_2 only extractions being similar. When extracting $\hat{q}/T^3$ on R_{AA} data only, we obtain $\hat{q}/T^3 = 7^{+3}_{-3}$, which is comparatively smaller than the $\hat{q}/T^3 = 11^{+3}_{-3}$ obtained from the CTv1.0 model in [155]; the smaller extracted $\hat{q}/T^3$ extracted in the CTv2.0 model is consistent with the findings of Sec. 3.2.5, where we showed that the CTv2.0 model systematically produces more energy loss than the CTv1.0 model.

The most striking feature of fig. 3.26 is the relatively small value of the extracted coupling, $\alpha_s^{\text{eff}} = 0.17^{+0.05}_{-0.05}$, obtained when the extraction is performed using only v_3 experimental data. This value is approximately 40% smaller than the couplings extracted

from either the R_{AA} or v_2 data. The discrepancy between the α_s^{eff} and $\hat{q}/T^3$ values extracted from v_3 and those extracted from R_{AA} and v_2 suggests that the model is unable to simultaneously describe all three observables. Both the $v_2\&v_3$ and $R_{AA}\&v_3$ combined extractions yield $\alpha_s^{\text{eff}} \simeq 0.29^{+0.05}_{-0.05}$. However, these values are largely dominated by the v_2 and R_{AA} datasets, respectively, because they contain substantially more data points than the v_3 dataset: 80 points for v_2, 69 points for R_{AA}, and only 41 points for v_3. Consequently, the influence of the v_3 data on the combined fits is comparatively weak. It should be noted that the uncertainties across the different extractions are fully correlated, so one should not, for instance, compare the bottom of the v_2 only or R_{AA} only extractions to the top of the v_3 only extraction.

In fig. 3.27, we show the extracted values of α_s^{eff} as a function of the lower p_T bound of the experimental data included in the extraction. Extractions using large system R_{AA} RHIC data are shown as blue diamonds. Extractions using only large system R_{AA} data from the LHC are shown as red triangles, while extractions using large system R_{AA} and v_2 data from the LHC are shown as gray diamonds. We see that the extracted value of α_s^{eff} for LHC data extracted on R_{AA} data alone and on $R_{AA} + v_2$ data stabilize when the lower p_T bound is greater than 20 GeV. The extracted value of α_s^{eff} for RHIC data alone is relatively stable across all lower p_T bounds. The instability of the extracted α_s^{eff} at small lower p_T bounds for the LHC data is an indication that our model is unable to accurately describe the low-p_T data. Thus, we use the lower p_T bound of 20 GeV for the LHC data to ensure that we are in the region of phase space where our model is expected to be valid, and to avoid the region where non-perturbative effects are expected to be significant.

3.5 Results

In this section we present the results of our constrained model to large and small system data for high-p_T R_{AB} and v_2. In Sec. 3.5.1, we find that our model—which is tuned to large system data—is able to quantitatively and simultaneously describe R_{AA} and v_2 across a comprehensive set of large system experimental data. In Sec. 3.5.2, we then ex-

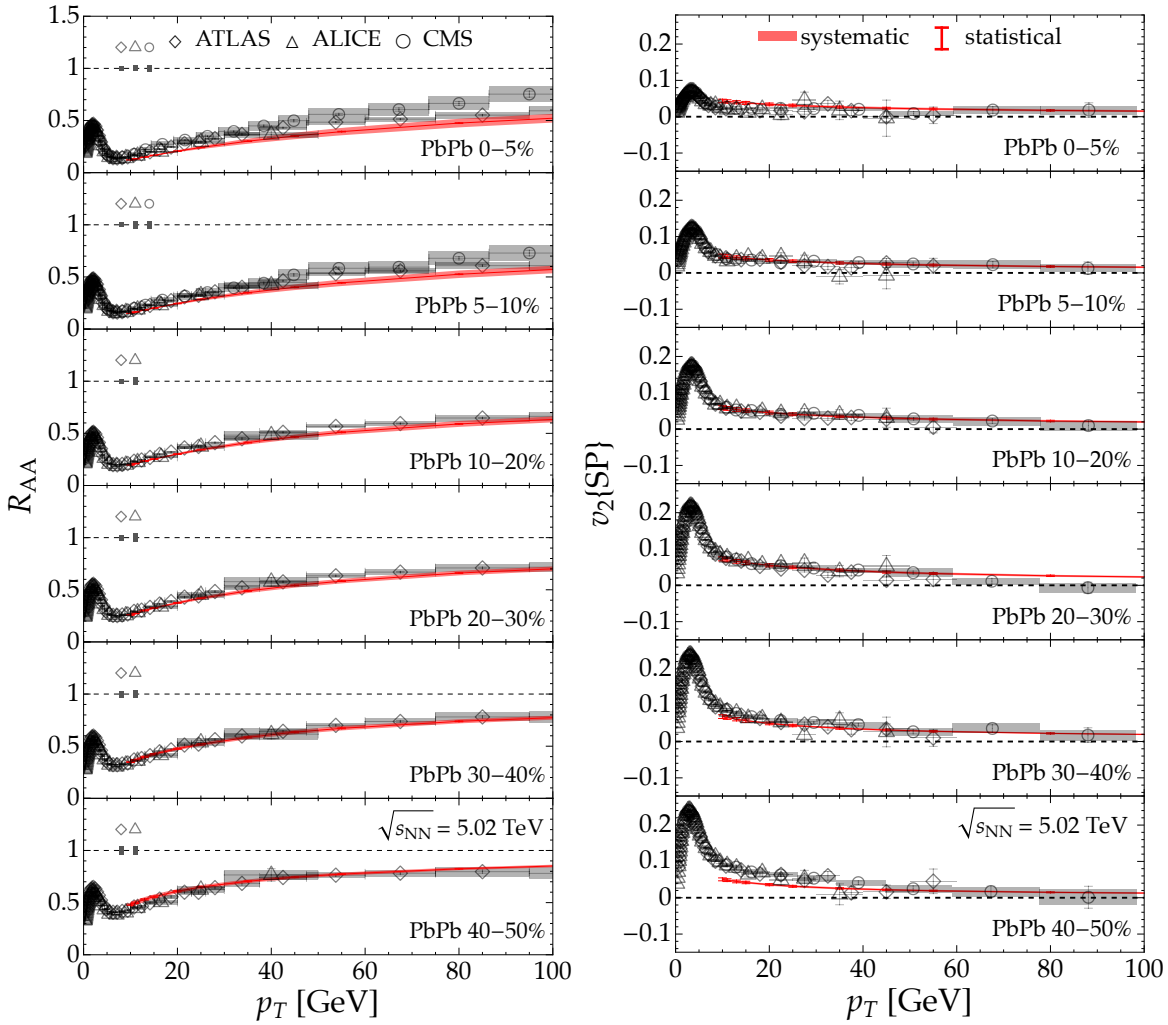

Figure 3.28: The left and right columns compare our energy loss model results for $\mathrm{Pb}+\mathrm{Pb}$ R_{AA} and $v_2\{\mathrm{SP}\}$ at $\sqrt{s_{NN}} = 5.02$ TeV for charged particles, respectively, as functions of p_T across multiple centrality classes, with data from ATLAS [141, 211], ALICE [227, 229], and CMS [77, 210]. Experimental data are shown with statistical (bars) and systematic (boxes) uncertainties, while theory results are shown in red with statistical (bars) and systematic (bands) uncertainties, along with central values (lines). Diamonds, triangles, and circles denote ATLAS, ALICE, and CMS data, respectively. Bands around unity are experimental normalization uncertainties.

trapolate our model to small systems and make predictions for R_{AB} and v_2. Our main findings in Sec. 3.5.2 are that our model predicts a significant suppression of high-p_T hadrons in small systems, and that the predicted v_2 for small systems is essentially zero across all p_T and centrality classes.

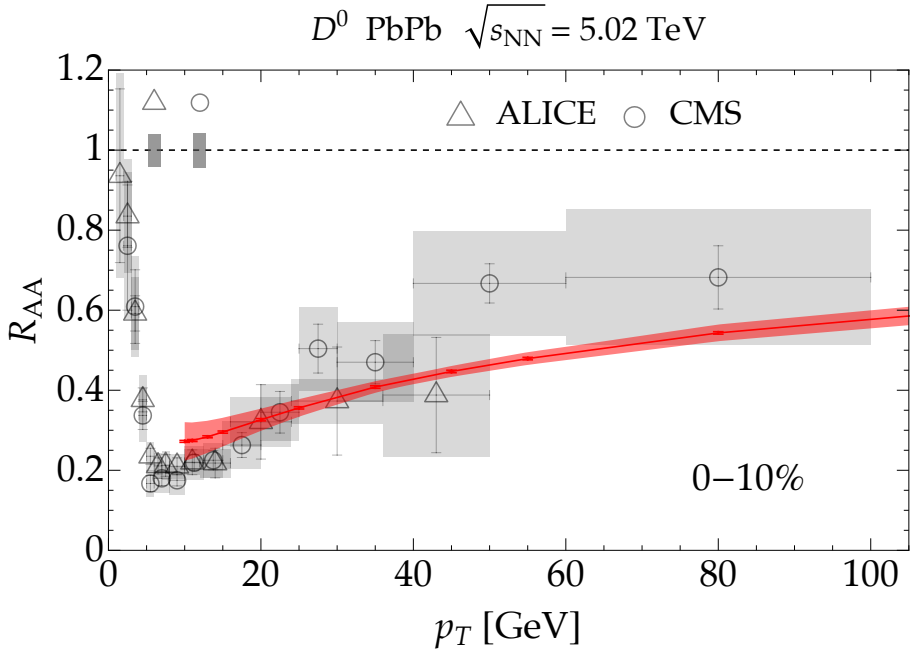

Figure 3.29: Large system $R_{AA}(p_T)$ results for D^0 mesons in $\mathrm{Pb} + \mathrm{Pb}$ collisions at $\sqrt{s_{NN}} = 5.02$ TeV at 0-10% centrality. Experimental data are from ALICE[226] and CMS [228], and are shown with statistical (bars) and systematic (boxes) uncertainties, while theory results are shown in red with statistical (bars) and systematic (bands) uncertainties, along with central values (lines). Bands around unity are experimental normalization uncertainties.

3.5.1 Comparison to large system data

In the left and right columns of fig. 3.28, we compare the results from the constrained energy loss model to representative large-system experimental data from ATLAS, ALICE, and CMS for R_{AA} [77, 141, 227] and v_2 [210, 211, 229] in $\mathrm{Pb} + \mathrm{Pb}$ collisions at $\sqrt{s_{NN}} = 5.02$ TeV. From fig. 3.28, one can see that our model simultaneously provides a good quantitative description of the p_T and centrality dependence of both the R_{AA} and v_2 in large systems.

In fig. 3.29 we compare our model to representative R_{AA} data for D^0 mesons in $\mathrm{Pb} + \mathrm{Pb}$ collisions at $\sqrt{s_{NN}} = 5.02$ TeV at 0-10% centrality from ALICE [226] and from [228]. From fig. 3.29, we see that our constrained energy loss model is able to quantitatively describe the p_T dependence of the D^0 meson R_{AA} in $\mathrm{Pb} + \mathrm{Pb}$ collisions at $\sqrt{s_{NN}} = 5.02$ TeV at 0-10% centrality.

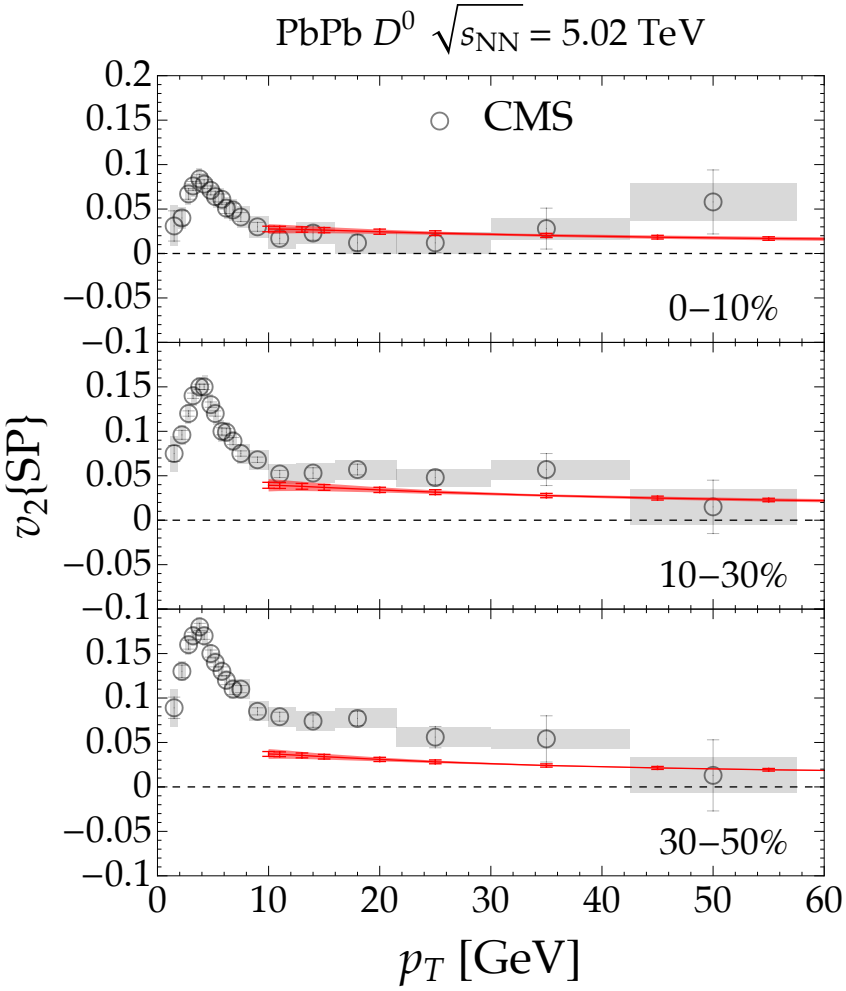

Figure 3.30: Large system $v_2(p_T)$ results for D^0 mesons in $\mathrm{Pb}+\mathrm{Pb}$ collisions at $\sqrt{s_{NN}} = 5.02$ TeV at 0-10% centrality (top), 10-30% centrality (middle), and 30-50% centrality (bottom). Experimental data are from [213], and are shown with statistical (bars) and systematic (boxes) uncertainties, while theory results are shown in red with statistical (bars) and systematic (bands) uncertainties, along with central values (lines).

In fig. 3.30, we compare our model's $v_2\{SP\}$ to representative data for D^0 mesons in $\mathrm{Pb}+\mathrm{Pb}$ collisions at $\sqrt{s_{NN}} = 5.02$ TeV from CMS [213] at 0-10% centrality (top), 10-30% centrality (middle), and 30-50% centrality (bottom). From fig. 3.30, we see that our constrained energy loss model describes well the p_T dependence of the D^0 meson v_2 in $\mathrm{Pb}+\mathrm{Pb}$ collisions, but the centrality dependence of the model is slightly weaker than the centrality dependence of the experimental data.

In fig. 3.31, we compare our model to representative R_{AA} data for π^0 mesons in $\mathrm{Au}+\mathrm{Au}$ collisions at $\sqrt{s_{NN}} = 0.2$ TeV for a range of centralities from PHENIX [222]. From fig. 3.31, we see that our constrained energy loss model is able to quantitatively describe the p_T dependence and the centrality dependence of the π^0 R_{AA} in $\mathrm{Au}+\mathrm{Au}$

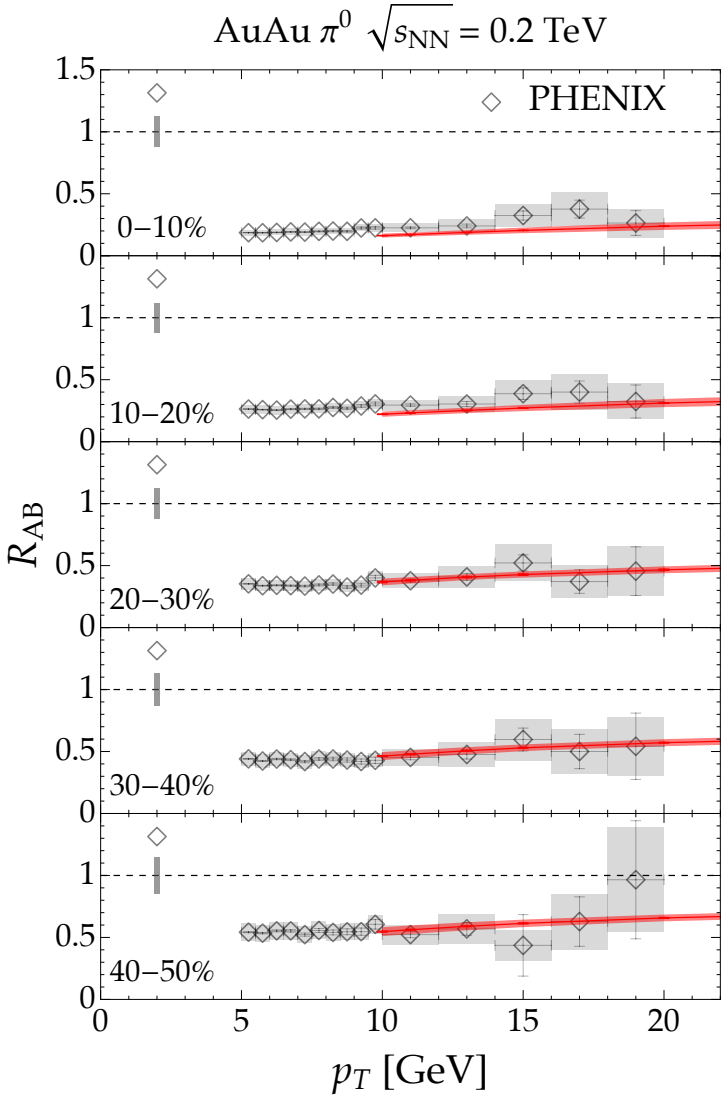

Figure 3.31: Large system $R_{AA}(p_T)$ results for π^0 mesons in $\mathrm{Au} + \mathrm{Au}$ collisions at $\sqrt{s_{NN}} = 0.2$ TeV for a range of centralities Experimental data are from [222], and are shown with statistical (bars) and systematic (boxes) uncertainties, while theory results are shown in red with statistical (bars) and systematic (bands) uncertainties, along with central values (lines). Bands around unity are experimental normalization uncertainties.

collisions at $\sqrt{s_{NN}} = 0.2$ TeV.

In summary, Sec. 3.5.1 demonstrates that our energy loss model is able to simultaneously describe the R_{AA} and v_2 data in large systems at both RHIC and the LHC, for heavy and light flavour hadrons, and across a wide range of p_T and centrality. In figures 3.28 to 3.31 we have shown a comparison to a representative set of all available large system data; in fig. C.2 and fig. C.3, we show the full comparison of our model to all large system data available at the time of this writing. The ability of our model to

simultaneously describe the R_{AA} and v_2 data across a wide range of large system data is a highly non-trivial result, and the success of our model in describing the large system data allows us to confidently extrapolate our model to make predictions for small systems, which we present in Sec. 3.5.2.

Note that a full comparison of our model to all large and small system data is available in the appendix C.3.

3.5.2 Predictions for small systems

In fig. 3.32, we present model predictions for small systems. The individual panels show R_{AB} for $\mathrm{Ne}+\mathrm{Ne}$ [244] (first) and $\mathrm{O}+\mathrm{O}$ [153, 154] (second) at $\sqrt{s_{NN}} = 5.36$ TeV, and for $p+\mathrm{Pb}$ [77, 141, 227] (third) at $\sqrt{s_{NN}} = 5.02$ TeV. From fig. 3.32, we see that extrapolating to the small symmetric systems of $\mathrm{Ne}+\mathrm{Ne}$ and $\mathrm{O}+\mathrm{O}$, our model gives a good quantitative description of the minimum bias R_{AA} as a function of p_T. The situation for $R_{p\mathrm{Pb}}$ is less clear; our model is in qualitative agreement with ALICE [227] but in qualitative disagreement with ATLAS [141] and CMS [77] $R_{p\mathrm{Pb}}$.

In fig. 3.33, we present model predictions for $R_{d\mathrm{Au}}$ in $d+\mathrm{Au}$ collisions at $\sqrt{s_{NN}} = 0.2$ TeV for 0-5% (top), 60-88%(middle), and 0-100% (bottom) centrality classes and compare the model's predictions to photon normalized π^0 $R_{d\mathrm{Au}}$ data from PHENIX [147]. From fig. 3.33, we see that our model is in quantitative agreement with the PHENIX data for all centrality classes, thereby improving upon the qualatative agreement that was found in CTv1.0 [155].

In fig. 3.34, we present $v_2\{\mathrm{SP}\}$ predictions for $p+\mathrm{Pb}$ collisions at 0-10% centrality with $\sqrt{s_{NN}} = 5.02$ TeV, that are compared to ATLAS [148], ALICE [149], and CMS [150] data. The ATLAS data corresponds to a measurement of $v_2\{2\}$ at 0-5% centrality with $\sqrt{s_{NN}} = 8.16$ TeV, the ALICE data corresponds to a measurement of $v_2\{2\}$ at 0-10% centrality with $\sqrt{s_{NN}} = 5.02$ TeV, and the CMS data corresponds to a measurement of $v_2\{4\}$ using the four-subevent method with $185 \leq N_{\mathrm{trk}}^{\mathrm{offline}} < 250 \approx 0-5\%$ centrality at $\sqrt{s_{NN}} = 8.16$ TeV. From fig. 3.34, it is evident that our model predicts $v_2^{p\mathrm{Pb}}\{\mathrm{SP}\} \approx 0$,

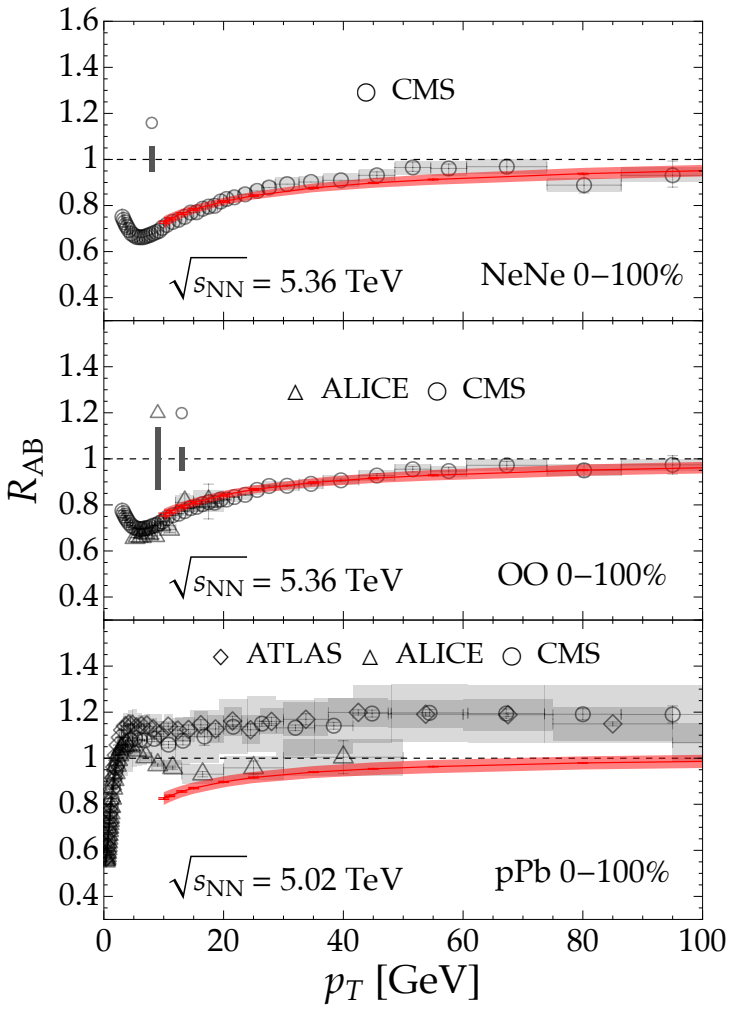

Figure 3.32: Predictions for charged particle small-system data: the top panels show R_{AB} for minimum bias $\mathrm{Ne}+\mathrm{Ne}$ (first) at $\sqrt{s_{NN}} = 5.36$ TeV [244], for minimum bias $\mathrm{O}+\mathrm{O}$ (second) at $\sqrt{s_{NN}} = 5.36$ TeV [153, 154], and for minimum bias $p+\mathrm{Pb}$ (third) at $\sqrt{s_{NN}} = 5.02$ TeV [77, 141, 227]. Experimental data are shown with statistical (bars) and systematic (boxes) uncertainties, while theory results are shown in red with statistical (bars) and systematic (bands) uncertainties, along with central values (lines). Diamonds, triangles, and circles denote ATLAS, ALICE, and CMS data, respectively. Bands around unity are experimental normalization uncertainties. Normalization uncertainties for $R_{p\mathrm{Pb}}$ are 4.6%, 3.9%, and 2.3% for ATLAS [141], ALICE [227], and CMS [77], respectively; the $R_{p\mathrm{Pb}}$ uncertainties are not shown for visual purposes.

which is in strong disagreement with all data [148–150].

In fig. 3.35, we show high-p_T R_{AB} (top row), $v_2^{\rm hard}$ (middle row) calculated, and $v_2\{\mathrm{SP}\}$ (bottom row) constrained model results for $\mathrm{Pb}+\mathrm{Pb}$ and predictions for $\mathrm{Ne}+\mathrm{Ne}$, $\mathrm{O}+\mathrm{O}$, and $p+\mathrm{Pb}$. Results are shown as a function of p_T (left column) and centrality (right column). Recall that the $v_2^{\rm hard}$—which *is not* comparable to data—is calculated from eq. 3.70 and the $v_2\{\mathrm{SP}\}$—which *is* comparable to data—is calculated from eq. 3.79.

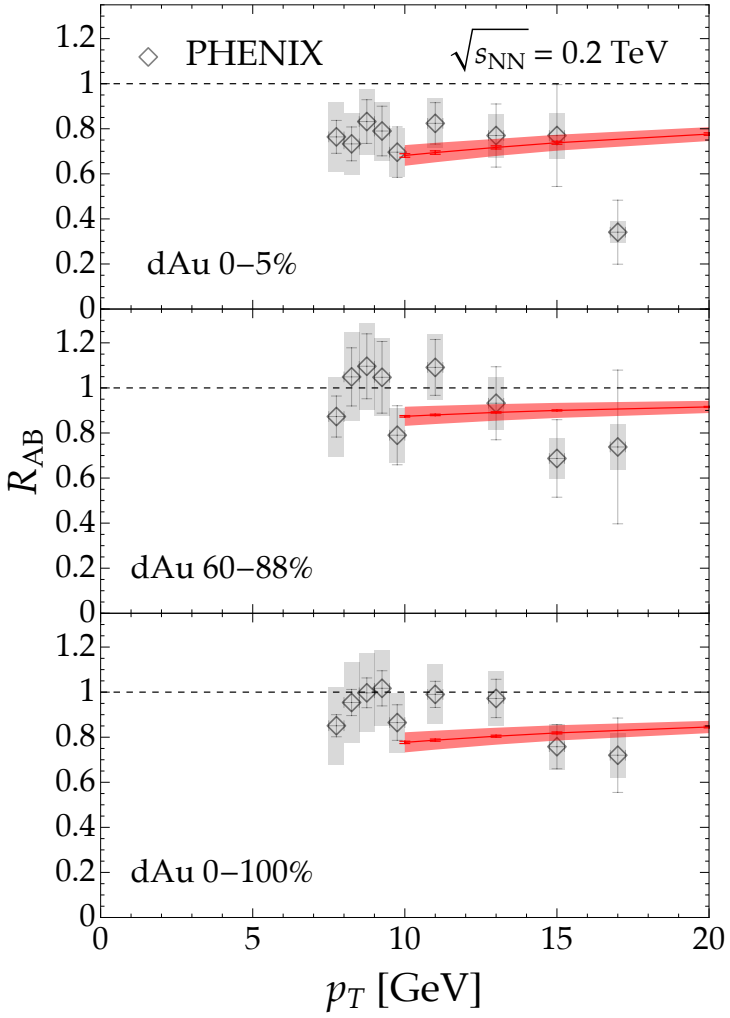

Figure 3.33: Energy loss predictions of $R_{d\rm Au}$ compared to photon normalized π^0 $R_{d\rm Au}$ data from PHENIX [147] at $\sqrt{s_{NN}} = 0.2$ TeV for 0-5% (top), 60-88%(middle), and 0-100% (bottom) centrality classes. Experimental data are shown with statistical (bars) and systematic (boxes) uncertainties, while theory results are shown in red with statistical (bars) and systematic (bands) uncertainties, along with central values (lines). Diamonds, triangles, and circles denote ATLAS, ALICE, and CMS data, respectively.

Data are omitted for visual clarity. In the top row, we show that $R_{\rm PbPb}$ is significantly suppressed (~ 0.3), while the small systems $R_{\rm OO}$, $R_{\rm NeNe}$ and $R_{p\rm Pb}$ all show similar signs of non-negligible suppression (~ 0.75–0.85). Despite R_{AB} predictions significantly less than unity, the $v_2^{\rm hard}$ in all the small systems are small (~ 0.005 at $p_T \sim 15$ GeV). In the bottom row of fig. 3.35 we show that while $v_2^{\rm hard} \approx v_2\{\rm SP\}$ for $\rm Pb+Pb$, $v_2^{\rm hard} > v_2\{\rm SP\} \approx 0$ for $\rm Ne+Ne$, $\rm O+O$, and $p+\rm Pb$.

The small $v_2^{\rm hard}$ values in fig. 3.35 can be understood by examining the results of fig. 3.36. In the left column of fig. 3.36 we show hydrodynamic temperature profiles at the formation time of the medium ($\tau_0 = 0.4$ fm/c) of representative events for the

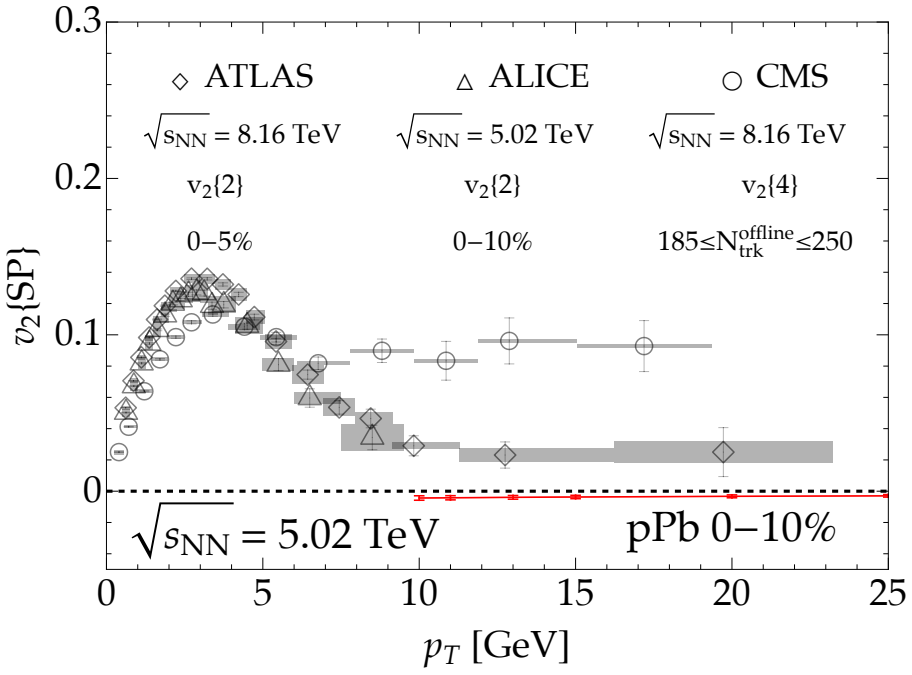

Figure 3.34: Predictions of $v_2\{\text{SP}\}$ for $0-10\%$ $p+\text{Pb}$ at $\sqrt{s_{NN}}=5.02$ TeV compared to ATLAS [148] (0-5%, $\sqrt{s_{NN}}=8.16$ TeV, $v_2\{2\}$), ALICE [149] (0-10%, $\sqrt{s_{NN}}=5.02$ TeV, $v_2\{2\}$), and CMS [150] ($185\leq N_{\text{trk}}^{\text{offline}}<250\approx 0-5\%$, $\sqrt{s_{NN}}=8.16$ TeV, $v_2\{4\}$, four-subevent method). Experimental data are shown with statistical (bars) and systematic (boxes) uncertainties, while theory results are shown in red with statistical (bars) and systematic (bands) uncertainties, along with central values (lines). Diamonds, triangles, and circles denote ATLAS, ALICE, and CMS data, respectively.

collision systems of $\text{Pb}+\text{Pb}$ (top), $\text{Ne}+\text{Ne}$ (second), $\text{O}+\text{O}$ (third), and $p+\text{Pb}$ (bottom). In the middle ($\alpha_s=0.3$) and right ($\alpha_s=0.45$) columns of fig. 3.36, we compare $1+v_2^{\text{hard}}\cos\left(2(\phi-\psi_2^{\text{hard}})\right)$ (solid) and $R_{AB}\left(p_T,\phi\right)/R_{AB}\left(p_T\right)$ (dotted). The hydrodynamic temperature profiles have been rotated so as to align the ψ_2^{hard} angles with the horizontal axis. The results in the middle and right columns of fig. 3.36 are calculated using events that correspond to those in the left column of fig. 3.36.

In fig. 3.36, one sees that there is an anisotropy in the hydrodynamic temperature profiles of the $\text{Pb}+\text{Pb}$, $\text{Ne}+\text{Ne}$, $\text{O}+\text{O}$, and $p+\text{Pb}$ collision systems. The top row shows that our energy loss model is sensitive to the difference in path lengths that arise due to the anisotropy of the temperature profile in the large collision system of $\text{Pb}+\text{Pb}$. However, the bottom three rows show that despite increasing the strong coupling from 0.3 to 0.45, our energy loss model is weakly sensitive to the difference in path lengths that arise due to the anisotropy of the temperature profiles in the small

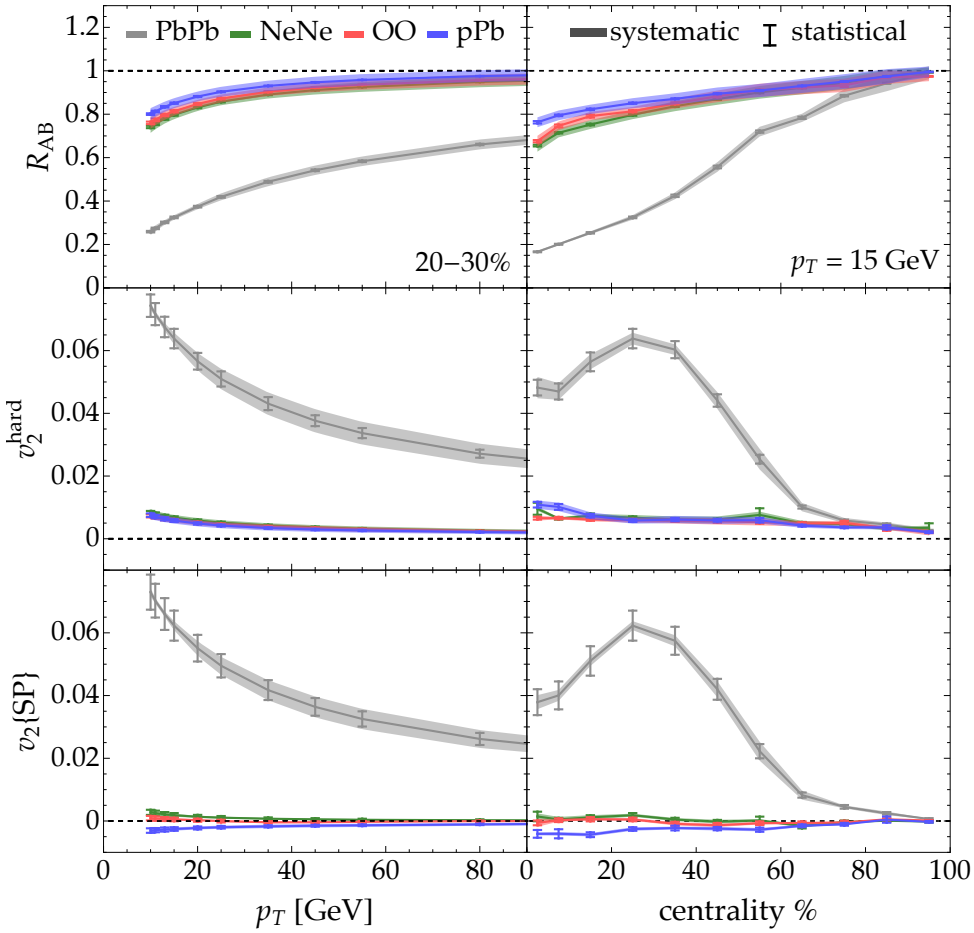

Figure 3.35: Model predictions for R_{AB} (top), v_2^{hard} (middle), $v_2\{\text{SP}\}$ (bottom) as a function of p_T (left) and centrality (right) for $\text{Pb} + \text{Pb}$ (gray), $\text{Ne} + \text{Ne}$ (green), $\text{O} + \text{O}$ (red), and $p + \text{Pb}$ (blue) collision systems. The left panel shows model predictions for the 20-30% centrality class and the right panel shows model predictions at a fixed p_T of 15 GeV. The v_2^{hard} is calculated from eq. 3.70 and the $v_2\{\text{SP}\}$ is calculated from eq. 3.72. Results are shown with statistical uncertainties (bars), systematic uncertainties (bands), and central values (lines).

collision systems of $\text{Ne} + \text{Ne}$, $\text{O} + \text{O}$, and $p + \text{Pb}$.

The $v_2\{\text{SP}\} \approx 0$ result in small systems can be understood by examining fig. 3.37, where we plot the folded distribution of $\psi_2^{\text{hard}} - \psi_2^{\text{soft}}$ for $\text{Pb}+\text{Pb}$ (top), $\text{Ne}+\text{Ne}$ (second), $\text{O}+\text{O}$ (third), and $p+\text{Pb}$ (bottom) collision systems. All distributions shown in fig. 3.37 are generated at 20-30% centrality, with $p_T = 15$ GeV and $\alpha_s = 0.3$. Note that the shapes of the distributions are relatively insensitive to the choice of these phase space parameters. The "folded" mapping maps all angles into the domain $[-\pi/2, \pi/2]$; this mapping is chosen to ensure that the magnitude of the largest difference between ψ_2^{hard} and ψ_2^{soft} occurs at $\pi/2$.

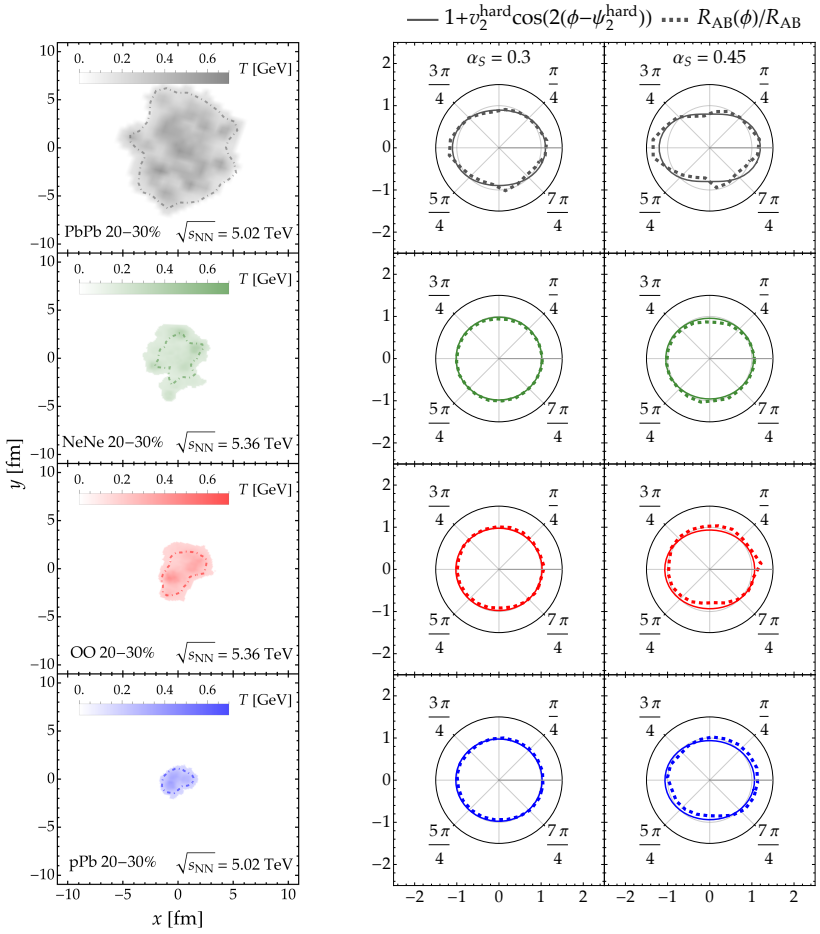

Figure 3.36: Left: Hydrodynamic temperature profiles at the formation time of the medium $\tau_0 = 0.4$ fm/c for $\mathrm{Pb}+\mathrm{Pb}$ (top), $\mathrm{Ne}+\mathrm{Ne}$ (second), $\mathrm{O}+\mathrm{O}$ (third), and $p+\mathrm{Pb}$ (bottom) collision systems at 20-30% centrality. The dot-dashed lines over the temperature profiles are plotted for visual purposes and are calculated as the integral of the temperature profile from the origin in the azimuthal direction ϕ. Center (Right): Dashed lines show the calculated $R_{AB}(\phi)/R_{AB}$ for $\alpha_s = 0.3$ ($\alpha_s = 0.45$) plotted on a polar axis; the curves are calculated using the corresponding hydrodynamic events from the left panel. The solid lines are $1 + v_2^{\rm hard}\cos(2(\phi - \psi_2^{\rm hard}))$, where $v_2^{\rm hard}$ and $\psi_2^{\rm hard}$ are calculated from the energy-loss model using the corresponding hydrodynamic events from the left panel. For visual purposes, all figures are rotated so that the $\psi_2^{\rm hard}$ angles align with the horizontal axis. All results from the energy-loss model are shown here with $|\mathbf{k}|_{\rm max}$ multiplier = 1 and with p_T = 15 GeV.

In fig. 3.37, we show that the prediction of $v_2\{\mathrm{SP}\} \approx 0$ in small systems arises because the orientation of the participant plane defined by hard particles and the participant plane defined by soft particles become decorrelated (one can see from eq. 3.79 that the event averaged cosine when the hard- and soft-participant planes in small systems are decorrelated will result in $v_2\{\mathrm{SP}\} \approx 0$). We see that for the $\mathrm{Pb}+\mathrm{Pb}$ collision system, the folded distribution of $\psi_2^{\rm hard} - \psi_2^{\rm soft}$ is peaked around zero and is well-approximated by a Gaussian of width $\sigma = 0.35$ radians, and thus the participant planes in the hard

and soft sectors are strongly correlated. Both $\mathrm{Ne}+\mathrm{Ne}$ and $\mathrm{O}+\mathrm{O}$ collisions systems are well-approximated by the uniform distribution $1/\pi$ over the entire angular range. Qualitatively, the $\mathrm{Ne}+\mathrm{Ne}$ system shows a slightly stronger correlation than the $\mathrm{O}+\mathrm{O}$ system, but the correlation is still weak compared to the $\mathrm{Pb}+\mathrm{Pb}$ system. Thus, we refer to the participant planes in the hard and soft sectors as weakly correlated and decorrelated in the $\mathrm{Ne}+\mathrm{Ne}$ and $\mathrm{O}+\mathrm{O}$ systems, respectively. In the $p+\mathrm{Pb}$ system, the distribution of $\psi_2^{\mathrm{hard}}-\psi_2^{\mathrm{soft}}$ shows a double peak structure around $\pm\pi/2$, indicating that the participant planes in the hard and soft sectors are actually anti-correlated. Quantitatively, we calculate r, the Pearson correlation coefficient [245] between the ψ_2^{hard} and ψ_2^{soft} angles for each collisions system. A value of r close to 1 indicates perfect correlation, while a value close to -1 indicates perfect anti-correlation, and $r=0$ indicates decorrelation. For the distributions in fig. 3.37, we find that $r_{\mathrm{Pb+Pb}}=0.48$, $r_{\mathrm{Ne+Ne}}=0.17$, $r_{\mathrm{O+O}}=-0.05$, and $r_{p+\mathrm{Pb}}=-0.09$. Note that the decorrelation between ψ_2^{hard} and ψ_2^{soft} is not an artifact of numerical instability in the calculation of ψ_2^{hard}; we have verified this claim in appendix C.2.

We will now argue why our findings of $v_2\{\mathrm{SP}\}\approx 0$ for small systems is independent of the energy loss model. In fig. 3.38, we show the event-averaged $\cos(2[\psi_2^{\mathrm{hard}}-\psi_2^{\mathrm{soft}}])$ (top), v_2^{hard} (middle), and $v_2\{\mathrm{SP}\}$ (bottom) as a function of α_s for $\mathrm{Pb}+\mathrm{Pb}$ (gray), $\mathrm{Ne}+\mathrm{Ne}$ (green), $\mathrm{O}+\mathrm{O}$ (red), and $p+\mathrm{Pb}$ (blue) collision systems at 20-30% centrality with $p_T=15$ GeV. By scanning through a range of α_s, we are able to effectively cover the predictions of a wide range of energy loss models. We notice that as α_s is increased, the v_2^{hard} increases, but the event averaged cosine between ψ_2^{hard} and ψ_2^{soft} remains relatively constant. Thus, we conclude that the v_2^{hard} Fourier coefficients are dependent on the energy loss model, but the decorrelation between ψ_2^{hard} and ψ_2^{soft} is robust against changes in energy loss models. Since the decorrelation between ψ_2^{hard} and ψ_2^{soft} is robust against changes in energy loss models, we conclude that the prediction of $v_2\{\mathrm{SP}\}\approx 0$ for small systems is independent of the energy loss model.

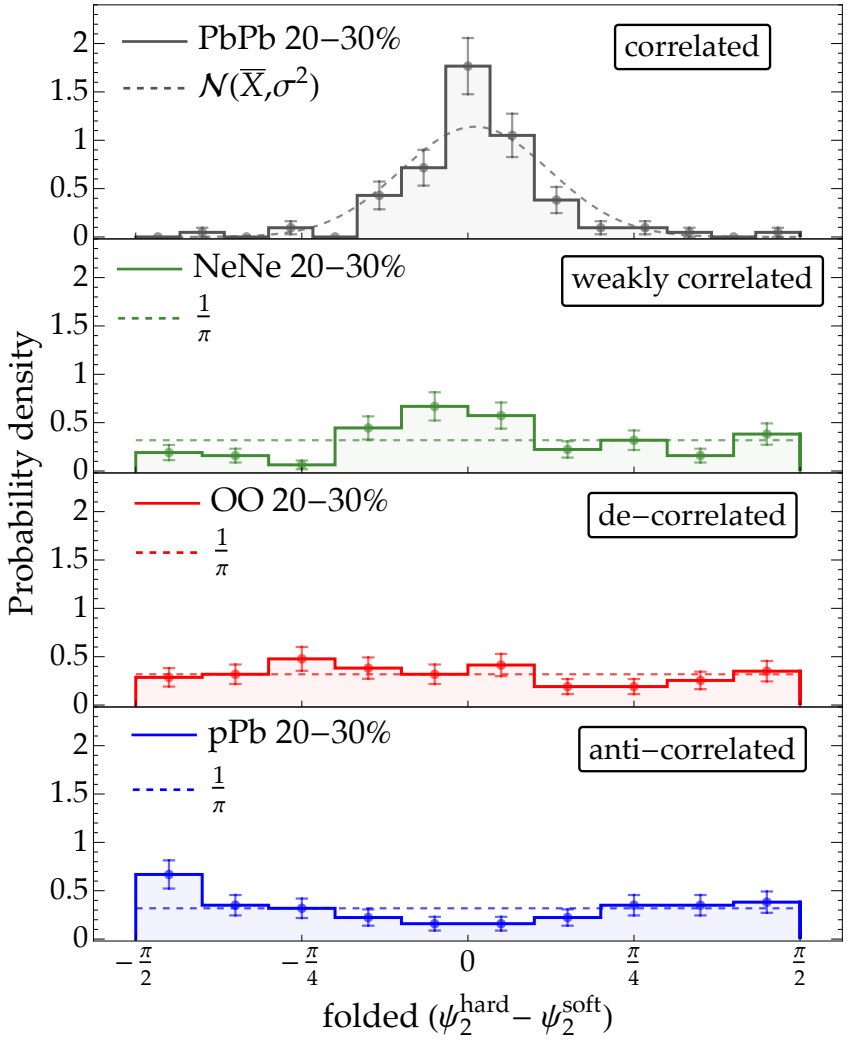

Figure 3.37: Probability distributions of folded $(\psi_2^{\text{hard}} - \psi_2^{\text{soft}})$ for $\mathrm{Pb}+\mathrm{Pb}$ (top), $\mathrm{Ne}+\mathrm{Ne}$ (second row), $\mathrm{O}+\mathrm{O}$ (third row), and $p+\mathrm{Pb}$ (bottom) collision systems in the 20-30% centrality class. For visual purposes, in the $\mathrm{Pb}+\mathrm{Pb}$ panel, we plot a normal distribution $N(\bar{X},\sigma^2)$ of mean $\bar{X}=0.03$ and standard deviation $\sigma=0.35$; in the $\mathrm{Ne}+\mathrm{Ne}$, $\mathrm{O}+\mathrm{O}$ and $p+\mathrm{Pb}$ panels, we plot the constant distribution of $1/\pi$. All distributions are generated with α_s = 0.3, p_T = 15 GeV, and with $|\mathbf{k}|_{\max}$ multiplier = 1. Statistical uncertainties are shown in each bin with error bars.

3.6 Conclusions

In this chapter, we developed and applied a pQCD-based energy loss framework to compute high-p_T R_{AB} and v_n in small collision systems. We provided a detailed account of both the radiative and elastic energy loss mechanisms that underpin the model and carefully described how the medium is sampled dynamically along each parton trajectory on an event-by-event basis. We further described in detail how the high-p_T

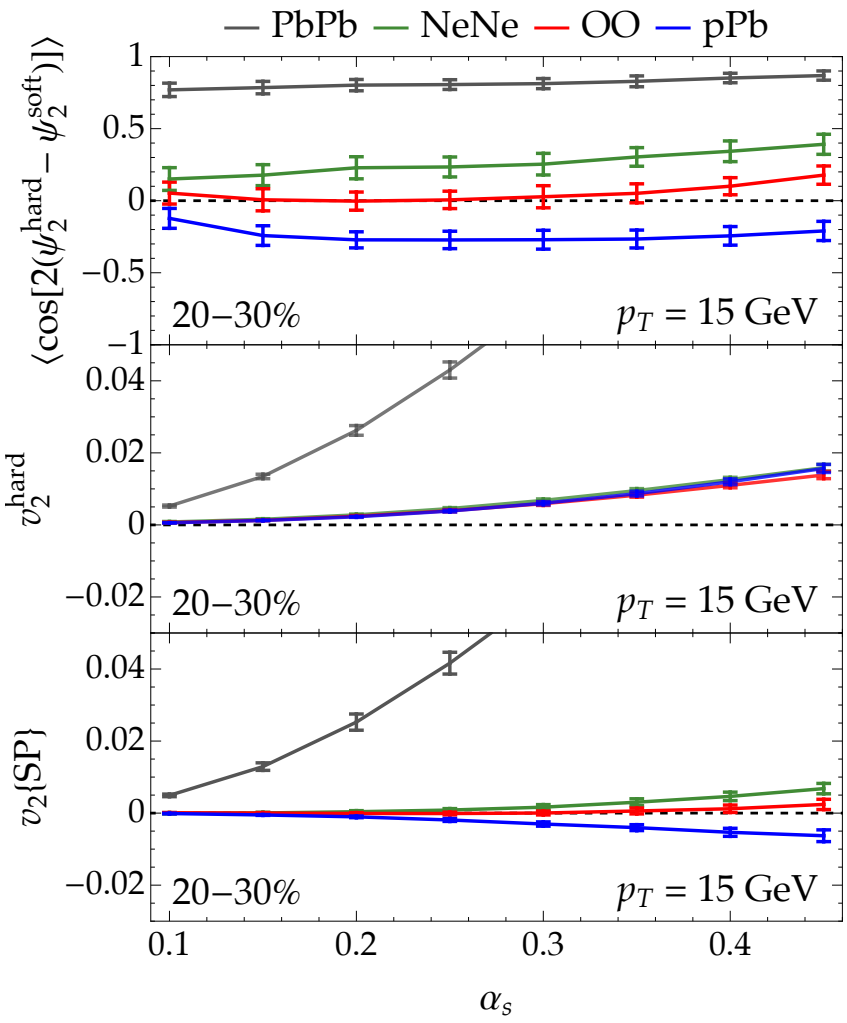

Figure 3.38: Dependence on the effective strong coupling α_s of the event-averaged $\cos(2[\psi_2^{\rm hard}-\psi_2^{\rm soft}])$ (top), $v_2^{\rm hard}$ (middle), and $v_2\{\rm SP\}$ (bottom) for $\rm Pb+Pb$ (gray), $\rm Ne+Ne$ (green), $\rm O+O$ (red), and $p+\rm Pb$ (blue) collision systems. All results are shown for 20-30% centrality at fixed $p_T = 15$ GeV with $|\mathbf{k}|_{\rm max}$ multiplier set to 1. Statistical uncertainties are indicated by error bars.

R_{AB} and v_n are computed within the energy loss formalism, adopting a procedure in which the v_n is calculated by coupling the hard-sector azimuthal anisotropy to the soft-sector participant plane in a manner that mirrors the procedure used in experiment. A comprehensive statistical analysis was performed to calibrate the model against large system high-p_T R_{AA} and v_2 data from RHIC and the LHC, and the resulting constrained model was then used to make predictions for small collision systems.

One of the findings of the CTv2.0 model is that replacing the static effective medium approximation of the CTv1.0 model [146, 155, 159, 163, 171] with a full dynamic treatment of the hydrodynamic evolution leads to a systematic increase in the predicted

energy loss. However, the increase of energy loss does not lead to a change in the suppression predicted by the model, as the increase in energy loss is compensated by a corresponding decrease in the effective strong coupling α_s^{eff} extracted from the calibration to large system data.

The CTv2.0 model was designed to provide a sophisticated calculation of the energy loss of a hard parton moving through a hydrodynamically evolving medium on an event-by-event basis using a pQCD formalism. The most straightforward approach would have been to use the hydrodynamic background directly in the energy-loss calculation; however, this approach is computationally intractable. Instead, in this chapter, we parametrized the effects of the medium density and the path length associated with each trajectory, thereby reducing the computational time of the energy loss by roughly seven orders of magnitude. As demonstrated in Sec. 3.2.4, evaluating the energy loss using the parametrized approach reproduces the results obtained with the full hydrodynamic temperature profile to a high degree of accuracy.

By performing a χ^2 minimization against high-p_T experimental data, we extracted an effective strong coupling constant of $\alpha_s^{\text{eff}} = 0.30^{+0.06}_{-0.06}$ and a corresponding jet transport coefficient $\hat{q}/T^3 = 7^{+3}_{-3}$ from LHC large system R_{AA} & v_2 data. Additionally, when performing a χ^2 minimization against high-p_T experimental R_{AA} data from RHIC, an effective strong coupling constant of $\alpha_s^{\text{eff}} = 0.37^{+0.08}_{-0.08}$ was extracted; a larger value of α_s^{eff} at RHIC is consistent with the expectation that the effective coupling is larger at the lower medium temperatures reached at RHIC. A key finding of this calibration is that extractions performed using LHC-R_{AA} data alone and LHC-v_2 data alone yield mutually consistent values of α_s^{eff}, suggesting that our model coherently describes both observables within a single parameter set. However, when the extraction is performed using LHC v_3 data, a significantly smaller value of $\alpha_s^{\text{eff}} = 0.17^{+0.05}_{-0.05}$ is obtained. Since the uncertainties in the α_s^{eff} extraction across R_{AA}, v_2, and v_3 datasets are fully correlated, the discrepancy between the α_s^{eff} extractions indicates a possible tension which may arise from two sources: either there are important systematic effects that differ between v_2 and v_3 measurements, or our energy loss model is missing relevant physics that is necessary to describe v_3 in addition to R_{AA} and v_2.

The constrained model extrapolated to small collision systems successfully pre-

dicted minimum bias $R_{AA}(p_T)$ for both $\mathrm{Ne}+\mathrm{Ne}$ and $\mathrm{O}+\mathrm{O}$ collision systems. For minimum bias $p+\mathrm{Pb}$ collisions, our results were in qualitative agreement with the ALICE measurement of $R_{p\mathrm{Pb}} \lesssim 1$ [227], but were in disagreement with the measurements above unity reported by ATLAS [141] and CMS [77]. Additionally, our model was able to reproduce the PHENIX measurement [147] of $R_{d\mathrm{Au}}$ for all centrality classes; in particular the definite suppression measured in the 0-5% centrality class for $d+\mathrm{Au}$ collisions is in agreement with our model's prediction of $R_{d\mathrm{Au}} < 1$. The measured suppression in $d+\mathrm{Au}$ is in stark contrast to the definite enhancement measured in the 0-5% centrality class for $p+\mathrm{Pb}$ collisions by ATLAS [141]. The qualitative disagreement between $R_{d\mathrm{Au}}$ and $R_{p\mathrm{Pb}}$ measurements is suggestive of non-trivial subtleties that arise in the measurement of hadron spectra from asymmetric small systems; for instance, selection biases may be present in the determination of N_{coll} from the Glauber model in asymmetric small systems, as proposed by [147, 237, 246–249].

Our central finding was that across all small collision systems, centrality classes, and p_T considered, the model yielded $v_2^{\mathrm{hard}} \lesssim 0.01$ and $-0.005 \lesssim v_2\{\mathrm{SP}\} \lesssim 0.005$, with the scalar-product v_2 being consistent with zero. Our model's predictions are thus in strong disagreement with the positive $v_2\{\mathrm{SP}\}$ reported in $p+\mathrm{Pb}$ by ATLAS [148], ALICE [149], and CMS [150]. The model's prediction of vanishing of $v_2\{\mathrm{SP}\}$ in small systems was traced to a decorrelation between the hard-sector and soft-sector participant plane angles ψ_2^{hard} and ψ_2^{soft}. In $\mathrm{Pb}+\mathrm{Pb}$ collisions, ψ_2^{hard} and ψ_2^{soft} are strongly correlated. However, in small systems ψ_2^{hard} and ψ_2^{soft} are weakly correlated ($\mathrm{Ne}+\mathrm{Ne}$), decorrelated ($\mathrm{O}+\mathrm{O}$) and mildly anti-correlated ($p+\mathrm{Pb}$). Importantly, this decorrelation was found to be largely insensitive to the value of the effective coupling, suggesting that the prediction $v_2\{\mathrm{SP}\} \approx 0$ is a robust feature of final-state energy loss models rather than an artifact of our specific implementation. We therefore expect this result to hold generically across similar final state energy loss frameworks for both symmetric and asymmetric small collision systems.

In light of the prediction of $v_2\{\mathrm{SP}\} \approx 0$ for small systems from any final state energy loss model, if the positive $v_2\{\mathrm{SP}\}$ observed in $p+\mathrm{Pb}$ [148–150] is not attributable to final-state energy loss, its origin must lie elsewhere. Simple parameter tuning within an energy loss framework is unlikely to resolve the discrepancy, pointing instead to

the need for additional physical mechanisms. Possible candidates include sub-eikonal corrections [250–253], though these are expected to be small and to diminish with increasing p_T. An additional possible source of missing relevant physics is the treatment of pre-thermalization time energy loss [158, 254–256], which becomes more relevant as the system size decreases. However, despite the increase in the importance of energy loss at early times in small systems, we do not expect the inclusion of early time energy loss to change our prediction that $v_2\{\mathrm{SP}\} \approx 0$ holds robustly across energy loss models, since excluding energy loss before thermalization has been shown to increase the high-p_T v_2 [219, 257–259]. One can get a qualitative feel for why excluding early time energy loss enhances high-p_T v_2 by thinking of drilling a hole of radius τ_0 in the middle of a collision: the presence of this hole enhances the relative size difference between the major and minor axis of the geometry. Another potentially important physical effect that is missing is a possible initial state correlation between the geometry and the initial direction of propagation of the hard particle [260–265]. A promising future direction of work is to investigate soft-hard production within one theoretical framework [266, 267].

On the theoretical side, a worthwhile future direction would be to examine whether correlations exist between ψ_2^{hard} and ψ_n^{soft} for $n \neq 2$. Given the orthogonality of different Fourier modes, such correlations would be surprising, but if present they could offer a novel experimental handle for extracting high-p_T v_2 in small systems.

Several experimental directions would be particularly valuable in testing the picture developed here. A measurement of $v_2\{2\}$ with both particles at high-p_T—while statistically challenging—would circumvent the hard-soft decorrelation that suppresses $v_2\{\mathrm{SP}\}$ in our model. A mass-dependent study of high-p_T v_2 would provide an important test of whether the anisotropy has a partonic origin. A measurement of electroweak boson v_2 in small systems, analogous to the CMS Z-boson measurement in $\mathrm{Pb}+\mathrm{Pb}$ [268], would offer a valuable initial-state baseline. Regarding the CMS measurement [150] of high-p_T v_2 in $p+\mathrm{Pb}$ using four-particle correlations with four subevents—which yields a value comparable in magnitude to that in $\mathrm{Pb}+\mathrm{Pb}$ and a factor of four larger than the two-particle measurements by ATLAS and ALICE [148, 149]—an independent confirmation from ATLAS and/or ALICE would be extremely in-

formative. Additionally, a measurement of high-p_T v_2 in $d + \mathrm{Au}$ at the LHC would provide an important comparison to the asymmetric small system $p + \mathrm{Pb}$ results of $0 < v_2^{p\mathrm{Pb}}\{SP\} \ll v_2^{p\mathrm{Pb}}\{4\}$.

Most valuable of all would be a full experimental analysis of high-p_T v_2 in $\mathrm{Ne} + \mathrm{Ne}$ and $\mathrm{O} + \mathrm{O}$ collisions. As of the time of this writing, there exists low-p_T measurements [160, 161] and preliminary high-p_T measurements [162] of v_2 in these small collision systems. A smooth extrapolation of the low-p_T anisotropy measurements [160, 161] into the high-p_T sector yields a $v_2 \simeq 0.05$, which is consistent with the preliminary high-p_T data [162]. If the v_2 in $\mathrm{Ne} + \mathrm{Ne}$ and $\mathrm{O} + \mathrm{O}$ collisions is indeed found to be large and positive, this result, combined with the large v_2 already observed in $p + \mathrm{Pb}$ collisions [148–150], would indicate that the mechanism driving the measured anisotropy in small systems is not unique to asymmetric collisions, and that the origin of this anisotropy must be something other than final-state energy loss.

Chapter 4

Conclusions and Outlook

Quantum Chromodynamics represents the culmination of over two-thousand years of humanity's curiosity concerning the fundamental constituents of matter. QCD has cemented the existence of quarks and gluons as being on par with matter's most fundamental degrees of freedom currently known, and its predictions have been undeniably confirmed by experiment.

Despite the success of QCD, the theory remains, in several important respects, an incompletely understood description of Nature. For example: a derivation of colour confinement directly from first principles [269–271] and an establishment on analytical grounds of the existence of the Yang–Mills mass gap [272] are currently unsolved problems. This thesis addresses two more tractable open problems in QCD. The first concerns the non-holonomic gauges routinely used in QCD, whose mathematical subtleties have largely been overlooked. The second concerns the many-body phenomenology of QCD matter, which remains rich and only partially understood, especially in small systems.

The principal results of this thesis provide clear insight into both of these problems. Chapter 2 demonstrates that the variational procedure underlying standard gauge fixing is indeed valid for the standard gauges used in the literature. Chapter 3 shows that final-state energy loss cannot be the source of observed anisotropy in the hadron spectra of small collision systems.

More specifically, Chapter 2 revisited the derivation of the Euler-Lagrange equations for classical field theories subject to non-holonomic constraints, constraints that depend on derivatives of the fields. Motivated by Flannery's point-particle result that the transposition rule $\delta(\dot{q}^i) = \frac{d}{dt}(\delta q^i)$ fails for general non-holonomic constraints [39], we developed a functional formalism sufficient to ask the analogous question in a classical field theory context; *i.e.* does $\delta(\partial_\nu A^\mu) = \partial_\nu(\delta A^\mu)$ hold for non-holonomic gauge constraints? We showed that the transposition rule does survive in classical field theory for the class of constraints we defined as *integrable non-holonomic constraints*—a class that includes the Coulomb and Lorenz gauges, but excludes gauges such as the 't Hooft-Veltman gauge. Our proof that the transposition rule holds for integrable non-holonomic constraints places the standard treatment of gauge-fixing for the Coulomb and Lorenz gauges on a rigorous footing for the first time, while identifying the naïve use of non-integrable gauges as potentially leading to incorrect physics.

Chapter 3 developed the CTv2.0 pQCD energy-loss model which incorporates finite path-length corrections appropriate for small collision systems and computes high-p_T R_{AB} and v_n by propagating high-p_T partons through a hydrodynamic medium on an event-by-event basis. Calibrated to large-system RHIC and LHC data, the model simultaneously and quantitatively describes R_{AA} and v_2 across a wide range of p_T and centrality, and its extrapolation to $\mathrm{Ne} + \mathrm{Ne}$ and $\mathrm{O} + \mathrm{O}$ correctly predicts the observed suppression of charged-particle yields [153, 154, 244]. The central result of this chapter showed that across every small collision system, symmetric or asymmetric, the model predicts $v_2\{\mathrm{SP}\} \approx 0$, in direct conflict with the large and positive v_2 measured in small systems [148–150, 162]. We traced this result to a geometric decorrelation between the participant planes of the hard and soft sectors in small systems, and argued that the decorrelation—and hence the vanishing of v_2—is a generic prediction of *any* final-state energy-loss model.

The two studies presented in this thesis naturally suggest distinct directions for future investigation. In Chapter 2, we argued that the transposition rule will likely fail for general non-integrable non-holonomic gauges such as the 't Hooft–Veltman gauge. We expect that the naïve use of these general gauges would lead to the field-theoretic analogue of the (physically incorrect) vakonomic equations of motion that

arise in non-holonomic point-particle mechanics. However, preliminary investigations suggest that, in the context of classical electromagnetism, the correct $\vec{E}$ and $\vec{B}$ fields can be derived from general non-holonomic gauges [127]. Understanding why a seemingly incorrect gauge-fixing procedure nevertheless reproduces the correct physical fields remains an open and curious problem.

In Chapter 3, we showed that the vanishing of high-p_T v_2 in small collision systems is a robust consequence of final-state energy-loss models, implying that the large and positive anisotropy observed experimentally in small collision systems must originate from sources different to path-length dependent energy loss. Two possible sources of the large high-p_T v_2 include: sub-eikonal corrections [250–253] and a possible initial-state correlation between the geometry and the initial direction of propagation of the hard parton [260–265].

In conclusion, if one is to accept QCD's status as one of humanity's most fundamental theories of nature, we must at minimum demand that it satisfy both mathematical consistency and experimental verification. This thesis confronts exactly these two demands: it establishes the consistency and clarifies the domain of validity of QCD's formal machinery, while showing that our understanding of emergent QCD matter both remains incomplete.

Bibliography

[1] G. S. Kirk, J. E. Raven, and M. Schofield, *The Presocratic Philosophers: A Critical History with a Selection of Texts*, 2nd ed. (Cambridge University Press, 1983).

[2] C. Taylor, *The Atomists: Leucippus and Democritus: Fragments* (University of Toronto Press, 1999).

[3] A. Pyle, *Atomism and its Critics: Problem Areas Associated with the Development of the Atomic Theory of Matter from Democritus to Newton* (Thoemmes Press, Bristol, 1995).

[4] A. de Lavoisier, *Traité élémentaire de chimie*, Traité élémentaire de chimie No. v. 1 (Déterville, 1801).

[5] J. Dalton, *A New System of Chemical Philosophy*, Cambridge Library Collection - Physical Sciences (Cambridge University Press, 2010).

[6] D. I. Mendeleev, Zeitschrift für Chemie **12**, 405 (1869).

[7] J. J. Thomson, Phil. Mag. **44**, 293 (1897).

[8] A. Einstein, Annalen der Physik **322**, 549 (1905).

[9] E. Rutherford, Phil. Mag. Ser. 6 **21**, 669 (1911).

[10] N. Bohr, Phil. Mag. Ser. 6 **26**, 1 (1913).

[11] W. Heisenberg, Z. Phys. **33**, 879 (1925).

[12] P. A. M. Dirac, Proc. Roy. Soc. Lond. A **109**, 642 (1925).

[13] W. Pauli, Z. Phys. **31**, 765 (1925).

[14] E. Schrödinger, Annalen Phys. **384**, 361 (1926).

[15] J. Chadwick, Nature **129**, 312 (1932).

[16] G. D. Rochester and C. C. Butler, Nature **160**, 855 (1947).

[17] V. E. Barnes *et al.*, Phys. Rev. Lett. **12**, 204 (1964).

[18] M. Gell-Mann, Phys. Lett. **8**, 214 (1964).

[19] G. Zweig, "An SU(3) model for strong interaction symmetry and its breaking. Version 2," in *DEVELOPMENTS IN THE QUARK THEORY OF HADRONS. VOL. 1. 1964 - 1978*, edited by D. B. Lichtenberg and S. P. Rosen (1964) pp. 22–101.

[20] M. Gell-Mann, *The Quark and the Jaguar: Adventures in the Simple and the Complex* (W. H. Freeman and Company, New York, 1994).

[21] J. Joyce, *Finnegans Wake* (Faber and Faber, London, 1939).

[22] E. D. Bloom *et al.*, Phys. Rev. Lett. **23**, 930 (1969).

[23] M. Breidenbach, J. I. Friedman, H. W. Kendall, E. D. Bloom, D. H. Coward, H. C. DeStaebler, J. Drees, L. W. Mo, and R. E. Taylor, Phys. Rev. Lett. **23**, 935 (1969).

[24] J. D. Bjorken and E. A. Paschos, Phys. Rev. **185**, 1975 (1969).

[25] R. P. Feynman, Phys. Rev. Lett. **23**, 1415 (1969).

[26] D. J. Gross and F. Wilczek, Phys. Rev. Lett. **30**, 1343 (1973).

[27] H. D. Politzer, Phys. Rev. Lett. **30**, 1346 (1973).

[28] S. L. Glashow, Nucl. Phys. **22**, 579 (1961).

[29] S. Weinberg, Phys. Rev. Lett. **19**, 1264 (1967).

[30] A. Salam, Conf. Proc. C **680519**, 367 (1968).

[31] F. J. Ynduráin, *Quantum Chromodynamics: An Introduction to the Theory of Quarks and Gluons*, Texts and Monographs in Physics (Springer-Verlag, New York, 1983).

[32] R. K. Ellis, W. J. Stirling, and B. R. Webber, *QCD and collider physics*, Vol. 8 (Cambridge University Press, 2011).

[33] F. Takahashi *et al.* (Particle Data Group), Int. J. Mod. Phys. A **41**, 2630011 (2026).

[34] G. Sterman and S. Weinberg, Phys. Rev. Lett. **39**, 1436 (1977).

[35] G. Hanson *et al.*, Phys. Rev. Lett. **35**, 1609 (1975).

[36] J. D. Jackson, *Classical Electrodynamics* (Wiley, 1998).

[37] J. D. Jackson and L. B. Okun, Rev. Mod. Phys. **73**, 663 (2001), arXiv:hep-ph/0012061.

[38] A. Zangwill, *Modern electrodynamics* (Cambridge Univ. Press, Cambridge, 2013).

[39] M. R. Flannery, Journal of Mathematical Physics **52**, 032705 (2011).

[40] W. R. Hamilton, Philosophical Transactions of the Royal Society of London **124**, 247 (1834).

[41] A. D. Lewis and R. M. Murray, International Journal of Non-Linear Mechanics **30**, 793 (1995).

[42] L. H. Ryder, *Quantum Field Theory*, 2nd ed. (Cambridge University Press, 1996).

[43] J. C. Collins and M. J. Perry, Phys. Rev. Lett. **34**, 1353 (1975).

[44] E. W. Kolb and M. S. Turner, *The Early Universe*, Vol. 69 (Taylor and Francis, 2019).

[45] J. W. Harris and B. Muller, Ann. Rev. Nucl. Part. Sci. **46**, 71 (1996), arXiv:hep-ph/9602235.

[46] W. Busza, K. Rajagopal, and W. van der Schee, Ann. Rev. Nucl. Part. Sci. **68**, 339 (2018), arXiv:1802.04801 [hep-ph].

[47] R. Pasechnik and M. Šumbera, Universe **3**, 7 (2017), arXiv:1611.01533 [hep-ph].

[48] T. Niida and Y. Miake, AAPPS Bull. **31**, 12 (2021), arXiv:2104.11406 [nucl-ex].

[49] J. W. Harris and B. Müller, Eur. Phys. J. C **84**, 247 (2024), arXiv:2308.05743 [hep-ph].

[50] S. Brandstetter *et al.*, Nature Phys. **21**, 52 (2025), arXiv:2308.09699 [cond-mat.quant-gas].

[51] G. Aad *et al.* (ATLAS), Phys. Rev. Lett. **110**, 182302 (2013), arXiv:1212.5198 [hep-ex].

[52] G. Aad *et al.* (ATLAS), Phys. Lett. B **725**, 60 (2013), arXiv:1303.2084 [hep-ex].

[53] B. B. Abelev *et al.* (ALICE), Phys. Rev. C **90**, 054901 (2014), arXiv:1406.2474 [nucl-ex].

[54] V. Khachatryan *et al.* (CMS), Phys. Rev. Lett. **115**, 012301 (2015), arXiv:1502.05382 [nucl-ex].

[55] J. L. Nagle and W. A. Zajc, Ann. Rev. Nucl. Part. Sci. **68**, 211 (2018), arXiv:1801.03477 [nucl-ex].

[56] P. Huovinen and P. V. Ruuskanen, Ann. Rev. Nucl. Part. Sci. **56**, 163 (2006), arXiv:nucl-th/0605008.

[57] P. Huovinen, Int. J. Mod. Phys. E **22**, 1330029 (2013), arXiv:1311.1849 [nucl-th].

[58] S. Jeon and U. Heinz, Int. J. Mod. Phys. E **24**, 1530010 (2015), arXiv:1503.03931 [hep-ph].

[59] R. Derradi de Souza, T. Koide, and T. Kodama, Prog. Part. Nucl. Phys. **86**, 35 (2016), arXiv:1506.03863 [nucl-th].

[60] A. Jaiswal and V. Roy, Adv. High Energy Phys. **2016**, 9623034 (2016), arXiv:1605.08694 [nucl-th].

[61] C. Shen and L. Yan, Nucl. Sci. Tech. **31**, 122 (2020), arXiv:2010.12377 [nucl-th].

[62] M. Gyulassy and L. McLerran, Nucl. Phys. A **750**, 30 (2005), arXiv:nucl-th/0405013.

[63] L. Apolinário, Y.-J. Lee, and M. Winn, Prog. Part. Nucl. Phys. **127**, 103990 (2022), arXiv:2203.16352 [hep-ph].

[64] X.-N. Wang and U. A. Wiedemann, "QGP@50: More than Four Decades of Jet Quenching," (2025), arXiv:2508.18794 [hep-ph].

[65] M. Cacciari, S. Frixione, and P. Nason, JHEP **03**, 006 (2001), arXiv:hep-ph/0102134.

[66] I. Vitev and M. Gyulassy, Phys. Rev. Lett. **89**, 252301 (2002), arXiv:hep-ph/0209161.

[67] G.-Y. Qin and X.-N. Wang, Int. J. Mod. Phys. E **24**, 1530014 (2015), arXiv:1511.00790 [hep-ph].

[68] E. Braaten and M. H. Thoma, Phys. Rev. D **44**, 1298 (1991).

[69] E. Braaten and M. H. Thoma, Phys. Rev. D **44**, R2625 (1991).

[70] M. Gyulassy, P. Levai, and I. Vitev, Nucl. Phys. B **594**, 371 (2001), arXiv:nucl-th/0006010.

[71] M. Djordjevic and M. Gyulassy, Nucl. Phys. A **733**, 265 (2004), arXiv:nucl-th/0310076.

[72] S. Cao and X.-N. Wang, Rept. Prog. Phys. **84**, 024301 (2021), arXiv:2002.04028 [hep-ph].

[73] J. D. Bjorken, *Energy Loss of Energetic Partons in Quark-Gluon Plasma: Possible Extinction of High p_T Jets in Hadron-Hadron Collisions*, Tech. Rep. FERMILAB-Pub-82/59-THY (Fermi National Accelerator Laboratory, Batavia, IL, USA, 1982).

[74] K. Aamodt *et al.* (ALICE), Phys. Lett. B **696**, 30 (2011), arXiv:1012.1004 [nucl-ex].

[75] S. Chatrchyan *et al.* (CMS), Eur. Phys. J. C **72**, 1945 (2012), arXiv:1202.2554 [nucl-ex].

[76] G. Aad *et al.* (ATLAS), JHEP **09**, 050 (2015), arXiv:1504.04337 [hep-ex].

[77] V. Khachatryan *et al.* (CMS), JHEP **04**, 039 (2017), arXiv:1611.01664 [nucl-ex].

[78] T. Isobe (PHENIX), AIP Conf. Proc. **842**, 56 (2006), arXiv:nucl-ex/0604016.

[79] R. Baier, Y. L. Dokshitzer, A. H. Mueller, S. Peigne, and D. Schiff, Nucl. Phys. B **483**, 291 (1997), arXiv:hep-ph/9607355.

[80] B. G. Zakharov, JETP Lett. **65**, 615 (1997), arXiv:hep-ph/9704255.

[81] M. Connors, C. Nattrass, R. Reed, and S. Salur, Rev. Mod. Phys. **90**, 025005 (2018), arXiv:1705.01974 [nucl-ex].

[82] S. Acharya *et al.* (ALICE), JHEP **09**, 006 (2018), arXiv:1805.04390 [nucl-ex].

[83] B. Betz and M. Gyulassy, JHEP **08**, 090 (2014), [Erratum: JHEP 10, 043 (2014)], arXiv:1404.6378 [hep-ph].

[84] J. Xu, J. Liao, and M. Gyulassy, Chin. Phys. Lett. **32**, 092501 (2015), arXiv:1411.3673 [hep-ph].

[85] J. Noronha-Hostler, B. Betz, J. Noronha, and M. Gyulassy, Phys. Rev. Lett. **116**, 252301 (2016), arXiv:1602.03788 [nucl-th].

[86] J. Xu, J. Liao, and M. Gyulassy, JHEP **02**, 169 (2016), arXiv:1508.00552 [hep-ph].

[87] D. Zigic, I. Salom, J. Auvinen, M. Djordjevic, and M. Djordjevic, Phys. Lett. B **791**, 236 (2019), arXiv:1805.04786 [nucl-th].

[88] W. Zhao, W. Ke, W. Chen, T. Luo, and X.-N. Wang, Phys. Rev. Lett. **128**, 022302 (2022), arXiv:2103.14657 [hep-ph].

[89] B. Bert and W. A. Horowitz, (2025), arXiv:2505.20684 [hep-th].

[90] B. Bert, C. Faraday, and W. A. Horowitz, (2026), arXiv:2603.21861 [hep-ph].

[91] C. R. Galley, Phys. Rev. Lett. **110**, 174301 (2013), arXiv:1210.2745 [gr-qc].

[92] A. Rothkopf and W. A. Horowitz, "A Unifying Action Principle for Classical Mechanical Systems," (2024), arXiv:2409.11063 [physics.class-ph].

[93] P. W. Higgs, Phys. Rev. Lett. **13**, 508 (1964).

[94] F. Englert and R. Brout, Phys. Rev. Lett. **13**, 321 (1964).

[95] G. S. Guralnik, C. R. Hagen, and T. W. B. Kibble, Phys. Rev. Lett. **13**, 585 (1964).

[96] P. A. M. Dirac, *Lectures on Quantum Mechanics* (Yeshiva University, New York, 1964).

[97] M. Bohm, A. Denner, and H. Joos, *Gauge theories of the strong and electroweak interaction* (Springer, 2001).

[98] M. Henneaux and C. Teitelboim, *Quantization of Gauge Systems* (Princeton University Press in association with the Centro de Estudios Cientificos de Santiago, 1992).

[99] M. E. Peskin and D. V. Schroeder, *An Introduction to Quantum Field Theory* (Addison-Wesley, Reading, USA, 1995).

[100] S. Weinberg, *The Quantum Theory of Fields, Volume 1* (Cambridge University Press, 1995).

[101] S. Weinberg, *The Quantum Theory of Fields, Volume 2* (Cambridge University Press, 1996).

[102] A. Zee, *Quantum field theory in a nutshell* (Princeton University Press, 2003).

[103] M. Srednicki, *Quantum Field Theory* (Cambridge University Press, 2007).

[104] S. Coleman, *Lectures of Sidney Coleman on Quantum Field Theory* (WSP, Hackensack, 2018).

[105] J. Koplik, Nucl. Phys. B **146**, 413 (1978).

[106] R. B. Mann, G. Mckeon, and S. Phillips, Can. J. Phys. **62**, 1129 (1984).

[107] G. Mckeon, S. B. Phillips, S. S. Samant, and T. N. Sherry, Can. J. Phys. **63**, 1343 (1985).

[108] R. Parthasarathy, J. Phys. A **21**, 4593 (1988).

[109] J. A. Gracey, JHEP **04**, 012 (2005), arXiv:hep-th/0504051.

[110] J. A. Gracey, J. Phys. A **40**, 13989 (2007), arXiv:0710.1260 [hep-th].

[111] G. B. de Gracia, B. M. Pimentel, and L. Rabanal, Nucl. Phys. B **948**, 114750 (2019).

[112] D. T. Tran and K. H. Phan, Chin. Phys. C **47**, 053106 (2023), arXiv:2211.15116 [hep-ph].

[113] K. H. Phan, D. T. Tran, and A. T. Nguyen, Commun. in Phys. **33**, 235 (2023), arXiv:2305.04009 [hep-ph].

[114] W. Greiner and J. Reinhardt, *Field Quantization*, Classical Theoretical Physics (Springer, 1996).

[115] F. G. Friedlander and M. S. Joshi, *Introduction to the Theory of Distributions*, 2nd ed. (Cambridge University Press, Cambridge, 1998).

[116] E. Engel and R. M. Dreizler, *Density Functional Theory: An Advanced Course*, Theoretical and Mathematical Physics (Springer, 2011).

[117] W. Cheney, *Analysis for Applied Mathematics*, 2nd ed. (Springer, New York, 2001).

[118] R. Gâteaux, Comptes Rendus de l'Académie des Sciences, Paris **157**, 325 (1913).

[119] D. Dugger and P. J. Lambert, The Journal of Economic Inequality **12**, 149 (2014).

[120] H. Goldstein, *Classical Mechanics* (Addison-Wesley, 1980).

[121] J. Taylor, *Classical Mechanics* (University Science Books, 2005).

[122] A. M. Bloch, *Nonholonomic Mechanics and Control*, 2nd ed., Interdisciplinary Applied Mathematics, Vol. 24 (Springer-Verlag New York, 2015).

[123] I. M. Gelfand and S. V. Fomin, *Calculus of Variations* (Dover Publications, Mineola, NY, 2000) translated and edited by Richard A. Silverman. Originally published in 1963 by Prentice-Hall.

[124] J. Cortés, M. de León, D. M. de Diego, and S. Martínez, SIAM Journal on Control and Optimization **41**, 1389 (2002), https://doi.org/10.1137/S036301290036817X.

[125] J. Gaset, M. Lainz, A. Mas, and X. Rivas, Geom. Mech. **01**, 153 (2024), arXiv:2211.17058 [math-ph].

[126] F. Talamucci, "On the transpositional relation for nonholonomic systems," (2025), arXiv:2506.15729 [physics.class-ph].

[127] B. Bert, A. Rothkopf, and W. A. Horowitz, (2026), in preparation.

[128] W. A. Horowitz and A. Rothkopf, (2024), arXiv:2408.14420 [math-ph].

[129] K. H. Ackermann *et al.* (STAR), Phys. Rev. Lett. **86**, 402 (2001), arXiv:nucl-ex/0009011.

[130] C. Adler *et al.* (STAR), Phys. Rev. C **66**, 034904 (2002), arXiv:nucl-ex/0206001.

[131] K. Aamodt *et al.* (ALICE), Phys. Rev. Lett. **105**, 252302 (2010), arXiv:1011.3914 [nucl-ex].

[132] J. Rafelski and B. Muller, Phys. Rev. Lett. **48**, 1066 (1982), [Erratum: Phys.Rev.Lett. 56, 2334 (1986)].

[133] J. Adams *et al.* (STAR), Phys. Rev. Lett. **92**, 182301 (2004), arXiv:nucl-ex/0307024.

[134] B. B. Abelev *et al.* (ALICE), Phys. Lett. B **728**, 216 (2014), [Erratum: Phys.Lett.B 734, 409–410 (2014)], arXiv:1307.5543 [nucl-ex].

[135] T. Matsui and H. Satz, Phys. Lett. B **178**, 416 (1986).

[136] S. Chatrchyan *et al.* (CMS), JHEP **05**, 063 (2012), arXiv:1201.5069 [nucl-ex].

[137] B. Abelev *et al.* (ALICE), Phys. Rev. Lett. **109**, 072301 (2012), arXiv:1202.1383 [hep-ex].

[138] B. B. Abelev *et al.* (ALICE), Phys. Lett. B **728**, 25 (2014), arXiv:1307.6796 [nucl-ex].

[139] J. Adam *et al.* (ALICE), Phys. Lett. B **758**, 389 (2016), arXiv:1512.07227 [nucl-ex].

[140] J. Adam *et al.* (ALICE), JHEP **06**, 050 (2016), arXiv:1603.02816 [nucl-ex].

[141] G. Aad *et al.* (ATLAS), JHEP **07**, 074 (2023), arXiv:2211.15257 [hep-ex].

[142] S. Acharya *et al.* (ALICE), Phys. Lett. B **827**, 136943 (2022), arXiv:2104.03116 [nucl-ex].

[143] X. Zhang and J. Liao, (2013), arXiv:1311.5463 [nucl-th].

[144] Z.-B. Kang, I. Vitev, and H. Xing, Phys. Rev. C **92**, 054911 (2015), arXiv:1507.05987 [hep-ph].

[145] W. Ke and I. Vitev, Phys. Rev. C **107**, 064903 (2023), arXiv:2204.00634 [hep-ph].

[146] C. Faraday and W. A. Horowitz, Phys. Lett. B **864**, 139437 (2025), arXiv:2411.09647 [hep-ph].

[147] N. J. Abdulameer *et al.* (PHENIX), Phys. Rev. Lett. **134**, 022302 (2025), arXiv:2303.12899 [nucl-ex].

[148] G. Aad *et al.* (ATLAS), Eur. Phys. J. C **80**, 73 (2020), arXiv:1910.13978 [nucl-ex].

[149] S. Acharya *et al.* (ALICE), JHEP **08**, 234 (2024), arXiv:2212.12609 [nucl-ex].

[150] V. Chekhovsky *et al.* (CMS), Phys. Rev. Lett. **135**, 071903 (2025), arXiv:2502.07525 [nucl-ex].

[151] A. Huss, A. Kurkela, A. Mazeliauskas, R. Paatelainen, W. van der Schee, and U. A. Wiedemann, Phys. Rev. C **103**, 054903 (2021), arXiv:2007.13758 [hep-ph].

[152] J. Brewer, A. Mazeliauskas, and W. van der Schee, in *Opportunities of OO and pO collisions at the LHC* (2021) arXiv:2103.01939 [hep-ph].

[153] A. Hayrapetyan *et al.* (CMS), (2025), arXiv:2510.09864 [nucl-ex].

[154] ALICE Collaboration, "ALI-PREL-617876," https://alice-figure.web.cern.ch/node/35718 (2024).

[155] C. Faraday and W. A. Horowitz, JHEP **11**, 019 (2025), arXiv:2505.14568 [hep-ph].

[156] W. van der Schee, I. Kolbé, G. Nijs, K. Ruhani, I. Ahmed, and S. Iqbal, "Three models for charged hadron nuclear modification from light to heavy ions," (2025), arXiv:2509.04299 [nucl-th].

[157] B. G. Zakharov, Pisma Zh. Eksp. Teor. Fiz. **122**, 437 (2025), arXiv:2509.07741 [hep-ph].

[158] D. Pablos and A. Takacs, "Bayesian Constraints on Pre-Equilibrium Jet Quenching and Predictions for Oxygen Collisions," (2025), arXiv:2509.19430 [hep-ph].

[159] C. Faraday, B. Bert, J. Brand, W. Vogelsang, and W. A. Horowitz, (2025), arXiv:2512.17832 [hep-ph].

[160] A. Hayrapetyan *et al.* (CMS), (2025), arXiv:2510.02580 [nucl-ex].

[161] G. Aad *et al.* (ATLAS), Phys. Rev. C **113**, 045205 (2026), arXiv:2509.05171 [nucl-ex].

[162] S. Tuo (CMS), "Azimuthal anisotropy of charged particles with transverse momentum up to 50 GeV in OO, NeNe, and PbPb collisions," Talk presented at Hard Probes 2026, Nashville, TN, 22–26 June 2026 (2026), cMS Collaboration.

[163] C. Faraday and W. A. Horowitz, Phys. Rev. C **111**, 054911 (2025), arXiv:2408.14426 [nucl-th].

[164] B. G. Zakharov, JETP Lett. **63**, 952 (1996), arXiv:hep-ph/9607440.

[165] R. Baier, Y. L. Dokshitzer, A. H. Mueller, S. Peigne, and D. Schiff, Nucl. Phys. B **484**, 265 (1997), arXiv:hep-ph/9608322.

[166] R. Baier, Y. L. Dokshitzer, A. H. Mueller, S. Peigne, and D. Schiff, Nucl. Phys. B **478**, 577 (1996), arXiv:hep-ph/9604327.

[167] R. Baier, Y. L. Dokshitzer, A. H. Mueller, and D. Schiff, Nucl. Phys. B **531**, 403 (1998), arXiv:hep-ph/9804212.

[168] S. Wicks, W. Horowitz, M. Djordjevic, and M. Gyulassy, Nucl. Phys. A **784**, 426 (2007), arXiv:nucl-th/0512076.

[169] G. D. Moore and D. Teaney, Phys. Rev. C **71**, 064904 (2005), arXiv:hep-ph/0412346.

[170] D. Zigic, I. Salom, J. Auvinen, P. Huovinen, and M. Djordjevic, Front. in Phys. **10**, 957019 (2022), arXiv:2110.01544 [nucl-th].

[171] C. Faraday, A. Grindrod, and W. A. Horowitz, Eur. Phys. J. C **83**, 1060 (2023), arXiv:2305.13182 [hep-ph].

[172] I. Kolbe and W. A. Horowitz, Phys. Rev. C **100**, 024913 (2019), arXiv:1511.09313 [hep-ph].

[173] I. Kolbe, *Short path length pQCD corrections to energy loss in the quark gluon plasma*, Master's thesis, Cape Town U. (2015), arXiv:1509.06122 [hep-ph].

[174] V. V. Klimov, Sov. Phys. JETP **55**, 199 (1982).

[175] H. A. Weldon, Phys. Rev. D **26**, 1394 (1982).

[176] H. A. Weldon, Phys. Rev. D **26**, 2789 (1982).

[177] R. D. Pisarski, Phys. Rev. Lett. **63**, 1129 (1989).

[178] E. Braaten and R. D. Pisarski, Nucl. Phys. B **337**, 569 (1990).

[179] S. Wicks, *Fluctuations with small numbers: Developing the perturbative paradigm for jet physics in the QGP at RHIC and LHC*, Other thesis, Columbia University (2008).

[180] T. Renk, Phys. Rev. C **85**, 044903 (2012), arXiv:1112.2503 [hep-ph].

[181] D. Molnar and D. Sun, Nucl. Phys. A **932**, 140 (2014), arXiv:1405.4848 [nucl-th].

[182] D. Zigic, I. Salom, J. Auvinen, M. Djordjevic, and M. Djordjevic, J. Phys. G **46**, 085101 (2019), arXiv:1805.03494 [nucl-th].

[183] J. Xu, A. Buzzatti, and M. Gyulassy, JHEP **08**, 063 (2014), arXiv:1402.2956 [hep-ph].

[184] M. Gyulassy, P. Levai, and I. Vitev, Nucl. Phys. B **571**, 197 (2000), arXiv:hep-ph/9907461.

[185] C. Shen, (2025), private communication.

[186] B. Schenke, P. Tribedy, and R. Venugopalan, Phys. Rev. C **86**, 034908 (2012), arXiv:1206.6805 [hep-ph].

[187] B. Schenke, P. Tribedy, and R. Venugopalan, Phys. Rev. Lett. **108**, 252301 (2012), arXiv:1202.6646 [nucl-th].

[188] B. Schenke, C. Shen, and P. Tribedy, Phys. Rev. C **102**, 044905 (2020), arXiv:2005.14682 [nucl-th].

[189] B. Schenke, S. Jeon, and C. Gale, Phys. Rev. Lett. **106**, 042301 (2011), arXiv:1009.3244 [hep-ph].

[190] B. Schenke, S. Jeon, and C. Gale, Phys. Rev. C **82**, 014903 (2010), arXiv:1004.1408 [hep-ph].

[191] B. Schenke, S. Jeon, and C. Gale, Phys. Rev. C **85**, 024901 (2012), arXiv:1109.6289 [hep-ph].

[192] S. A. Bass *et al.*, Prog. Part. Nucl. Phys. **41**, 255 (1998), arXiv:nucl-th/9803035.

[193] M. Bleicher *et al.*, J. Phys. G **25**, 1859 (1999), arXiv:hep-ph/9909407.

[194] W. A. Horowitz and B. A. Cole, Phys. Rev. C **81**, 024909 (2010), arXiv:0910.1823 [hep-ph].

[195] H. Clayton, M. D. Sievert, and W. A. Horowitz, Eur. Phys. J. C **82**, 437 (2022), arXiv:2110.14737 [hep-ph].

[196] W. A. Horowitz, *Probing the Frontiers of QCD*, Other thesis, Columbia University (2010), arXiv:1011.4316 [nucl-th].

[197] C. Faraday and W. A. Horowitz, in *67th Annual Conference of the South African Institute of Physics* (2023) arXiv:2309.06246 [hep-ph].

[198] M. Gyulassy, P. Levai, and I. Vitev, Phys. Lett. B **538**, 282 (2002), arXiv:nucl-th/0112071.

[199] C. Andres, L. Apolinário, F. Dominguez, and M. G. Martinez, JHEP **11**, 025 (2024), arXiv:2307.06226 [hep-ph].

[200] E. W. Weisstein, "Levenberg–marquardt method," MathWorld – A Wolfram Resource (2025), accessed: 2025-12-26.

[201] M. L. Miller, K. Reygers, S. J. Sanders, and P. Steinberg, Ann. Rev. Nucl. Part. Sci. **57**, 205 (2007), arXiv:nucl-ex/0701025.

[202] R. J. Glauber and G. Matthiae, Nucl. Phys. B **21**, 135 (1970).

[203] S. Chatrchyan *et al.* (CMS), Phys. Rev. Lett. **106**, 212301 (2011), arXiv:1102.5435 [nucl-ex].

[204] S. Chatrchyan *et al.* (CMS), Phys. Lett. B **710**, 256 (2012), arXiv:1201.3093 [nucl-ex].

[205] W. A. Horowitz and M. Gyulassy, Nucl. Phys. A **872**, 265 (2011), arXiv:1104.4958 [hep-ph].

[206] M. Cacciari, P. Nason, and C. Oleari, JHEP **04**, 006 (2006), arXiv:hep-ph/0510032.

[207] D. de Florian, R. Sassot, and M. Stratmann, Phys. Rev. D **75**, 114010 (2007), arXiv:hep-ph/0703242.

[208] B. B. Abelev *et al.* (ALICE), Phys. Rev. C **90**, 034904 (2014), arXiv:1405.2001 [nucl-ex].

[209] A. M. Sirunyan *et al.* (CMS), Phys. Rev. Lett. **120**, 202301 (2018), arXiv:1708.03497 [nucl-ex].

[210] A. M. Sirunyan *et al.* (CMS), Phys. Lett. B **776**, 195 (2018), arXiv:1702.00630 [hep-ex].

[211] M. Aaboud *et al.* (ATLAS), Eur. Phys. J. C **78**, 997 (2018), arXiv:1808.03951 [nucl-ex].

[212] M. Aaboud *et al.* (ATLAS), Phys. Rev. C **98**, 044905 (2018), arXiv:1805.05220 [nucl-ex].

[213] A. M. Sirunyan *et al.* (CMS), Phys. Lett. B **816**, 136253 (2021), arXiv:2009.12628 [hep-ex].

[214] A. Tumasyan *et al.* (CMS), Phys. Lett. B **850**, 138389 (2024), arXiv:2212.01636 [nucl-ex].

[215] G. Aad *et al.* (ATLAS), Phys. Rev. C **112**, 024910 (2025), arXiv:2412.15658 [nucl-ex].

[216] R. Snellings, New J. Phys. **13**, 055008 (2011), arXiv:1102.3010 [nucl-ex].

[217] M. Luzum and H. Petersen, J. Phys. G **41**, 063102 (2014), arXiv:1312.5503 [nucl-th].

[218] M. Luzum and J.-Y. Ollitrault, Phys. Rev. C **87**, 044907 (2013), arXiv:1209.2323 [nucl-ex].

[219] C. Andres, N. Armesto, H. Niemi, R. Paatelainen, and C. A. Salgado, Phys. Lett. B **803**, 135318 (2020), arXiv:1902.03231 [hep-ph].

[220] D. Zigic, J. Auvinen, I. Salom, M. Djordjevic, and P. Huovinen, Phys. Rev. C **106**, 044909 (2022), arXiv:2208.09886 [hep-ph].

[221] P. D. Group, Progress of Theoretical and Experimental Physics **2022**, 083C01 (2022), https://academic.oup.com/ptep/article-pdf/2022/8/083C01/49175539/ptac097.pdf.

[222] A. Adare *et al.* (PHENIX), Phys. Rev. C **87**, 034911 (2013), arXiv:1208.2254 [nucl-ex].

[223] A. Adare *et al.* (PHENIX), Phys. Rev. C **77**, 064907 (2008), arXiv:0801.1665 [nucl-ex].

[224] S. Cao *et al.* (JETSCAPE), Phys. Rev. C **104**, 024905 (2021), arXiv:2102.11337 [nucl-th].

[225] R. Ehlers *et al.* (JETSCAPE), Phys. Rev. C **111**, 054913 (2025), arXiv:2408.08247 [hep-ph].

[226] S. Acharya *et al.* (ALICE), JHEP **10**, 174 (2018), arXiv:1804.09083 [nucl-ex].

[227] S. Acharya *et al.* (ALICE), JHEP **11**, 013 (2018), arXiv:1802.09145 [nucl-ex].

[228] A. M. Sirunyan *et al.* (CMS), Phys. Lett. B **782**, 474 (2018), arXiv:1708.04962 [nucl-ex].

[229] S. Acharya *et al.* (ALICE), JHEP **07**, 103 (2018), arXiv:1804.02944 [nucl-ex].

[230] A. Adare *et al.* (PHENIX), Phys. Rev. Lett. **101**, 232301 (2008), arXiv:0801.4020 [nucl-ex].

[231] S. Acharya *et al.* (ALICE), Phys. Rev. C **101**, 044907 (2020), arXiv:1910.07678 [nucl-ex].

[232] S. Acharya *et al.* (ALICE), Phys. Rev. Lett. **120**, 102301 (2018), arXiv:1707.01005 [nucl-ex].

[233] S. Acharya *et al.* (ALICE), Eur. Phys. J. C **84**, 813 (2024), arXiv:2211.04384 [nucl-ex].

[234] A. Hayrapetyan *et al.* (CMS), Phys. Rept. **1115**, 219 (2025), arXiv:2405.10785 [nucl-ex].

[235] K. Adcox *et al.* (PHENIX), Nucl. Phys. A **757**, 184 (2005), arXiv:nucl-ex/0410003.

[236] J. Adams *et al.* (STAR), Nucl. Phys. A **757**, 102 (2005), arXiv:nucl-ex/0501009.

[237] S. Acharya *et al.* (ALICE), Phys. Lett. B **793**, 420 (2019), arXiv:1805.05212 [nucl-ex].

[238] K. M. Burke *et al.* (JET), Phys. Rev. C **90**, 014909 (2014), arXiv:1312.5003 [nucl-th].

[239] C. Andrés, N. Armesto, M. Luzum, C. A. Salgado, and P. Zurita, Eur. Phys. J. C **76**, 475 (2016), arXiv:1606.04837 [hep-ph].

[240] M. Xie, X.-N. Wang, and H.-Z. Zhang, Phys. Rev. C **103**, 034911 (2021), arXiv:2003.02441 [hep-ph].

[241] M. Xie, W. Ke, H. Zhang, and X.-N. Wang, Phys. Rev. C **108**, L011901 (2023), arXiv:2206.01340 [hep-ph].

[242] N. Armesto *et al.*, Phys. Rev. C **86**, 064904 (2012), arXiv:1106.1106 [hep-ph].

[243] R. Ehlers *et al.*, Phys. Rev. C **111**, 054913 (2025), arXiv:2408.08247 [hep-ph].

[244] A. Belyaev *et al.* (CMS), (2026), arXiv:2602.21325 [nucl-ex].

[245] J. Benesty, J. Chen, Y. Huang, and I. Cohen, "Pearson correlation coefficient," in *Noise Reduction in Speech Processing*, Springer Topics in Signal Processing (Springer, 2009).

[246] A. Bzdak, V. Skokov, and S. Bathe, Phys. Rev. C **93**, 044901 (2016), arXiv:1408.3156 [hep-ph].

[247] G. David, J. Phys. Conf. Ser. **589**, 012005 (2015), arXiv:1409.6788 [nucl-ex].

[248] M. Kordell and A. Majumder, Phys. Rev. C **97**, 054904 (2018), arXiv:1601.02595 [nucl-th].

[249] C. Loizides and A. Morsch, Phys. Lett. B **773**, 408 (2017), arXiv:1705.08856 [nucl-ex].

[250] N. Armesto, C. A. Salgado, and U. A. Wiedemann, Phys. Rev. Lett. **93**, 242301 (2004), arXiv:hep-ph/0405301.

[251] A. V. Sadofyev, M. D. Sievert, and I. Vitev, Phys. Rev. D **104**, 094044 (2021), arXiv:2104.09513 [hep-ph].

[252] Y. Fu, J. Casalderrey-Solana, and X.-N. Wang, Phys. Rev. D **107**, 054038 (2023), arXiv:2204.05323 [hep-ph].

[253] J. Bahder, H. Rahman, M. D. Sievert, and I. Vitev, Phys. Rev. Res. **8**, L012016 (2026), arXiv:2412.05474 [nucl-th].

[254] A. Kurkela, A. Mazeliauskas, J.-F. Paquet, S. Schlichting, and D. Teaney, Phys. Rev. C **99**, 034910 (2019), arXiv:1805.00961 [hep-ph].

[255] K. Boguslavski, A. Kurkela, T. Lappi, F. Lindenbauer, and J. Peuron, Phys. Lett. B **850**, 138525 (2024), arXiv:2303.12595 [hep-ph].

[256] S. P. Adhya and K. Tywoniuk, (2024), arXiv:2409.04295 [hep-ph].

[257] D. Zigic, B. Ilic, M. Djordjevic, and M. Djordjevic, Phys. Rev. C **101**, 064909 (2020), arXiv:1908.11866 [hep-ph].

[258] S. Stojku, J. Auvinen, M. Djordjevic, P. Huovinen, and M. Djordjevic, Phys. Rev. C **105**, L021901 (2022), arXiv:2008.08987 [nucl-th].

[259] C. Andres, L. Apolinário, F. Dominguez, M. G. Martinez, and C. A. Salgado, JHEP **03**, 189 (2023), arXiv:2211.10161 [hep-ph].

[260] K. Dusling and R. Venugopalan, Phys. Rev. D **87**, 094034 (2013), arXiv:1302.7018 [hep-ph].

[261] Y. Hagiwara, Y. Hatta, B.-W. Xiao, and F. Yuan, Phys. Lett. B **771**, 374 (2017), arXiv:1701.04254 [hep-ph].

[262] B. Blok, C. D. Jäkel, M. Strikman, and U. A. Wiedemann, JHEP **12**, 074 (2017), arXiv:1708.08241 [hep-ph].

[263] M. Mace, V. V. Skokov, P. Tribedy, and R. Venugopalan, Phys. Rev. Lett. **121**, 052301 (2018), [Erratum: Phys.Rev.Lett. 123, 039901 (2019)], arXiv:1805.09342 [hep-ph].

[264] I. Soudi and A. Majumder, Phys. Lett. B **859**, 139105 (2024), arXiv:2308.14702 [hep-ph].

[265] I. Soudi *et al.* (JETSCAPE), Phys. Rev. C **112**, 014905 (2025), arXiv:2407.17443 [hep-ph].

[266] E. Carrió and D. Pablos, (2026), arXiv:2603.12346 [hep-ph].

[267] C. Faraday, W. A. Horowitz, and B. Schenke, "Work in preparation," (2026).

[268] A. M. Sirunyan *et al.* (CMS), Phys. Rev. Lett. **127**, 102002 (2021), arXiv:2103.14089 [hep-ex].

[269] K. G. Wilson, Phys. Rev. D **10**, 2445 (1974).

[270] J. Greensite, Prog. Part. Nucl. Phys. **51**, 1 (2003), arXiv:hep-lat/0301023.

[271] J. Greensite, *An introduction to the confinement problem*, Vol. 821 (2011).

[272] A. M. Jaffe and E. Witten, "Quantum Yang-Mills theory," (2000).

[273] J. le Rond d'Alembert, *Traité de dynamique* (Paris, 1743).

[274] I. Newton, *Philosophiæ Naturalis Principia Mathematica* (Royal Society, London, 1687).

[275] T. M. Apostol, *Mathematical Analysis*, 2nd ed. (Addison-Wesley, Reading, Massachusetts, 1974).

[276] W. Rudin, *Principles of Mathematical Analysis*, 3rd ed. (McGraw-Hill, New York, 1976).

[277] B. Efron and R. J. Tibshirani, *An Introduction to the Bootstrap* (Chapman & Hall, New York, 1993).

[278] J. Adam *et al.* (ALICE), Phys. Rev. C **91**, 064905 (2015), arXiv:1412.6828 [nucl-ex].

[279] U. A. Acharya *et al.* (PHENIX), Phys. Rev. C **105**, 064902 (2022), arXiv:2111.05756 [nucl-ex].

[280] B. I. Abelev *et al.* (STAR), Phys. Rev. C **80**, 044905 (2009), arXiv:0907.2721 [nucl-ex].

[281] A. Adare *et al.* (PHENIX), Phys. Rev. C **92**, 034913 (2015), arXiv:1412.1043 [nucl-ex].

Appendix A

d'Alembert's Principle for Non-Holonomic Constraints

Here, we make use of d'Alembert's principle [120, 273] to derive the equations of motion for a system of N particles under the influence of M non-holonomic constraints.

Denote the M non-holonomic constraints as

$$g_k(\vec{r}_1, \ldots, \vec{r}_N, \dot{\vec{r}}_1, \ldots, \dot{\vec{r}}_N) = 0, \quad k = 1, \ldots, M, \tag{A.1}$$

where $\vec{r}_i$ and $\dot{\vec{r}}_i$ are the position and the velocity of the i^{th} particle in Cartesian coordinates, respectively. Now, the M non-holonomic constraints will each impose a force on the particles in the system; we shall denote the force coming from the constraints acting on particle i as $\vec{F}_i^{\text{constraint}}$. In what follows, we will consider infinitesimal virtual displacements of the particles in the system, $\delta\vec{r}_i$, that are consistent with the constraints—*i.e.* virtual displacements that do not move the particles off the surface of constraint. We will also require that forces of constraint do no virtual work on the system, *i.e.*

$$\vec{F}_i^{\text{constraint}} \cdot \delta\vec{r}_i = 0. \tag{A.2}$$

From Newton's second law [274] for a system of N particles with mass m[1], we have

$$\vec{F}_i = m\ddot{\vec{r}}_i, \quad i = 1, \ldots, N, \tag{A.3}$$

where $\vec{F}_i$ is the net force acting on particle i. Now, the force $\vec{F}_i$ can be decomposed into two components: the applied force $\vec{F}_i^{\text{applied}}$ and the constraint force $\vec{F}_i^{\text{constraint}}$, such that

$$\vec{F}_i = \vec{F}_i^{\text{applied}} + \vec{F}_i^{\text{constraint}}. \tag{A.4}$$

Making use of eq. A.2, eq. A.3, and eq. A.4, we get:

$$0 = \vec{F}_i^{\text{applied}} + \vec{F}_i^{\text{constraint}} - m\ddot{\vec{r}}_i, \tag{A.5a}$$

$$\implies 0 = \left(\vec{F}_i^{\text{applied}} - m\ddot{\vec{r}}_i\right) \cdot \delta\vec{r}_i. \tag{A.5b}$$

Equation A.5b is known as *d'Alembert's principle* [120, 273].

We now write our Cartesian coordinates, $\vec{r}_i$, in terms of generalized coordinates, q_j. That is, we write $\vec{r}_i = \vec{r}_i(q_1, \ldots, q_n)$, where $n = d \times N$, and d is the number of spatial dimensions. Then, by making use of the chain rule, we have the following [2]:

$$\dot{\vec{r}}_i = \frac{\partial \vec{r}_i}{\partial q_j}\dot{q}_j, \tag{A.6a}$$

$$\delta\vec{r}_i = \frac{\partial \vec{r}_i}{\partial q_j}\delta q_j. \tag{A.6b}$$

We now consider the term, $\vec{F}_i^{\text{applied}} \cdot \delta\vec{r}_i$, from d'Alembert's principle in eq. A.5b. Making use of the chain rule, we have:

$$\vec{F}_i^{\text{applied}} \cdot \delta\vec{r}_i = -\frac{\partial V}{\partial r_{\ell,i}}\frac{\partial r_{\ell,i}}{\partial q_j}\delta q_j \tag{A.7a}$$

$$= -\frac{\partial V}{\partial q_j}\delta q_j \tag{A.7b}$$

where $r_{\ell,i}$ is the ℓ^{th} component of the position vector $\vec{r}_i$, and we have assumed that the applied forces are conservative, and thus can be derived from a potential V.

[1] We choose the mass of all the particles to be equal for the sake of simplicity, but this is not a necessary assumption.

[2] In this appendix, we make use of Einstein summation convention.

Turning our attention to the term, $m\ddot{\vec{r}}_i \cdot \delta\vec{r}_i$, from d'Alembert's principle in eq. A.5b, we have:

$$m\ddot{\vec{r}}_i \cdot \delta\vec{r}_i = m\ddot{\vec{r}}_i \cdot \left(\frac{\partial \vec{r}_i}{\partial q_j}\delta q_j\right) \tag{A.8a}$$

$$= m\left[\frac{d}{dt}\left(\dot{r}_{\ell,i}\frac{\partial r_{\ell,i}}{\partial q_j}\right) - \dot{r}_{\ell,i}\frac{d}{dt}\left(\frac{\partial r_{\ell,i}}{\partial q_j}\right)\right]\delta q_j, \tag{A.8b}$$

in eq. A.8b, we have made use of the product rule. Next, we make use of the following relation [39]

$$\frac{\partial r_{\ell,i}}{\partial q_j} = \frac{\partial \dot{r}_{\ell,i}}{\partial \dot{q}_j}, \tag{A.9}$$

and the fact that we may commute the order of differentiation with respect to time and differentiation with respect to the generalized coordinates, *i.e.*

$$\frac{d}{dt}\left(\frac{\partial r_{\ell,i}}{\partial q_j}\right) = \frac{\partial \dot{r}_{\ell,i}}{\partial q_j}. \tag{A.10}$$

Using eq. A.9 and A.10, we can rewrite eq. A.8b as:

$$m\ddot{\vec{r}}_i \cdot \delta\vec{r}_i = m\left[\frac{d}{dt}\left(\dot{r}_{\ell,i}\frac{\partial \dot{r}_{\ell,i}}{\partial \dot{q}_j}\right) - \dot{r}_i\frac{\partial \dot{r}_i}{\partial q_j}\right]\delta q_j \tag{A.11a}$$

$$= \left[\frac{d}{dt}\left(\frac{\partial}{\partial \dot{q}_j}\left(\frac{m\dot{r}_{\ell,i}\dot{r}_{\ell,i}}{2}\right)\right) - \frac{\partial}{\partial q_j}\left(\frac{m\dot{r}_{\ell,i}\dot{r}_{\ell,i}}{2}\right)\right]\delta q_j \tag{A.11b}$$

$$= \left[\frac{d}{dt}\left(\frac{\partial T}{\partial \dot{q}_j}\right) - \frac{\partial T}{\partial q_j}\right]\delta q_j, \tag{A.11c}$$

where we have defined the kinetic energy of the system as

$$T \equiv \frac{1}{2}m\dot{r}_{\ell,i}\dot{r}_{\ell,i}. \tag{A.12}$$

Gathering our results from eq. A.7b and A.11c, we can rewrite d'Alembert's principle in eq. A.5b as:

$$0 = \frac{\partial V}{\partial q_j}\delta q_j + \left[\frac{d}{dt}\left(\frac{\partial T}{\partial \dot{q}_j}\right) - \frac{\partial T}{\partial q_j}\right]\delta q_j \tag{A.13a}$$

$$= \left[\frac{d}{dt}\left(\frac{\partial (T-V)}{\partial \dot{q}_j}\right) - \frac{\partial (T-V)}{\partial q_j}\right]\delta q_j \tag{A.13b}$$

$$= \left[\frac{d}{dt}\left(\frac{\partial L}{\partial \dot{q}_j}\right) - \frac{\partial L}{\partial q_j}\right]\delta q_j \tag{A.13c}$$

where we have assumed the potential V is independent of $\dot{q}_j$, and we have defined the Lagrangian of the system as

$$L = T - V. \tag{A.14}$$

It is important to note that the n virtual displacements, δq_j, are not independent, since they are constrained by the M non-holonomic constraints; thus, one may not, at this point, set the term in square brackets in eq. A.13c to zero as one would in the case of unconstrained systems. Instead, one must use the method of Lagrange multipliers to find the equations of motion for the system; this procedure will form the subject of what follows.

Since the virtual displacements, $\delta\vec{r}_i$, respect the M non-holonomic constraints, the virtual displacements of the generalized coordinates, δq_j, must also respect the M non-holonomic constraints. Thus, we have

$$\delta g_k = \frac{\partial g_k}{\partial \dot{q}_j}\delta\dot{q}_j + \frac{\partial g_k}{\partial q_j}\delta q_j = 0, \quad k = 1, \ldots, M. \tag{A.15}$$

Furthermore, we will require that the constraints are satisfied for all time, *i.e.*

$$\frac{dg_k}{dt} = \frac{\partial g_k}{\partial \dot{q}_j}\ddot{q}_j + \frac{\partial g_k}{\partial q_j}\dot{q}_j = 0, \quad k = 1, \ldots, M. \tag{A.16}$$

Now, it will be useful to distinguish between the generalized coordinates that are constrained and those that are unconstrained. Denote the M' (with $M' \leq M$) constrained generalized coordinates as q_j^D, $j = 1, \ldots, M'$, the $n - M'$ unconstrained generalized coordinates as q_j^I, $j = 1, \ldots, n - M'$, and continue to denote the set of all generalized coordinates as q_j, $j = 1, \ldots, n$. With this notation in hand, we may write eq. A.16 as

$$0 = \frac{\partial g_k}{\partial \dot{q}_j^D}\ddot{q}_j^D + \frac{\partial g_k}{\partial \dot{q}_j^I}\ddot{q}_j^I + \frac{\partial g_k}{\partial q_j}\dot{q}_j \tag{A.17a}$$

$$= G_{kj}\ddot{q}_j^D + \frac{\partial g_k}{\partial \dot{q}_j^I}\ddot{q}_j^I + \frac{\partial g_k}{\partial q_j}\dot{q}_j, \tag{A.17b}$$

where we have defined the matrix $G_{kj} = \partial g_k / \partial \dot{q}_j^D$. Next, we follow [39] and assume that the matrix G_{kj} is invertible, and denote its inverse as G^{-1}_{jk}. Solving for $\ddot{q}_j^D$, we

obtain

$$\ddot{q}_i^D = -G_{ik}^{-1}\left(\frac{\partial g_k}{\partial \dot{q}_j^I}\ddot{q}_j^I + \frac{\partial g_k}{\partial q_j}\dot{q}_j\right). \tag{A.18}$$

We now examine the variation of the q_i^D coordinates:

$$\delta q_i^D = \frac{\partial q_i^D}{\partial q_j^I}\delta q_j^I \tag{A.19a}$$

$$= \frac{\partial \ddot{q}_i^D}{\partial \ddot{q}_j^I}\delta q_j^I, \tag{A.19b}$$

in eq. A.19b, we have used a similar expression to eq. A.9. Next, we insert eq. A.18 into eq. A.19b to obtain the following:

$$\delta q_i^D = \frac{\partial}{\partial \ddot{q}_j^I}\left[-G_{ik}^{-1}\left(\frac{\partial g_k}{\partial \dot{q}_j^I}\ddot{q}_j^I + \frac{\partial g_k}{\partial q_j}\dot{q}_j\right)\right]\delta q_j^I \tag{A.20a}$$

$$= -G_{ik}^{-1}\frac{\partial g_k}{\partial \dot{q}_j^I}\delta q_j^I \tag{A.20b}$$

$$\implies 0 = G_{ki}\delta q_i^D + \frac{\partial g_k}{\partial \dot{q}_j^I}\delta q_j^I \tag{A.20c}$$

$$= \frac{\partial g_k}{\partial \dot{q}_j^D}\delta q_j^D + \frac{\partial g_k}{\partial \dot{q}_j^I}\delta q_j^I \tag{A.20d}$$

$$= \frac{\partial g_k}{\partial \dot{q}_j}\delta q_j \tag{A.20e}$$

Gathering our results, we have:

$$0 = \overbrace{\left[\frac{d}{dt}\left(\frac{\partial L}{\partial \dot{q}_j}\right) - \frac{\partial L}{\partial q_j}\right]}^{\equiv A^j}\delta q_j \tag{A.21a}$$

$$0 = \overbrace{\frac{\partial g_k}{\partial \dot{q}_j}}^{\equiv B_k^j}\delta q_j. \tag{A.21b}$$

From eq. A.21b, the allowed virtual displacements, $\delta\vec{q} = (\delta q_1, \ldots, \delta q_n)$, form a subspace

$$\mathcal{S} = \{\delta\vec{q} : \vec{B}_k \cdot \delta\vec{q} = 0, k = 1, \ldots, M\}. \tag{A.22}$$

The orthogonal complement of $\mathcal{S}$ is by definition

$$\mathcal{S}^{\perp} = \text{span}\{\vec{B}_k : k = 1, \ldots, M\}. \tag{A.23}$$

From eq. A.21a, we see that $\vec{A} \in \mathcal{S}^{\perp}$; thus, there exist M scalars, λ_k, such that

$$\vec{A} = \lambda_k \vec{B}_k \tag{A.24a}$$

$$\implies \frac{d}{dt}\left(\frac{\partial L}{\partial \dot{q}_j}\right) - \frac{\partial L}{\partial q_j} = \lambda_k \frac{\partial g_k}{\partial \dot{q}_j}. \tag{A.24b}$$

The equations of A.24b are the equations of motion for a system of N particles under the influence of M non-holonomic constraints. The λ_k are Lagrange multipliers that must be determined by solving eq. A.24b together with the M non-holonomic constraints.

Appendix B

Functional Formalism

B.1 Proofs of Chain Rule and Product Rule Relations for Functional Valued Functionals

B.1.1 Proof of the Chain Rule for Functional Derivatives

Here, we shall prove the chain rule for functional derivatives in eq. 2.21a. Consider the function-valued functional $G \in \mathscr{G}$, and suppose we compose G with a set of function-valued functionals $\{G^j \in \mathscr{G} : j = 1, \ldots, m\}$. Then, using the definition in eq. 2.22b, we

have:

$$\frac{\partial G(x)}{\partial h_i(y)} \equiv \left.\frac{\partial G[\{G^j[h_1(\cdot),\ldots,h_i(\cdot)+\alpha\delta^d(\cdot-y),\ldots,h_n(\cdot)](\circ):j=1,\ldots,m\}](x)}{\partial\alpha}\right|_{\alpha=0} \tag{B.1a}$$

$$= \left.\frac{\partial G[\{G^j(\alpha|i)(\circ):j=1,\ldots,m\}](x)}{\partial\alpha}\right|_{\alpha=0} \tag{B.1b}$$

$$= \frac{\partial}{\partial\alpha}\left(G\left[\left\{G^j(0|i)(\circ)+\alpha\left(\left.\frac{\partial G^j(\alpha|i)(\circ)}{\partial\alpha}\right|_{\alpha=0}\right):j=1,\ldots,m\right\}\right](x)\right)\Bigg|_{\alpha=0} \tag{B.1c}$$

$$= \sum_{j=1}^{m}\frac{\partial}{\partial\alpha}\left(G\left[\ldots,G^j(0|i)(\circ)+\alpha\left(\left.\frac{\partial G^j(\alpha|i)(\circ)}{\partial\alpha}\right|_{\alpha=0}\right),\ldots,\right](x)\right)\Bigg|_{\alpha=0} \tag{B.1d}$$

where in eq. B.1b we have introduced the notation $G^j(\alpha|i)(\circ) \equiv G^j[h_1(\cdot),\ldots,h_i(\cdot)+\alpha\delta^d(\cdot-y),\ldots,h_n(\cdot)](\circ)$, while in eq. B.1c we have treated each $G^j(\alpha|i)$ as a function of the variable α, and expanded around $\alpha = 0$ to first order. Passing from eq. B.1c to eq. B.1d, we changed the α derivative acting on all the $G^j(\alpha|i)$ functionals simultaneously, to the α derivative acting on each $G^j(\alpha|i)$ functional individually. This is simply an application of the ordinary chain rule for differentiation with respect to the real variable α. Now, recall the definition of the functional derivative in eq. 2.17, which we state here for an arbitrary function-valued functional $\tilde{G}$ for the sake of the reader's convenience:

$$\int d^dz\frac{\partial\tilde{G}(x)}{\partial h_j(z)}\gamma_j(z) \equiv \left.\frac{\partial\tilde{G}[h_1(\cdot),\ldots,h_j(\cdot)+\alpha\gamma_j(\cdot),\ldots,h_n(\cdot)](x)}{\partial\alpha}\right|_{\alpha=0}, \tag{B.2}$$

Comparing eq. B.1d with eq. B.2, we see that we may write:

$$\frac{\partial G(x)}{\partial h_i(y)} = \sum_{j=1}^{m}\int d^dz\,\frac{\partial G(x)}{\partial G^j(0|j)(z)}\left.\frac{\partial G^j(\alpha|i)(z)}{\partial\alpha}\right|_{\alpha=0} \tag{B.3}$$

Disentangling the notation, we see that $G^j(0|j)(z) = G^j[h_1(\cdot), \ldots, h_i(\cdot), \ldots, h_n(\cdot)](z)$, furthermore we have

$$\left.\frac{\partial G^j(\alpha|i)(z)}{\partial \alpha}\right|_{\alpha=0} = \left.\frac{\partial G^j[h_1(\cdot), \ldots, h_i(\cdot) + \alpha\delta^d(\cdot - y), \ldots, h_n(\cdot)](z)}{\partial \alpha}\right|_{\alpha=0} \tag{B.4a}$$

$$= \frac{\partial G^j(z)}{\partial h_i(y)}, \tag{B.4b}$$

in eq. B.4b we have used eq. 2.18 to express the derivative with respect to α in terms of a functional derivative. Finally, eq. B.3 then becomes;

$$\frac{\partial G(x)}{\partial h_i(y)} = \sum_{j=1}^{m} \int d^d z \, \frac{\partial G(x)}{\partial G^j(z)} \, \frac{\partial G^j(z)}{\partial h_i(y)}, \tag{B.5}$$

as stated in eq. 2.21a.

B.1.2 Proof of the Chain Rule for Variations

Here we shall prove the chain rule for variations in eq. 2.21b. Consider the function-valued functional $G \in \mathscr{G}$, and suppose we compose G with a set of function-valued functionals $\{G^j \in \mathscr{G} : j = 1, \ldots, m\}$. Then, using the definition in eq. 2.22d, we have:

$$\delta G(x) \equiv \sum_{i=1}^{n} \Big\{ G[\{G^j[h_1(\cdot), \ldots, h_i(\cdot) + \alpha\gamma_i(\cdot), \ldots, h_n(\cdot)](\circ) : j = 1, \ldots, m\}](x) \tag{B.6a}$$

$$- G[\{G^j[h_1(\cdot), \ldots, h_i(\cdot), \ldots, h_n(\cdot)](\circ) : j = 1, \ldots, m\}](x) \Big\}$$

$$= \sum_{i=1}^{n} \left(\left.\frac{\partial G[\{G^j[h_1(\cdot), \ldots, h_i(\cdot) + \alpha\gamma_i(\cdot), \ldots, h_n(\cdot)](\circ) : j = 1, \ldots, m\}](x)}{\partial \alpha}\right|_{\alpha=0} \right) \alpha \tag{B.6b}$$

$$= \sum_{i=1}^{n} \left(\left.\frac{\partial G[\{G^j_\gamma(\alpha|i)(\circ) : j = 1, \ldots, m\}](x)}{\partial \alpha}\right|_{\alpha=0} \right) \alpha \tag{B.6c}$$

$$= \sum_{i=1}^{n} \sum_{j=1}^{m} \left(\left.\frac{\partial G[G^1_\gamma(0|i)(\circ), \ldots, G^j_\gamma(\alpha|i)(\circ), \ldots, G^m_\gamma(0|i)(\circ)](x)}{\partial \alpha}\right|_{\alpha=0} \right) \alpha \tag{B.6d}$$

in eq. B.6b we have performed a series expansion in infinitesimal real parameter α, while in eq. B.6c we have used the notation $G^j_\gamma(\alpha|i)(\circ) \equiv G^j[h_1(\cdot), \ldots, h_i(\cdot)+\alpha\gamma_i(\cdot), \ldots, h_n(\cdot)](\circ)$. In eq. B.6d we have applied the ordinary chain rule for differentiation with respect to α. We may treat each $G^j_\gamma(\alpha|i)$ as a function of the variable α, and expand around $\alpha = 0$ to first order as follows:

$$\delta G(x) = \sum_{i=1}^{n}\sum_{j=1}^{m} \frac{\partial}{\partial\alpha}\left(G[\ldots, G^j_\gamma(0|i)(\circ) + \alpha\left(\left.\frac{\partial G^j_\gamma(\alpha|i)(\circ)}{\partial\alpha}\right|_{\alpha=0}\right), \ldots](x)\right)\Bigg|_{\alpha=0} \alpha \tag{B.7}$$

Now, recall the definition of the functional derivative in eq. 2.17, which we restate here for an arbitrary function-valued functional $\tilde{G}$ for the sake of the reader's convenience:

$$\int d^d z \frac{\partial\tilde{G}(x)}{\partial h_j(z)}\gamma_j(z) \equiv \left.\frac{\partial\tilde{G}[h_1(\cdot), \ldots, h_j(\cdot) + \alpha\gamma_j(\cdot), \ldots, h_n(\cdot)](x)}{\partial\alpha}\right|_{\alpha=0}, \tag{B.8}$$

Comparing eq. B.7 with eq. B.8, we see that we may write:

$$\delta G(x) = \left(\sum_{i=1}^{n}\sum_{j=1}^{m}\int d^d z \, \frac{\partial G(x)}{\partial G^j(0|j)(z)}\left.\frac{\partial G^j(\alpha|i)(z)}{\partial\alpha}\right|_{\alpha=0}\right)\alpha \tag{B.9a}$$

$$= \sum_{j=1}^{m}\int d^d z \, \frac{\partial G(x)}{\partial G^j(z)}\left(\sum_{i=1}^{n}\left.\frac{\partial G^j(\alpha|i)(z)}{\partial\alpha}\right|_{\alpha=0}\alpha\right) \tag{B.9b}$$

$$= \sum_{j=1}^{m}\int d^d z \, \frac{\partial G(x)}{\partial G^j(z)}\,\delta G^j(z), \tag{B.9c}$$

in eq. B.9b we have undone the $G^j(\alpha|i)(z)$ notation introduced earlier, while in eq. B.9c we have used the definition of the variation from eq. 2.19. Thus, we have shown that:

$$\delta G(x) = \sum_{j=1}^{m}\int d^d z \, \frac{\partial G(x)}{\partial G^j(z)}\,\delta G^j(z), \tag{B.10}$$

as stated in eq. 2.21b.

B.1.3 Proof of the Chain Rule for Spacetime Derivatives

Here we shall prove the chain rule for spacetime derivatives in eq. 2.21c. We assume that the function-valued functional $G \in \mathscr{G}$ has the following translational property:

$$G[h_1(\cdot + y), \ldots, h_n(\cdot + y)](x) = G[h_1(\cdot), \ldots, h_n(\cdot)](x + y). \tag{B.11a}$$

Suppose we are now to compose G with a set of function-valued functionals $\{G^j \in \mathscr{G} : j = 1, \ldots, m\}$, that is

$$G(x) = G[\{G^j[h_1(\cdot), \ldots, h_n(\cdot)](\circ) : j = 1, \ldots, m\}](x). \tag{B.12a}$$

To continue with the proof, we shall define the following useful notation:

$$G^j_\alpha(x) \equiv G^j[h_1(\cdot), \ldots, h_n(\cdot)](x + \alpha e^\nu) \tag{B.13a}$$

$$\gamma^j_\alpha(x) \equiv \frac{G^j_\alpha(x) - G^j_0(x)}{\alpha}, \tag{B.13b}$$

where e^ν is a unit vector in the ν direction and $G^j_0(x) = G^j[h_1(\cdot), \ldots, h_n(\cdot)](x)$. Now, to compute the spacetime derivative of G, we begin with the definition of a spacetime derivative in the ν direction:

$$\partial^x_\nu G(x) \equiv \lim_{\alpha \to 0} \frac{G(x + \alpha e^\nu) - G(x)}{\alpha} \tag{B.14a}$$

$$= \lim_{\alpha \to 0} \frac{1}{\alpha} \Big(G[\{G^j[h_1(\cdot), \ldots, h_n(\cdot)](\circ) : j = 1, \ldots, m\}](x + \alpha e^\nu) \tag{B.14b}$$

$$- G[\{G^j[h_1(\cdot), \ldots, h_n(\cdot)](\circ) : j = 1, \ldots, m\}](x) \Big)$$

$$= \lim_{\alpha \to 0} \frac{1}{\alpha} \Big(G[\{G^j[h_1(\cdot), \ldots, h_n(\cdot)](\circ + \alpha e^\nu) : j = 1, \ldots, m\}](x) \tag{B.14c}$$

$$- G[\{G^j[h_1(\cdot), \ldots, h_n(\cdot)](\circ) : j = 1, \ldots, m\}](x) \Big)$$

$$= \lim_{\alpha \to 0} \frac{1}{\alpha} \Big(G[\{G^j_\alpha(\circ) : j = 1, \ldots, m\}](x) - G[\{G^j_0(\circ) : j = 1, \ldots, m\}](x) \Big), \tag{B.14d}$$

in eq. B.14c we have used the translational property of G from eq. B.11, while in eq. B.14d we have used the condensed notation introduced in eq. B.13a. Now, we may treat G as a function of the variable α, and expand around $\alpha = 0$ to first order as follows:

$$\partial^x_\nu G(x) = lim_{\alpha\to 0}\frac{1}{\alpha}\left(\frac{\partial G[\{G^j_\alpha(\circ) : j = 1,\dots,m\}](x)}{\partial\alpha}\bigg|_{\alpha=0}\alpha\right) \tag{B.15a}$$

$$= \frac{\partial G[\{G^j_0(\circ) + \alpha\gamma^j_\alpha(\circ) : j = 1,\dots,m\}](x)}{\partial\alpha}\bigg|_{\alpha=0} \tag{B.15b}$$

$$= \sum_{j=1}^{m}\frac{\partial G[G^1_0(\circ),\dots,G^j_0(\circ) + \alpha\gamma^j_\alpha(\circ),\dots,G^n_0(\circ)](x)}{\partial\alpha}\bigg|_{\alpha=0}, \tag{B.15c}$$

in eq. B.15b we have used the definition of γ^j_α from eq. B.13b to write $G^j_\alpha(\circ) = G^j_0(\circ) + \alpha\gamma^j_\alpha(\circ)$, and in eq. B.15c we have applied the ordinary chain rule for differentiation with respect to real variable α. Recall the definition of the functional derivative in eq. 2.17, which we restate here for an arbitrary function-valued functional $\tilde{G}$ for the sake of the reader's convenience:

$$\int d^d z\frac{\partial\tilde{G}(x)}{\partial h_j(z)}\gamma_j(z) \equiv \frac{\partial\tilde{G}[h_1(\cdot),\dots,h_j(\cdot) + \alpha\gamma_j(\cdot),\dots,h_n(\cdot)](x)}{\partial\alpha}\bigg|_{\alpha=0}, \tag{B.16}$$

Comparing eq. B.15c with eq. B.16, we see that we may write:

$$\partial^x_\nu G(x) = \sum_{j=1}^{m}\int d^d z\,\frac{\partial G(x)}{\partial G^j_0(z)}\left(lim_{\alpha\to 0}\,\gamma^j_\alpha(z)\right) \tag{B.17a}$$

$$= \sum_{j=1}^{m}\int d^d z\,\frac{\partial G(x)}{\partial G^j(z)}\,\left(lim_{\alpha\to 0}\,\frac{G^j[h_1(\cdot),\dots,h_n(\cdot)](z + \alpha e^\nu) - G^j[h_1(\cdot),\dots,h_n(\cdot)](z)}{\alpha}\right) \tag{B.17b}$$

$$= \sum_{j=1}^{m}\int d^d z\,\frac{\partial G(x)}{\partial G^j(z)}\,\partial^z_\nu G^j(z), \tag{B.17c}$$

in eq. B.17b we have expanded the $G^j_\alpha(z)$ and γ^j_α notation introduced in eq. B.13a and B.13b, while in eq. B.17c we have used the definition of the spacetime derivative. Thus, we have shown that:

$$\partial^x_\nu G(x) = \sum_{j=1}^{m}\int d^d z\,\frac{\partial G(x)}{\partial G^j(z)}\,\partial^z_\nu G^j(z), \tag{B.18}$$

as stated in eq. 2.21c.

B.1.4 Proof of Product Rule for Variations

In this section, we shall prove the product rule for variations. Consider two function-valued functionals $G_1, G_2 \in \mathscr{G}$, with G_1 and G_2 dependent on n_1 and n_2 functions respectively. Now, take $n = \max(n_1, n_2)$, so that we may write $G_1(x) = G_1[h_1(\cdot), \ldots, h_n(\cdot)](x)$ and $G_2(x) = G_2[h_1(\cdot), \ldots, h_n(\cdot)](x)$. We may then form the function-valued functional $G_3 \in \mathscr{G}$ defined as the product of G_1 and G_2:

$$G_3(x) \equiv G_1(x) G_2(x), \tag{B.19}$$

and we may write

$$G_3(x) = G_3[h_1(\cdot), \ldots, h_n(\cdot)](x) = G_1[h_1(\cdot), \ldots, h_n(\cdot)](x) G_2[h_1(\cdot), \ldots, h_n(\cdot)](x). \tag{B.20}$$

Now, making use of eq. 2.19b, we compute the variation of G_3 as:

$$\delta G_3(x) = \sum_{i=1}^{n} \left(\frac{\partial G_3[h_1(\cdot), \ldots, h_i(\cdot) + \alpha\gamma_i(\cdot), \ldots, h_n(\cdot)](x)}{\partial \alpha} \bigg|_{\alpha=0} \right) \alpha \tag{B.21a}$$

$$= \sum_{i=1}^{n} \left(\frac{\partial (G_1[\ldots, h_i(\cdot) + \alpha\gamma_i(\cdot), \ldots](x)\; G_2[\ldots, h_i(\cdot) + \alpha\gamma_i(\cdot), \ldots](x))}{\partial \alpha} \bigg|_{\alpha=0} \right) \alpha \tag{B.21b}$$

$$= \sum_{i=1}^{n} \left(\frac{\partial G_1[h_1(\cdot), \ldots, h_i(\cdot) + \alpha\gamma_i(\cdot), \ldots, h_n(\cdot)](x)}{\partial \alpha} \bigg|_{\alpha=0} G_2[h_1(\cdot), \ldots, h_n(\cdot)](x) \right. \tag{B.21c}$$

$$\left. + G_1[h_1(\cdot), \ldots, h_n(\cdot)](x) \frac{\partial G_2[h_1(\cdot), \ldots, h_i(\cdot) + \alpha\gamma_i(\cdot), \ldots, h_n(\cdot)](x)}{\partial \alpha} \bigg|_{\alpha=0} \right) \alpha$$

in eq. B.21c we have applied the ordinary product rule for differentiation with respect to α. Now, using the definition of the variation from eq. 2.19, we may write:

$$\delta G_3(x) = \delta G_1(x)\; G_2(x) + G_1(x)\; \delta G_2(x), \tag{B.22}$$

thus proving the product rule for variations.

B.2 Useful Identities for the Proof of the Transposition Rule

B.2.1 Translational Property of B

The function-valued functional B defined in eq. 2.10 has the form

$$B = B[\partial_\nu A^\mu(\cdot) : \nu, \mu \neq \mu_D](x) \equiv -\sum_{\nu \neq \mu_D} \partial_\nu f^\nu[A^\mu : \mu \neq \mu_D](x). \tag{B.23}$$

Recall that the function-valued functional f^ν was assumed to have the functional power-series expansion in eq. 2.7. Thus, we may write B as

$$B[\partial_\nu A^\mu(\cdot) : \nu, \mu \neq \mu_D](x) = -\sum_{\nu \neq \mu_D} \partial_\nu \Bigg(\sum_{I=0}^{\infty} c^\nu_{i_0,\ldots,i_{d-1}} \\ (A^0(x))^{i_0} \ldots (A^{\mu_D - 1}(x))^{i_{\mu_D - 1}} (A^{\mu_D + 1}(x))^{i_{\mu_D + 1}} \ldots (A^{d-1}(x))^{i_{d-1}} \Bigg). \tag{B.24}$$

Now, if one considers $B[\partial_\nu A^\mu(\cdot) : \nu, \mu \neq \mu_D](x + y)$, then one will find:

$$B[\partial_\nu A^\mu(\cdot) : \nu, \mu \neq \mu_D](x + y) = -\sum_{\nu \neq \mu_D} \partial^x_\nu \Bigg(\sum_{I=0}^{\infty} c^\nu_{i_0,\ldots,i_{d-1}} \tag{B.25a}$$

$$(A^0(x + y))^{i_0} \ldots (A^{\mu_D - 1}(x + y))^{i_{\mu_D - 1}} (A^{\mu_D + 1}(x + y))^{i_{\mu_D + 1}} \ldots (A^{d-1}(x + y))^{i_{d-1}} \Bigg)$$

$$= B[\partial_\nu A^\mu(\cdot + y) : \nu, \mu \neq \mu_D](x). \tag{B.25b}$$

Thus, we have shown that $B[\partial_\nu A^\mu(\cdot) : \nu, \mu \neq \mu_D](x + y) = B[\partial_\nu A^\mu(\cdot + y) : \nu, \mu \neq \mu_D](x)$, which will allow us to make use of the chain rule for spacetime derivatives

from eq. 2.21c when we compute the spacetime derivative of B. That is, we may write

$$\partial^x_\mu B[\partial_\nu A^\mu(\cdot) : \nu, \mu \neq \mu_D](x) = \sum_{\rho,\sigma\neq\mu_D} \int d^d z \, \frac{\partial B(x)}{\partial(\partial^z_\rho A^\sigma(z))} \, \partial^z_\mu(\partial^z_\rho A^\sigma(z)). \tag{B.26}$$

B.2.2 2^{nd} Order Functional Derivatives Commute

Using eq. 2.18, we may write the second order functional derivative of a functional $F \in \mathscr{F}$ as

$$\frac{\partial^2 F}{\partial h_j(z)\partial h_i(y)} = \frac{\partial^2 F[h_1(\cdot), \ldots, h_i(\cdot) + \alpha\delta^d(\cdot - y), \ldots, h_j(\cdot) + \beta\delta^d(\cdot - z), \ldots, h_n(\cdot)]}{\partial\beta\partial\alpha}\bigg|_{\alpha=\beta=0}, \tag{B.27}$$

where we assume that the partial derivatives $\partial_\alpha F$ and $\partial_\beta F$ exist and are themselves differentiable with respect to both α and β. Thus, the mixed partial derivatives $\partial^2 F/\partial\alpha\partial\beta$ and $\partial^2 F/\partial\beta\partial\alpha$ also exist and are equal by Schwarz's theorem [275, 276]. Therefore, we have

$$\frac{\partial^2 F}{\partial h_j(z)\partial h_i(y)} = \frac{\partial^2 F}{\partial h_i(y)\partial h_j(z)}. \tag{B.28}$$

B.2.3 Variation of the Functional Derivative of B

The functional derivative of B with respect to $\partial^y_\rho A^\sigma(y)$ is given by

$$\frac{\partial B(x)}{\partial(\partial^y_\rho A^\sigma(y))} = \frac{\partial B[\ldots, \partial_\rho A^\sigma(\cdot) + \alpha\delta^d(\cdot - y), \ldots](x)}{\partial\alpha}\bigg|_{\alpha=0}. \tag{B.29}$$

Taking the variation of this expression, we have

$$\delta\left(\frac{\partial B(x)}{\partial(\partial^y_\rho A^\sigma(y))}\right) = \delta\left(\frac{\partial B[\ldots,\partial_\rho A^\sigma(\cdot)+\alpha\delta^d(\cdot-y),\ldots](x)}{\partial\alpha}\bigg|_{\alpha=0}\right) \tag{B.30a}$$

$$= \sum_{\rho',\sigma'\neq\mu_D}\frac{\partial}{\partial\beta}\Bigg(\tag{B.30b}$$

$$\frac{\partial B[\ldots,\partial_\rho A^\sigma(\cdot)+\alpha\delta^d(\cdot-y),\ldots,\partial_{\rho'}A^{\sigma'}(\cdot)+\beta\gamma^{\sigma'}_{\rho'},\ldots](x)}{\partial\alpha}\bigg|_{\alpha=0}\Bigg)\Bigg|_{\beta=0}$$

$$= \frac{\partial}{\partial\alpha}\Bigg(\sum_{\rho',\sigma'\neq\mu_D} \tag{B.30c}$$

$$\frac{\partial B[\ldots,\partial_\rho A^\sigma(\cdot)+\alpha\delta^d(\cdot-y),\ldots,\partial_{\rho'}A^{\sigma'}(\cdot)+\beta\gamma^{\sigma'}_{\rho'},\ldots](x)}{\partial\beta}\bigg|_{\beta=0}\Bigg)\Bigg|_{\alpha=0}$$

$$= \frac{\partial}{\partial\alpha}\left(\delta B[\ldots,\partial_\rho A^{\sigma,\alpha}_y(\cdot),\ldots](x)\right)\Big|_{\alpha=0}. \tag{B.30d}$$

In eq. B.30d we have defined $\partial_\rho A^{\sigma,\alpha}_y(\cdot) \equiv \partial_\rho A^\sigma(\cdot)+\alpha\delta^d(\cdot-y)$. Next, we will use the chain rule for variations from eq. 2.21b to write δB in terms of the variations of its arguments as follows:

$$\delta B(x) = \int d^dz\,\frac{\partial B[\ldots,\partial_\rho A^{\sigma,\alpha}_y(\cdot),\ldots](x)}{\partial(\partial^z_\rho A^{\sigma,\alpha}_y(z))}\,\delta(\partial^z_\rho A^{\sigma,\alpha}_y(z)) \tag{B.31}$$

$$+\sum_{(\rho',\sigma')\neq(\rho,\sigma,\mu_D)}\int d^dz\,\frac{\partial B[\ldots,\partial_\rho A^{\sigma,\alpha}_y(\cdot),\ldots](x)}{\partial(\partial^z_{\rho'}A^{\sigma'}(z))}\,\delta(\partial^z_{\rho'}A^{\sigma'}(z)),$$

where in eq. B.31 we have broken the sum over ρ' and σ' into the term where $(\rho', \sigma') = (\rho, \sigma)$, and the terms where $(\rho', \sigma') \neq (\rho, \sigma)$. Inserting eq. B.31 into eq. B.30d, we have

$$\delta\left(\frac{\partial B(x)}{\partial(\partial_\rho^y A^\sigma(y))}\right) = \int d^d z\, \frac{\partial B[\ldots, \partial_\rho A^\sigma(\cdot), \ldots](x)}{\partial(\partial_\rho^z A^\sigma(z))} \frac{\partial}{\partial\alpha}\left(\delta(\partial_\rho^z A_y^{\sigma,\alpha}(z))\right)\Big|_{\alpha=0} \tag{B.32a}$$

$$+ \int d^d z\, \frac{\partial}{\partial\alpha}\left(\frac{\partial B[\ldots, \partial_\rho A_y^{\sigma,\alpha}(\cdot), \ldots](x)}{\partial(\partial_\rho^z A_y^{\sigma,\alpha}(z))}\right)\Big|_{\alpha=0} \delta(\partial_\rho^z A^\sigma(z))$$

$$+ \sum_{(\rho',\sigma')\neq(\rho,\sigma,\mu_D)} \int d^d z\, \frac{\partial}{\partial\alpha}\left(\frac{\partial B[\ldots, \partial_\rho A_y^{\sigma,\alpha}(\cdot), \ldots](x)}{\partial(\partial_{\rho'}^z A^{\sigma'}(z))}\right)\Big|_{\alpha=0} \delta(\partial_{\rho'}^z A^{\sigma'}(z))$$

$$= \int d^d z\, \frac{\partial B[\ldots, \partial_\rho A^\sigma(\cdot), \ldots](x)}{\partial(\partial_\rho^z A^\sigma(z))} \frac{\partial}{\partial\alpha}\left(\delta(\partial_\rho^z A_y^{\sigma,\alpha}(z))\right)\Big|_{\alpha=0} \tag{B.32b}$$

$$+ \sum_{(\rho',\sigma')\neq(\mu_D)} \int d^d z\, \frac{\partial}{\partial\alpha}\left(\frac{\partial B[\ldots, \partial_\rho A_y^{\sigma,\alpha}(\cdot), \ldots](x)}{\partial(\partial_{\rho'}^z A^{\sigma'}(z))}\right)\Big|_{\alpha=0} \delta(\partial_{\rho'}^z A^{\sigma'}(z))$$

$$= \int d^d z\, \frac{\partial B[\ldots, \partial_\rho A^\sigma(\cdot), \ldots](x)}{\partial(\partial_\rho^z A^\sigma(z))} \frac{\partial}{\partial\alpha}\left(\delta(\partial_\rho^z A_y^{\sigma,\alpha}(z))\right)\Big|_{\alpha=0} \tag{B.32c}$$

$$+ \sum_{(\rho',\sigma')\neq(\mu_D)} \int d^d z\, \frac{\partial^2 B(x)}{\partial(\partial_\rho^z A^\sigma(y))\partial(\partial_{\rho'}^z A^{\sigma'}(z))} \delta(\partial_{\rho'}^z A^{\sigma'}(z))$$

in eq. B.32b we have recombined the sums over ρ' and σ' back into a single sum. Then, if one pays attention to the remaining α derivative in eq. B.32c, one will find:

$$\frac{\partial}{\partial\alpha}\left(\delta(\partial_\rho^z A_y^{\sigma,\alpha}(z))\right)\Big|_{\alpha=0} = \frac{\partial}{\partial\alpha}\left(\partial_\rho(\delta A^{\sigma,\alpha}(z))\right)\Big|_{\alpha=0} \tag{B.33a}$$

$$= \frac{\partial}{\partial\alpha}\left(\partial_\rho(A^{\sigma,\alpha}(z) + \beta\gamma_\rho^\sigma(z) - A^{\sigma,\alpha}(z))\right)\Big|_{\alpha=0} \tag{B.33b}$$

$$= \partial_\rho \frac{\partial}{\partial\alpha}\left(\beta\gamma_\rho^\sigma(z)\right)\Big|_{\alpha=0} \tag{B.33c}$$

$$= 0, \tag{B.33d}$$

where in eq. B.33a we have the transposition rule for independent field components from eq. 2.27, and in eq. B.33c we have used the fact that α and β are independent

variables, so that $\partial_\alpha \beta = 0$. Thus, we have shown that

$$\delta\left(\frac{\partial B(x)}{\partial(\partial^y_\rho A^\sigma(y))}\right) = \sum_{(\rho',\sigma')\neq(\mu_D)} \int d^d z \, \frac{\partial^2 B(x)}{\partial(\partial^y_\rho A^\sigma(y))\partial(\partial^z_{\rho'} A^{\sigma'}(z))} \, \delta(\partial^z_{\rho'} A^{\sigma'}(z)) \tag{B.34a}$$

$$= \sum_{(\rho',\sigma')\neq(\mu_D)} \int d^d z \, \frac{\partial^2 B(x)}{\partial(\partial^z_{\rho'} A^{\sigma'}(z))\partial(\partial^y_\rho A^\sigma(y))} \, \delta(\partial^z_{\rho'} A^{\sigma'}(z)), \tag{B.34b}$$

in eq. B.34b we commuted the order of the functional derivatives using the result from eq. B.28.

B.2.4 2^{nd} Order Functional Derivative of B

Consider acting the spacetime derivative ∂^x_μ on the functional derivative of B with respect to $\partial^z_\rho A^\sigma(z)$:

$$\partial^x_\mu\left(\frac{\partial B(x)}{\partial(\partial^z_\rho A^\sigma(z))}\right) = \partial^x_\mu\left(\frac{\partial B[\ldots,\partial_\rho A^\sigma(\cdot)+\alpha\delta^d(\cdot-z),\ldots](x)}{\partial\alpha}\bigg|_{\alpha=0}\right) \tag{B.35a}$$

$$= \frac{\partial}{\partial\alpha}\left(\partial^x_\mu B[\ldots,\partial_\rho A^\sigma(\cdot)+\alpha\delta^d(\cdot-z),\ldots](x)\right)\bigg|_{\alpha=0} \tag{B.35b}$$

$$= \frac{\partial}{\partial\alpha}\left(\partial^x_\mu B[\ldots,\partial_\rho A^{\sigma,\alpha}_z(\cdot),\ldots](x)\right)\bigg|_{\alpha=0}, \tag{B.35c}$$

in eq. B.35c we have defined $\partial_\rho A^{\sigma,\alpha}_z(\cdot) \equiv \partial_\rho A^\sigma(\cdot) + \alpha\delta^d(\cdot - z)$. In appendix B.2.1, we showed that B has the translational property, which allows us to make use of the chain rule for spacetime derivatives from eq. 2.21c to write $\partial^x_\mu B$ in terms of the functional

derivatives of B. Thus, we have

$$\partial^x_\mu\left(\frac{\partial B(x)}{\partial(\partial^z_\rho A^\sigma(z))}\right) = \frac{\partial}{\partial\alpha}\Bigg(\int d^dy\,\frac{\partial B[\ldots,\partial_\rho A^{\sigma,\alpha}_z(\cdot),\ldots](x)}{\partial(\partial^y_\rho A^{\sigma,\alpha}_z(y))}\partial^y_\mu(\partial^y_\rho A^{\sigma,\alpha}_z(y)) \tag{B.36a}$$

$$+\sum_{(\rho',\sigma')\neq(\rho,\sigma,\mu_D)}\int d^dy\,\frac{\partial B[\ldots,\partial_\rho A^{\sigma,\alpha}_z(\cdot),\ldots](x)}{\partial(\partial^y_{\rho'} A^{\sigma'}(y))}\partial^y_\mu(\partial^y_{\rho'} A^{\sigma'}_z(y))\Bigg)\Bigg|_{\alpha=0}$$

$$=\int d^dy\,\frac{\partial B[\ldots,\partial_\rho A^{\sigma}(\cdot),\ldots](x)}{\partial(\partial^y_\rho A^{\sigma}(y))}\frac{\partial}{\partial\alpha}\left(\partial^y_\mu(\partial^y_\rho A^{\sigma,\alpha}_z(y))\right)\Big|_{\alpha=0} \tag{B.36b}$$

$$+\int d^dy\,\frac{\partial}{\partial\alpha}\left(\frac{\partial B[\ldots,\partial_\rho A^{\sigma,\alpha}_z(\cdot),\ldots](x)}{\partial(\partial^y_\rho A^{\sigma,\alpha}_z(y))}\right)\Big|_{\alpha=0}\partial^y_\mu(\partial^y_\rho A^{\sigma}(y))$$

$$+\sum_{(\rho',\sigma')\neq(\rho,\sigma,\mu_D)}\int d^dy\,\frac{\partial}{\partial\alpha}\left(\frac{\partial B[\ldots,\partial_\rho A^{\sigma,\alpha}_z(\cdot),\ldots](x)}{\partial(\partial^y_{\rho'} A^{\sigma'}(y))}\right)\Big|_{\alpha=0}\partial^y_\mu(\partial^y_{\rho'} A^{\sigma'}_z(y))$$

$$=\int d^dy\,\frac{\partial B[\ldots,\partial_\rho A^{\sigma}(\cdot),\ldots](x)}{\partial(\partial^y_\rho A^{\sigma}(y))}\frac{\partial}{\partial\alpha}\left(\partial^y_\mu(\partial^y_\rho A^{\sigma,\alpha}_z(y))\right)\Big|_{\alpha=0} \tag{B.36c}$$

$$+\sum_{(\rho',\sigma')\neq(\mu_D)}\int d^dy\,\frac{\partial^2 B(x)}{\partial(\partial^z_\rho A^\sigma(z))\partial(\partial^y_{\rho'} A^{\sigma'}(y))}\partial^y_\mu(\partial^y_{\rho'} A^{\sigma'}_z(y)),$$

in eq. B.36a we have broken the sum from the spacetime chain rule into two pieces, one that runs over all $(\rho',\sigma')\neq(\rho,\sigma,\mu_D)$, and then we included the remaining ρ,σ part of the sum. If we now shift our focus to the remaining α derivative in eq. B.36c, we will find the following:

$$\frac{\partial}{\partial\alpha}\left(\partial^y_\mu(\partial^y_\rho A^{\sigma,\alpha}_z(y))\right)\Big|_{\alpha=0}=\frac{\partial}{\partial\alpha}\left(\partial^y_\mu[\partial^y_\rho A^\sigma(y)+\alpha\delta^d(y-z)]\right)\Big|_{\alpha=0}=\partial^y_\mu\delta^d(y-z). \tag{B.37}$$

Inserting eq. B.37 into eq. B.36c, we find

$$\partial^x_\mu\left(\frac{\partial B(x)}{\partial(\partial^z_\rho A^\sigma(z))}\right)=\int d^dy\,\frac{\partial B[\ldots,\partial_\rho A^{\sigma}(\cdot),\ldots](x)}{\partial(\partial^y_\rho A^{\sigma}(y))}\partial^y_\mu\delta^d(y-z) \tag{B.38a}$$

$$+\sum_{(\rho',\sigma')\neq(\mu_D)}\int d^dy\,\frac{\partial^2 B(x)}{\partial(\partial^z_\rho A^\sigma(z))\partial(\partial^y_{\rho'} A^{\sigma'}(y))}\partial^y_\mu(\partial^y_{\rho'} A^{\sigma'}_z(y))$$

$$=-\partial^z_\mu\left(\frac{\partial B(x)}{\partial(\partial^y_\rho A^{\sigma}(y))}\right) \tag{B.38b}$$

$$+\sum_{(\rho',\sigma')\neq(\mu_D)}\int d^dy\,\frac{\partial^2 B(x)}{\partial(\partial^z_\rho A^\sigma(z))\partial(\partial^y_{\rho'} A^{\sigma'}(y))}\partial^y_\mu(\partial^y_{\rho'} A^{\sigma'}_z(y)),$$

where in eq. B.38b, we used integration by parts to move the spacetime derivative off the δ. Finally, we may rearrange eq. B.38b to obtain

$$\partial_\mu^x \left(\frac{\partial B(x)}{\partial(\partial_\rho^z A^\sigma(z))} \right) + \partial_\mu^z \left(\frac{\partial B(x)}{\partial(\partial_\rho^y A^\sigma(y))} \right) = \sum_{(\rho',\sigma') \neq (\mu_D)} \int d^d y \, \frac{\partial^2 B(x)}{\partial(\partial_\rho^z A^\sigma(z)) \partial(\partial_{\rho'}^y A^{\sigma'}(y))} \partial_\mu^y (\partial_{\rho'}^y A_z^{\sigma'}(y)). \tag{B.39}$$

B.3 Examples of Functional Formalism

In this appendix, we shall provide simple examples of the functional formalism introduced in Sec. 2.2.1 to help illustrate how it works in practice.

Example 1

Define $F[f(\circ)]$ and $G[f(\circ)]$ as follows:

$$F[f(\circ)] \equiv \int d^d x \; f(x) \tag{B.40a}$$

$$G[f(\circ)](x) \equiv f^2(x). \tag{B.40b}$$

Clearly, F and G are examples of a functional and a function-valued functional, respectively. We may freely compose F and G to obtain

$$F[G[f(\cdot)]\circ] = F[f^2(\circ)] = \int d^d x f^2(x). \tag{B.41}$$

Now, as illustration of the chain rule for functional derivatives, eq. 2.21a, we shall compute the functional derivative of $F[G[f(\cdot)]\circ]$ with respect to $f(y)$ by directly using eq. B.41, and then by using the chain rule for functional derivatives in eq. 2.21a, showing that both methods yield the same result. First, we compute the functional

derivative directly from eq. B.41:

$$\frac{\partial F[G[f(\cdot)]\circ]}{\partial f(y)} = \frac{\partial}{\partial \alpha}\left(F[G[f(\cdot)+\alpha\delta^d(\cdot-y)]\circ]\right)\Big|_{\alpha=0} \tag{B.42a}$$

$$= \frac{\partial}{\partial \alpha}\left(F[(f(\circ)+\alpha\delta^d(\circ-y))^2]\right)\Big|_{\alpha=0} \tag{B.42b}$$

$$= \frac{\partial}{\partial \alpha}\left(\int d^dx(f(x)+\alpha\delta^d(x-y))^2\right)\Big|_{\alpha=0} \tag{B.42c}$$

$$= \frac{\partial}{\partial \alpha}\left(\int d^dx\left\{f^2(x)+2\alpha f(x)\delta^d(x-y)+\left(\alpha\delta^d(x-y)\right)^2\right\}\right)\Big|_{\alpha=0} \tag{B.42d}$$

$$= 2\int d^dx f(x)\delta^d(x-y) \tag{B.42e}$$

$$= 2f(y), \tag{B.42f}$$

in eq. B.42a, we have used eq. 2.22b. Note that in eq. B.42d, the term proportional to $(\delta^d(x-y))^2$ should be written as $\lim_{\beta\to 0}(\delta^d_\beta(x-y))^2$, where $\delta^d_\beta(x-y)$ is a regularized delta function that approaches the Dirac delta function as $\beta \to 0$. This term is in general ill-defined unless one takes the limit to $\alpha = 0$ first. Now, we shall compute the same functional derivative using the left-hand side of the chain rule for functional derivatives in eq. 2.21a:

$$\frac{\partial F[G[f(\cdot)]\circ]}{\partial f(y)} = \int d^dz\, \frac{\partial F[G[f(\cdot)]\circ]}{\partial G[f(\cdot)](z)}\,\frac{\partial G[f(\cdot)](z)}{\partial f(y)} \tag{B.43a}$$

$$= \int d^dz\, \frac{\partial}{\partial \alpha}\left(F[G[f(\cdot)]\circ+\alpha\delta^d(\circ-z)]\right)\Big|_{\alpha=0}\,\frac{\partial}{\partial \beta}\left(G[f(\cdot)+\beta\delta^d(\cdot-y)](z)\right)\Big|_{\beta=0} \tag{B.43b}$$

$$= \int d^dz\, \frac{\partial}{\partial \alpha}\left(\int d^dx f^2(x)+\alpha\delta^d(x-z)\right)\Big|_{\alpha=0}\,\frac{\partial}{\partial \beta}\left((f(z)+\beta\delta^d(z-y))^2\right)\Big|_{\beta=0} \tag{B.43c}$$

$$= \int d^dz d^dx\ \left(\delta^d(x-z)\right)\left(2f(z)\delta^d(z-y)\right) \tag{B.43d}$$

$$= 2f(y), \tag{B.43e}$$

where in eq. B.43a we have used eq. 2.22c. We see that both methods of computing the functional derivative yield the same result, thus illustrating how the chain rule for functional derivatives works in practice.

Example 2

In this example, we shall illustrate the use of the derivative chain rule in eq. 2.21c. We define the following function-valued functional

$$H[f(\circ)](x) \equiv \ln(f(x)). \tag{B.44}$$

We may then form the composition of G from eq. B.40b and H to obtain

$$H[G[f(\circ)]](x) = H[f^2(\circ)](x) = 2\ln(f(x)). \tag{B.45}$$

Computing the left-hand side of the derivative chain rule in eq. 2.21c, we find:

$$\partial_\nu^x H[G[f(\circ)]](x) = \partial_\nu^x(2\ln(f(x))) \tag{B.46a}$$

$$= \frac{2}{f(x)}\,\partial_\nu^x f(x). \tag{B.46b}$$

Now, we shall compute the right-hand side of the derivative chain rule in eq. 2.21c:

$$\sum_{j=1}^{m}\int d^d z\,\frac{\partial H[G[f(\circ)](\cdot)](x)}{\partial G[f(\circ)](z)}\partial_\nu^z G[f(\circ)](z) = \int d^d z\left[\frac{\partial}{\partial\alpha}\left(H[G[f(\circ)](\cdot)+\alpha\delta^d(\cdot-z)](x)\right)\Big|_{\alpha=0}\right. \tag{B.47a}$$

$$\left.\times\,\partial_\nu^z(f^2(z))\right]$$

$$= \int d^d z\left[\frac{\partial}{\partial\alpha}\left(\ln(f^2(x)+\alpha\delta^d(x-z))\right)\Big|_{\alpha=0}\right. \tag{B.47b}$$

$$\left.\times\,2f(z)\,\partial_\nu^z f(z)\right]$$

$$= \int d^d z\,\frac{1}{f^2(x)}\,\delta^d(x-z)\,2f(z)\,\partial_\nu^z f(z) \tag{B.47c}$$

$$= \frac{2}{f(x)}\,\partial_\nu^x f(x), \tag{B.47d}$$

where in eq. B.47a we made use of eq. 2.22c. We see that both sides of the derivative chain rule in eq. 2.21c yield the same result, thus illustrating how the derivative chain

rule works in practice.

B.4 Condensed Notation

For the sake of notational convenience we shall abbreviate some the verbose aspects of the notation developed thus far. We shall drop the $(\cdot)$ notation, and write

$$G[G_1[f(\cdot)](\circ), \ldots, G_n[f(\cdot)](\circ)](x) = G[G_1[f], \ldots, G_n[f]](x), \tag{B.48}$$

where the context should make it clear that the various terms require arguments to be inputted. Furthermore, we shall often omit the integrals and the arguments (x) and (y) in terms like

$$\frac{\partial F[G[f(\cdot)](\circ)]}{\partial f(y)} = \int d^d x \, \frac{\partial F[G[f(\cdot)](\circ)]}{\partial G[f(\cdot)](x)} \frac{\partial G[f(\cdot)](x)}{\partial f(y)}. \tag{B.49}$$

Instead we shall write

$$\frac{\partial F[G[f(\cdot)](\circ)]}{\partial f(y)} = \frac{\partial F}{\partial G} \frac{\partial G}{\partial f}. \tag{B.50}$$

Our chain rule relations now read as:

$$\frac{\partial F[G_1, \ldots, G_n]}{\partial f} = \sum_{k=1}^{n} \frac{\partial F}{\partial G_k} \frac{\partial G_k}{\partial f} \tag{B.51a}$$

$$\delta F = \sum_{k=1}^{n} \frac{\partial F}{\partial G_k} \delta G_k \tag{B.51b}$$

$$\partial_\mu G[G_1, \ldots, G_n] = \sum_{k=1}^{n} \frac{\partial G}{\partial G_k} \partial_\mu G_k. \tag{B.51c}$$

Appendix C

Energy loss predicts no v_2 in small systems

C.1 Comparison to CUJET2.0 formalism

Here, we present a comparison of the CUJET2.0 formalism [183] to the DGLV formalism presented in Sec. 3.2.1. The purpose of this comparison is show that the formalism used in Chapter 3 is mutually consistent with the CUJET2.0 formalism, and that the differences between the two formalisms are due to different conventions.

The kernel of a single gluon emission in the CUJET2.0 formalism is given by the relation (*cf.* eq. B.17 in [183])

$$\begin{aligned} x_E \frac{dN_g^{n=1}}{dx_E}(\mathbf{x}_0, \phi) =& \frac{18 C_R \alpha_s^3}{\pi^2} \frac{4+n_f}{16+9n_f} \int d\tau \rho_C(\mathbf{z}) \int d\mathbf{k} \int d\mathbf{q} |\tilde{v}(\mathbf{q})|^2 \\ & \times \frac{-2(\mathbf{k}-\mathbf{q})}{(\mathbf{k}-\mathbf{q})^2 + \chi^2(\mathbf{z})} \left(\frac{\mathbf{k}}{\mathbf{k}^2 + \chi^2(\mathbf{z})} - \frac{(\mathbf{k}-\mathbf{q})}{(\mathbf{k}-\mathbf{q})^2 + \chi^2(\mathbf{z})} \right) \\ & \times \left(1 - \cos\left(\frac{(\mathbf{k}-\mathbf{q})^2 + \chi^2(\mathbf{z})}{2x_+ E} \tau \right) \right) \\ & \times \left(\frac{x_E}{x_+} \right) J\left(x_+(x_E)\right) \end{aligned} \tag{C.1}$$

where $\mathbf{z} \equiv (x_0 + \tau\cos\phi, y_0 + \tau\sin\phi; \tau)$ and the medium density ρ_C in the CUJET2.0

formalism is taken as

$$\rho_C \equiv \rho_q + \rho_g \tag{C.2a}$$

$$= \frac{(16+n_f)\zeta(3)}{\pi^2} T^3 \tag{C.2b}$$

$$= \frac{16+n_f}{4(4+n_f)} \rho. \tag{C.2c}$$

In eq. C.2b, we have made use of the thermodynamic relations in eq. 3.43, while in eq. C.2c we have used the definition of the medium density ρ as given in eq. 3.43e. The potential $|\tilde{v}(\mathbf{q})|^2$ in CUJET2.0 is given by

$$|\tilde{v}(\mathbf{q})|^2 = \frac{1}{\mathbf{q}^2\left(\mathbf{q}^2+\mu^2\right)}, \tag{C.3}$$

while the χ^2 parameter is defined as

$$\chi^2 = M^2 x_+^2 + m_g^2(\mathbf{z})\left(1-x_+\right) \approx M^2 x_+^2 + m_g^2, \tag{C.4}$$

The gluon fractional energy x_E and fractional momentum x_+ are related via

$$x_+\left(x_E\right) = \frac{1}{2} x_E \left(1+\sqrt{1-\left(\frac{k_\perp}{x_E E}\right)^2}\right), \tag{C.5}$$

and the Jacobian $J\left(x_+\right)$ in eq. C.1 is given by

$$J\left(x_+\left(x_E\right)\right) \equiv \frac{dx_+}{dx_E} = \frac{1}{2}\left(1+\left(1-\left(\frac{k_\perp}{x_E E}\right)^2\right)^{-1}\right). \tag{C.6}$$

To match the CUJET2.0 formalism to the DGLV formalism presented in eq. 3.11, we take $x_+ \to x$, $\phi \to 0$ and $\tau \to z$.

C.2 Uncertainty on ψ_2^{hard} extraction

In this section we explore whether the decorrelation between the hard and soft sectors (fig. 3.37) is due to numerical uncertainties associated with the extraction of ψ_2^{hard}.

To explore how large the uncertainty due to the finite set of angles used in the extraction of ψ_2^{hard} is, we perform a bootstrap analysis [277]. Our procedure is outlined as follows: for each event, ℓ, we extract $\psi_2^{\text{hard},\ell}$ using eq. 3.69 where the R_{AB}^{ℓ} in eq. 3.69 is calculated by linearly interpolating through the full set of 20 angles. We then randomly remove 5 angles from the set of 20 angles and extract $\psi_2^{\text{hard},\ell,b}$ with

$$\psi_n^{\text{hard},\ell,b} = \frac{1}{n}\text{arctan2}\left(\int_0^{2\pi} d\phi\, R_{AB}^{\ell,b}(\phi)\cos(n\phi), \int_0^{2\pi} d\phi\, R_{AB}^{\ell,b}(\phi)\sin(n\phi)\right), \tag{C.7}$$

where the $R_{AB}^{\ell,b}$ in eq. C.7 is calculated by linearly interpolating through the remaining 15 angles; this process is repeated $B = 100$ times (other choices of B lead to similar results) to obtain a set of data of the form

$$\{\psi_n^{\text{hard},\ell,1}, \psi_n^{\text{hard},\ell,2}, \ldots, \psi_n^{\text{hard}\ell,B}\}. \tag{C.8}$$

We then calculate the standard error with the following [277]

$$\sigma_{SE}^{\ell} = \sqrt{\frac{1}{B-1}\sum_{b=1}^{B}(\psi_n^{\text{hard}\ell,b} - \psi_n^{\text{hard},\ell})^2}. \tag{C.9}$$

To obtain the standard error for each collision system per centrality class, σ_{SE}, we average the standard error from eq. C.9 over all events in the centrality class.

In fig. C.1, we show the average standard error σ_{SE} for ψ_2^{hard} for $\text{Pb} + \text{Pb}$ (gray), $\text{Ne} + \text{Ne}$ (green), $\text{O} + \text{O}$ (red), and $p + \text{Pb}$ (blue) collision systems over multiple centrality classes. We find a non-negligible uncertainty of $\sigma_{SE} \approx \pi/8$ across the majority of collision systems and centrality classes. However, a simple model in which the ob-

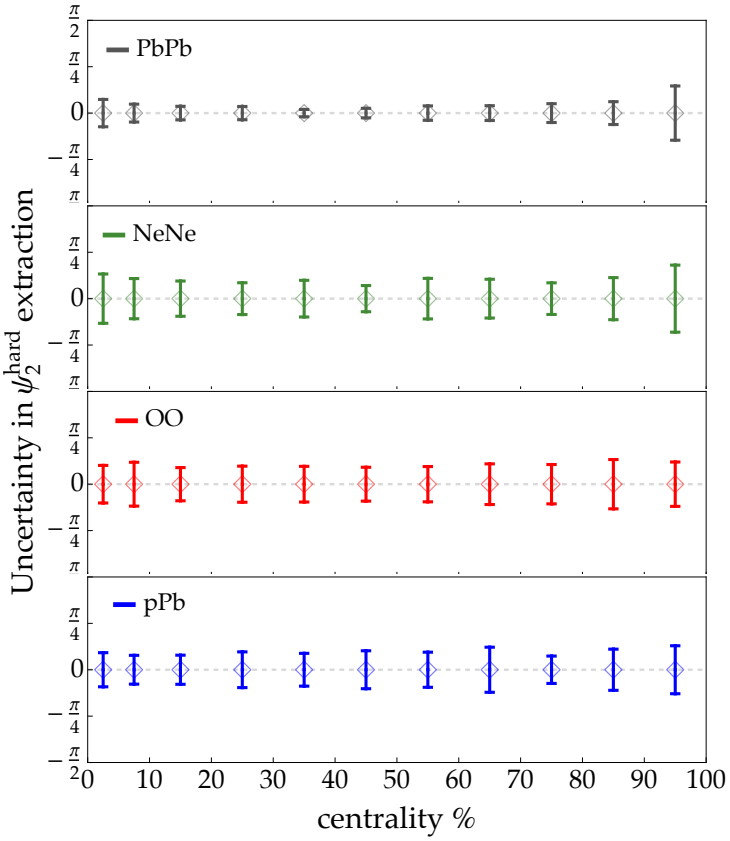

Figure C.1: Uncertainty of ψ_2^{hard} calculated using eq. C.9. Results are shown for $\mathrm{Pb}+\mathrm{Pb}$ (gray), $\mathrm{Ne}+\mathrm{Ne}$ (green), $\mathrm{O}+\mathrm{O}$ (red), and $p+\mathrm{Pb}$ (blue) collision systems as function of centrality with $p_T = 15$ GeV.

served distribution of $\psi_2^{\text{hard}} - \psi_2^{\text{soft}}$ is decomposed into contributions from numerical extraction uncertainties and genuine physical decorrelation shows that an uncertainty of this magnitude is insufficient to explain the decorrelation seen in fig. 3.37 for $\mathrm{Ne}+\mathrm{Ne}$, $\mathrm{O}+\mathrm{O}$, and $p+\mathrm{Pb}$. A genuine physical decorrelation between the hard and soft reference angles is therefore required in these systems.

Thus we conclude that the decorrelation between ψ_2^{hard} and ψ_2^{soft} is not an artifact of numerical uncertainties in the extraction of ψ_2^{hard}.

C.3 Comparison of energy loss model to all R_{AA} and v_n data

In this section we show a comparison of our model to all available high-p_T R_{AA} and v_n data in $\mathrm{Pb}+\mathrm{Pb}$, $\mathrm{Au}+\mathrm{Au}$, $\mathrm{p}+\mathrm{Pb}$, and $d+\mathrm{Au}$ collision systems from the LHC and RHIC. In fig. C.2, we show a comparison of our model to all available high-p_T R_{AA} data, while in fig. C.3, we show a comparison of our model to all available high-p_T v_n data.

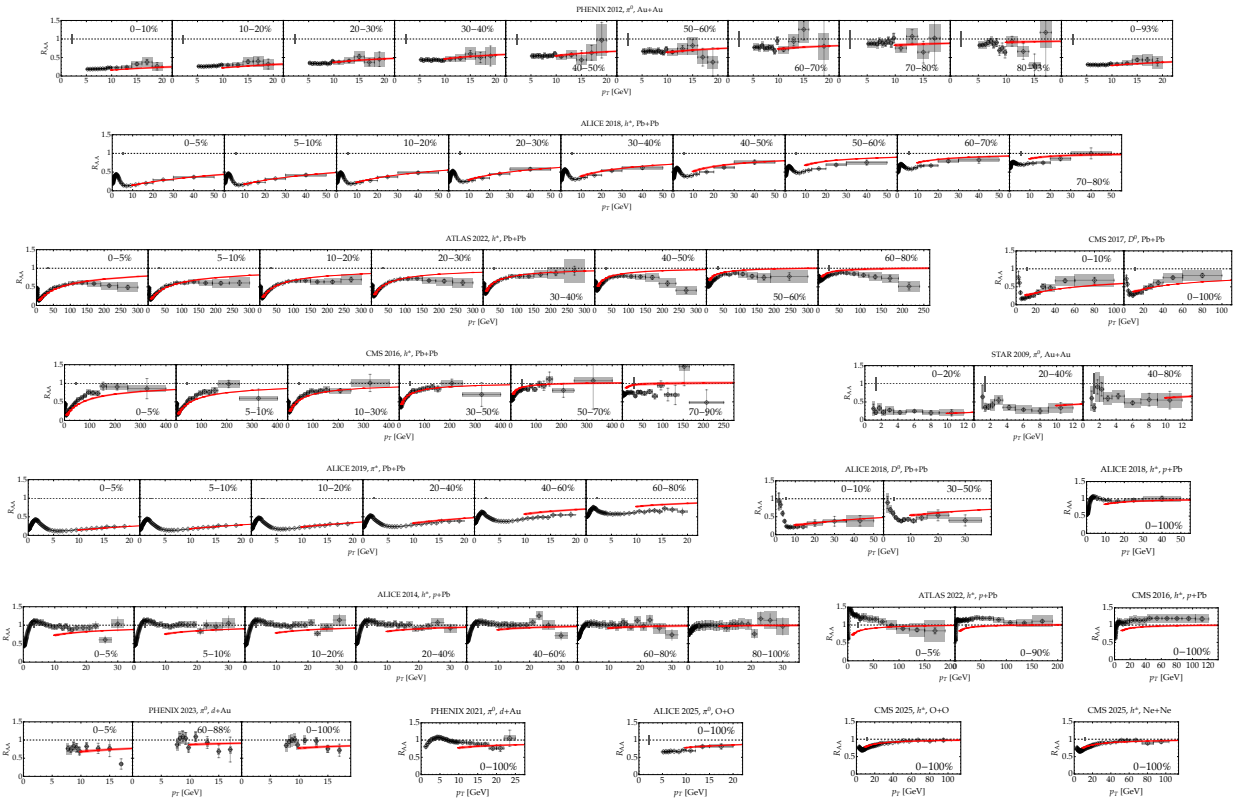

Figure C.2: Comparison of our model to all available R_{AB} data for $\mathrm{Pb}+\mathrm{Pb}$, $\mathrm{Au}+\mathrm{Au}$, $\mathrm{p}+\mathrm{Pb}$, $\mathrm{d}+\mathrm{Au}$, $\mathrm{O}+\mathrm{O}$, and $\mathrm{Ne}+\mathrm{Ne}$ collision systems. Experimental data are shown with statistical (bars) and systematic (boxes) uncertainties, while theory results are shown in red with statistical (bars) and systematic (bands) uncertainties, along with central values (lines). Data are taken from ALICE 2014 $h^{\pm}$ $p+\mathrm{Pb}$ [278], ALICE 2018 D^0 $\mathrm{Pb}+\mathrm{Pb}$ [226], ALICE 2018 $h^{\pm}$ $\mathrm{Pb}+\mathrm{Pb}$ [227], ALICE 2018 $h^{\pm}$ $p+\mathrm{Pb}$ [227], ALICE 2019 $\pi^{\pm}$ $\mathrm{Pb}+\mathrm{Pb}$ [231], ALICE 2025 π^0 $\mathrm{O}+\mathrm{O}$ [154], ATLAS 2022 $h^{\pm}$ $\mathrm{Pb}+\mathrm{Pb}$ [141], ATLAS 2022 $h^{\pm}$ $p+\mathrm{Pb}$ [141], CMS 2016 $h^{\pm}$ $\mathrm{Pb}+\mathrm{Pb}$ [77], CMS 2016 $h^{\pm}$ $\mathrm{Pb}+\mathrm{Pb}$ [77], CMS 2016 $h^{\pm}$ $p+\mathrm{Pb}$ [77], CMS 2017 D^0 $\mathrm{Pb}+\mathrm{Pb}$ [228], CMS 2025 $h^{\pm}$ $\mathrm{Ne}+\mathrm{Ne}$ [153], CMS 2025 $h^{\pm}$ $\mathrm{O}+\mathrm{O}$ [153], PHENIX 2008 π^0 $\mathrm{Au}+\mathrm{Au}$ [230], PHENIX 2012 π^0 $\mathrm{Au}+\mathrm{Au}$ [222], PHENIX 2021 π^0 $d+\mathrm{Au}$ [279], PHENIX 2023 π^0 $d+\mathrm{Au}$ [147], STAR 2009 π^0 $\mathrm{Au}+\mathrm{Au}$ [280].

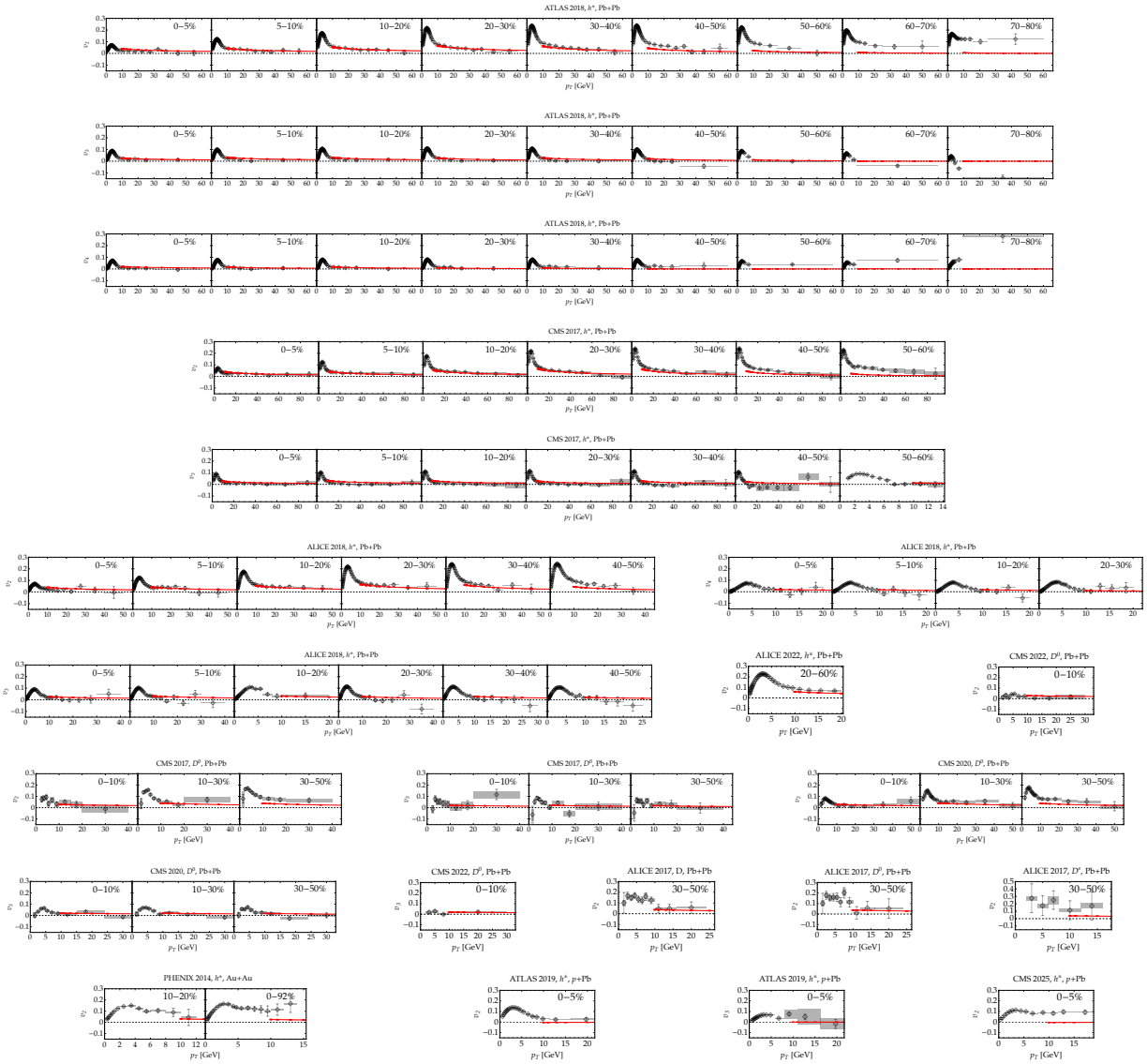

Figure C.3: Comparison of our model to all available v_n data for $\mathrm{Pb}+\mathrm{Pb}$, $\mathrm{Au}+\mathrm{Au}$, and $\mathrm{p}+\mathrm{Pb}$ collision systems. Experimental data are shown with statistical (bars) and systematic (boxes) uncertainties, while theory results are shown in red with statistical (bars) and systematic (bands) uncertainties, along with central values (lines). Data are taken from ALICE 2017 D^0 $\mathrm{Pb}+\mathrm{Pb}$ [232], ALICE 2017 D $\mathrm{Pb}+\mathrm{Pb}$ [232], ALICE 2018 $h^{\pm}$ $\mathrm{Pb}+\mathrm{Pb}$ [229], ALICE 2022 $h^{\pm}$ $\mathrm{Pb}+\mathrm{Pb}$ [149], ATLAS 2018 $h^{\pm}$ $\mathrm{Pb}+\mathrm{Pb}$ [211], ATLAS 2019 $h^{\pm}$ $p+\mathrm{Pb}$ [148], CMS 2017 D^0 $\mathrm{Pb}+\mathrm{Pb}$ [209], CMS 2017 $h^{\pm}$ $\mathrm{Pb}+\mathrm{Pb}$ [210], CMS 2020 D^0 $\mathrm{Pb}+\mathrm{Pb}$ [213], CMS 2022 D^0 $\mathrm{Pb}+\mathrm{Pb}$ [214], CMS 2025 $h^{\pm}$ $p+\mathrm{Pb}$ [150], PHENIX 2014 $h^{\pm}$ $\mathrm{Au}+\mathrm{Au}$ [281].